

# Spin-valley optoelectronics based on two-dimensional materials.

**Thèse N° 7473**

Présentée le 30 août 2019

à la Faculté des sciences et techniques de l'ingénieur  
Laboratoire d'électronique et structures à l'échelle nanométrique  
Programme doctoral en microsystèmes et microélectronique

pour l'obtention du grade de Docteur ès Sciences

par

**Dmitrii UNUCHEK**

Acceptée sur proposition du jury

Prof. E. D. N. Matioli, président du jury  
Prof. A. Kis, directeur de thèse  
Prof. T. Korn, rapporteur  
Prof. B. Urbaszek, rapporteur  
Prof. O. Yazyev, rapporteur

2019



Don't drink, don't love  
But keep compliance  
You have only one life  
So dedicate it to science

*Folklore*

To my dear Lena  
To my parents



# Acknowledgments

This section is dedicated to the people whose influence shaped my four-year-long PhD journey. Their support and invaluable contributions made this thesis possible.

I would like to start with expressing my gratitude to my supervisor Prof. Andras Kis for giving me an opportunity to be a part of his group with an outstanding environment and cutting edge equipment. I am grateful for his ideas and all the challenging but interesting projects I had a chance to work on during my doctoral work. I would like to thank Andras for the motivation, support, and guidance.

I am also very grateful to the thesis jury members: Prof. Elisa Matioli, Prof. Oleg Yazev, Prof. Bernhard Urbaszek and Prof. Tobias Korn for their time and efforts in improving this thesis, but also for interesting questions and useful discussions raised during the defense.

I would like to thank my closest collaborators Ahmet, Alberto and Juanfra. Days and nights spent on experimental measurements and scientific discussions brought us together as close friends, and I hope this friendship will last long after my graduation. I admire Ahmet's scientific vision and experience, which brought a lot of value in this work. I wish him to find a faculty position of his dream. I was also inspired by Alberto's creative and technology-oriented thinking as well as by Juanfra's passion for optics. I am sure they will make more scientific discoveries, and I wish them smooth thesis defense in the nearest future. It was a real pleasure but also big luck to work in one team with these bright minds.

Further, I am very grateful to the people I met in the laboratory four years ago for their support, advice and guidance. Particularly I would like to thank Oriol, Dmitry, Kolyo and Yen-Cheng, who taught me optical experiments, microfabrication, monolayer transfer and many more. Their hard work and dedication to research inspired me for the next years. I want to thank Dmitry for all scientific discussions and useful suggestions he made regarding my projects. I am very grateful to Kolyo and Yen-Cheng for their kindness and sense of humor, for all those bright moments in my memory. I am also grateful to the Dumitru and HoKwon for their hard work in material growth.

## Acknowledgments

---

I also would like to thank younger group members who recently joined the LANES group: Yanfei, Cheol-Yeon, Utku, Zhing, Zhe, Mukesh and Guilherme. I am very grateful for their help, advice and support.

Special thanks go to the wonderful members of LBEN group: Evgenii, Martina and Michael, not only for collaboration but also for a wonderful time spent together. I am also grateful to their supervisor, Prof. Aleksandra Radenovic for all her help and advice.

Next, I would like to acknowledge the people with whom we organized a summer school in Davos. The hard work of Alberto, Juan, Li Bing and Alex, led to the smashing success of this event. Although this initiative appeared to consume a lot of time and required a lot of work, the effort of all organizers definitely worth it. It was a unique experience and I truly enjoyed that time of the close work with co-organizers.

I am also thankful for the administrative support of Souad whose help with all the challenges is very much appreciated. In addition, I would like to thank CMi cleanroom staff members, and in particular Zdenek, Remy and Guy for their help in microfabrication, but also for their kindness and patience in resolving technical issues.

I am also grateful to Andras, Alberto, Ahmet and Juan for proofreading this thesis, which significantly improved its readability. I am also sending to France my thank you to Lena and Ivan who helped me a lot with the french version of the thesis abstract.

Moving beyond the colleagues, I am very grateful to my flatmates Ivan, Masha, Mike and Sergey for their friendship and for the fun moments we spent together.

My deepest gratitude goes to my parents for all their love, support and dedication. I am very grateful for all those efforts they invested into me and my education. I am also grateful to my brother who was guiding me for many years, for shaping me when I was growing up and for our current friendship.

Finally, I would like to acknowledge my beloved Lena who tolerates me for almost 8 years. Your patience is truly exceptional. Thank you for your love and smiles. Thank you for sharing the best moments of my life. Thank you for inspiring me and motivating me for new adventures. Thank you for making me a better version of myself. Thank you for everything!

*Lausanne, July 2019*

*Dmitrii Unuchek*

# Abstract

Two-dimensional (2D) materials, in particular graphene and transition metal dichalcogenides (TMDC), have attracted great scientific interest over the last decade, revealing exceptional mechanical, electrical and optical properties. Owing to their layered nature, subnanometer-thick single-layer forms of these crystals can be chemically grown or mechanically isolated, representing an ultimately scaled-down platform for further miniaturization of electronic devices. Indeed, the large family of 2D materials contains hundreds of members, including metals, semiconductors, insulators, and others, covering the whole spectrum of potential applications. Availability of all necessary building blocks for the construction of all-2D solid-state devices makes this platform ideal for fabrication of ultrathin, transparent and flexible devices.

Extensively investigated graphene has demonstrated excellent electrical properties. However, the absence of a bandgap is an obstacle for its interaction with light and therefore limits applications in optics. In this aspect, atomically thin TMDC semiconductors appear to be an alternative, more promising platform, as they possess a direct band gap in the visible range in the monolayer form. Despite being only three atoms thick, these semiconductors demonstrate exceptionally large light absorption, efficient light emission, and strong light-matter interaction, attracting justified interest from the optics community. We will focus on their potential applications for optoelectronics in Chapter 4.

Even more, broken inversion symmetry and strong spin-orbit coupling in single-layer TMDC crystals reveal a new quantum number, the so-called valley index. Indeed, this unique degree of freedom of charge carriers is known for some materials since the 1970s. However, in the case of 2D semiconductors, spin-valley locking mechanism and valley-contrasting optical selection rules open new ways for addressing, manipulation and sensing of this pseudospin, opening the whole new field of valleytronics. Due to the large splitting of the valence band, spin and valley degree of freedom become locked in these atomically thin materials. We employ this unique feature in Chapter 5 for indirect injection of spins into graphene by pumping valley polarized carriers in an adjacent TMDC monolayer. Being gapless, graphene does not allow direct optical injection of spins.

Another striking feature of 2D materials is their unique ability to be stacked in vertical heterostructures with strong electrical coupling between layers. The weak van der Waals

## Abstract

---

force, which keeps components together, provides freedom in the assembly process, so that a lattice mismatch or a twist angle become unimportant in the first approximation. This provides a novel platform for harvesting complementary properties of the constituent materials, allowing the engineering of new artificial meta-materials as we demonstrate in Chapter 6. Furthermore, synergistic effects in van der Waals heterostructures enable completely new properties and phenomena, which do not exist in the single materials, with twist angle being an important knob for tuning these effects. We observe and exploit such novel phenomena arising in heterostructures of 2D semiconductors in the last chapter of this thesis.

On the way to the realization of practical optoelectronic and valleytronic applications, this thesis studies the fundamental aspects of rich spin-valley physics of atomically thin semiconductors.

**Keywords:** Two-dimensional (2D) materials, van der Waals heterostructures (vdW HS), transition metal dichalcogenides (TMDC), molybdenum disulphide ( $\text{MoS}_2$ ), molybdenum diselenide ( $\text{MoSe}_2$ ), tungsten diselenide ( $\text{WSe}_2$ ), graphene, optoelectronics, spin/valleytronics, photodetectors, light emitting diodes, interlayer excitons.



## Résumé

Matériaux bidimensionnels (2D), en particulier graphène et dichalcogénures de métaux de transition (TMDC) ont suscité un grand intérêt scientifique au cours de la dernière décennie révélant ses propriétés mécaniques, électriques et optiques exceptionnelles. Grace à sa structure en couches particulière, des monocouches sous-nanométriques de ces cristaux peuvent être cultivées chimiquement ou isolées mécaniquement, représentant une réduction ultime dans la direction verticale pour la miniaturisation des appareils électroniques. En effet, la famille de matériaux bidimensionnels contient une grande variété de membres, parmi lesquels les métaux, semi-conducteurs, isolants et autres, couvrant le spectre complet des applications potentielles. La disponibilité de toutes les composantes nécessaires pour la construction de dispositifs d'état-solide rend ce type de matériaux idéal pour la fabrication de dispositifs ultraminces, transparentes et flexibles.

Le graphène, qui a été profondément étudié, a démontré d'excellentes propriétés électriques. Cependant l'absence de la bande interdite constitue un obstacle pour son interaction avec la lumière et limite donc ses applications en optique. Pour cette raison, les semi-conducteurs de TMDC semblent être une alternative car ils possèdent une bande interdite directe dans le domaine du visible lorsqu'ils sont amincis en forme de monocouches. Ayant seulement trois atomes d'épaisseur, ces semi-conducteurs présentent l'absorption de la lumière exceptionnellement importante, l'émission de lumière efficace et l'interaction lumière-matière forte. Ces particularités suscitent l'intérêt croissant de la communauté optique. Nous effectuons des recherches plus approfondies de leurs applications potentielles pour l'optoélectronique au Chapitre 4.

De plus, la symétrie de l'inversion brisée et un fort couplage spin-orbite dans des cristaux TMDC monocouches révèlent un nouveau nombre quantique, l'index de vallée. En effet, ce degré de liberté unique de porteurs de charges est connu pour certains matériaux depuis les années 1970. Pourtant, dans le cas des semi-conducteurs 2D le mécanisme de blocage de spin-vallée et les règles de la sélection optique du contraste dans la vallée ouvrent de nouvelles façons d'adresser, de manipuler et de détecter ce pseudospin, ouvrant ainsi le tout nouveau paradigme de la valléetronique. En raison de la grande scission de la bande de valence, les degrés de liberté de le spin et de la vallée devient enfermés dans ces matériaux atomiquement minces. Nous utilisons cette caractéristique unique au Chapitre 5 pour l'injection indirecte de spins dans le graphène en pompant des porteurs polarisés de

la vallée dans la monocouche TMDC adjacente. N'étant pas étalé, le graphène ne permet pas l'injection optique directe de spins.

Une autre caractéristique remarquable des matériaux 2D est leur capacité unique à être empilés dans des hétérostructures verticales avec un fort couplage électrique entre les couches. Les forces faibles de van der Waals, qui gardent les composantes ensemble, offrent une liberté dans le processus d'assemblage, de sorte qu'une discordance des réseaux cristallins ou un désalignement en torsion devient négligeables dans l'approximation au premier ordre. Ceci fournit une nouvelle plateforme pour exploiter les propriétés complémentaires des matériaux constitutifs, permettant ainsi de concevoir de nouveaux matériaux artificiels, comme il sera démontré en détail au Chapitre 6. Par ailleurs, les effets synergiques dans les hétérostructures de van der Waals développent des propriétés et des phénomènes totalement nouveaux qui n'existaient pas dans les matériaux indépendants. L'angle de torsion a un rôle important pour l'ajustement de ces effets. Nous observons et exploitons ces nouveaux phénomènes apparaissant dans les hétérostructures de semi-conducteurs 2D dans le dernier chapitre de cette thèse.

Sur le chemin de la réalisation d'applications optoélectroniques et valléetroniques, cette thèse étudie les aspects fondamentaux de la physique spin-vallée de semi-conducteurs atomiquement minces.

**Mots-clés :** Matériaux bidimensionnels (2D), hétérostructures de van der Waals (vdW HS), dichalcogénures de métaux de transition (TMDC), disulfure de molybdène ( $\text{MoS}_2$ ), diséléniure de molybdène ( $\text{MoSe}_2$ ), diséléniure de tungstène ( $\text{WSe}_2$ ), graphène, opto-électronique, spin/valléetronique, photodétecteur, diode électroluminescente, excitons intercouches.

# Contents

<b>Acknowledgments</b>	<b>i</b>
<b>Abstract</b>	<b>iii</b>
<b>Contents</b>	<b>ix</b>
<b>List of Figures</b>	<b>xi</b>
<b>1 Introduction</b>	<b>1</b>
<b>2 Properties and synthesis of TMDCs</b>	<b>3</b>
2.1 Introduction . . . . .	3
2.2 Two-dimensional materials . . . . .	4
2.2.1 Semimetallic graphene . . . . .	4
2.2.2 Semiconducting TMDCs . . . . .	7
2.2.3 Insulating boron nitride . . . . .	14
2.2.4 Other materials . . . . .	14
2.3 Van der Waals heterostructures . . . . .	15
2.3.1 Alignment matters — moiré superlattices . . . . .	16
2.3.2 Band-alignment matters — interlayer excitons . . . . .	19
2.4 Conclusion and outlook . . . . .	21
<b>3 Experimental techniques</b>	<b>23</b>
3.1 Introduction . . . . .	23
3.2 Device fabrication . . . . .	23
3.2.1 Monolayer isolation . . . . .	24
3.2.2 Heterostructures production . . . . .	29
3.2.3 Microfabrication . . . . .	32
3.3 Electrical measurement techniques . . . . .	37
3.3.1 Electrostatic gating . . . . .	37
3.3.2 Four-terminal sensing . . . . .	40
3.3.3 Lock-in amplifier . . . . .	41
3.4 Optical measurement techniques . . . . .	43

## Contents

---

3.4.1	Photocurrent . . . . .	43
3.4.2	Electroluminescence . . . . .	45
3.4.3	Photoluminescence . . . . .	45
3.4.4	Other types of measurements . . . . .	48
<b>4</b>	<b>Optoelectronic devices</b>	<b>51</b>
4.1	Introduction . . . . .	51
4.2	Light emitting diodes . . . . .	53
4.2.1	Introduction . . . . .	53
4.2.2	LED based on a vertical p-n junction . . . . .	53
4.2.3	LED based on a lateral p-n junction with an Al <sub>2</sub> O <sub>3</sub> gate dielectric . . . . .	57
4.2.4	LED based on a lateral p-n junction with an h-BN gate dielectric . . . . .	64
4.2.5	Conclusion . . . . .	70
4.3	MoS <sub>2</sub> Photodetector integrated with a photonic circuit . . . . .	71
4.3.1	Introduction . . . . .	71
4.3.2	Fabrication and optimization of photonic structures . . . . .	72
4.3.3	Photodetector integrated with waveguide . . . . .	75
4.3.4	Improved architectures of the integrated photodetector . . . . .	83
4.4	Conclusion and outlook . . . . .	88
<b>5</b>	<b>Optospintronic devices</b>	<b>89</b>
5.1	Introduction . . . . .	89
5.2	Optical spin injection in graphene <i>via</i> proximity coupling with WSe <sub>2</sub> . . . . .	91
5.2.1	Device fabrication . . . . .	92
5.2.2	Graphene spin channel characterization . . . . .	93
5.2.3	Optospintronic device characterization . . . . .	96
5.2.4	Optical spin injection into graphene . . . . .	97
5.2.5	Control experiment — half-wave modulation . . . . .	100
5.2.6	Control experiment — ellipticity dependence . . . . .	102
5.2.7	Control experiment — constant polarization . . . . .	104
5.2.8	Conclusion . . . . .	106
5.3	Modulation of spin transport in a graphene-WSe <sub>2</sub> heterostructure . . . . .	107
5.3.1	Introduction . . . . .	107
5.3.2	Heterostructure characterization . . . . .	108
5.3.3	Spin transport characterization . . . . .	109
5.3.4	Field-effect spin switch . . . . .	112
5.3.5	Optical spin switch . . . . .	114
5.4	Conclusion and outlook . . . . .	116

<b>6</b>	<b>Excitonic devices</b>	<b>117</b>
6.1	Introduction . . . . .	117
6.2	State-of-the-art . . . . .	119
6.3	Electrical control of interlayer excitons . . . . .	121
6.3.1	Introduction . . . . .	121
6.3.2	Optical characterization of interlayer excitons . . . . .	121
6.3.3	Electrical tuning of interlayer excitons . . . . .	126
6.3.4	Electrical control of polarization state . . . . .	133
6.3.5	Interlayer excitons in magnetic field . . . . .	138
6.3.6	Discussion . . . . .	142
6.3.7	Additional structures . . . . .	145
6.3.8	Conclusion . . . . .	146
6.4	Valley-polarized excitonic transistor . . . . .	147
6.4.1	Introduction . . . . .	147
6.4.2	Towards electrical control of exciton diffusion . . . . .	148
6.4.3	Heterotrilayer device . . . . .	149
6.4.4	Optical characterization . . . . .	151
6.4.5	Diffusion boosted by high exciton density . . . . .	155
6.4.6	Valley excitonic transistor . . . . .	159
6.4.7	Excitonic trap . . . . .	163
6.4.8	Towards high-temperature operation . . . . .	167
6.4.9	Conclusion . . . . .	169
6.5	Room temperature excitonic transistor . . . . .	171
6.5.1	Introduction . . . . .	171
6.5.2	MoS <sub>2</sub> /WSe <sub>2</sub> interlayer excitons . . . . .	171
6.5.3	Excitonic switch . . . . .	173
6.5.4	Exciton drift currents . . . . .	184
6.5.5	Reconfigurable potential . . . . .	185
6.5.6	Discussion . . . . .	187
6.5.7	Conclusion . . . . .	188
6.6	Conclusion and outlook . . . . .	189
<b>7</b>	<b>Conclusion</b>	<b>191</b>
	<b>Abbreviations &amp; Symbols</b>	<b>193</b>
	<b>Bibliography</b>	<b>223</b>
	<b>List of Publications</b>	<b>225</b>
	<b>Curriculum Vitae</b>	<b>227</b>



# List of Figures

2.1	Representative two-dimensional materials . . . . .	3
2.2	Quantum charge transport in graphene monolayer . . . . .	5
2.3	Spin transport in graphene . . . . .	6
2.4	Single-layer MoS <sub>2</sub> transistor . . . . .	8
2.5	Single layer TMDCs . . . . .	9
2.6	Excitons in single-layers of TMDCs . . . . .	10
2.7	Optical initialization of a valley state . . . . .	12
2.8	Valley hall effect in a bilayer MoS <sub>2</sub> . . . . .	13
2.9	Van der Waals heterostructures . . . . .	15
2.10	Moiré patterns in van der Waals heterostructures . . . . .	17
2.11	Magic-angle twisted bilayer graphene . . . . .	18
2.12	Interlayer excitons in van der Waals heterostructures . . . . .	19
3.1	Mechanical exfoliation . . . . .	24
3.2	Imaging of semiconducting monolayers . . . . .	26
3.3	Imaging of non-semiconducting monolayers . . . . .	28
3.4	Transfer techniques . . . . .	30
3.5	Microfabrication process flow . . . . .	33
3.6	Metal deposition . . . . .	34
3.7	Etching . . . . .	36
3.8	Dual gating . . . . .	39
3.9	Four-terminal sensing . . . . .	41
3.10	Lock-in amplifier . . . . .	42
3.11	Optical setup for PD and LED . . . . .	44
3.12	Optical setup for PL . . . . .	47
3.13	Raman and reflection spectra . . . . .	49
4.1	Vertical p-n junction . . . . .	54
4.2	Characterization of the vertical heterostructure . . . . .	56
4.3	LED based on a lateral p-n junction . . . . .	58
4.4	Fabrication process of the lateral LED with the Al <sub>2</sub> O <sub>3</sub> dielectric layer . . . . .	59

## List of Figures

---

4.5	Electrical characterization of the lateral LED with an Al <sub>2</sub> O <sub>3</sub> dielectric layer . . . . .	60
4.6	Device with multiple junctions . . . . .	62
4.7	Degradation of the lateral LED with Al <sub>2</sub> O <sub>3</sub> dielectric layer . . . . .	63
4.8	Fabrication process of the lateral LED with the h-BN dielectric layer . . . . .	64
4.9	Electrical characterization of the lateral LED with the h-BN dielectric layer . . . . .	66
4.10	Optical characterization of the lateral LED with the h-BN dielectric layer . . . . .	68
4.11	Photocurrent generation in the lateral p-n junction . . . . .	69
4.12	MoS <sub>2</sub> -based photodetector integrated in a photonic circuit . . . . .	71
4.13	Fundamental modes of the waveguide . . . . .	72
4.14	Structural characterization of fabricated photonic structures . . . . .	73
4.15	Optical characterization of photonic structures . . . . .	74
4.16	Fabrication of integrated photodetector . . . . .	76
4.17	Effect of monolayer MoS <sub>2</sub> and metal contacts on light propagation in the waveguide . . . . .	78
4.18	Drain-source $I_{DS} - V_{DS}$ characteristics of the photodetector . . . . .	79
4.19	Optoelectronic properties of the photodetector . . . . .	80
4.20	Photocurrent maps . . . . .	82
4.21	Time dependency of the photoresponse . . . . .	83
4.22	Fabrication of photodetectors with alternative architecture . . . . .	84
4.23	Fast response and low-power operation of MoS <sub>2</sub> -based photodetectors . . . . .	85
4.24	MoS <sub>2</sub> photoluminescence on different substrates . . . . .	86
5.1	Schematics of the device . . . . .	91
5.2	Device fabrication . . . . .	92
5.3	Electrical characterization of the graphene spin valve . . . . .	94
5.4	Gate voltage-characterization of graphene spin valve . . . . .	95
5.5	Electrical and optical characterization of optospintronics devices . . . . .	97
5.6	Optical spin injection into graphene . . . . .	98
5.7	Non-local signal as a function of back gate voltage . . . . .	100
5.8	Non-local signal at half-wave modulation . . . . .	101
5.9	Ellipticity dependence of the non-local signal . . . . .	103
5.10	Non-local signal at constant polarization . . . . .	105
5.11	Schematic of the spin switch device . . . . .	107
5.12	Device characterization . . . . .	108
5.13	Non-local measurements of spin transport in graphene and heterostructure . . . . .	111
5.14	Field-effect spin switch using the WSe <sub>2</sub> /Gr heterostructure . . . . .	112
5.15	Gate dependent spin transport . . . . .	114
5.16	Optical spin switch . . . . .	115
6.1	State-of-the-art excitonic devices . . . . .	120



6.2	Optical characterization of a WSe <sub>2</sub> /MoSe <sub>2</sub> heterostructure . . . . .	122
6.3	Interlayer exciton doublet . . . . .	123
6.4	Excitation power dependence of interlayer exciton emission . . . . .	124
6.5	Temperature dependence of interlayer exciton emission . . . . .	125
6.6	Dual-gate device . . . . .	126
6.7	Device characterization . . . . .	128
6.8	Linear Stark effect . . . . .	129
6.9	Effect of electron concentration on interlayer exciton emission . . . . .	130
6.10	Effect of gating on the device optical properties . . . . .	132
6.11	Polarization-resolved PL . . . . .	134
6.12	Polarization resolved PL gate maps . . . . .	135
6.13	Electrical control of polarization . . . . .	136
6.14	Polarization switching action . . . . .	137
6.15	Effect of the magnetic field on intralayer excitons . . . . .	138
6.16	Effect of magnetic field on interlayer excitons . . . . .	140
6.17	Zeeman splitting of the interlayer doublet . . . . .	142
6.18	Atomic registries in the moiré pattern . . . . .	144
6.19	PL from additional structures . . . . .	146
6.20	Exciton transport modulation in the heterobilayer . . . . .	148
6.21	Heterotrilayer device fabrication and characterization . . . . .	150
6.22	Heterotrilayer device with h-BN spacer. . . . .	151
6.23	Optical characterization . . . . .	152
6.24	Temperature dependence of PL intensity and polarization . . . . .	153
6.25	Gate dependence of PL intensity and polarization . . . . .	154
6.26	Power dependence of the PL spectrum . . . . .	155
6.27	Exciton diffusion . . . . .	157
6.28	Fitting of the diffusion curves . . . . .	158
6.29	Effective diffusion length . . . . .	159
6.30	Numerical simulations . . . . .	160
6.31	Excitonic valley switch . . . . .	161
6.32	Cut-lines detailing the operation of the valley transistor device . . . . .	163
6.33	Electrostatic trap . . . . .	164
6.34	Electrostatic control of exciton concentration . . . . .	165
6.35	Valley-exciton switch operation at 100 K . . . . .	167
6.36	Exciton switch operation at 150 K . . . . .	168
6.37	Interlayer excitons in the WSe <sub>2</sub> /MoS <sub>2</sub> vdW heterostructure . . . . .	172
6.38	Schematic of the excitonic switch . . . . .	173
6.39	Heterostructure fabrication . . . . .	174
6.40	Device optical characterization . . . . .	175

## List of Figures

---

6.41 Numerical simulation of the interlayer exciton in the external field . . . . .	176
6.42 Modelling of exciton diffusion . . . . .	179
6.43 Excitonic transistor operation at room temperature . . . . .	180
6.44 Excitonic transistor input and output . . . . .	181
6.45 Exciton transistor . . . . .	182
6.46 Reference experiments . . . . .	182
6.47 Excitonic transistor characterization . . . . .	183
6.48 Biasing of the excitonic device . . . . .	184
6.49 Electrically reconfigurable energy landscape . . . . .	186
6.50 Schematic depiction of the control over the light emission . . . . .	187

# 1 Introduction

Solid-state devices utilize particles for their operation. A ubiquitous example is conventional electronics, which relies on the manipulation of the charge degree of freedom to transfer, store and process information. However, it has recently faced various obstacles with the maintenance of the constant scaling predicted by Moore's law [1]. Apart from challenges related to the efficient gating of an ultra-short channel, a big issue lurks in metallic interconnects used for signal transfer between processing units [2]. The dense packaging leads to increased power consumption and limited speed of data processing, due to the Joule heating and parasitic capacitance correspondingly. The need to improve the power efficiency of charge-based devices and circuits is motivating research into new paradigms that would rely on novel approaches and materials.

One of the promising approaches toward the improvement of electrical devices is the implementation of on-chip photonic networks for fast and energy efficient data transfer between processing nodes, in analogy to the wide-spread optical fibers for long-distance communication [3]. However, this would require electrical-to-optical interconnects for efficient transformation of the signal transferred with photons or electrons. In this aspect, two-dimensional materials rise as an attractive platform for miniature integrated optoelectronics, due to their atomic thickness, outstanding mechanical, electrical, and more importantly, optical properties, which we describe in Chapter 2. In Chapter 4 we employ these materials for a realization of required optoelectronic elements for electrical-to-optical interconnects.

To overcome the fundamental limitations of electrical devices, different degrees of freedom could be harnessed in new device concepts. Using the electron spin, for example, has been considered as an attractive alternative to charge-based devices [4]. Another possibility consists of manipulating the valley degree of freedom [5], associated with extremes of occupied band. In this regard, 2D semiconductors such as transition metal dichalcogenides are particularly attractive for valley manipulation, as their band structure

## Chapter 1. Introduction

---

has inequivalent valleys suitable for the realization of a binary pseudospin system [6]. Moreover, in these materials, optically initialized valley state can be further employed for spin transport due to the spin-valley locking effect. We employ this approach in Chapter 5, where we harvest complementary properties of graphene and TMDC monolayers for the realization of complex spin-valley devices for a new generation computational devices.

Another approach in the realization of innovative computing systems relies on indirect excitons in artificial heterostructures [7]. Excitons represent a natural interconnection between established electronic data processing and fast optical data transmission. While electron-based devices need a conversion to interface with optical systems, excitonic devices could directly link to optics, while at the same time maintaining high scalability in their size [8]. However, excitons in most bulk semiconductors exist only at cryogenic temperatures due to their small binding energies [9]. Recently, this limitation has been lifted by the discovery of room-temperature excitons in 2D semiconductors with large binding energies opening a new avenue for practical excitonic devices. In Chapter 6 we stack two semiconducting monolayers with type-II band alignment, in order to create a system with interlayer excitons where electrons and holes are hosted in different layers. This has several advantages: first, interlayer excitons have a vertical dipole moment, enabling the way for electrical manipulation; secondly, due to the spatial separation, their lifetime is greatly enhanced, revealing long-distance transport of these quasi-particles. We also employ long preservation of valley state by interlayer excitons for the demonstration of a polarization switch as well as the valley-excitonic transistor: new-generation quantum devices based on valley-encoded information.

In the last Chapter, we summarize achieved results of this thesis and give a short overlook on further research possibilities.

## 2 Physical properties of 2D materials

### 2.1 Introduction

The appearance and fast development of the 2D field started in 2004 with the physical isolation and further characterization of graphene - single layer form of graphite - by A. Geim and K. Novoselov [10]. From the beginning, these gapless materials showed unique electrical and mechanical properties, attracting enormous interest of the research community which resulted in delivering the Nobel prize to the two pioneers [11].

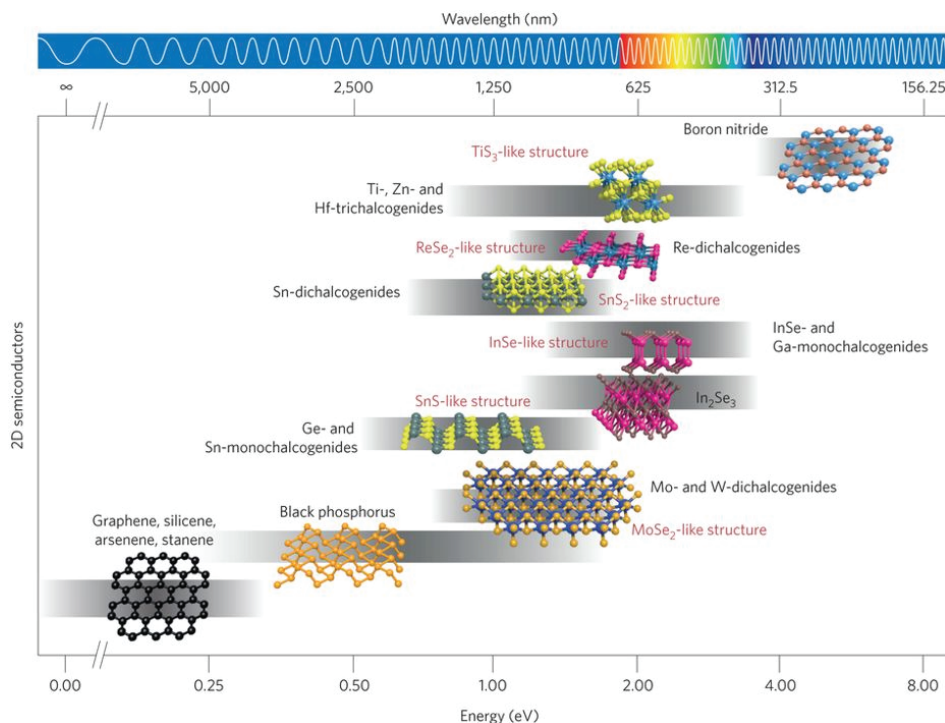


**Figure 2.1** – Representative two-dimensional materials. Available bandgap values ranging from several  $\mu\text{eV}$  in graphene, to visible spectra in TMDCs, and to 6 eV in h-BN. Figure reproduced from ref.[12] with permission of Nature Publishing Group.

However, the graphene is not the only two-dimensional material that holds promise for technological advances. The family of 2D materials has grown significantly beyond this semimetallic material, to include atomically thin insulators, superconductors, topological insulators and semiconductors with various bandgaps covering the whole spectra of potential applications in optics [12], as shown in Figure 2.1. Indeed, nowadays the library of materials, possible for exfoliation accounts hundreds of different species, and therefore we can not cover them all in this section. Instead, we focus on materials and properties, which are particularly important in the framework of this thesis. We also cover here some aspects of the heterostructures made out of these materials as they play a significant role in this work.

## 2.2 Two-dimensional materials

### 2.2.1 Semimetallic graphene

Graphene (Gr) is only one atom thick layer of carbon with honeycomb lattice structure, which realize an unusual electron band structure, presented in Figure 2.2a. The bandgap of this material is bridged in the corners of the first Brillouin zone (K-points), revealing zero-effective-mass linear dispersion of electrons in those points of symmetry, so-called Dirac cones.

Semiconductor-like energy diagram with a vanishing bandgap is revealed by the electrical field effect in graphene [10] with high channel resistivity recorded in the proximity of charge neutrality or Dirac point (Figure 2.2b). This exceptional appearance of the mass-less Dirac fermions made a whole new branch of relativistic effects accessible within low-dimensional condensed matter physics [13].

### Quantum effects in electrical transport

The low density of defects in graphene gives rise to ballistic transport of charge carriers on a micrometer scale [14]. This allowed observation of such quantum-mechanical macroscopic phenomena like quantum Hall effect (QHE)[15, 16], with typical Shubnikov–de Haas oscillations plotted in Figure 2.2c. Demonstration of QHE even at room temperature (though at extremely high magnetic field) [17] makes graphene a verily unique system in application to metrological standards.

Indeed, performance of this wonder material is often limited by the surrounding environment, which includes the underlying substrate. By excluding this factor in suspended or encapsulated devices, graphene has demonstrated mobility as large as one million

## 2.2. Two-dimensional materials

$\text{cm}^2/\text{V}\cdot\text{s}$  at  $10^{12} \text{ cm}^{-2}$  carrier density [14, 18], which is truly exceptional taking into account the atomic thickness of this material. Realization of extremely high quality devices allowed observation of another peculiar phenomenon, which relies on electron–electron interaction – fractional Quantum Hall effect [19, 20]. In Figure 2.2d we show a Landau fan demonstrating states with fractional filling factors.

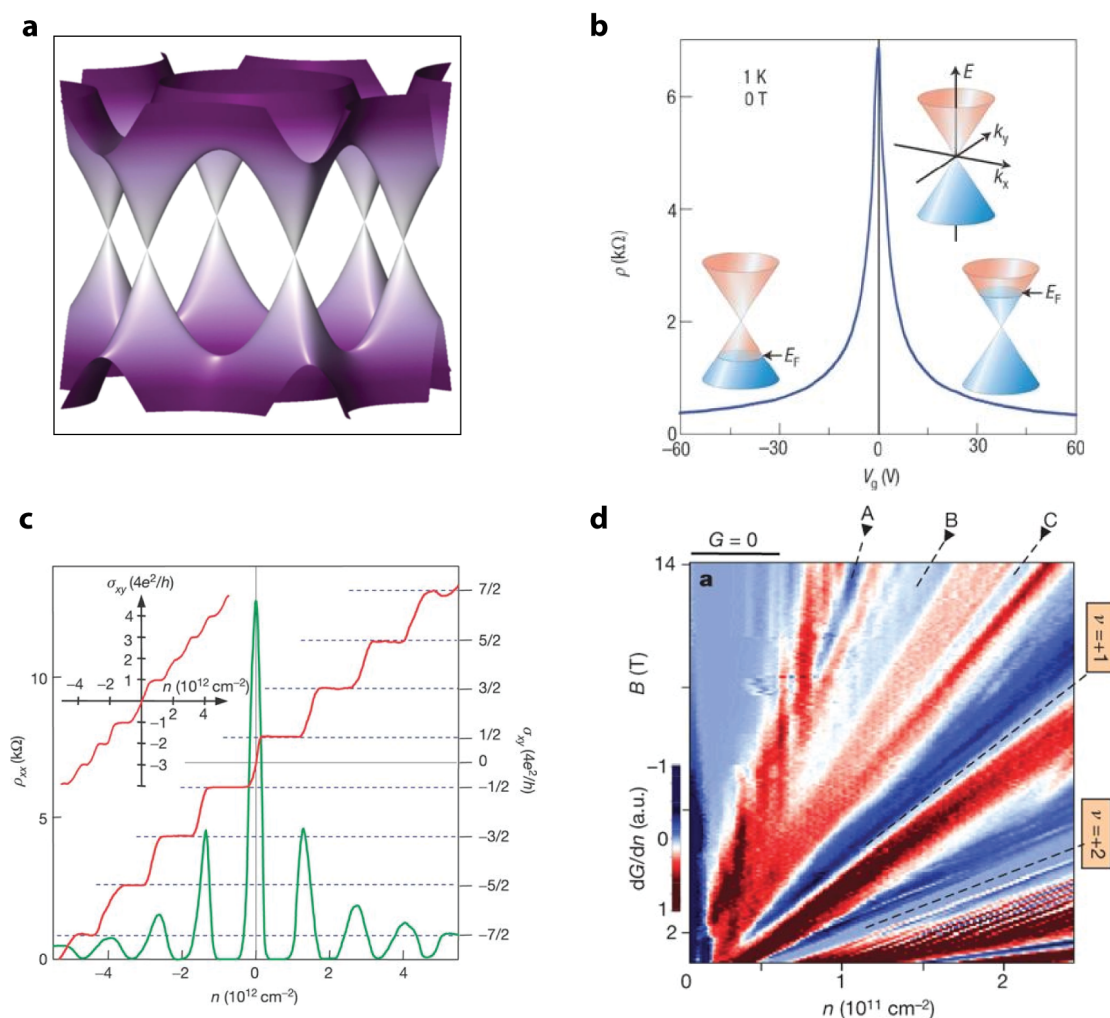


**Figure 2.2** – Quantum charge transport in graphene monolayer. (a) Band structure of graphene. Adapted from ref.[11] with permission of APS. (b) Electrical field effect in graphene. High resistance of channel conductivity reveals Dirac point. Inset shows position of the Fermi level in the conical band structure depending on the applied voltage. Adapted from ref.[13] with permission of Nature Publishing Group. (c) Quantum Hall effect in the graphene observed by measuring of Hall conductivity and longitudinal resistance. Adapted from ref.[15] with permission of Nature Publishing Group. (d) Landau fan diagram unfolding fractional quantum Hall effect. Adapted from ref.[19] with permission of Nature Publishing Group.

Spin transport

Apart from excellent charge carrier transport, graphene is also attractive for spintronic applications, which aims spin transport and processing as a new paradigm for logic devices. Combining in itself high carrier mobility and electrostatically controllable charge density, low spin-orbit coupling [21] and negligible hyperfine interaction [22], graphene appears to be an exceptional material for transporting spin-dependent current [20]. Indeed, it demonstrates the longest spin relaxation length achieved in any material system at room temperature [23, 24, 25, 26].

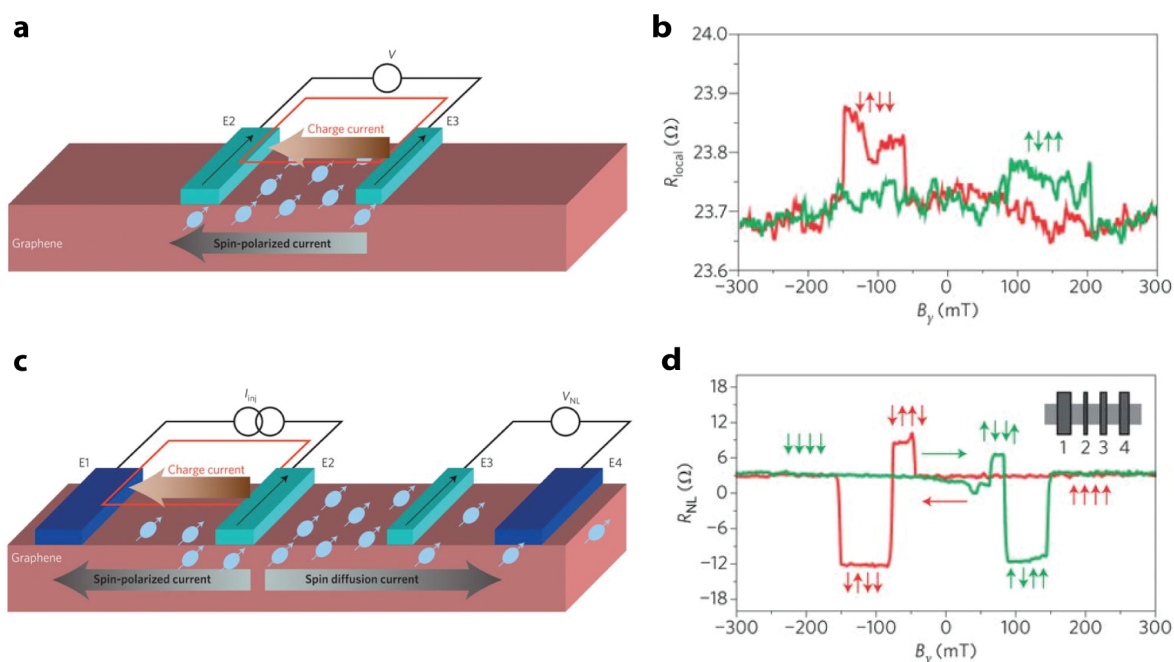


**Figure 2.3** – Spin transport in graphene. (a) Local spin transport measurement scheme and (b) the corresponding magnetoresistance signal in a graphene-based device. (c) Non-local spin transport measurement scheme and (d) the corresponding non-local resistance signal in a graphene-based device. Figure adapted from ref.[20] with permission of Nature Publishing Group.

In Figure 2.3 we present characterization of typical graphene-based spintronic devices that was used to demonstrate room temperature spin transport by N. Tombros *et al.* [23]. A schematic and a plot in Figure 2.3a,b shows local magnetoresistance measurements where spin and charge transport occurs in the idem channel. The same magnetic electrodes are used for polarization and analysis of the current. However, spin transport can be spatially isolated from the charge current under the 4-terminal non-local geometry, as presented in Figure 2.3c,d. One pair of electrodes is used for injection of spin-polarized current. While charge transport occurs between these electrodes, the spin diffuses in both directions



and can therefore be detected by another pair of magnetized electrodes, which probe the spin-related chemical potential of the system.

Although graphene proved to be a favorable candidate for spin transport, the weak spin-orbit coupling and the absence of spin-addressable optical selection rules appear to cause limitations on the pathway towards realization of a spin-logic device with efficient and non-destructive optical spin injection. Indeed, in Chapter 4 we will demonstrate that this problem can be overcome by employing hybrid structures made of two-dimensional materials.

### Optical properties

In sharp contrast to electrical and spintronic performance, graphene has quite poor optical properties. Because of the absence of a bandgap, it is not suitable for light emission, and light absorption is also limited. Therefore, graphene-based photodetectors demonstrate rather low sensitivity. These devices also suffer from large off-currents due to the same reason [27]. Nevertheless, graphene photodetectors can sense light in the wide range of wavelengths, including near- and infrared photons. They also demonstrate fast photoresponse in the GHz range [28] and can be easily integrated with photonic waveguides, making graphene a promising candidate for on-chip telecommunication solutions.

Indeed, opening a bandgap in graphene was explored as an approach to improve its optical performance. These methods include chemical functionalization, quantum confinement by narrowing it into nanoribbons, or exploiting bilayer flakes [29]. However an alternative for optoelectronic applications would be to employ other 2D crystals which possess semiconducting character. We focus on those materials in the following section.

### 2.2.2 Semiconducting TMDCs

Transition metal dichalcogenides (TMDCs) are a family of semiconducting materials with the common structure of  $\text{MX}_2$ , where layer of transition metal atoms (M) is sandwiched between two layers of chalcogen atom (X). Therefore, a single layer of this crystal has a thickness of 3 atoms with about 7 Å interlayer separation. In Figure 2.4a, we show the crystalline structure of molybdenum disulfide ( $\text{MoS}_2$ ), so far the most studied material of this family. This is due to its robustness, air stability and natural occurrence in the form of molybdenite mineral. However, in this thesis we will also study other TMDCs, like molybdenum diselenide ( $\text{MoSe}_2$ ) and tungsten diselenide ( $\text{WSe}_2$ ), with similar structures.

Similarly to graphite, compound layers of bulk TMDC are weakly bounded to each other by the van der Waals (vdW) force. They can be therefore isolated in a stable single layer

form, which demonstrate exceptional mechanical [30, 31], electrical [32, 33, 34, 35] and optical [36, 37, 38] properties, with an unique spin-valley physics [6, 39, 40].

### Electrical properties

Mechanical isolation of a single-layer crystal of the semiconducting molybdenum disulfide allowed B. Radisavljevic *et al.* [41] to realize the first high quality field effect transistor (FET) based on a MoS<sub>2</sub> monolayer. Atomic thickness of the semiconducting channel in this device is considerably smaller than the gate induced depletion region. This provides precise control over the charge carrier density, directly linked to the drain-source current of the transistor, revealing an ON/OFF ratio as large as 10<sup>8</sup> [42]. Figure 2.4b shows  $I_{DS} - V_{BG}$  transfer characteristic of that transistor. Only electron transport can be observed, and this is indeed very typical for MoS<sub>2</sub> monolayers (while in other TMDCs ambipolar transport is observed), since holes are getting trapped on different types of defects including sulfur vacancies. Actually, high density of defects is the main drawback of these materials which strongly limits mobility of the charge carriers.

Nevertheless, recent advances in materials growth [43, 44] and device fabrication [45] allowed realization of devices with mobilities higher than thousands of cm<sup>2</sup>/V·s. This is sufficiently good for observation of the Shubnikov–de Haas oscillations in MoS<sub>2</sub> [46] (Figure 2.9b), MoSe<sub>2</sub> [47] and WSe<sub>2</sub> [48] monolayers, as well as quantized transport through MoS<sub>2</sub> point-contacts [49], unveiling rich spin physics of this material, which we will soon discuss in detail.

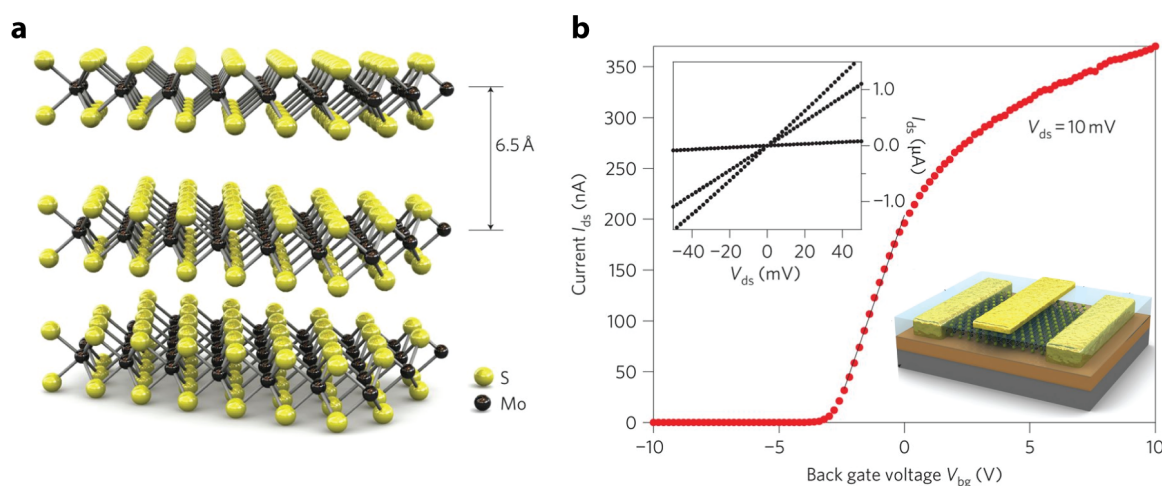


**Figure 2.4** – Single-layer MoS<sub>2</sub> transistor. (a) Atomic structure of MoS<sub>2</sub>, an example of a TMDC material. (b) Transfer characteristic of the field effect transistor based on MoS<sub>2</sub> monolayer. Inset shows set of  $I - V$  curves acquired at different gate voltages, as well as schematic representation of the fabricated device. Figures adapted from ref.[41] with permission of Nature Publishing Group.

### Optical properties

Properties of 2D monolayers are often very different from those of their bulk counterpart, and TMDCs are not an exception. When the semiconducting crystal is thinned down to several layers, its band structure experiences changes, as shown in Figure 2.5a. The bandgap becomes bigger due to the quantum confinement in the vertical direction, in a similarity with quantum dots. As a result of this alteration, initially indirect bulk semiconductor acquires direct bandgap in the monolayer limit.

This sharp transition has crucial consequences on the optical properties of the material, since generation and recombination of electron-hole pairs in the case of a direct transition does not require additional phonon momentum. As the result, photoluminescence (PL) quantum yield of monolayers increases several orders of magnitude if compared to a bilayer crystal [50, 51], as seen in Figure 2.5b. Efficient light emission combined with the bandgap energy lying in the visible spectrum make these materials promising candidates for the new generation of light emitting devices [52, 53]. In addition, TMDCs monolayers absorb 15% of the incident light, making it suitable for optoelectronic applications such as ultrasensitive photodetectors [54], solar cells [55] and many others [36, 38].

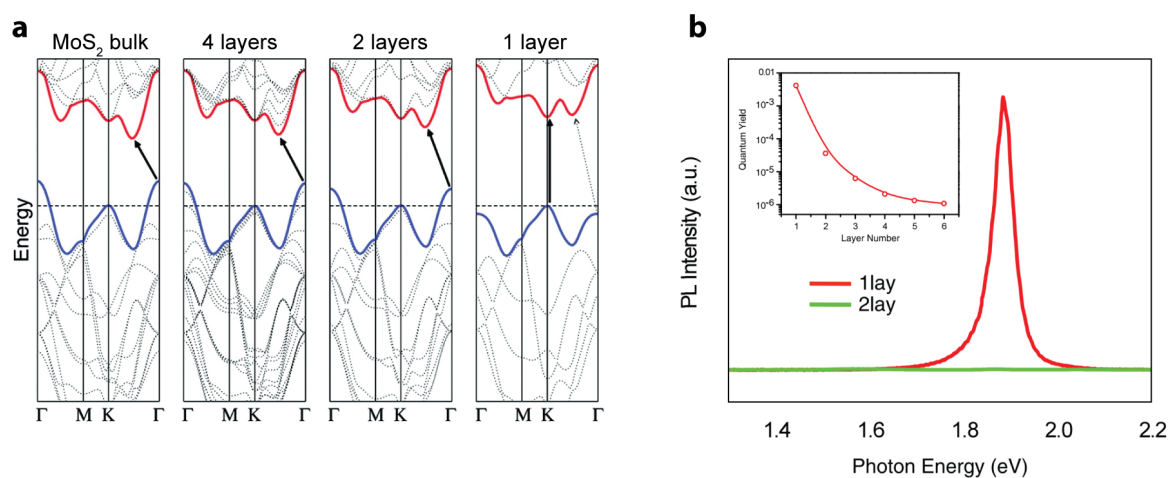


**Figure 2.5** – Single layer TMDCs. (a) Calculated thickness-dependent band structures of MoS<sub>2</sub>. Indirect to direct bandgap transition occurs at the monolayer limit. Figure adapted with permission from ref. [50]. ©2010 American Physical Society. (b) Photoluminescence observed from mono- (red) and bilayer (green) MoS<sub>2</sub> flakes. Inset shows PL quantum yield as a function of layer numbers. Adapted from ref.[51] with permission of APS.

Aside from practical applications in optoelectronics, these materials also hold great interest for fundamental science due to the strongly pronounced excitonic and many-body effects. They were extensively studied by the community in recent years, as summarized in Figure 2.6.

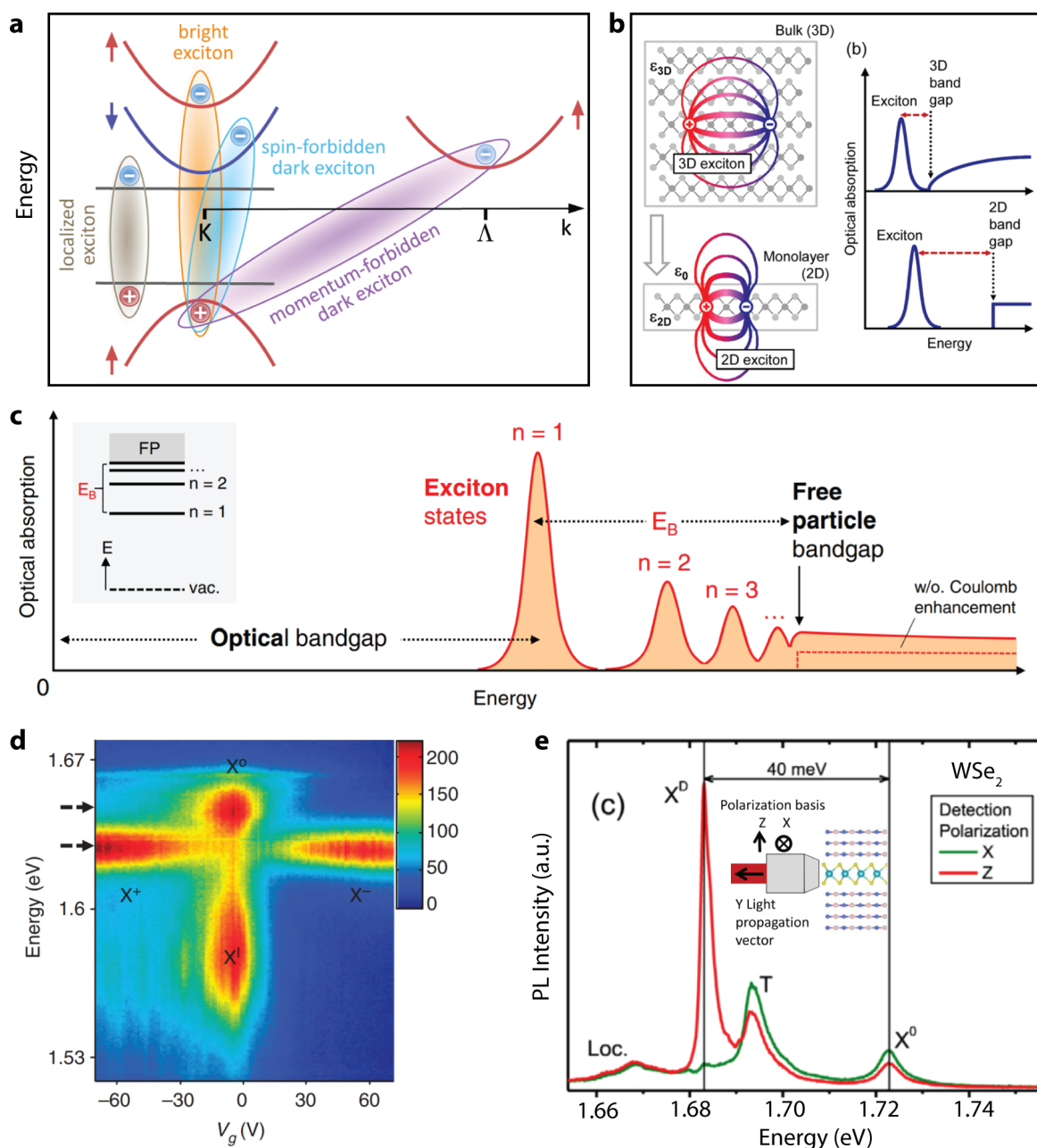


**Figure 2.6** – Excitons in single-layers of TMDCs. (a) Different types of excitons and band structure of a tungsten-based TMDC monolayer with spin-forbidden lowest energy transition. Adapted from ref.[38] with permission of Nature Publishing Group. (b) Excitons in bulk (top) and monolayer (bottom) have different energy spectra (left) due to the change in the dielectric environment. Adapted from ref.[56] with permission of APS. (c) Typical absorption spectra of a TMDC monolayer revealing exciton ground and excited states. Adapted from ref.[57] with permission of APS. (d) Gate dependent PL spectra showing neutral and charged excitons in a  $\text{WSe}_2$  monolayer. Adapted from ref.[58] with permission of Nature Publishing Group. (e) Observation of dark exciton in a  $\text{WSe}_2$  monolayer by in-plane PL measurement scheme. Adapted from ref.[59] with permission of APS.

The Coulomb interaction between electrons and holes is strongly screened in bulk crystals, resulting in the low binding energy of excitons. In contrast to 3D-systems, dielectric screening is considerably reduced in TMDC monolayers, suggesting a strong enhancement of the Coulomb interaction [56]. This increases binding energy by several orders of magnitude, separating optical and transport bandgap by hundreds of meV, as shown in Figure 2.6b. Such tightly-bound excitons dominate the optical response and survive even at room temperature, which we exploit in Chapter 6.

Exciton – a bound electron-hole pair – is a hydrogen-like quasiparticle and can therefore be excited to different levels similarly to Rydberg-like series. This is schematically shown in Figure 2.6c. As many as five excited states can be observed in the reflection spectra [56], limited by the decrease of energy separation and oscillator strength, which makes observation of higher excited states challenging. We note that energy of these excited states strongly deviates from what is expected for a 2D-hydrogen atom, mainly due to the non-homogeneous dielectric screening in the monolayer limit [56, 57].

Extraordinarily strong Coulomb interaction gives rise to many-body effects like formation of charged excitons or trions, biexcitons (exciton-exciton molecule) and other more complex species [60], clearly observed at low temperatures. Power-dependent photoluminescence reveals biexcitons [61, 62, 63], while gate-dependent PL measurements allows identification of charged excitons [58], as presented in Figure 2.6d.

Finally, the complex band structure of TMDC monolayers (Figure 2.6a) gives rise to a whole spectrum of different types of excitons, including the high-energy B exciton (arising from the valence band splitting), excitons localized on defects [64, 65, 66], and so-called dark excitons with electrons and holes having opposite spins. The later ones are normally absent from the PL spectrum (forbidden by optical selection rules), but can be brightened with a magnetic field [67, 68], coupled to surface plasmon-polaritons [69] or observed using an in-plane detection scheme [59], as presented in Figure 2.6e.

### **Spin-valley coupled physics**

By thinning down to the monolayer limit, TMDCs not only acquire a direct bandgap but also lose their inversion symmetry that has strong consequences on their band diagrams and behaviour in general. Electric field generated by the charge displacement between metallic atom and two chalcogen atoms cannot be compensated in the absence of inversion symmetry. This leads to the strong interaction between spins and orbitals of the carriers, mimicking large magnetic fields up to  $10^2$ - $10^3$  T [70], causing spin-dependent energy splitting, as well as orienting spins along the out-of-plane direction.

As we mentioned above, the direct bandgap of TMDC monolayers is located in the six

## Chapter 2. Properties and synthesis of TMDCs

corners ( $K$  points) of the first Brillouin zone of the hexagonal lattice, which are referred to as valleys (Figure 2.7a). Strong spin-orbit coupling (SOC) in these materials leads to spin-dependent splitting of the conduction (tens of meV) and more importantly of the valence band (hundreds of meV). Since spin state poses odd parity under time reversal, opposite signs of band splitting are dictated by the time-reversal relation between  $K$  and  $-K$  valleys. The resulting spin- and valley-resolved energy band diagram of a TMDC monolayer in  $K/-K$  points is schematically depicted in Figure 2.7b.

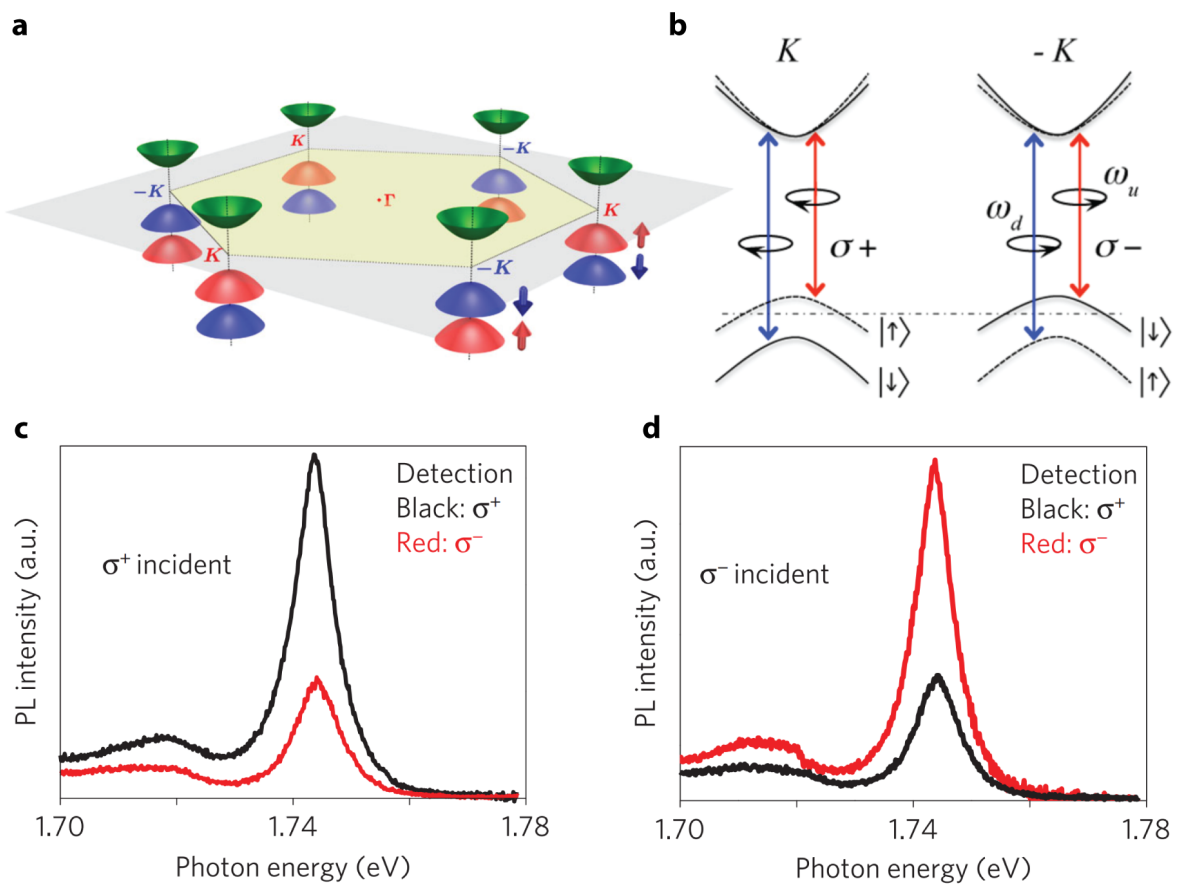


**Figure 2.7** – Optical initialization of a valley state. (a) Schematic of the TMDC band structure, illustrating valence and conduction bands extremes in the  $K/K'$  points. (b) Valley-dependent optical selection rules. Figures (a,b) adapted from ref.[6] with permission of APS. (c,d) Polarization resolved photoluminescence spectra measured on  $\text{WSe}_2$  monolayer when optically pumped with right- (c) or left (d) handed light. Figures (c,d) adapted from ref.[39] with permission of Nature Publishing Group.

Apart from spin, each valley is also associated with two other valley-contrasting pseudo-vectors, namely the Berry curvature and orbital magnetic moment [6, 39]. The first one ( $\mathbf{\Omega}$ ) acts as a magnetic flux in the reciprocal space, and therefore directly affects charge transport. The second one ( $\mathbf{m}_V$ , often referred to as a valley-pseudospin) determines optical

selection rules which allow optical initialization and read-out of the valley state with circularly polarized light [71, 72], as shown in Figures 2.7c,d.

Inter-valley scattering requires a spin flip as well as a large change of momentum. The valley index is therefore assumed to be a robust and an attractive degree of freedom (DOF) for information storage and transport in future valleytronic devices [37, 40].

### The valley Hall effect

The appearance of a Lorentz-like forces proportional to  $\mathbf{\Omega}$  and applied on carriers drifting in external electric field is another consequence of the Berry curvature effectively acting as a magnetic field in the k-space. This force gives rise to an anomalous velocity transversal to the field direction, which deflects carrier trajectories in opposite directions for K/-K valleys. Similarly to the spin Hall effect, this phenomena is called valley Hall effect (VHE) and was initially realized in a MoS<sub>2</sub> monolayer by K. F. Mak *et al.* [73].

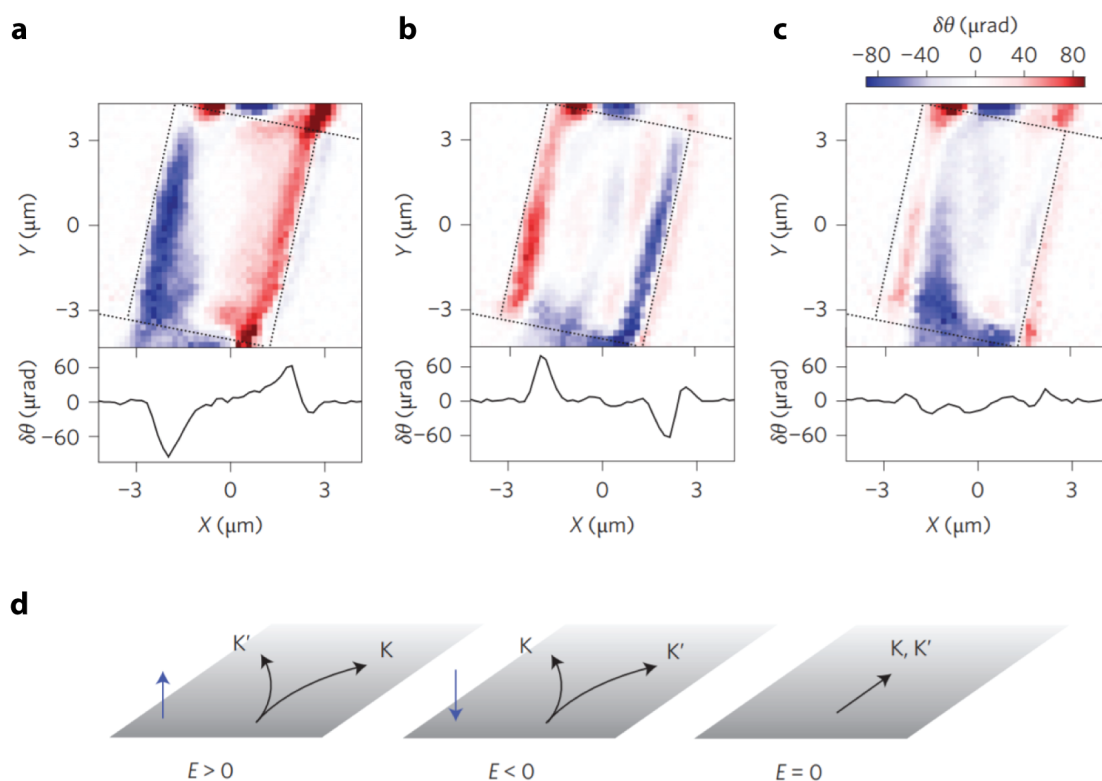


**Figure 2.8** – Valley hall effect in a bilayer MoS<sub>2</sub>. (a-c) Spatial distribution of the Kerr signal from the MoS<sub>2</sub> bilayer measured at different gate voltages, revealing magnetic moment accumulation at the edges of the flake, when inversion symmetry is broken with applied electric field (a,b). (d) Schematic illustration of the separation of carriers from different valleys as a result of the VHE. Figures adapted from ref.[74] with permission of Nature Publishing Group.

Valley Hall effect causes accumulation of carriers from different valleys (e.g. opposite magnetic moment) on the opposite edges of the conducting channel, and can therefore be probed with techniques sensitive to magnetism like magneto-optic Kerr effect measurements [74, 75]. Figure 2.8 shows an example of such measurements carried out on a MoS<sub>2</sub> bilayer with restored inversion symmetry that can be further broken by the application of an electric field in the vertical direction.

### 2.2.3 Insulating boron nitride

Hexagonal boron nitride (h-BN) is an atomically thin insulator with crystal structure similar to the graphene, where the A (B) sub-lattice is occupied by boron (nitrogen) atoms. In this thesis we employ h-BN for two reasons. First, we use it as an atomically flat, dangling bonds-free substrate and a gate dielectric in alternative to the rough SiO<sub>2</sub> or HfO<sub>2</sub> which has strong charge inhomogeneities [44]. Second, we exploit it for electrical spin injection/detection in graphene spin valves as a pin-hole-free atomically thin tunnel barrier [76].

We should also note here that atomic defects in a large bandgap h-BN have recently appeared as an attractive platform for the realization of single-photon quantum emitters [77, 78, 79, 80].

### 2.2.4 Other materials

In addition to the basic conductors, semiconductors and insulators, the family of 2D materials hosts materials with less conventional properties, including superconductors, Mott insulator, (anti-)ferromagnets, topological insulators or more exotic topological phases. We briefly discuss some of them below.

While many TMDCs crystals demonstrate charge density waves and superconductivity in bulk, only some of them preserve these phases in the 2D limit [43]. Firstly, NbSe<sub>2</sub> in 2H phase was demonstrated to be a superconductor [81]. Interestingly, the very same material in the 1T phase appeared to be a Mott insulator [82]. Recently, the MoSe<sub>2</sub> monolayer was also demonstrated to acquire a superconductivity under the strong electrostatic doping [83, 84]. Ising nature of superconductivity and strong SOC of this materials reveals a large critical field in the in-plane direction.

Recent discovery of ferromagnetism in Cr<sub>2</sub>Ge<sub>2</sub>Te<sub>6</sub> [85] and layer-dependent magnetism in CrI<sub>3</sub> [86] opened the whole new area of two-dimensional magnetism [87, 88]. Interestingly, the magnetic order in the latter material can be also controlled electrostatically [89, 90], however the main disadvantage of these materials which limits their practical applications are low Curie temperature and their instability in ambient conditions. In this aspect, robust



and stable PtSe<sub>2</sub> appears as an alternative to above-mentioned materials, being reported to host defect-induced magnetism [91].

## 2.3 Van der Waals heterostructures

One of the most fascinating feature of 2D materials is their ability to be stacked in a complex van der Waals heterostructures (HS) by means of growth or layer-by-layer mechanical assembly [92, 93], as the latter is schematically presented in Figure 2.9a. This capability gives unprecedented freedom to engineer novel structures, which do not exist in nature and are not available in the frame of conventional materials.

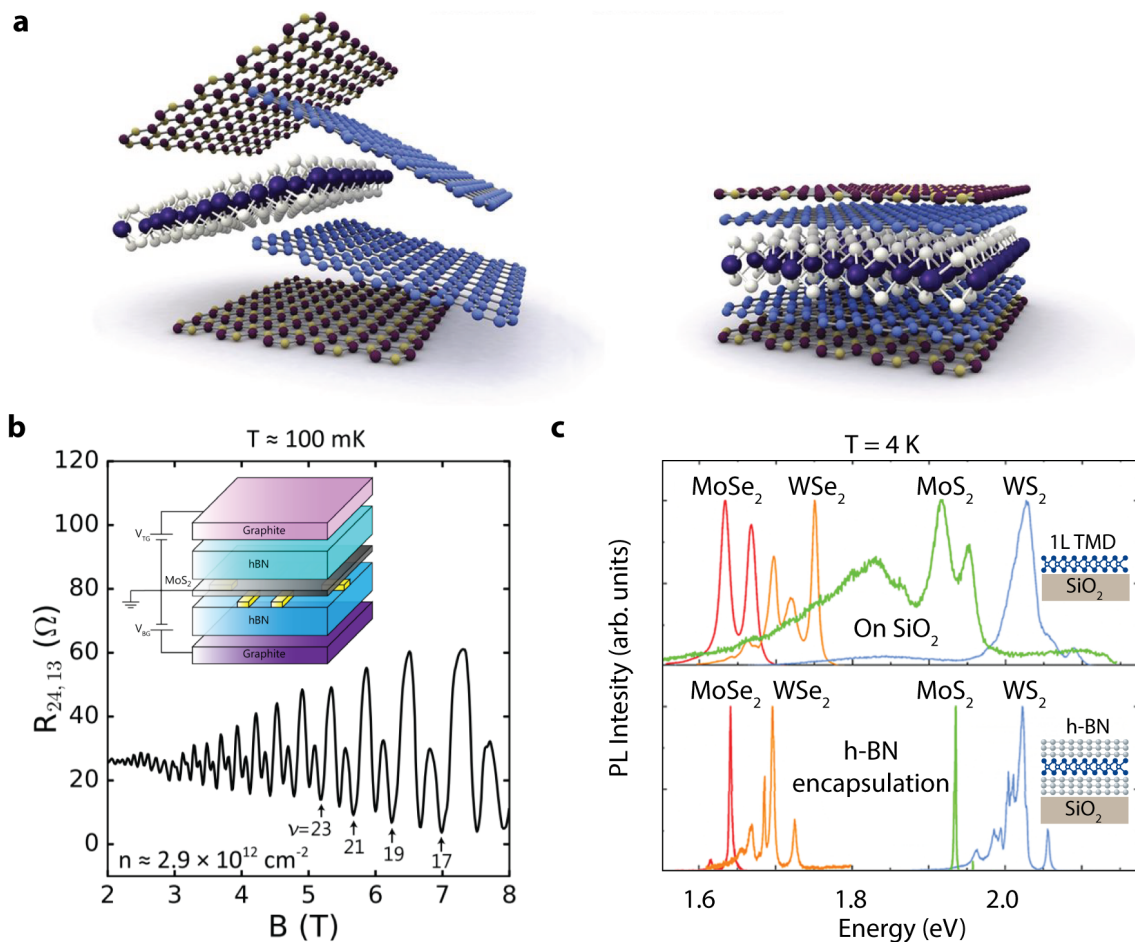


**Figure 2.9** – Van der Waals heterostructures. (a) Schematic illustration of a vdW heterostructure fabrication. Figure adapted from K. S. Novoselov, *et al.* “2D materials and van der Waals heterostructures.” *Science* **2016**, 353.6298: 9439, ref.[93]. Reprinted with permission from AAAS. (b) Observation of Shubnikov–de Haas oscillations in a high quality h-BN sandwiched MoS<sub>2</sub> monolayer. Adapted from ref.[46] with permission of APS. (c) Ultra-narrow excitonic lines of high quality TMDC monolayers encapsulated in h-BN. Adapted from ref.[94] with permission of APS.

There might be different reasons and motivations for the assembly of van der Waals heterostructures out of 2D materials including harvesting and extending already outstanding properties of the constituent crystals. We discuss hereafter several major paradigms of their employment:

- **To build.** The large family of 2D materials contains members covering the whole spectra of properties. Therefore virtually any conventional device can be realized on a 2D platform. For instance, complex devices like non-volatile memory cell [95] or above mentioned optoelectronic devices were also recently realized using van der Waals heterostructures.
- **To improve.** All-2D heterostructure with employment of high quality h-BN layer and flat graphene gates excludes extrinsic sources of disorder, revealing the full potential of these materials. Such h-BN encapsulation was employed by multiple research groups to push investigated materials towards their intrinsic limits [18, 44, 45] for the observation of the quantum Hall effect (QHE) in TMDCs (Figure 2.9b) and the fractional QHE in graphene (Figure 2.2d), or for approaching the homogeneous limit of excitonic linewidth in TMDCs [94] (Figure 2.9c).
- **To combine.** Stacking materials with complementary functionalities makes it possible to combine their properties within the heterostructure. This allows realization of novel artificial metamaterials composed of 2D layers with carefully engineered features. Moreover, one layer can borrow the property of another layer by proximity effects [96, 97]. We employ this approach in Chapter 5, where we harvest the long spin diffusion length of graphene together with strong SOC strength, as well as spin-dependent optical selection rules in  $\text{WSe}_2$  in their heterostructure.
- **To discover.** Finally but most importantly, constituent materials in van der Waals heterostructures can be strongly affected by synergistic effects which unfold completely new properties and emerging novel phenomena, which did not exist in the independent layers [98].

We would like to focus the attention of the reader on the latter point by presenting here several fascinating examples of novel phenomena, which owe their appearance to interlayer interaction in van der Waals heterostructures.

### 2.3.1 Alignment matters — moiré superlattices

One of the major difference between epitaxially-grown heterostructures and their 2D counterparts is the weak nature of van der Waals interaction between compound layers in the

latter case. Strongly coupled layers are therefore weakly interacting from the mechanical point of view. This provides freedom in the assembling of materials with different lattices or alignments without inducing large stresses at the interface, provoking observation of different outstanding physical phenomena, like the ones presented below.

#### Superlattice in Gr/h-BN heterostructure

Small lattice mismatch of  $\sim 2\%$  between graphene and h-BN results in a long-range moiré pattern [99] when assembled together in a van der Waals heterostructure as shown in Figure 2.10a. Interaction between layers strongly affects the band structure of graphene, inducing bandgap opening in minibands due to the formation of superlattice Brillouin zones [100]. This effect is visible in graphene transfer characteristic ( $I_{DS} - V_G$ ) as satellite Dirac points in Figure 2.10b.

Presence of the moiré superlattice also allows the observation of normally inaccessible fractal patterns in graphene electronic spectrum at high magnetic fields, called Hofstadter butterfly. These characteristic patterns were recently observed by several research groups in high quality graphene/h-BN heterostructures [101, 102, 103]. We show an example of such fractal spectrum in Figure 2.10c.

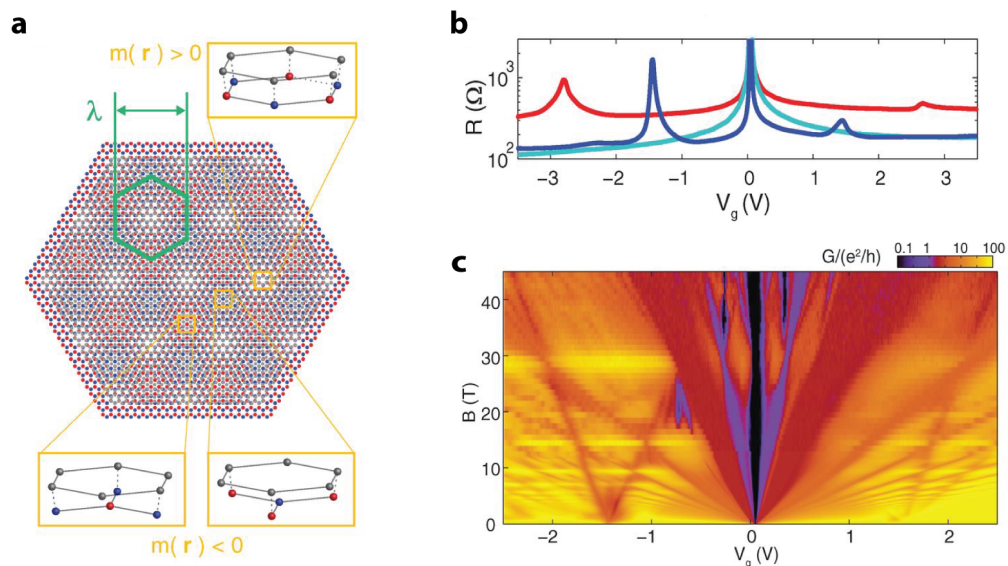


**Figure 2.10** – Moiré patterns in van der Waals heterostructures. (a) Schematic illustration of the moiré pattern appearing in a graphene/h-BN heterostructure. (b) Appearance of the satellite Dirac points in the transfer characteristic of the heterostructure. (c) Measured fractal Hofstadter butterfly spectrum in the magnetic field. Figures adapted from B. Hunt, *et al.* “Massive Dirac fermions and Hofstadter butterfly in a van der Waals heterostructure.” *Science* **2013**, 340.6139, pp: 1427-1430, ref.[103]. Reprinted with permission from AAAS.

### Strong correlation in twisted bilayer graphene

Another knob in the design of a new van der Waals heterostructures is the relative alignment between constituent crystals, which allows the engineering of the electronic band structures. Indeed, this approach gave rise to a whole new concept, called “twistronics”. And the twisted bilayer graphene (BLG) is one of the exciting examples of this novel paradigm [98].

In contrast to the Gr/h-BN heterostructure, bilayer graphene does not produce moiré pattern, unless one layer is twisted with respect to another one. At relatively small alignment angles, two layers are strongly coupled and form patterns with a long-range periodicity, which considerably modifies band structure of BLG. Figure 2.11b demonstrates that at a particular twist angle, also called the “magic angle”, flattening of moiré Bloch bands results in a system with nearly-zero Dirac velocity and strongly interacting carriers.

Such a strongly correlated system at a magic twist angle was initially predicted theoretically by Bistritzer *et al.* [104]. Recently, emergence of unexpected behaviour in bilayer graphene with a twist angle of  $\sim 1.1^\circ$  was experimentally demonstrated by Cao *et al.* [105, 106].

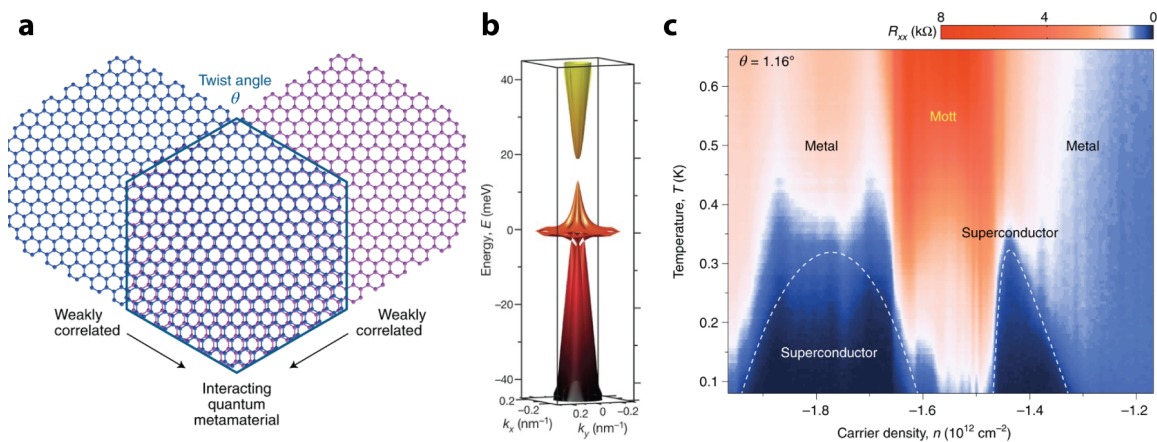


**Figure 2.11** – Magic-angle twisted bilayer graphene (a) Moiré pattern in a twisted bilayer graphene. Figure adapted from [98] with permission of Nature Publishing Group. (b) Band structure of the first mini-Brillouin zones revealing formation of the flat band. (c) Experimentally observed phase diagram of the twisted bilayer near half filling state. Figure adapted from ref.[106] with permission of Nature Publishing Group.

In the case of half-filled moiré bands, strong electron interaction turns twisted BLG into Mott insulator [105]. However, when doping level deviates from half filling, bilayer graphene becomes superconducting as was demonstrated by the same group [106]. The phase diagram presented in Figure 2.11 reveals domes, previously observed in systems

with high-temperature superconductivity, making this type of system interesting for understanding the physics of high- $T_c$  superconductors.

### 2.3.2 Band-alignment matters — interlayer excitons

Interlayer excitons in TMDC heterobilayers is another fascinating example of new phenomena arising in the van der Waals platform, which hold particular importance in the framework of this thesis. Indeed, similar systems were realized based on conventional coupled quantum wells. However, van der Waals heterostructures are advantageous due to the large Coulomb interaction, strong valley effects and presence of the geometrical degrees of freedom in the heterostructure arrangement. While only a short overview is presented here, more on this topic can be found in Chapter 6.

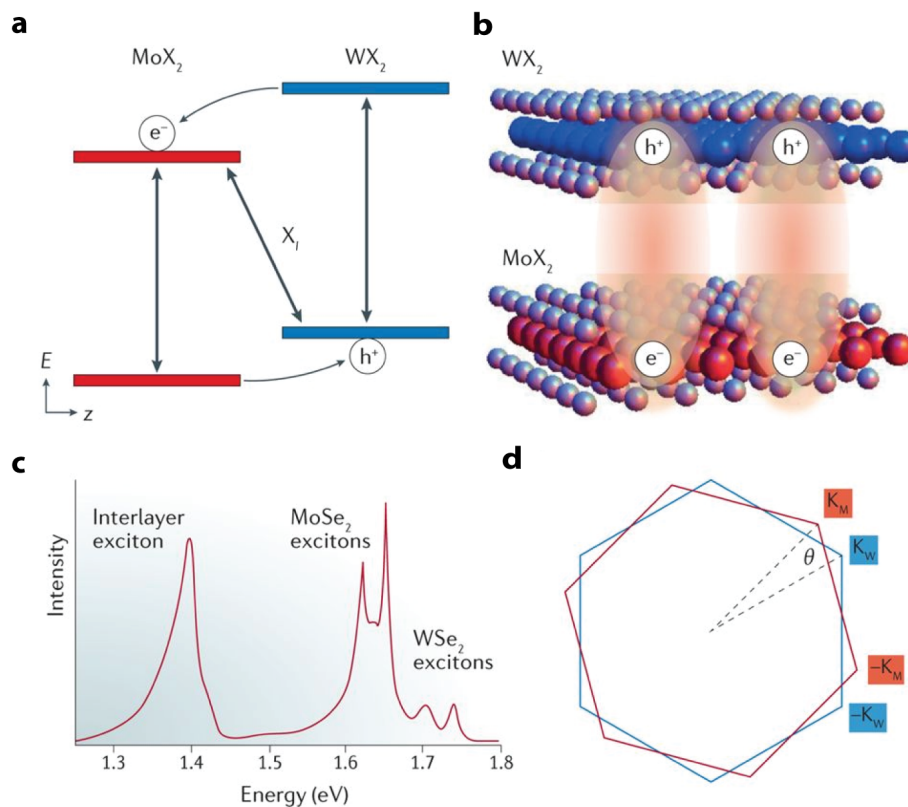


**Figure 2.12** – Interlayer excitons in van der Waals heterostructures. (a) Band alignment of constituent TMDC layers. (b) Formation of spatially indirect interlayer excitons. (c) Low energy PL emission of interlayer excitons. (d) Representation of the misalignment in the reciprocal space. Figure reproduced from ref.[107] with permission of Nature Publishing Group.

Having a large library of 2D semiconductors with different values of bandgaps and band

offset [108], it is possible to choose a pair of materials which poses a type-II band offset. A heterobilayer assembled from these materials represents an atomically sharp vertical p-n junction with corresponding electrical and optical behaviours [109]. Electrons and holes in these systems find energy minimums in the opposite layers as schematically depicted in Figure 2.12a, and therefore experience ultrafast transfer to the corresponding layer [110]. Owing to the reduced dielectric screening of the Coulomb interaction, optically or electrically injected electron-hole pairs produce tightly-bounded excitons which extend in both layers. These spatially indirect electron-hole bound pairs are often called interlayer excitons (IX).

Interlayer excitons in vdW heterostructures are interesting for fundamental investigations but they also hold great promise for potential excitonic and valleytronic applications due to the following reasons. First of all, spatial charge separation decreases recombination rate revealing long lifetimes of these species in the range of hundreds of ns [111, 112]. Due to the same reason, IXs possess an out-of-plane dipole moment, which opens the door for exciton transport manipulation [113]. Owing to the large binding energy, these excitons can be observed even at room temperature. Moreover, similarly to the excitons in constituent layers, IXs shows optically addressable rich valley properties with long valley polarization lifetimes [114]. Last but not the least, properties of interlayer excitons can be uniquely engineered relying on relative lattice mismatch or alignment rotation.

### **Moiré and interlayer excitons**

Similarly to the Gr/h-BN heterostructure, constituent TMDC layers employed for the realization of interlayer excitons have a slight lattice mismatch, which reveals long range moiré patterns even in well-aligned structures. Formation of these patterns was directly observed by scanning probe microscopy [115], and signatures of the moiré-related effects were recently reported independently by several research groups [116, 117, 118, 119]. Moreover, effects of the local registries in the superlattice were predicted to strongly affect valley properties of the interlayer excitons [120, 121], which we discuss in Chapter 6.

Another tool for tuning of IX properties arises from the twist angle between constituent layers. Relative misalignment of layers also rotates the corresponding Brillouin zones, shifting the K point away from each other as presented in Figure 2.12c. Lattice twist was predicted to produce anomalous light cones with exciton polarization locked to their velocity direction, giving new possibilities for optical injection in future valleytronic devices [122].

## 2.4 Conclusion and outlook

In this chapter, we provided a brief overview of the properties of some of the 2D materials. We also discussed the concept of van der Waals assembly for harvesting existing properties as well as revealing novel phenomena.

We note that this overview is not complete by any means, due to impossibility of fully covering rich physics of 2D materials within one chapter. We therefore made a focus on those materials, properties and phenomena which play significant roles in this thesis. We encourage the reader to get acquainted with above-mentioned review articles for a more complete picture of the 2D-universe.





## 3 Experimental Techniques

### 3.1 Introduction

The experimental part of this thesis is based on three pillars: device fabrication, electrical characterization, and optical measurements. The first one, device fabrication, is the basis for every experiment and therefore its description cannot be neglected. The second and third one, namely electrical and optical measurements, hold particular importance in the context of this thesis since they are integral parts of the characterization of optoelectronic device. In this chapter, we will review some general aspects of the employed experimental techniques, while specific details for each particular device or type of measurements can be found in corresponding Chapters 4-6.

### 3.2 Device fabrication

Device fabrication techniques exploited in this thesis could be split in two parts. Fabrication steps specific for the 2D community like monolayers isolation and stacking into heterostructures (HS) were carried out in our laboratory (Laboratory for Nanoscale Electronics and Structures, LANES). On the other hand conventional semiconductor industry microfabrication processes like electron beam lithography, metallization, etching and annealing, were performed in the class-100 (ISO 5) clean room of the center of micronanotechnology (CMi) at EPFL.

The fabrication starts with substrate preparation that is 270 nm-thick silicon oxide ( $\text{SiO}_2$ ) on top of  $n^{++}$ -doped silicon (Si). The degenerately-doped silicon layer acts as global back gate in fabricated devices, while the chlorinated oxide layer serves as gate dielectric with improved break-down limit. Thickness of the oxide layer is optimized to yield the highest optical contrast (defined by light interference [123]) for monolayer TMDCs, making it possible to identify ultrathin layers deposited on the substrate. Following steps includes

## Chapter 3. Experimental techniques

---

photolithography, reactive ion etching of oxide, metal evaporation and lift-off for markers embedding. These are required for future electron-beam lithography alignment. Finally, the wafer is diced into 12x12 mm<sup>2</sup> chips.

### 3.2.1 Monolayer isolation

As described in the previous chapter, most of the attractive properties of 2D materials appear in their monolayer limit. For instance, massless Dirac fermions in graphite, or rich spin-valley physics in TMDCs with broken inversion symmetry and direct band gap, can be observed only in the single-layer form of these materials. Generally speaking, monolayers of 2D materials could be obtained in two different ways: "top-down" method of exfoliation from the bulk material, and "bottom-up" method of single-layer growth. There exist many other methods like liquid exfoliation, Chemical Vapor Transport (CVT), molecular beam epitaxy (MBE), however all these were not employed within this thesis. In this section we will focus on mechanical exfoliation of high quality crystals and large area chemical vapor deposition (CVD) growth.

#### Mechanical exfoliation

This technique, known for a long time, became widespread after pioneering works in graphene [10] and MoS<sub>2</sub> [41, 51] and since then has been greatly improved. Mechanical exfoliation is a relatively simple technique that exploits weak van der Waals interaction between compound layers of 2D materials.

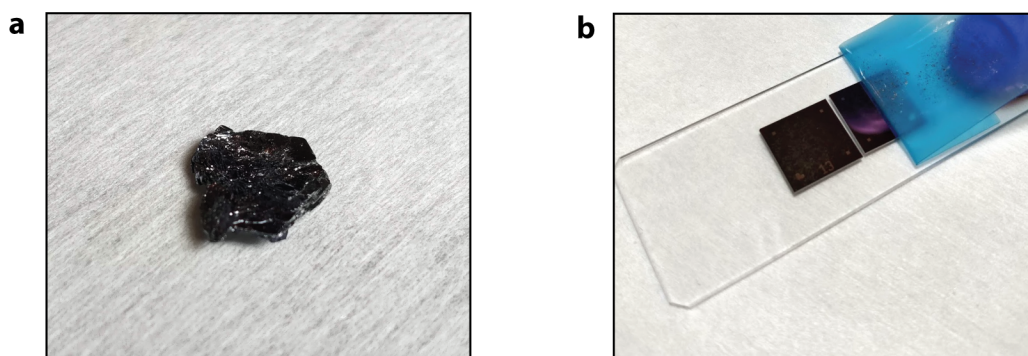


**Figure 3.1** – Mechanical exfoliation. (a) MoS<sub>2</sub> bulk crystal used for mechanical exfoliation. (b) Final step is peeling off sticky tape with crystals from the substrate.

The first step is obtaining of a high-quality bulk crystal (Figure 3.1a) that will serve as source of exfoliated monolayers. This could be highly oriented pyrolytic graphite (HOPG) for graphene, natural molybdenite for MoS<sub>2</sub> or synthetic bulk crystals for other TMDCs. All of these bulk materials can be purchased from various suppliers. Defect-free h-BN

source crystals were grown in Japan by our collaborators K. Watanabe and T. Taniguchi. Once the bulk crystal is ready, it is approached with a piece of low-residue sticky tape in order to cleave and peel-off piece of the crystal. The part of the tape with this piece is then brought in touch with clean part in order to cleave the crystal another time. This step is then gently repeated several times in order to "open" the bulk crystal more and more until it covers major part of the tape surface. Once it is done, the side of tape with freshly cleaved crystals is applied on a Si/SiO<sub>2</sub> substrate. Before this, for better results, the target surface is exposed to 300 W oxygen plasma for 10 min. This pretreatment activates the surface, which significantly improves monolayer yield. In order to further increase substrate-crystal interaction, the chip covered with tape can be baked on a hot plate at 70° for 30 min. The final step of exfoliation, shown in Figure 3.1b is to slowly peel-off the tape from the substrate, leaving thin flakes including monolayers on the surface. Alternatively crystals can be exfoliated on a piece of polydimethylsiloxane (PDMS) polymer stamp for further transfers. The surface of the polymer is pre-treated with exposure to ozone in order to minimize residues [124] and baking step should be skipped.

This technique yields crystal with very good electrical and optical properties, and therefore was extensively employed across the thesis and is ubiquitously used in academical research. However it can not be easily transferred to industry due to its main disadvantage: low yield of monolayer crystals of arbitrary shape and random position on the substrate.

### Large area CVD growth

An alternative approach to the mechanical exfoliation is monolayer growth by chemical vapor deposition (CVD). In contrast to the bottom-up approach described above, this top-down technique results in a controllable growth of large single-crystalline grains. When employed on annealed sapphire, epitaxial growth conditions could be achieved when highly-oriented single crystalline grains merges together in a large area monolayer film. More details on the growth conditions can be found in the corresponding report of the first large-area epitaxial growth of MoS<sub>2</sub> [125].

MoS<sub>2</sub> and WSe<sub>2</sub> monolayers (grown by D. Dumcenco) were transferred by a wet-method from sapphire onto the final substrate for the device fabrication. Resulting monolayer quality is fairly good and this type of material was partially used for the fabrication of single-component devices in Chapter 4. However, when heterostructures were made from CVD materials as in Figure 3.2g-i, we could observe residues trapped in the interface between monolayer, mainly due to the wet transfer procedure, from sapphire to SiO<sub>2</sub>. Therefore all heterostructures used for spin injection or interlayer excitons, which required materials with ultimately-high optical quality and strong interlayer coupling, were fabricated from mechanically exfoliated monolayers assembled with dry transfer methods.

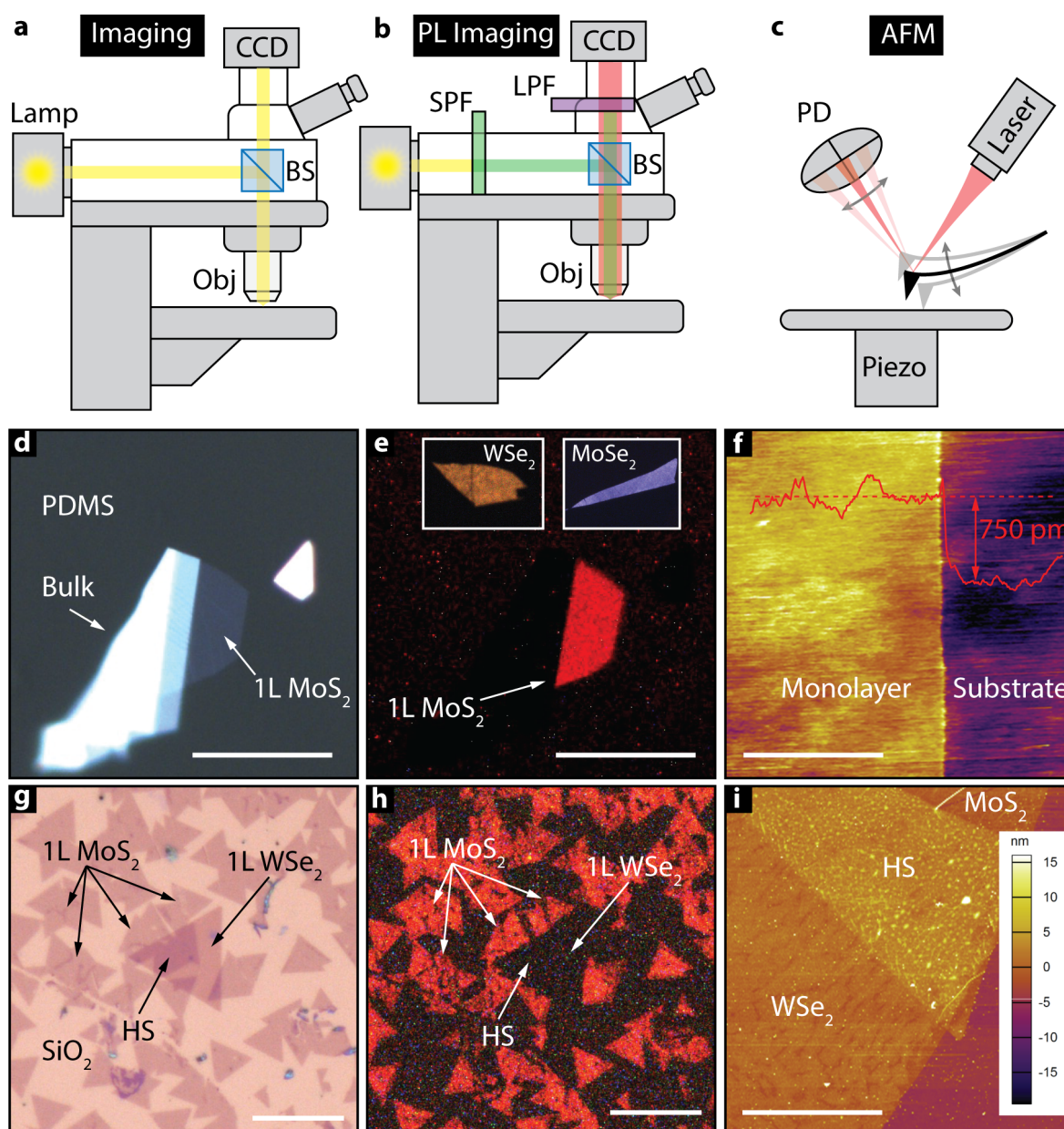


**Figure 3.2** – Imaging of semiconducting monolayers. Schematic illustrations of optical imaging (a), photoluminescence imaging (b) and atomic force microscopy (c). Yellow, green and red colors represent broad-spectrum, high and low energy light correspondingly. SPF is short-pass filter, LPF is long-pass filter, BS is beam splitter, Obj is objective, PD is photodetector. (d-f) Optical, PL and AFM micrographs of a monolayer flake mechanically exfoliated on PDMS polymer substrate. Scale bars are  $20\ \mu\text{m}$ ,  $20\ \mu\text{m}$  and  $250\ \text{nm}$  correspondingly. Insets in (e) shows PL emission images of the  $\text{WSe}_2$  and  $\text{MoSe}_2$  monolayer flakes for comparison with red emission of  $\text{MoS}_2$ . Inset of (f) shows AFM profile cross section with measured monolayer thickness of  $750\ \text{pm}$ . (g-i) Optical, PL and AFM micrographs of  $\text{MoS}_2/\text{WSe}_2$  heterostructure composed of CVD material transferred on  $\text{SiO}_2/\text{Si}$  substrate. Scale bars are  $20\ \mu\text{m}$ ,  $20\ \mu\text{m}$  and  $3\ \mu\text{m}$  correspondingly.

### Monolayer identification

The following step after mechanical exfoliation is searching for monolayers on the substrate surface. For this we use a conventional bright-field optical microscope with top illumination (*Olympus BX51M*), schematically depicted in Figure 3.2a. Even an ultra-thin flake on PDMS or SiO<sub>2</sub>/Si substrate provides optical contrast good enough to be recognized upon careful inspection, as shown in Figures 3.2d,g. Moreover it slightly depends on the number of layers in the flake and therefore with a bit of experience the thickness of the thin crystal can be directly revealed from the optical contrast.

However, optical contrast also depends on the magnification of the objective and illumination conditions, so misinterpretation might happen and additional verification is thus required. This is particularly important in the case of exfoliation on a transparent polymer substrate like PDMS, where the contrast is much weaker and relies only on the light absorption and reflectivity of the flake itself compared to the enhanced optical contrast on the 270 nm thick SiO<sub>2</sub> due to the interference. In order to solve this issue, as the part of this thesis, we have implemented photoluminescence (PL) imaging technique in the very same microscope used for identification of exfoliated material. The schematic of the technique is presented in Figure 3.2b. It relies on edge-pass filters, namely one short-pass filter (SPF) for sample illumination with high-energy photons and another long-pass filter (LPF) for detection of down-converted photons by PL emission process. In case of the TMDCs, only single-layer crystals are direct band-gap semiconductors, and therefore only monolayer appears bright in the PL images while thicker flakes remains dark, as shown in Figures 3.2e,h. Even though most of TMDC monolayers have relatively small bandgaps and therefore emit light in a near-infrared range (NIR), they still can be detected by a conventional silicon CMOS camera widely used with microscopes (here *FLIR GS3-U3-51S5C-C*). However, it is necessary to remove a protection filter normally installed on these types of cameras that blocks transmission of longer wavelengths. As shown in Figure 3.2e, resulting PL images have different colors depending on the source material, which serves as another instrument in our toolbox for flakes identification. Even more, exploiting an additional band-pass filter that transmits light of a particular crystal, we can investigate interlayer coupling strength and homogeneity of artificially built heterostructures as was initially proposed by Alexeev *et al.* [126]. Figure 3.2h shows an example of MoS<sub>2</sub> PL emission quenched in the heterostructure region, that indicates efficient coupling of MoS<sub>2</sub> and WSe<sub>2</sub>.

While PL imaging is a very useful techniques that greatly facilitates determination of direct band gap semiconductors, it can not be employed in case of semimetallic graphene (or insulating h-BN) due to their small (or large) bandgap. However there is a huge difference between these materials. Mechanical exfoliation of graphite yields multiple large and

well isolated atomically-thin graphene flakes. Moreover, even a single layer of graphene absorb several percent of incident light [127], and therefore can be easily identified by appearance color and contrast on the optical image (Figure 3.3). Opposed to graphene, hexagonal boron nitride is a difficult material to exfoliate. In addition, resulted flakes are almost entirely transparent since this material is a large bandgap dielectric. For instance, 1-3 layered h-BN on SiO<sub>2</sub>/Si chips and flakes thinner than 3 nm on PDMS substrate are almost invisible in an optical image. However there are several tricks that facilitates search and identification of thin layers. First, the optical contrast of h-BN reaches maximum in the yellow region of light spectrum. Therefore using a 600-nm band pass filter increases the contrast of the h-BN in microscopy images [128]. Second, as mentioned before, thin-film interference plays an important role in the optical contrast of the flake deposited on a sub-wavelength film. Thereby we have optimized thicknesses of the double-layer polymer on Si substrate in the way that even ultrathin flakes become visible upon exfoliation. Finally, in order to verify presence of a thin h-BN layer in a suspected region we were employing atomic force microscopy (AFM), as described below. Figures 3.3b,c show an example of a h-BN flake exfoliated on a double-layer polymer substrate, monolayer flake was imaged by optical microscope with band-pass filter and confirmed with AFM scan.

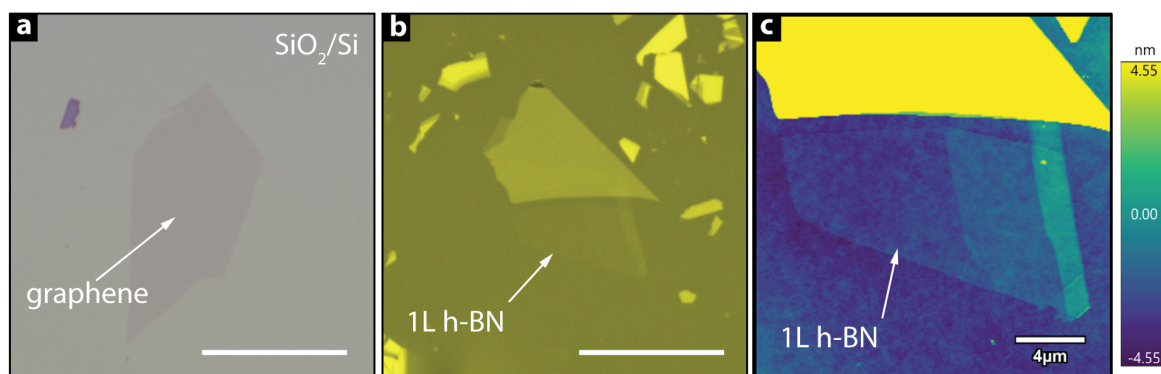


**Figure 3.3** – Imaging of non-semiconducting monolayers. (a) Optical image of a large graphene flake exfoliated on SiO<sub>2</sub>/Si substrate. (b) and (c) Optical and AFM micrograph of an ultra-thin h-BN crystal exfoliated on a double-layer polymer. Optical image is taken with 600-nm band pass yellow filter for a better contrast. Scale bar is 20  $\mu\text{m}$  for optical images and 4  $\mu\text{m}$  for AFM micrograph.

Once the thin flake have been found and pre-identified as monolayer by means of optical and PL imaging, it is additionally investigated by atomic force microscopy. This is a very powerful scanning probe technique, that allows imaging of the surface topography with sub-nanometer vertical resolution. Most of the AFM imaging was performed on the *Cypher* microscope (*Asylum Research*) with silicon cantilevers (*Olympus*, AC240TS) in the tapping mode. This non-destructive imaging regime is schematically depicted in Figure 3.2c. It is based on the surface raster scanning by an oscillating cantilever with a sharp tip. The

amplitude of oscillation depends on the tip-surface distance and is measured by the four-segment photodetector that receives laser beam reflected by the cantilever. Amplitude of oscillations is kept constant by a feedback loop linked to a piezoelectric stage, which adjusts height of the sample. Therefore voltage applied on the piezo is directly related to the surface topography that can be later reconstructed as a 3D profile. AFM imaging could serve as an additional confirmation of the flake thickness, when PL imaging is not possible. Example of a clean monolayer is shown in Figure 3.2f, with extracted thickness of 0.75 nm. Also this technique was routinely employed for cleanness verification of the crystal surface before proceeding with transfers and other fabrication steps. Similarly, heterostructures were investigated for trapped residues upon the transfer, as shown in Figure 3.2i.

### 3.2.2 Heterostructures production

Stacking of monolayers into van der Waals heterostructures is a unique tool for the 2D family that allows the creation of brand new artificial materials with engineered electrical and optical properties that are not present in constituent materials. Therefore it is important to know how to stack layers in a controllable way. In recent years, many different techniques were developed and at least five of those were employed during this thesis. Only two of these methods will be described here in details, since they result in the highest-quality structures, and vast majority of the presented devices in Chapters 4-6 were fabricate using these techniques.

Since single-layer crystallites have the ultimate surface-to-volume ratio, their electrical and optical properties strongly depends on surrounding environment. Therefore it is vital to limit surface contamination, such as glue from exfoliation, polymer residuals from stamp and absorbed water from air. In order to minimize transfer-related residues, structures should be fabricated using dry transfer methods in inert atmosphere inside the glovebox (*Inert PureLab HE*), as shown in Figure 3.4. This excludes contact between constituent layers and most of the contaminants, and therefore increases quality of the resulting heterostructures. Finally, for deterministic transfer one needs to be able to precisely position the stamp with crystal above the target. For this we employed a home-made transfer stage built by Andras Kis, installed inside the glove box. It is shown in 3.4b and represents a modified microscope where the target chip is placed on a vacuumized rotation stage. In addition, external heater and thermometer control the temperature of the target. Side camera helps controlling of the stamp-target separation distance. From opposite to camera side there is a holder for glass slide mounted on a set of remotely controlled stages that gives controls over  $x$ ,  $y$ ,  $z$  position and tilt of the stamp. The transfer process is monitored by the microscope camera. This state of the art setup allows alignment flexibility with many degrees of freedom while keeping micrometer precision.

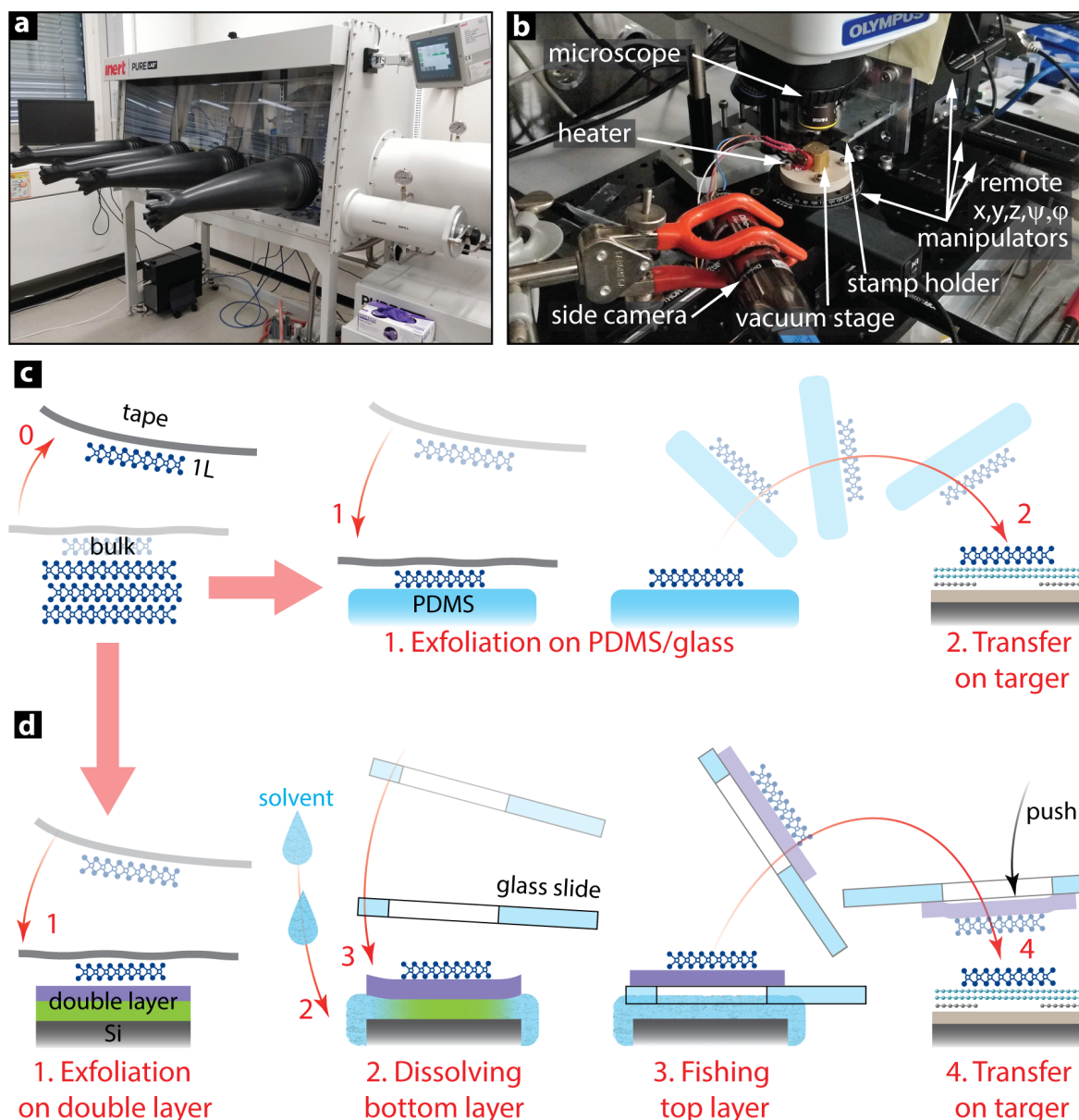


**Figure 3.4** – Transfer techniques. (a) Argon-filled glovebox with transfer stage inside. The stage itself is shown closer in (b). Schematic illustrations of main steps of two employed transfer methods: PDMS stamp technique (c) and double-layer polymer technique (d).

### PDMS transfer

This transfer technique relies on the viscoelastic properties of the PDMS polymer which has different behaviour in different time scales and temperatures. This allows balancing between competing flake-stamp and flake-substrate adhesion forces. This method was described in details by Castellanos-Gomez *et al.* [129], and was implemented and optimized as part of this thesis. Step by step procedure is schematically represented in Figure 3.4c.



The first step is exfoliation and identification of material on the PDMS stamp. For this we use commercially available *GelPak* bars, placed on a glass slide for additional rigidity. Exfoliation is performed at room temperature using standard white tape. As mentioned in the corresponding section, pretreatment of PDMS surface with UV-ozone helps to decrease polymer residuals. Once surface is inspected, flakes of suitable size and shape are found and their thickness confirmed with PL imaging or AFM. The flake of interest is marked on the back side of the glass slide and PDMS around the region is carefully chopped off and removed in order to leave a small polymer stamp attached to the glass slide, that can now be mounted on the transfer stage with the flake facing toward the target chip. The PDMS stamp is transparent, therefore the microscope can focus on both subject and target of the transfer, facilitating alignment. Once careful adjustments of both counterparts is performed, the height of the PDMS stamp is slowly decreased until it starts touching the substrate. Heating the substrate to 60°C brings the flake in contact with target, and consequent cooling down releases the flake from the viscoelastic polymer. Alternatively, the last step can be performed without heater. Slow mechanical peeling off of the stamp also should release the flake that preferentially adheres to the target .

This method is fast, simple and versatile. It is particularly good when large-area structures are required, since exfoliation on PDMS stamp yields large monolayer flakes. It is also sufficiently good for a transfer of any flake on the target structure like pre-patterned electrodes or photonic structures, or fabrication of a stack where single material is entirely encapsulated in the h-BN.

### **Double-layer transfer**

For more sophisticated heterostructures we employed rather complex method introduced by Mayorov *et al.* [130] and implemented by Ahmet Avsar. This transfer also starts with mechanical exfoliation of transferred crystal but this time on a double layer polymer spincoated on a silicon wafer. Thicknesses of the layers can be adjusted to optimize optical contrast of thin flakes for each material. After identification of a desired thin flake, the region around is scratched and the gap is carefully filled with a solvent that dissolves the bottom polymer. Released island of the top layer with the thin flake now can be fished with the a holed glass slide. Similarly to the previous method, the slide is then turned upside down, mounted to the transfer stage, aligned with target structure and pressed against the substrate. Last step is assisted with careful push of stamp with a fine needle that breaks the polymer film and brings the flake in contact with the target. The final step consists of the top polymer stripping in a hot acetone bath at 90°C for several hours and then rinsing with isopropanol (IPA). Main steps of this transfer method are shown in Figure 3.4d.

### Annealing

In order to remove residues related to exfoliation and transfer, the heterostructure fabrication is completed by annealing at high temperature (340°C) in vacuum ( $10^{-6}$  mbar) for at least 6 hours. This step helps to clean surface from contaminants. Also it promotes self-cleaning of van der Waals structures, when trapped on the interface residues are pushed away to merge in bubbles leaving large areas of clean heterostructure. Moreover, annealing improves electrical coupling of constituent layers.

### 3.2.3 Microfabrication

Device architecture varies a lot from experiment to experiment. Some of the devices exploit doped Si substrate as a global back gate, while others rely on local top and bottom gates and therefore require additional dielectric layers between the gate and the semiconductor heterostructure. Some of the devices are based on flakes of arbitrary shape while others should be patterned. Nevertheless, each of the studied devices experienced a similar microfabrication process flow performed in the cleanroom including lithography, metallization, dielectric deposition and etching. An example of device microfabrication process flow is shown in figure 3.5. The purpose of this section is to give a brief overview on exploited techniques which were optimized for 2D materials. More specific procedure for fabrication of silicon nitride photonic structures could be found in Chapter 4.

#### Electron beam lithography

The very first stage for any process whether it is metal deposition or etching, is the preparation of a customized mask aligned with the device. 2D flakes, randomly shaped and distributed on the substrate, require a tool that allows patterning of arbitrary masks. For this we have employed electron beam lithography (EBL, *Raith EBPG5000+*) placed in a vibration-free cleanroom which maintains a temperature of  $21^{\circ}\text{C} \pm 0.1^{\circ}\text{C}$ . This particular tool allows patterning of sub-10-nm features that can be placed on the substrate with 20 nm precision, well beyond the smallest feature size of 100 nm patterned in this thesis.

Once the desired pattern is designed in PC (*DesignCAD*) and exported into appropriate for EBL format, the substrate should be prepared for electron beam patterning. Namely it should be coated with electron sensitive resist and baked above glass transition temperature to make it solid. It is then exposed to a high-energy electron beam that breaks long polymer chains of the positive resist. In this thesis we employed two different polymers: high-molecular-weight poly(methyl methacrylate) (PMMA) and low-molecular-weight methyl methacrylate (MMA) in a bilayer configuration. Bottom layer MMA is more sensitive to electron exposure compared to the top PMMA. Therefore, upon exposure, PMMA/MMA

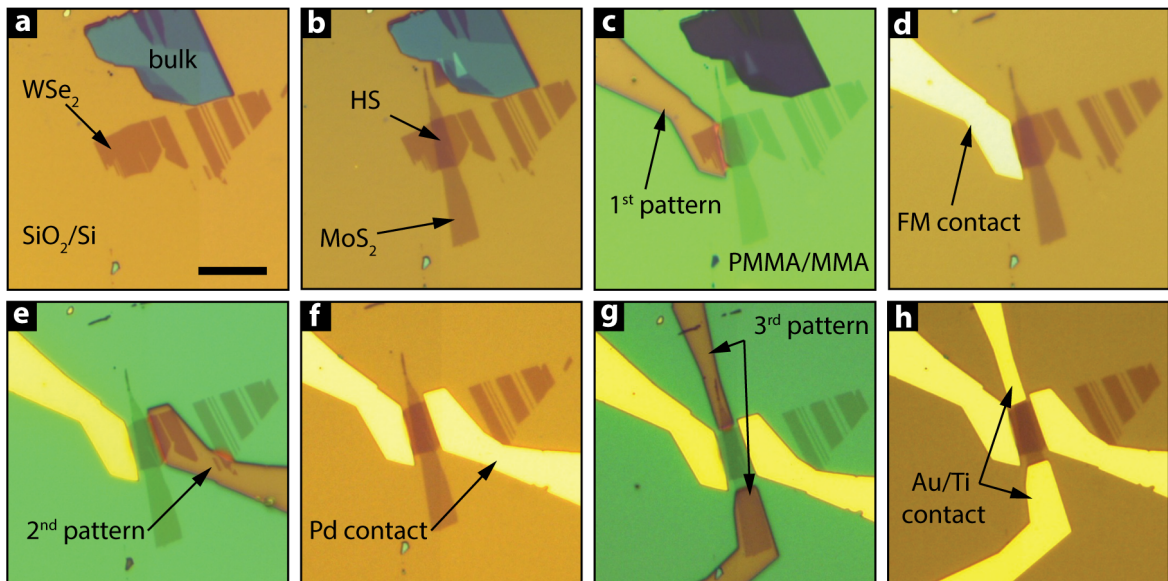


**Figure 3.5** – Optical images of example microfabrication process flow for device based on  $\text{MoS}_2/\text{WSe}_2$  heterostructure that requires deposition of contacts of three different metals. (a) Exfoliation of  $\text{WSe}_2$  on  $\text{SiO}_2/\text{Si}$  substrate. (b) Transfer of top  $\text{MoS}_2$  monolayer and consequential annealing. (c) EBL patterning of the first contact to the  $\text{WSe}_2$  flake: exposure and development. (d) Thermal evaporation of the ferromagnetic (FM) contact, liftoff. (e) EBL patterning of the second contact to the  $\text{WSe}_2$  flake. (f) Electron beam deposition of Pd contacts. (g) EBL patterning of contacts to the  $\text{MoS}_2$  flake. (h) Electron beam deposition of Au contacts with thin Ti buffer layer. Scale bar of all optical images is  $10\ \mu\text{m}$ .

bilayer provides undercut profile that helps to avoid coating of the resist sidewalls during the metal deposition, significantly facilitating lift-off. This process is schematically shown in Figure 3.6. Overall, the procedure for resist coating is the following:

- Spin coat bottom layer MMA EL6 at 4000 rpm for 60 s. Bake resist at  $180^\circ\text{C}$  for 5 min.
- Spin coat top layer PMMA A2 at 4000 rpm for 60 s. Bake resist at  $180^\circ\text{C}$  for 5 min.

If the pattern will be used as a mask for thin metal layer deposition or for etching, bilayer structure is not needed and single-layer polymer (PMMA A4, spincoated at 4000 rpm for 60 s) will be sufficiently good.

Now the substrate is ready for exposure. Here we employ electron beam accelerated by 100 kV tension. For small structures, where high precision is required, a beam current of 1 nA (roughly 5 nm diameter) is exploited. For coarse structures like bonding pads, we were using higher currents of 100 nA with a beam size of 50 nm.

In the next step, areas exposed to e-beam should be removed from the substrate. We were using the following procedure for pattern development

## Chapter 3. Experimental techniques

- Dip the chip in a beaker with 1:3 mixture of MIBK:IPA for 4 minutes. Rinse in cold IPA and dry with nitrogen gun.

We have noticed that standard development procedure might result in polymer cracks in the region with 2D materials (h-BN is particularly affected by this issue). Therefore another process has been employed to develop patterns on top of large h-BN flakes:

- Dip the chip in a beaker filled with a cold (4°C) mixture of water:IPA in 1:3 concentration for 2 minutes. Rinse in cold IPA and dry with nitrogen gun.

Now the mask is ready for following steps.

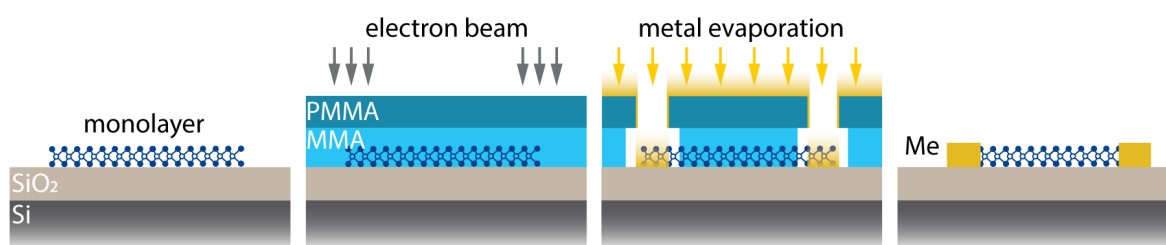


**Figure 3.6** – Schematic illustration of electron beam lithography employed with bilayer polymer mask that forms undercut shape for easy lift-off after metal deposition.

### Metal deposition

Electrical characterization of any device requires metallic contacts. Depending on the 2D material and on the desired carrier type (electron or hole) the material for contact might vary. It is necessary to minimize the height of the Schottky barrier formed at the interface of a metal and a semiconductor with different work function and electron affinity. In the case of MoS<sub>2</sub>, 50 nm gold (Au) contacts are known to provide good injection of electrons into the flake. However, gold layer has very poor adhesion with substrate and therefore a sticky buffer layer is required. For this, before Au deposition, we evaporate several nanometres of titanium, which hybridizes with both the monolayer and the top metal layer. In the case of WSe<sub>2</sub> and MoSe<sub>2</sub> semiconducting channels, we use 50 nm palladium (Pd) contacts, which provide good electron and hole injection. For a more comprehensive overview of electrical contacts to 2D materials, refer to the report of Alain *et al.* [131].

For spin injection and detection we used cobalt (Co) ferromagnetic contact with Ti capping layer, which prevents cobalt oxidation. As a tunnel barrier, that is required to overcome the conductivity mismatch, we have exploited ultra-thin h-BN flakes, preferably bilayers which are known to yield the highest spin polarization for graphene [76]. It is

important to mention that h-BN significantly reduces the work function of cobalt (from 5.5 eV to 3.5 eV [132]). This is good for electron transport, but makes impossible injection of holes into WSe<sub>2</sub>. In this case we evaporate permalloy (80% nickel and 20% iron) contacts which are sufficiently good for this purpose [133]. However with this material it is very difficult to perform lift-off, and often devices are damaged during the process.

For local back- and top-gates we deposit 5 nm of platinum (Pt) with 1-2 nm of chromium (Cr) buffer layer for improved adhesion. First of all, deposited platinum layer is very flat with low surface roughness value and therefore good as bottom electrodes. Second, 5 nm Pt layer demonstrates optical transmission above 50% and therefore is a good alternative to the transparent graphene top electrode.

Au, Pt, Pd, Cr and Ti layers were deposited in the *Leybold Optics LAB 600H* semiautomatic electron-gun evaporator at pressure around 10<sup>-6</sup> mbar. This tool has fairly big crucible-target separation of about 1 m, that facilitates liftoff and has positive effect on the film uniformity. Ferromagnetic metals sensitive to oxidation like Co and permalloy were deposited at a much lower pressures of 10<sup>-7</sup> mbar in the *Alcatel EVA 600* manual thermal/electron-gun evaporator. In addition, we pre-evaporate titanium with closed shutter for reaching even higher vacuum.

Lift-off is the final step to complete contacts deposition. We used following procedure:

- Leave chip in acetone from 10 minutes (for thin metal films) to overnight at room temperature.
- In case of pre-deposition of local back gates, before heterostructure stacking, gentle ultrasonication can be applied to facilitate lift-off
- Rinse with fresh acetone, isopropanol and dry with nitrogen gun.

### Etching

If required, the heterostructure can be patterned in a particular shape for specific measurements (like Hall bar structure) or in order to prevent shortcuts. For this purpose, the device with prepared by EBL mask is subjected to accelerated ion plasma which etches exposed material, as schematically depicted in Figure 3.7. We employed reactive ion etching (RIO) in *Alcatel 601E* and *Alcatel AMS 200 SE* machines. In order to remove ultra-thin TMDC or graphene layers we exposed these flakes to oxygen plasma (15 s, 300 W of RF power, 20 V chuck bias). For thicker flakes and for h-BN crystals which is much more resistant material, oxygen plasma is not effective any more, since it is also stripping the resist mask. In that case we employed SF<sub>6</sub> plasma in the similar condition and process time depended

## Chapter 3. Experimental techniques

strongly on the flake thickness. Another tool (*SPTS APS*) was used for more sophisticated fluorine etching chemistry, that was required for high aspect ratio structures with smooth walls in the case of photonic circuits fabrication.

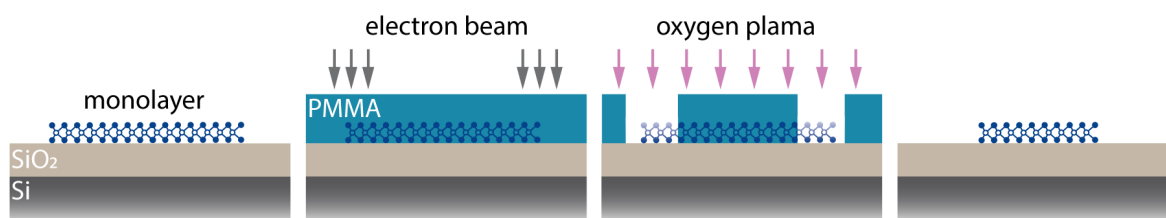


**Figure 3.7** – Schematic illustration of electron beam lithography employed with single layer polymer that forms mask for oxygen plasma etching of a TMDC monolayer.

### Atomic layer deposition

Devices with local gates require thin layers of dielectric that separates semiconducting channel and gate electrodes. One of the approaches to obtain this dielectric layer is to grow it by atomic layer deposition (ALD). The ALD process relies on a two different chemicals or precursors. Reactor chamber is purged with one precursor in a time which reacts with surface in a self-limiting manner. This results in a layer by layer growth of homogeneous high quality thin-films with well-defined thickness. In this thesis we were employing *BENEQ TFS200* ALD tool for hafnium dioxide (HfO<sub>2</sub>) growth. This high-k dielectric requires two precursors: Tetrakis(ethylmethylamido) hafnium (TEMAH) preheated to 80°C and water at room temperature. The chamber temperature is kept at 200°C resulting in 1 Å per cycle deposition rate. During this thesis work, it became obvious that ALD degrades the quality of TMDCs particularly when is grown on top of the flake. Therefore most of the devices presented here have h-BN crystals acting as ultra-smooth wide-gap gate dielectric, free of dangling bonds which can hybridize with 2D material and compromise its quality. The effect of ALD films on TMDCs properties will be discussed in details in Chapter 4.

### Metrology tools

For process optimization and verification of microfabrication result we have employed a set of metrological tools. As discussed above, atomic force microscopy was used for verification of deposited thicknesses and surface roughness estimation. Reflectometry (*Nanospec AFT-6100* and *FilMetric F20-UV*) and ellipsometry (*Sopra GES 5E*) tools were exploited for verification of the thicknesses and optical properties of thin dielectric films. Focused ion beam (FIB, *FEI Nova 600 NanoLab*) and scanning electron microscopy (SEM, *Zeis LEO 1550* and *Zeis MERLIN*) were employed for more comprehensive but invasive structural studies. Though these technique should be used with care as they compromise

quality of 2D material.

## 3.3 Electrical measurement techniques

This section provides a brief overview on the experimental techniques and instruments used to characterize electrical properties of explored materials. Also, here we discuss electrical measurement schemes that give insights into the optical properties of the studied devices.

### 3.3.1 Electrostatic gating

Most of the devices which will be presented in this thesis, whether it is a light-emitting diode with electrostatically established p-n junction, a phototransistor in the off state regime or more complicated heterostructures doped with electrons or holes, all of them rely on the possibility to efficiently control and modulate the charge carrier density in the system. This is possible in a field effect transistor (FET) configuration where a semiconducting channel, dielectric layer and gate electrode effectively form a capacitor. Application of a positive (negative) gate voltage attracts electrons (holes) to the semiconductor, practically shifting its Fermi level position closer to conduction (valence) band.

#### Global back gate

The simplest example of such device is an ultrathin crystal connected to a carriers reservoir (metal contact) on a  $\text{SiO}_2/\text{Si}$  substrate. In this device degenerately doped silicon acts as global back gate, and the oxide layer is the gate dielectric with  $d_{\text{ox}}$  thickness and  $\epsilon_{\text{ox}}$  dielectric constant. As have been said before, application of a gate voltage  $V_{\text{BG}}$  different from the charge neutrality point voltage ( $V_{\text{BG}}^0$ , where  $n = 0$ ) shifts the Fermi level  $E_{\text{F}}$ , changes the carrier density  $n$  and introduces an electric displacement field  $D$ . Values of the carrier concentration and applied field can then be found from a simple parallel capacitor model:

$$ne = C_{\text{BG}} \cdot (V_{\text{BG}} - V_{\text{BG}}^0) = \frac{C_{\text{Q}} \cdot C_{\text{ox}}}{C_{\text{Q}} + C_{\text{ox}}} \cdot (V_{\text{BG}} - V_{\text{BG}}^0) \quad (3.1)$$

$$D = C_{\text{ox}} \cdot \frac{eV_{\text{BG}} - E_{\text{F}}}{e} \quad (3.2)$$

where  $e$  is the elementary charge,  $C_{\text{ox}} = \epsilon_0 \epsilon_{\text{ox}} / d_{\text{ox}}$  is the oxide capacitance and  $C_{\text{Q}} = e^2 \text{DOS}(E_{\text{F}})$  is the quantum capacitance of the 2D crystal which depends on the density of states (DOS) at particular Fermi level.

### Dual gating

As clear from Equation 3.1, the higher the gate capacitance, the more efficient electrical coupling between gate and semiconducting channel, and therefore the less voltage is required to effectively modulate carrier density. For instance, capacitance of 270 nm SiO<sub>2</sub> is  $C_{\text{ox}} = 1.3 \times 10^{-8} \text{ F}\cdot\text{cm}^{-2}$ , while 17 nm thick h-BN flake has one order higher capacitance of  $C_{\text{h-BN}} = 1.3 \times 10^{-7} \text{ F}\cdot\text{cm}^{-2}$ . This is why using local gates with thin h-BN dielectric is more efficient for reaching high doping level. However the range of accessible charge carrier densities is determined by the maximal gate voltage that can be applied to the device, which in turns is limited by electrical breakdown of gate dielectric . Therefore employing two gate electrodes, schematically shown in Figure 3.8a, allows reaching higher carrier densities compared to a single gate structure.

Similarly to Equations 3.1 and 3.2, we can estimate carrier concentrations and displacement field in the dual gating configuration when applied top gate voltage  $V_{\text{TG}}$  with top dielectric capacitance of  $C_{\text{TG}}$ , and bottom gate voltage  $V_{\text{BG}}$  with bottom dielectric capacitance of  $C_{\text{BG}}$ :

$$ne = C_{\text{BG}} \cdot (V_{\text{BG}} - V_{\text{BG}}^0) + C_{\text{TG}} \cdot (V_{\text{TG}} - V_{\text{TG}}^0) \quad (3.3)$$

$$D = C_{\text{BG}} \cdot \frac{eV_{\text{BG}} - E_{\text{F}}}{e} - C_{\text{TG}} \cdot \frac{eV_{\text{TG}} - E_{\text{F}}}{e} \quad (3.4)$$

where  $V_{\text{TG}}^0$  and  $V_{\text{BG}}^0$  are gate voltages at which charge neutrality is reached.

### Constant electric field

Another advantage of the dual-gating scheme is its versatility. There are two independent degrees of freedom, namely voltages applied to the top and bottom gate electrodes. This allows us to separate contributions from the charge carriers and introduced electric field, revealing two different regimes. The first one, constant electric field line, allows modulation of the doping level while preserving applied electric field.

Let us assume a device, that is initially undoped ( $V_{\text{TG}}^0 = V_{\text{BG}}^0 = 0$ ) with top and bottom gate dielectric layer of the same material, for instance two h-BN layers with  $d_{\text{T}}$  and  $d_{\text{B}}$  corresponding thicknesses. Then from Equations 3.3 and 3.4 we can deduce conditions for  $V_{\text{TG}}$  and  $V_{\text{BG}}$  for zero electric field:

$$\text{if } V_{\text{TG}} = \frac{C_{\text{BG}}}{C_{\text{TG}}} \cdot V_{\text{BG}} = \frac{d_{\text{B}}}{d_{\text{T}}} \cdot V_{\text{BG}}, \quad (3.5)$$

$$\text{then } D = 0 \quad \text{and} \quad ne = C_{\text{BG}} \cdot V_{\text{BG}} + C_{\text{TG}} \cdot V_{\text{TG}}$$



### Constant carrier density

The second regime, constant doping line, allows application of a different electric field to the semiconducting channel, while preserving constant carrier density. Similarly to the Equation 3.5, we can deduce conditions for  $V_{TG}$  and  $V_{BG}$  when device stays in the neutrality point:

$$\text{if } V_{TG} = -\frac{C_{BG}}{C_{TG}} \cdot V_{BG} = -\frac{d_B}{d_T} \cdot V_{BG}, \quad (3.6)$$

$$\text{then } n = 0 \quad \text{and} \quad D = C_{BG} \cdot V_{BG} - C_{TG} \cdot V_{TG}$$

An example of measurements in this regime is shown in Figure 3.8b, where linear Stark shift was revealed from the PL measurements at different applied vertical electric fields, while carrier concentration was kept constant. In this particular case of a gated heterostructure, calculations of electric field  $E_z$  should take into account the thickness  $d_{HS}$  and the dielectric constant  $\epsilon_{h-BN}$  of the heterostructure:

$$E_z = \frac{V_{BG} - V_{TG}}{d_T + d_B + d_{HS}} \cdot \frac{\epsilon_{h-BN}}{\epsilon_{HS}} \quad (3.7)$$

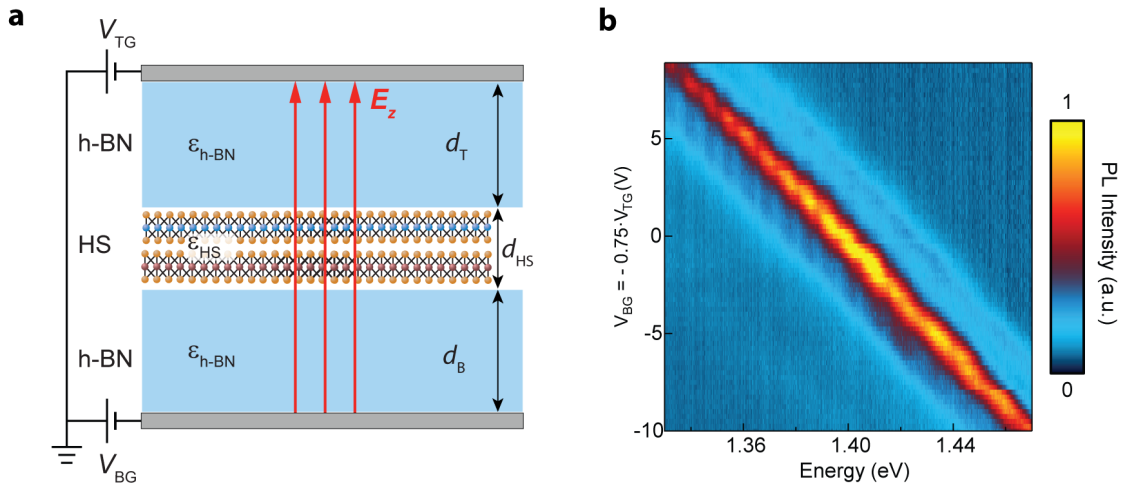


**Figure 3.8** – Dual gating of a heterostructure. (a) Schematic representation of a dual-gated device that is a  $d_{HS}$  thick heterostructure with  $\epsilon_{HS}$  dielectric constant encapsulated between two h-BN flakes with  $d_T$  and  $d_B$  thicknesses and  $\epsilon_{h-BN}$  dielectric constant. (b) Example of measurement of such a device at constant carrier relative permittivity.

It is crucial to note that in case of optical measurements, the real slope  $V_{TG}/V_{BG}$  might differ from the calculated one due to such an effect as photogating, that depends on the interface contamination and thereby strongly varies from device to device [134]. Therefore the actual slope of constant carrier density should be determined experimental for every structure.

### 3.3.2 Four-terminal sensing

Together with the carrier concentration, one of the most important electrical transport characteristics of a device are its resistivity  $\rho$  and carrier mobility  $\mu$ . When measured in a field effect transistor configuration, these two can be extracted from the  $I_{\text{DS}}-V_{\text{DS}}$  and  $I_{\text{DS}}-V_{\text{BG}}$  curves, as following:

$$\rho_{2\text{C}} = V_{\text{DS}}/I_{\text{DS}} \quad \text{and} \quad \mu_{2\text{C}} = \frac{\partial I_{\text{DS}}}{\partial V_{\text{BG}}} \frac{l_{\text{ch}}}{V_{\text{DS}} w_{\text{ch}} C} \quad (3.8)$$

where  $l_{\text{ch}}$  and  $w_{\text{ch}}$  are channel length and width correspondingly, and  $C$  is gate dielectric capacitance.

However, contacts leads and wires have non-zero resistivity. Also a Schottky barrier may form at the metal-semiconductor junction. All these effects strongly affect drain-source current and transfer characteristic, and therefore the extracted values also include contribution from the contact resistance. In order to only account the intrinsic properties of the material, excluding all other parasitic contributions, we use two external electrodes for current injection and two additional probes for measurement of voltage drop along the channel, as presented in Figure 3.9a. The 4-contact resistance and mobility are given by:

$$\rho_{4\text{C}} = V_{\text{xx}}/I_{\text{DS}} \quad \text{and} \quad \mu_{4\text{C}} = \frac{\partial I_{\text{DS}}}{\partial V_{\text{BG}}} \frac{l_{\text{xx}}}{V_{\text{xx}} w_{\text{ch}} C} \quad (3.9)$$

where  $l_{\text{xx}}$  is the separation between internal probes and  $V_{\text{xx}}$  is corresponding voltage drop which solely depends on the channel resistance and excludes contact resistance. Comparing two-contact and four-terminal resistances, one can easily extract contact resistance of electrodes by subtracting one from another with the appropriate normalization for the measured channel length. However, it is important to note that the extracted mobility will depend on the type of carrier, charge density and sample temperature. Figures 3.9b,c show an example of a graphene flake with deposited contacts for four-probe measurements, and corresponding channel resistivity, that reaches its maximum at Dirac point.

For drain-source bias application we employed integrate remote controller (*National Instruments PXI-1033* with *PXI-4461* module), while source was connected to the low noise current preamplifier (*Stanford Research SR570*) linked back to *PXI* for current measurements. This scheme results in a low noise level of read  $I_{\text{ds}}$  currents in order of 100 fA. Gate voltages were normally applied by source-measure unit with two independent output sources (*Agilent Keysight B2912A*) or by *Keithley 2400* measurement unit. For voltage measurements we used *Keithley 2000* multimeter. Also it is possible to carry out four-probe measurements using a lock-in amplifier, as explained below.

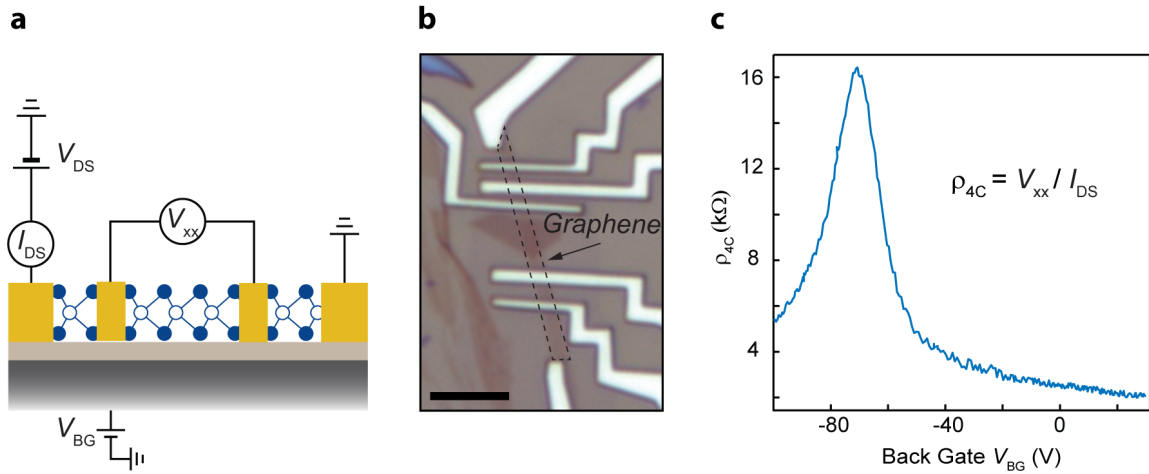


**Figure 3.9** – (a) Schematic illustration of the four-terminal sensing. (b) Optical image of graphene-based device in the field effect transistor configuration and its transport characteristic (c) measured in the four-terminal scheme.

### 3.3.3 Lock-in amplifier

Very often in this thesis, we had to measure weak but oscillating signals. For this purpose we employed measurement schemes with lock-in amplifiers (*Stanford research SR830*), which allow the elimination of noise, DC signal or any other signal at a frequency not equal to the reference one. Basically it works as a narrow band-pass filter, that is also sensitive to the signal phase. Without going deep into details, Figure 3.10a schematically illustrates the operation principle of a lock-in amplifier. Let's assume there is an experimental signal at frequency  $\omega$  that is hindered by noise. This signal is multiplied by the reference signal of the same frequency, so that output contains all types of high-frequency signals including second harmonic product and DC signal proportional to the amplitudes of signal and reference and cosine of their phase difference. The result of this operation is then processed through a low-pass filter associated with an integration time constant  $\tau$  so that only DC component survives and is used as a result output value of the instrument.

Apart from low-noise electrical measurements, like four-terminal sensing with internal reference signal, schemes with lock-in amplifiers were extensively employed for optical measurements. For instance, in Chapter 4 for the characterization of photodetectors we used the scheme represented in Figure 3.10b. Here the laser beam impinging on the device is periodically interrupted by an optical chopper controlled by the remote unit. The corresponding photocurrent is then locked to the reference signal from the chopper control unit, so that the lock-in output DC signal is proportional to the amplitude of photocurrent at the chopping frequency. First, this measurement configuration allows separation of the slow photoresponse from the fast one, making photocurrent mapping feasible. Second, it

is possible to investigate frequency characteristic of the fast photoresponse by sweeping the chopper rotation speed.

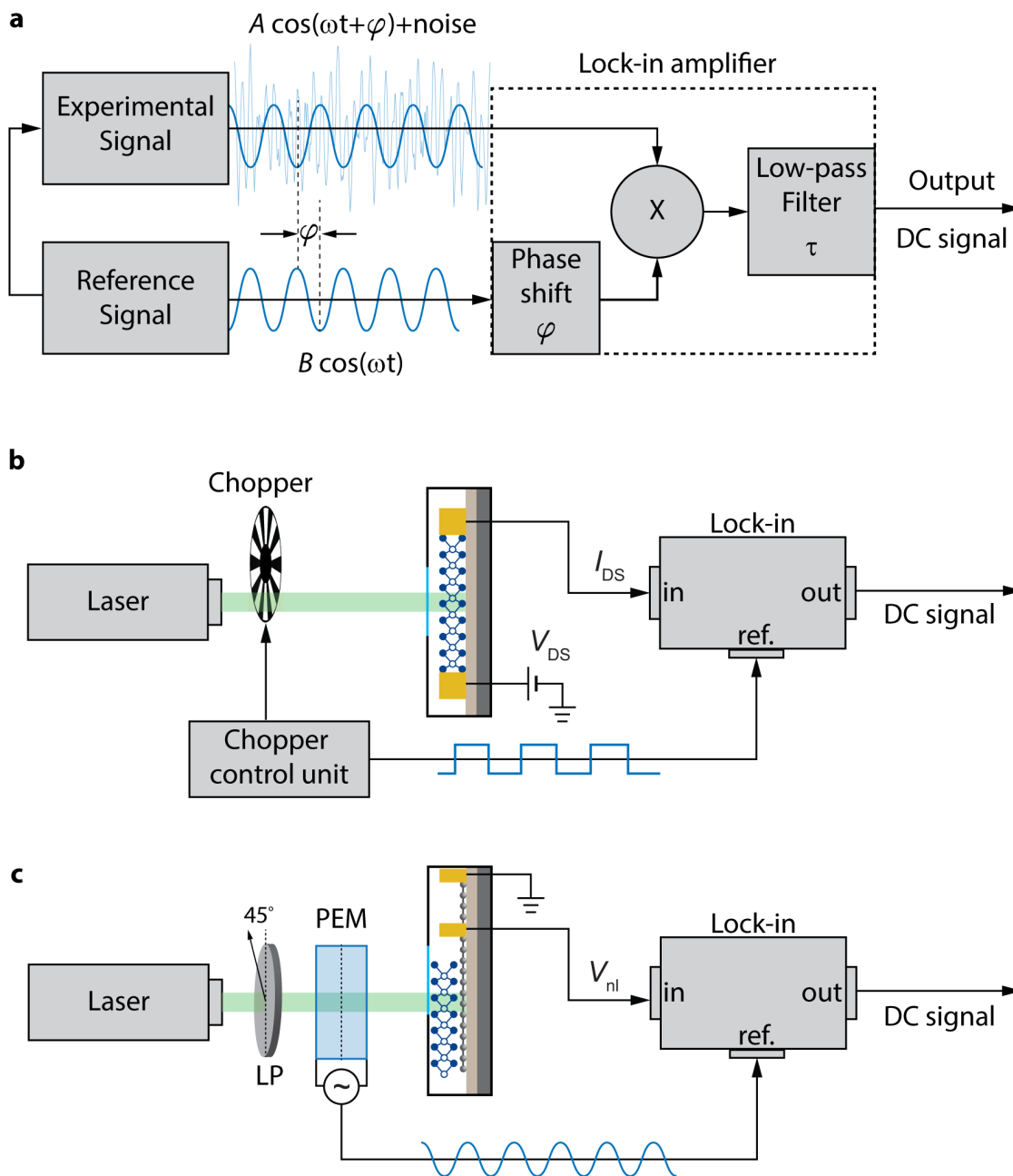


**Figure 3.10** – Lock-in amplifier. (a) Schematic illustration of the lock-in amplifier operation principle. (b) Example of experimental scheme for measurement of the fast component of photoresponse. Here incident light is periodically interrupted with chopper and measured current is locked to the reference frequency. (c) Example of experimental scheme for measurement of the non-local signal  $V_{nl}$  associated with the optical spin injection. Here polarization of incident light is modulated with photoelastic modulator (PEM) at 50.1 kHz and measured non-local signal is locked to this frequency. LP denotes linear polarizer.

Another example from Section 5 is a scheme employed for measurement of extremely weak non-local voltage associated with spin injection. The setup is schematically represented in Figure 3.10c and is similar to the one used for detection of the valley Hall effect in MoS<sub>2</sub> transistors reported by Mak *et al.* [73]. Here we polarize the incident laser beam using a linear polarizer, so that light polarization is oriented between slow and fast optical axes of a photoelastic modulator (PEM). It is an optical unit that introduces time dependent retardation to the transmitted beam. Therefore, in the quarter wave plate mode, PEM modulates polarization of the light in time at fundamental frequency of 50 kHz from right to left circular polarization with linear intermediate state. Then non-local voltage is measured on the probes deposited aside from the parked laser spot. This signal is locked to the external 50 kHz reference signal from the PEM control unit. The measurement scheme presented here eliminates noise and time-independent parasitic signals related to the photovoltaic effect on the heterostructure interface.

## 3.4 Optical measurement techniques

Optical measurements play an important role for the characterization of 2D materials and optoelectronic devices based on them. Therefore we designed, assembled and improved several optical setups while working on this thesis. Although different types of measurements were performed, they can be combined in three different groups, which are briefly presented in this section. The first one is photocurrent and photovoltaic measurements - harvesting of the incident light by a photodetector. The second one is the photoluminescence measurements - detection and analysis of the light emitted by an optoelectronic device. And the last one is the photoluminescence, which includes both absorption of a high energy light and collection of re-emitted down-converted light.

### 3.4.1 Photocurrent

For photocurrent and photovoltaic measurements it is necessary to position the incident light on the device. As source of light we used several continuous wave (CW) lasers, collimated and coupled to the same optical path by the set of dichroic mirrors. We have employed 488-nm (*Coherent*) and 647-nm (*Cobolt*) solid-state lasers, 633-nm HeNe laser (*Melles Griot*) and supercontinuum laser (*Fianium*) for wavelength-dependent studies.

As mentioned in the previous section, incident light can be modulated in time by optical chopper (intensity modulation) and photoelastic modulator (polarization modulation). It can be either polarized permanently by set of linear polarizer and retarded plates. The beam intensity can be adjusted by linear polarizer/analyzer pair, where the first one is mounted on remotely controlled motorized rotation stage. Then incident beam is

guided to a beam splitter that allows partial transmission of the light to a power meter and partially redirect light down towards the sample. The light is then focused by a long-working-distance high-numerical-aperture 50x objective lens. The objective is installed on a nanopositioner stage (*MCL Nano-LPS*) for fine positioning and implementation of spatial scans. Target device is mounted under the objective on a chip carrier wirebonded to the device contact pads and soldered to BNC wiring connected to measurement electrical instruments. Thus this device can be biased and gated, while photoinduced current or voltage are measured. On top of the beam splitter there is charge coupled device (CCD) camera (*Andor iXon Ultra DU897 BVF*) for device imaging when illuminated with white light. Discussed setup is presented in Figure 3.11 right.

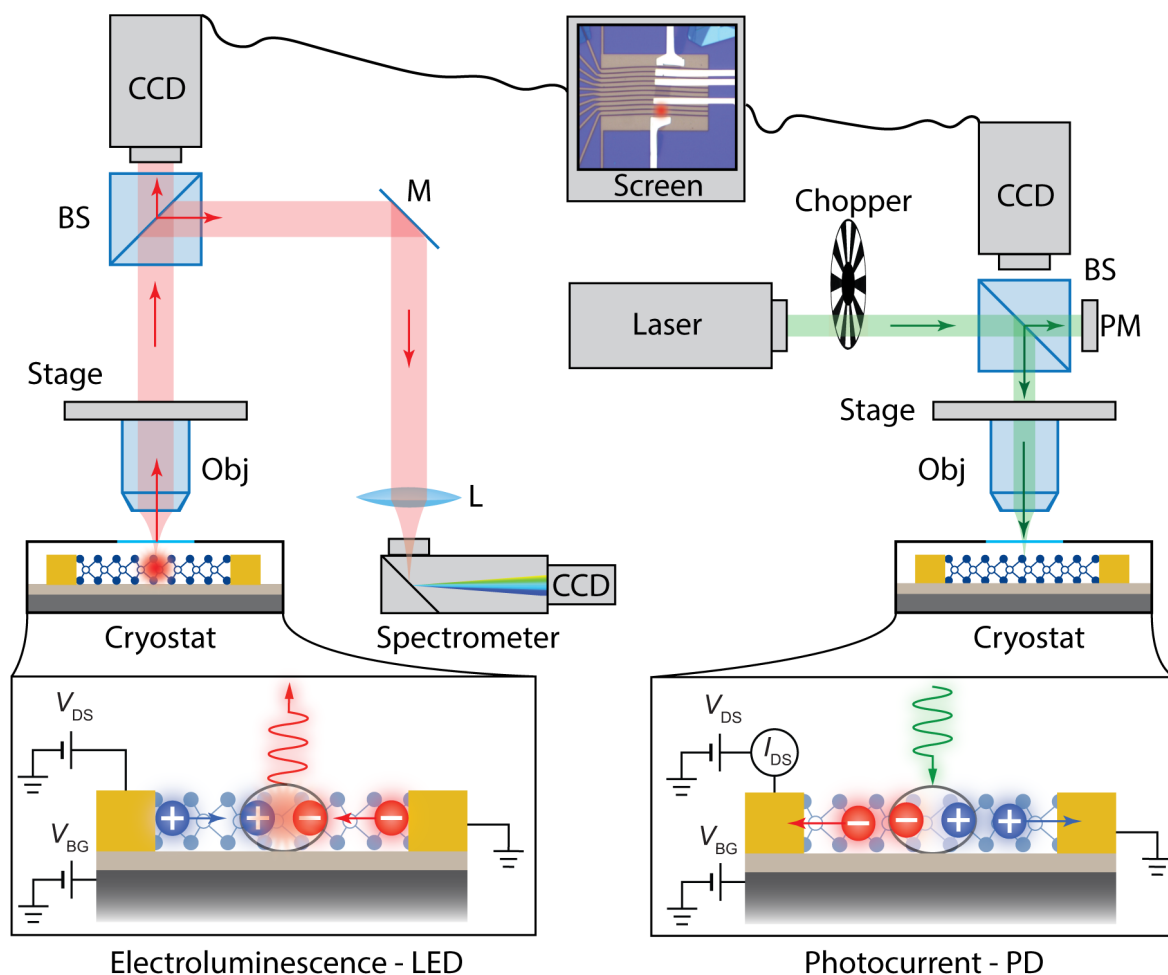


**Figure 3.11** – Schematic illustration of the optical setups for electroluminescence (left) and photocurrent/photovoltaic (right) measurements. BS is beam splitter, M is mirror, Obj is Objective, PM is power meter, CCD is charge-coupled device camera. Bottom cartoons represent electroluminescence process through recombination of electrically injected electron-hole pairs (left) and absorption of photon with photogenerated carriers which participate in the photocurrent of a biased phototransistor (right).

All measurements were performed in vacuum inside a liquid helium (He) flow cryostat with top optical window for light access. Two different *Oxford Instruments* cryostats were employed in this thesis: *Microstat HiRes* for fast cool-downs and *Microstat MO* for measurements in magnetic field. Both cryostats are equipped with sample heater, flow controller and helium pump that allows performing measurements at stable temperature from 300 K down to less than 4 K.

#### 3.4.2 Electroluminescence

Characterization of a light-emitting diode (LED) requires collection and analysis of the emitted light. In the setup for electroluminescence (EL) measurements, the device is similarly installed on the soldered chip carrier holder, wirebonded to the LED device for electrical manipulation inside a cryostat. Emitted photons are transmitted through an optical window of the cryostat and collected with a high NA objective lens. Depending on the bandgap of 2D material, this lens is optimized either for transmission of visible (VIS) or near-infrared (NIR) light. Similarly, two types of beam splitters with different anti-reflection coatings were employed for VIS and NIR light detection.

The objective is installed on a nanopositioner for optimization of light collection *via* fine adjustment, while cryostats are mounted on the mechanical positioning stages for course tuning. Then collected light is guided to a beam splitter that partially allows transmission towards the imaging CCD camera (*Andor iXon Ultra DU897 BVF*) which is also similarly used for the device imaging. Therefore, spatial intensity profile of the emitted light can be overlapped with real image of the device like shown as a screen in Figure 3.11.

Part of the collected light, incident to the beam splitter is redirected to a spectrograph (*Andor Shamrock 500i*), which is connected to a back-illuminated CCD camera (*Andor Newton 970*) for spectral analysis. Therefore emitted light is simultaneously characterized spectrally and spatially. The spectrometer camera is cooled down to  $-85^{\circ}\text{C}$  by internal Peltier thermoelectric element and external cooling liquid circulation. Combined with electron multiplication (EM) regime, cold CCD camera allows low-signal low-noise spectroscopy measurements. Spectrograph contains three diffraction gratings with different groove density and blaze wavelengths for various type of measurements. For better spectral resolution, electroluminescence emission is focused with a lens on

#### 3.4.3 Photoluminescence

An optical setup for micro-photoluminescence ( $\mu\text{PL}$ ) measurements requires both illumination of the device with incident light and collection of re-emitted photons. Therefore it

### Chapter 3. Experimental techniques

---

combines parts of the optical schemes for photocurrent and electroluminescence characterization. Such a PL setup is schematically represented in Figure 3.12.

Basically, a collimated laser beam is transmitted through a revolver with a set of neutral-density (ND) filters for step attenuation of the incident intensity. Then light is passed through a polarizer/analyzer pair, where the first one is installed on a remotely controlled rotation stage for gradual attenuation of the intensity, that is measured by a power meter installed behind a beam splitter. This splitter partially redirects light down. An objective on the nanopositioner stage allows diffraction-limited (width below  $1\ \mu\text{m}$ ) focusing of the incident light in the desired area of the device. The sample is mounted in vacuum inside the He-flow cryostat on a wired chip carrier holder. This allows the modulation of the carriers concentration and the application of external electric field on the sample. Also, an external magnetic field can be applied by a superconducting coil cooled down to 4 K. The cryostat itself is mounted on mechanical stage for coarse sample positioning.

Upon the absorption of higher-energy photons by a 2D semiconductor, an electron-hole pair is generated, and thermalized to extrema of the conduction (CB) and valence (VB) bands. If energy and momentum conservation conditions are satisfied, the electron-hole pair can recombine with photon emission at lower energy, corresponding to the optical band gap of the investigated semiconducting material.

Emitted photons are collected with the same high-NA objective, transmitted through the bottom beam splitter, and splatted by the top one into two detection arms. This allows simultaneous detection of spectral and spatial characteristics of the PL emission. An imaging CCD camera is positioned on the top side of the beam splitter. It allows spatial imaging of the exciton cloud. A flip mirror on the incident beam path, allows remote switch between laser excitation and white light device illumination for. This allows fast switching between device depiction mode and PL imaging mode.

Part of the light is reflected by the top beam splitter into another detection arm toward the spectrograph with externally cooled CCD camera for low-noise spectral characterization of the PL emission. Similarly to the previous section, light is focused on the spectrograph slit with a lens. Additionally, a Dove prism can be installed for rotation of the PL emission according to the slit. It can be projected on the diffraction grating in the way that resulted CCD image will represent spectrum versus coordinate diagram. Two long-pass filters installed in front of the imaging camera and at the entrance of spectrometer are used for removing laser beam, reflected from the surface of device.



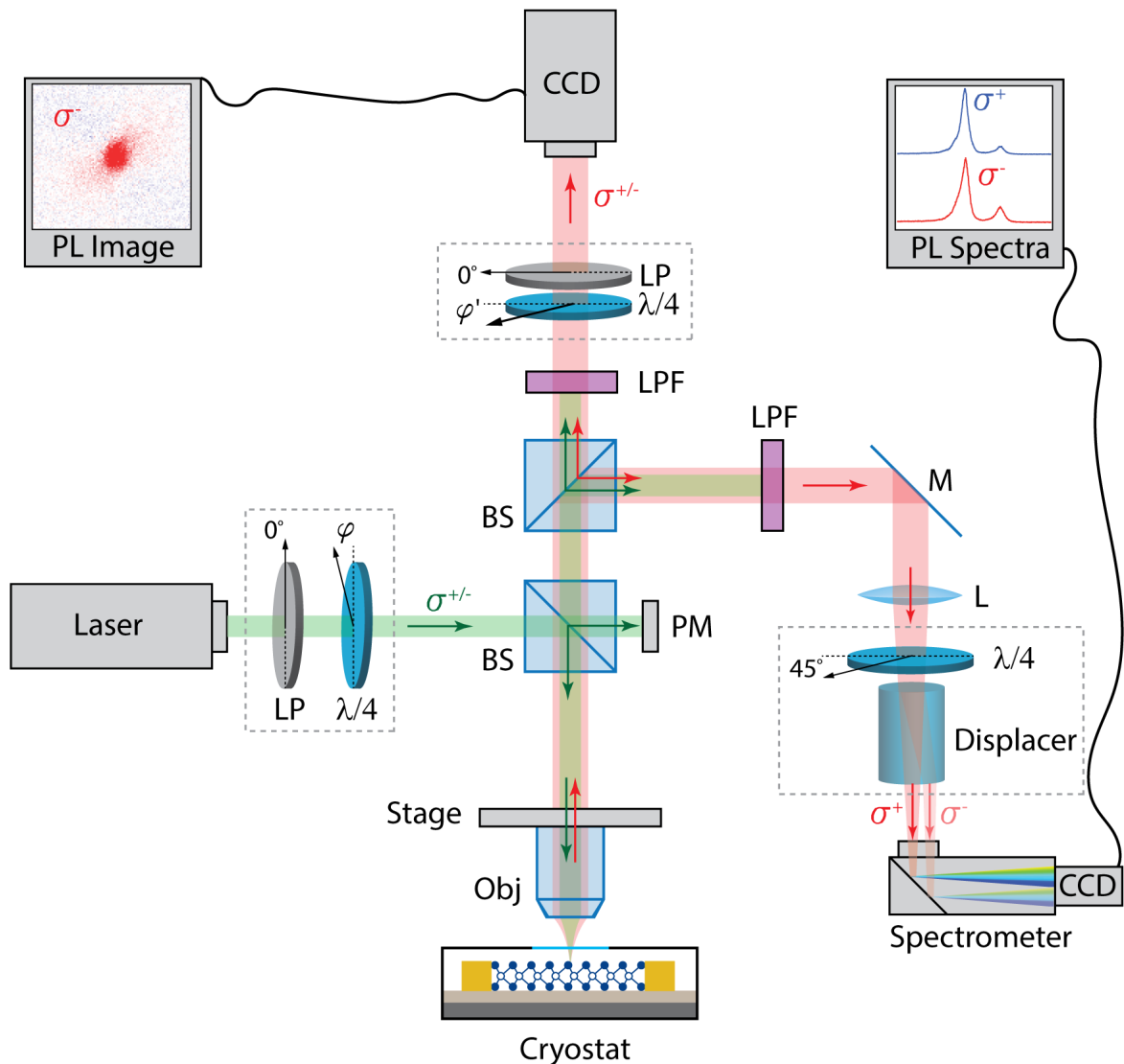


**Figure 3.12** – Schematic illustration of the optical setups for photoluminescence spectral and spatial imaging. Laser light source (right) emitted collimated beam, that is modulated in intensity and polarization, redirected via beam splitter to the power meter and down to the objective that focuses incident light on the sample placed inside a cryostat. Same objective is used for PL collection. Collected photons analyzed spatially with top CCD camera and spectrally by a side spectrometer with another attached CCD camera. BS is beam splitter, M is mirror, Obj is objective, CCD is charge-coupled device camera, PM is power meter, LP is linear polarizer, L is lens,  $\lambda/4$  is quarter-wave retarding plate. Green light with arrows represent higher-energy incident laser beam, while red light shows lower-energy emitted PL photons. Gray dashed areas represents optional elements for generation (left) and detection (top and right) of circularly polarized light, that includes linear polarizer, retarding plates and a displacer.

In order to perform polarization-resolved PL measurements it is necessary to generate circularly polarized incident light so that a specific valley is accessed. For this we employ a fixed linear polarizer (LP) and a consequent quarter-wave plate on a remotely controlled rotation stage. Depending on the relative alignment of the LP and the fast axis of the plate, the resulting polarization of the beam will be left (right) circularly or linearly polarized. Then, the collected PL emission should be analyzed for its polarization. For this we install another quarter-wave plate on a rotator and sequential linear polarizer fixed in front of the top CCD camera. This allows us to preferentially choose imaging polarization, depending on the position of the analyzing plate which is controlled remotely. Finally, in front of the spectrometer (after focusing lens) we install another quarter-wave plate fixed at  $45^\circ$  to the optical axis of the consecutive beam displacer made of birefringent Yttrium Orthovanadate. The plate convert left/right circular polarizations into basis of two perpendicular linear polarization which are separated by the beam displacer and simultaneously projected onto the diffraction grating and spectrometer camera, so that both spectra corresponding to left and right circularly polarized PL are captured simultaneously.

### 3.4.4 Other types of measurements

Described optical setup is very versatile and therefore can be employed for many other types of optical measurements by introducing small modifications.

For instance, placing on the excitation path a narrow band pass filter centered at the laser wavelength to "clean-up" the laser spectra and then installing a notch filter to remove the excitation wavelength just before the spectrometer allows us to measure phonon spectra of the investigated material. This so-called Raman spectroscopy is a powerful technique for the characterization of vibration modes that gives insights to the crystal structure, its defects, doping level and more. Figure 3.13a shows an example of the measured Raman spectrum of the WSe<sub>2</sub> monolayer encapsulated with h-BN flakes. Apart from the modes typical of WSe<sub>2</sub>, we can clearly see coupling of the h-BN phonons to the semiconductor electronic transitions, recently reported by two independent groups [135, 136].

Also, replacing incident laser with a collimated source of wide-spectra light (white-light) allows us to measure differential reflectivity spectra that highlight optical transitions of the characterized material. Example of such spectra for the very same sample (WSe<sub>2</sub> monolayer encapsulated with h-BN) is shown in Figure 3.13b, which demonstrates clear A-exciton peak. The advantage of this technique is the possibility to investigate band structure of an indirect semiconductor, inaccessible through photoluminescence measurements.

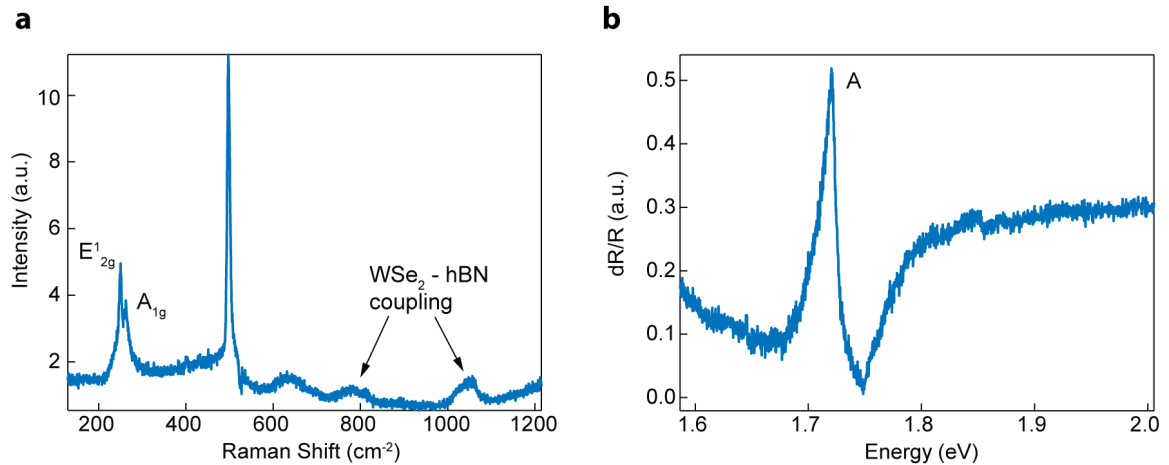


**Figure 3.13** – Structure characterization beyond photoluminescence. (a) Raman spectrum and (b) differential reflectivity spectrum of a WSe<sub>2</sub> monolayer encapsulated in h-BN. Measurements performed at 4 K.

Finally, such measurement techniques as magneto optical Kerr effect (MOKE), Faraday rotation, magnetic circular dichroism, second harmonic generation and others, were implemented in the current setup, along with realization of a separate ultra-fast setup for time resolved spectroscopy with femtosecond laser and streak camera for more comprehensive studies of the exciton dynamics. However all these go beyond the scope of this thesis and therefore will not be discussed here.



## 4 Optoelectronic devices

### 4.1 Introduction

One of the main challenges for today's information networks is to reduce power consumption while increasing speed of data transfer. In conventional networks, electrical signal is processed, transferred and read by metallic interconnects, where dense packing and speed of data processing are limited by Joule heating [137] and parasitic capacitance, respectively. Silicon photonics, on the contrary, holds promise for increasing speed and power efficiency of these networks [138, 139]. However, challenges in the design of integrated light-emitting devices and photodetectors have prevented the realization of practical circuits [3, 140].

Miniaturization of integrated devices for light modulation on silicon photonic platforms has brought attention to atomically thin two-dimensional materials [141], which can be easily fabricated on photonic structures, due to their outstanding mechanical and structural properties [30, 31].

Graphene has been extensively studied for data processing [27] and light detection [28]. However, this material suffers from high off currents [27] as well weak light coupling due to the absence of a band gap [142], which limits its applications for light emission and detection. Also it can not be employed for light emission. The remarkable electrical [41] and optoelectronic [143, 144] properties of 2D transition-metal dichalcogenides, including the presence of a direct band gap in the visible light range [50, 51], make them ideal candidates for this purpose. Besides realization of basic logic electrical devices [41], 2D semiconductors were demonstrated to be a promising material for light emission [52] and detection [145], with potential for the realization of optical to electrical interconnects [113, 146]. Such interconnects would be expected to operate over meter-scale distances or less, relaxing the wavelength requirements from those set by the optical fiber transmission windows. Large-scale growth by chemical vapor deposition has also been demonstrated [147, 148], which together with simplicity of device fabrication makes TMDC monolayers

## Chapter 4. Optoelectronic devices

---

good candidates for the fabrication of future optoelectronic devices.

In this chapter we will demonstrate such optoelectronic devices based on semiconductor monolayers, which hold promise as an interface between electrical signal processing and optical data transmission. The first part of the chapter is focused on realization of a tunable light-emitting diode (LED), while the second part demonstrates the first MoS<sub>2</sub> photodetector (PD) integrated with photonic circuits.

While MoS<sub>2</sub>-based high responsivity photodetectors have already been reported [28], their implementation in photonic circuits is still lacking. Here, we will bridge this gap by demonstrating integration of MoS<sub>2</sub> photodetectors with Si<sub>3</sub>N<sub>4</sub> photonic circuits, with three different device architectures to achieve either high photoresponse, fast operation speed or low operation voltages. This work was performed in a close and fruitful collaboration between Dmitrii Unuchek and Juan Francisco Gonzalez Marin, who are equally contributed authors of the article published in *npj 2D Materials and Applications*, 2019, 3:14 (DOI:10.1038/s41699-019-0096-4). There is a considerable overlap between this article [149] and the second part of the current chapter (Section 4.3).

## 4.2 Light emitting diodes

### 4.2.1 Introduction

First, we are aiming for a bright and stable source of light, a transceiver for efficient conversion of electrical data into optical signal. For this we fabricate a light-emitting diode that relies on the recombination of electron-hole pairs in the depletion region of a p-n junction that appears on the interface between regions with different doping levels. Generally speaking, such a p-n diode represents an essential element in optoelectronics and provides a well-established pathway for light emitters and solar cells fabrication. Here we will present different approaches towards obtaining atomically sharp p-n junctions. The first one relies on a vertically stacked heterostructure of two monolayer semiconductors, MoS<sub>2</sub> and WSe<sub>2</sub>, with different doping levels. The second approach exploits ambipolarity of a WSe<sub>2</sub> single-layer, where lateral p-n junction is established *via* spatially heterogeneous electrostatic doping. Finally, we demonstrate that using atomically flat h-BN crystal as a gate dielectric layer has a positive impact on device performance.

### 4.2.2 LED based on a vertical p-n junction

A typical p-n junction appears when n- and p-type semiconductors are brought in contact, and therefore it could be achieved in atomically thin limit by vertical stacking of monolayer semiconductors with different doping levels. Here we realize light-emitting diode based on a vertical p-n junction in a MoS<sub>2</sub>/WSe<sub>2</sub> heterostructure, first demonstrated by Cheng *et al.* [150] and schematically shown in Figure 4.1a.

Monolayer MoS<sub>2</sub> is known to be naturally n-doped [41] due to sulfur vacancies and the Fermi level pinning in the proximity of the conduction band [151]. Meanwhile, WSe<sub>2</sub> is slightly p-doped in ambient conditions. But more importantly, it demonstrates ambipolar transport [152] and therefore the type of doping can be controlled by the back gate voltage. Therefore, at a particular doping level, the heterostructure appears to be a vertical p-n junction that rectifies drain-source current with  $I - V$  characteristic typical for a diode, as shown in Figure 4.1b. When negative voltage is applied on the drain contacted to WSe<sub>2</sub>, the built-in potential is getting larger, preventing carriers to flow through the junction, which results in zero current. In contrast, positive bias decreases the potential barrier, making possible the injection of electrons from MoS<sub>2</sub> and holes from WSe<sub>2</sub> into the junction region where they recombine, leading to light emission. Example of such electroluminescence (EL) is shown in Figure 4.1d.

**Fabrication**

Fabrication of a typical device based on a vertical p-n junction starts with the transfer of MoS<sub>2</sub> on a pre-identified monolayer WSe<sub>2</sub>, followed by EBL patterning and evaporation of contacts. We were using Pd and Au/Ti electrodes to contact WSe<sub>2</sub> and MoS<sub>2</sub> respectively. Example of step-by-step fabrication procedure is shown in Chapter 3 and the resulting device is presented in Figure 4.1c. Both mechanically exfoliated and CVD grown crystals were employed, resulting in devices with similar characteristics. However, in the case of the CVD grown material, additional steps of electron beam lithography and oxygen plasma etching were performed in order to determine the geometry of the diode and to prevent undesired short circuits.

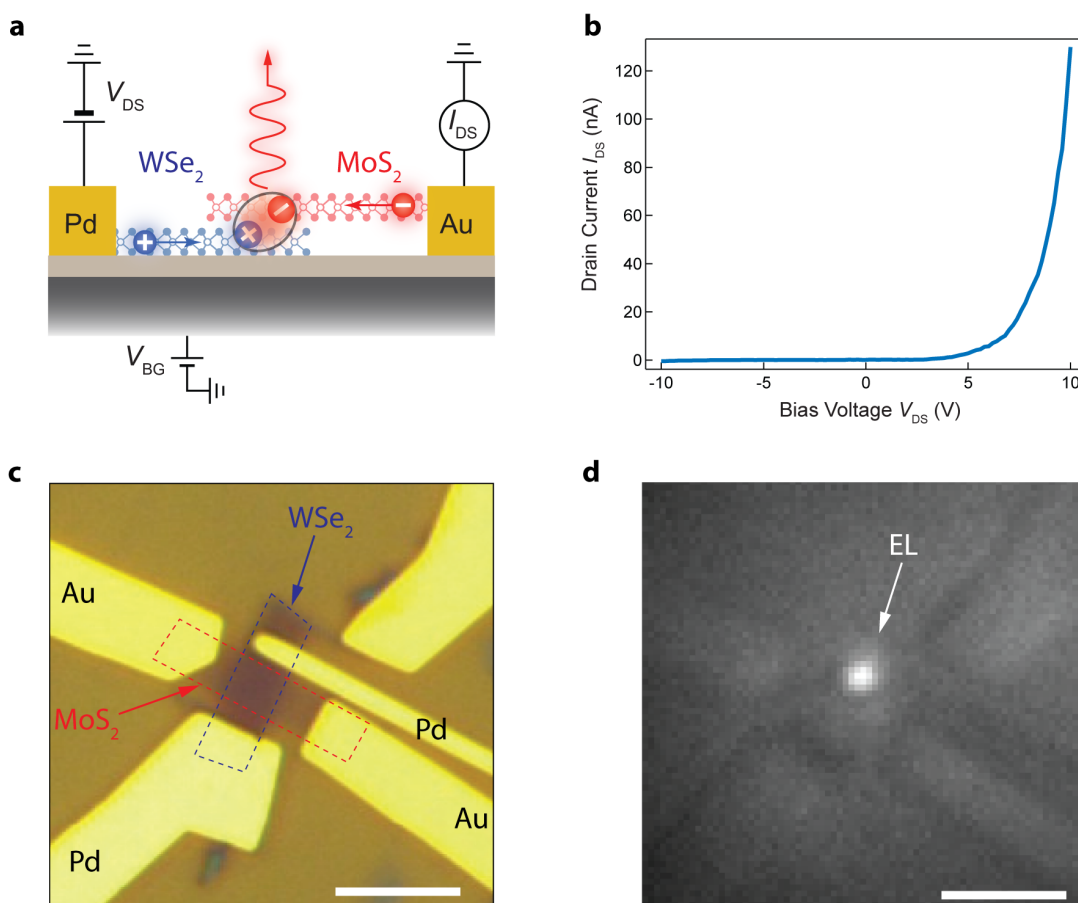


**Figure 4.1** – LED based on vertical p-n junction. (a) Device schematic. Vertical stacking of n-doped MoS<sub>2</sub> (red) and p-doped WSe<sub>2</sub> (blue) produces an atomically sharp p-n junction region where electrons and holes recombine with light emission.  $I_{DS} - V_{DS}$  characteristic of a resulting p-n diode reveals drain current rectification, shown in (b). (c) Optical image of a typical device based on MoS<sub>2</sub>/WSe<sub>2</sub> heterostructure, contacted with gold (Au) and palladium (Pd) electrodes. (d) CCD image of the electroluminescence from the device shown in (c) under a forward bias of 10 V. Outlines of the metallic contacts are also visible in this image. Scale bar for optical images is 5  $\mu$ m.



### Device characterization

Fabricated devices were electrically characterized by sweeping bias voltage and measuring drain current while keeping a constant gate potential. If a p-n junction is successfully established at a particular gate voltage, a diode-like  $I$ - $V$  characteristic could be measured. In this case electroluminescence is observed at forward biases above the threshold voltage, which entirely depends on the relative band alignment of the component materials. Example of such device characterization is shown in Figure 4.1b-d.

While we could observe all the effects described above in some of the devices, most of them did not demonstrate any electroluminescence, meaning that a p-n junction is not created. As was discussed before, we expect that at particular electrostatic gating MoS<sub>2</sub> is still n-doped whereas WSe<sub>2</sub> is already p-doped. While that can be true for some of the devices, in others we only see formation of an n-n resistor (both materials are electron-doped) without rectification behaviour at lower gate voltages [153], as shown in Figure 4.2a. This is because we rely on a natural doping-level of the crystals that can vary strongly from device to device depending on the materials supplier, growth conditions or even transfer- or storage-related contamination.

In order to investigate this problem in detail, we have fabricated a set of devices with additional pairs of electrodes on the monolayers. An example of such a device is shown in Figure 4.2b. Here, in addition to the heterostructure characterization (Figure 4.2a) we can independently investigate MoS<sub>2</sub> and WSe<sub>2</sub> crystals. Their  $I_{DS} - V_G$  transfer characteristics are shown in Figure 4.2c. As expected, MoS<sub>2</sub> is strongly n-doped while WSe<sub>2</sub> demonstrates ambipolar transport. Importantly, we do not observe intersection of the electron band of MoS<sub>2</sub> with the hole band of WSe<sub>2</sub>, which explains the shape of the map in Figure 4.2a and the absence of the gate range with p-n junction formation.

Since electrostatic doping is not efficient for our purpose, we try to change doping levels chemically by encapsulating the stack with 30-nm ALD-grown HfO<sub>2</sub> layer, which is known to dope MoS<sub>2</sub> with electrons. Measured gating curves of the same device after ALD deposition is shown in Figure 4.2d. We can clearly see the shift of the threshold voltage toward negative values indicating strong n-doping of the MoS<sub>2</sub> flake. Indeed, its sheet conductivity increases almost by two orders of magnitude at the same gate voltage. Being electron doped at -60 V gate voltage would be enough to form a p-n junction with the untreated WSe<sub>2</sub> flake. However this monolayer is also strongly affected by the HfO<sub>2</sub> deposition. Blue transport curve in Figure 4.2d reveals huge hysteresis and absence of the hole branch of conduction. This indicates strong degradation of the flake transport properties since it was exposed to the water vapor at 200°C, which causes formation of selenium vacancies and other types of defects.

## Chapter 4. Optoelectronic devices

As we can see from the obtained results, such a device configuration is not reliable since it does not allow independent doping control of the compound flakes in the MoS<sub>2</sub>/WSe<sub>2</sub> stack. Instead, both flakes are gated simultaneously and a p-n junction can not be formed in most of the structures. Therefore we explore alternative approaches for LED fabrication in the following section.

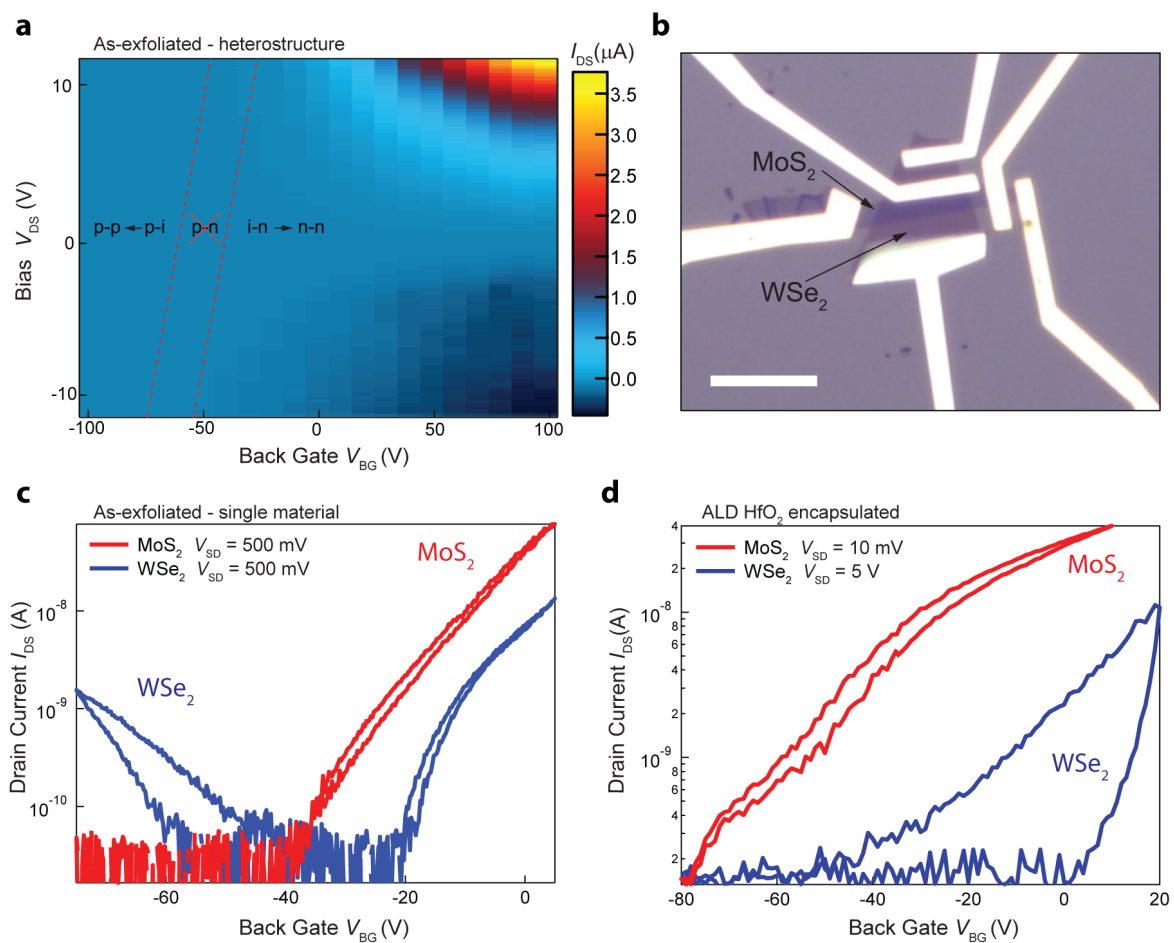


**Figure 4.2** – Characterization of vertical heterostructure. (a) Gate-bias map of the drain current through the heterostructure shown in (b). Dashed line represents regions where n-n and p-p resistors are formed with the p-n junction region expected to be in between them. It is however not observed in this device. (b) Optical micrograph of the device, that allows characterization of both the heterostructure and independent monolayers. Scale bar is 10  $\mu\text{m}$ .  $I_{DS} - V_{BG}$  transfer characteristic of the independent MoS<sub>2</sub> and WSe<sub>2</sub> monolayers before (c) and after (d) HfO<sub>2</sub> top encapsulation. Bias voltages are indicated in the graphs.

### 4.2.3 LED based on a lateral p-n junction with an $\text{Al}_2\text{O}_3$ gate dielectric

In this section we use a different approach for LED fabrication. Namely we present here light emitters based on electrically controlled lateral p-n junctions within a single  $\text{WSe}_2$  monolayer, known to be a direct semiconductor [154] with high quantum efficiency at room temperature [155]. In addition, these devices exploit ambipolar transport of  $\text{WSe}_2$ , that we have already demonstrated in Figure 4.2c. Application of positive gate voltages shifts the Fermi level closer to the conduction band, bringing more electrons into the channel, making it n-doped. In contrast, negative gate voltages deliver holes in  $\text{WSe}_2$ , resulting in p-doping. Therefore, spatially heterogeneous gating, where two parts of the device are doped electrostatically by opposite gate potentials, will establish a lateral p-n junction within the  $\text{WSe}_2$  monolayer.

Similarly to a conventional p-n diode, such a device will rectify current flowing in the channel. Moreover, under the forward bias electrons and holes will be injected into the junction region from opposite sides with consequent recombination and light emission. The heterogeneous gating is possible for instance by employing independent split gates as was reported by four independent groups [156, 157, 158, 159]. Schematic of such a LED is presented in Figure 4.3a.

#### Numerical simulations

Prior to device fabrication we perform numerical simulations in order to determine optimal parameters of the local backgate geometry. We are particularly interested in one of the free parameters that can be varied for device fabrication, the separation distance between gate electrodes that might alter the carrier transport through the channel.

Figures 4.3b-c show results for the device in the p-n configuration, when the two gates have opposite voltages. Spatial distribution of the electrical potential in the device is shown in Figure 4.3b, calculated for three values of the gate separation. The corresponding carrier density along the channel is plotted in Figure 4.3c. Formation of an intrinsic (i) region with nearly zero surface charge density above the gap is clear with the enlargement of gate separation gap. This intrinsic region appears because of ineffective electrostatic doping between gates and it can strongly affect carrier transport across the junction. On the one hand, a large intrinsic region makes the diode a worse rectifier. On the other hand, this layer extends the depletion region sensitive to light, which is an advantage for photodetector fabrication. For the light emission purpose we chose a 100-nm wide gate separation as an optimal trade-off between fabrication complexity and device efficiency. It is important to note, that the undoped region appears not only in the p-n diode configuration, but also in the FET configuration when both gates have the same potential. This region

increases resistivity of the n- or p-doped flake, and compromises extracted carrier mobility, decreasing it by orders of magnitude.

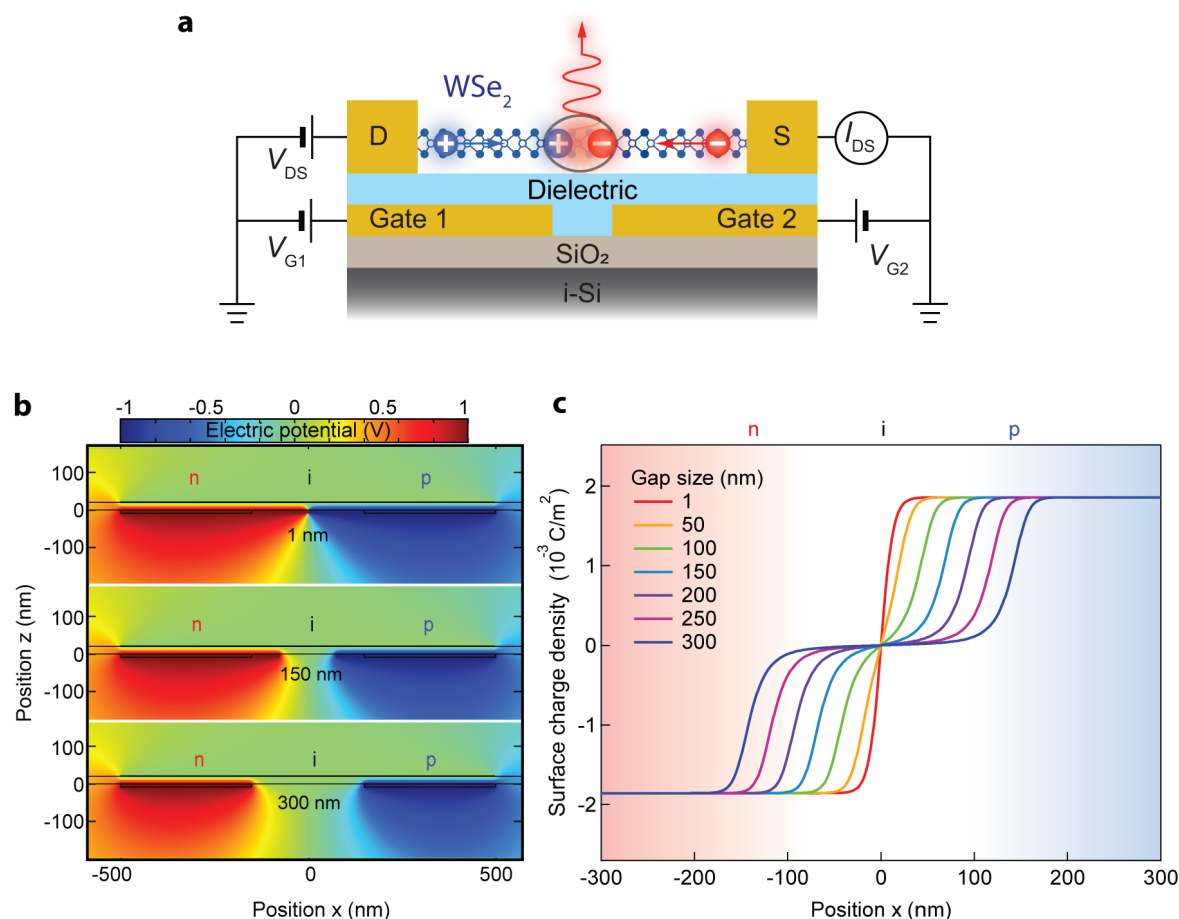


**Figure 4.3** – LED based on a lateral p-n junction. (a) Schematic of the device structure. Two independent local bottom gates establish the regions doped with electrons and holes. Under forward bias, both types of carriers can be injected from opposite sides with recombination in the intrinsic region. (b) Results of numerical simulations in the case of p-n junction configuration with following gate voltages  $V_{G1} = +1$  V and  $V_{G2} = -1$  V. Electrical potential distribution in the vertical cross sections of the device, calculated for three different gap sizes: 1 nm (top), 150 nm (center), 300 nm (bottom). (c) Corresponding charge densities in the channel for bigger set of gap dimensions. Clear formation of intrinsic region in the gap.

### Fabrication

We have fabricated devices presented in this section on an intrinsic silicon (i-Si) wafer with 270-nm oxide layer. We employ intrinsic silicon substrate in order to eliminate potential leakage currents. The process starts with electron beam patterning of the mask for further evaporation of local back gates. We aim at having a thin and flat gate array. For this we

deposit 6 nm of platinum with 2 nm chromium buffer layer for better adhesion to the substrate. Optical image of the resulting structure is shown in Figure 4.4a.

Following step, shown in Figure 4.4b, is atomic layer deposition of gate dielectric. Here we use a 20-nm thick  $\text{Al}_2\text{O}_3$  layer that has a  $4 \cdot 10^{-7} \text{ F/cm}^2$  capacitance per unit area compared to  $1.3 \cdot 10^{-8} \text{ F/cm}^2$  of the 270-nm thick  $\text{SiO}_2$  layer. Optionally, the gate dielectric is annealed in forming gas for the passivation of dangling bonds.

Figure 4.4c presents the next step which is mechanical exfoliation on PDMS stamp and identification of suitable  $\text{WSe}_2$  monolayers with following transfer on the gates covered with the dielectric. Fabrication procedure is completed by patterning, evaporation and liftoff of contact electrodes made of 50-nm thick palladium. The finished device is presented in Figure 4.4c and characterized in the following sections.

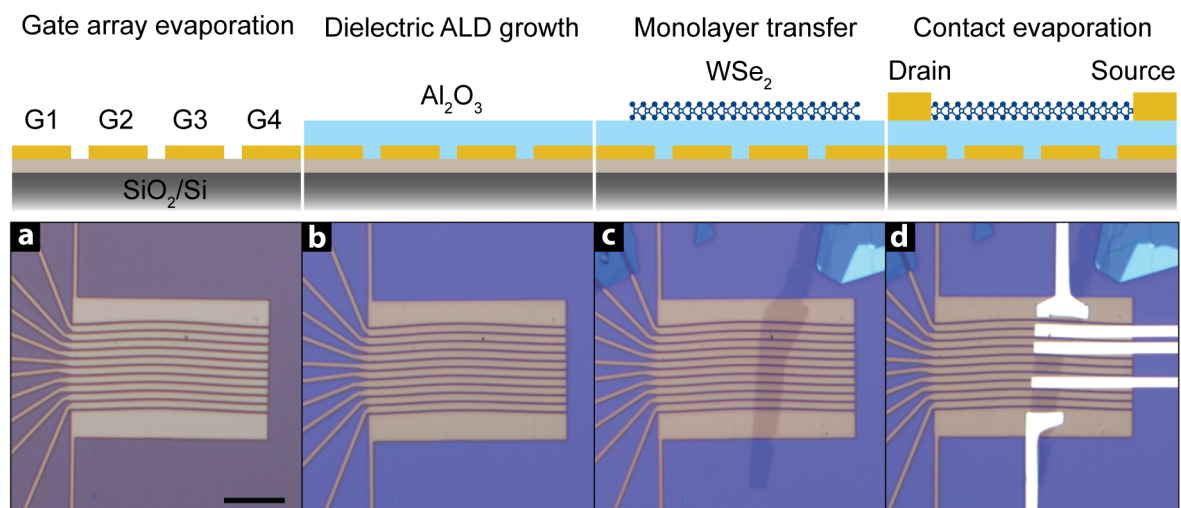


**Figure 4.4** – Fabrication process of the lateral LED with the  $\text{Al}_2\text{O}_3$  dielectric layer. Schematics on the top corresponds to the optical images on the bottom, demonstrating deposition of the thin platinum gate array (a), ALD growth of the 20 nm  $\text{Al}_2\text{O}_3$  gate dielectric layer (b), transfer of a monolayer  $\text{WSe}_2$  flake (c) and deposition of source and drain palladium contacts (d). Scale bar is 10  $\mu\text{m}$ .

### Electrical characterization

We start investigation of a fabricated device by characterizing the  $\text{WSe}_2$  monolayer flake, which is the core of our device. For this, we set it in the FET configuration with gate stripes connected together and swept simultaneously. Therefore, the device in this configuration effectively behaves as a field effect transistor with a small undoped region in the center.

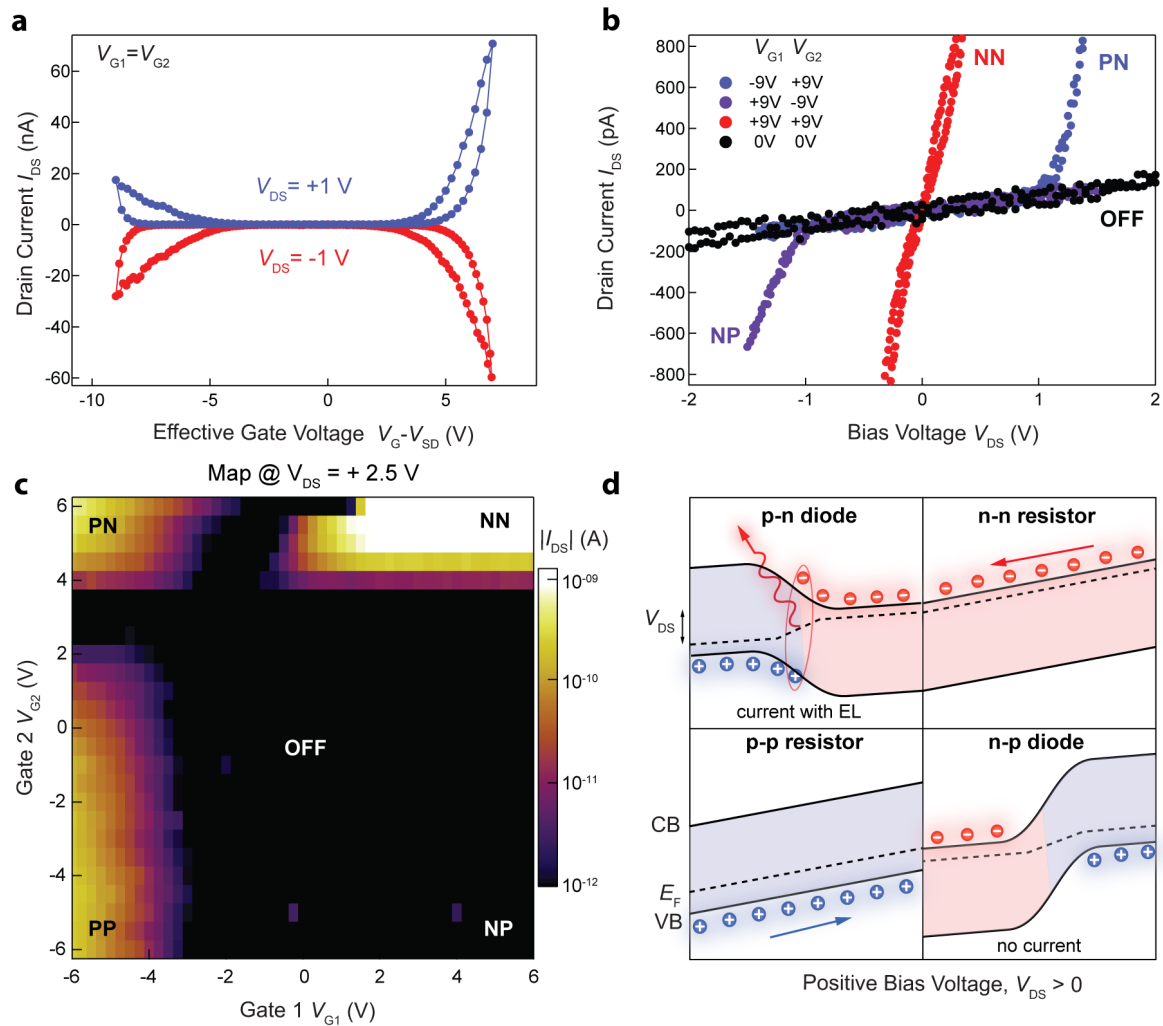


**Figure 4.5** – Electrical characterization of the lateral LED with an  $\text{Al}_2\text{O}_3$  dielectric layer. (a)  $I_{\text{DS}} - V_{\text{G}}$  transfer characteristic of the device in the configuration with gates connected and swept together. Blue curve corresponds to positive drain bias ( $V_{\text{DS}} = +1 \text{ V}$ ) while red one represents transport with negative bias ( $V_{\text{DS}} = -1 \text{ V}$ ). Applied bias is subtracted from the gate voltage in order to eliminate self-gating effect that shifts position of the transfer curve (b)  $I_{\text{DS}} - V_{\text{DS}}$  curves of the device in all possible gate configurations. (c) 2D map of the drain current as a function of the applied gate voltages revealing three islands of conductivity at positive bias ( $V_{\text{DS}} = +2.5 \text{ V}$ ). (d) Schematic illustrations of the band structures along the device channel in different regimes observed in the map (c). Blue and red areas correspond to p- and n-doped regions. CB is conduction band, VB is valence band,  $E_{\text{F}}$  is the Fermi level.

Here, we would like to mention the self-gating effect, which is particularly pronounced in devices with local gates like the one we are investigating here. The issue comes from the fact that the potential difference between the channel and the gate depends not only on the gate voltage but also on the applied bias. Therefore, the position of a measured transfer

characteristic depends on the drain-source potential difference. Thus we can extrapolate it to a zero-bias case by plotting drain current as function of the effective gate voltage which is the difference between gate and channel potentials. As the result of this operation, we can see two symmetrical curves in Figure 4.5a, which correspond to positive (blue) and negative (red) bias voltages.

As expected, we acquire ambipolar transport with access to both branches of conductivity. We observe hysteresis and a slight shift toward electron doping that we assign to the  $\text{Al}_2\text{O}_3$  substrate, which will be discussed later.

We measure the  $I - V$  curve when the flake is uniformly doped with electrons, which corresponds to the right corners of the transfer characteristic. We call this state of the device NN-configuration, that is one of three possible regimes for FET configuration, including hole-doped (PP) and undoped (OFF) device. Results of measurements are represented with red markers in Figure 4.5b. Linear  $I - V$  characteristic indicates the absence of the Schottky barrier on the metal- $\text{WSe}_2$  interface. Overlapping between top and bottom electrodes allows gating underneath the source and drain contacts. This decreases the barrier height and improves charge injection into the channel.

We now reconfigure the device in the p-n diode regime by applying gate voltages of opposite polarities ( $V_{G1} < 0$ , and  $V_{G2} > 0$ ). This significantly changes the device behaviour. Instead of a linear resistor-like  $I - V$  curve we now measure the strongly asymmetric curve shown in Figure 4.5b, blue markers. Rectification of the forward current indicates establishing of a p-n junction with hole (electron) doped regions on the side of drain (source) contact. By reversing gate voltages ( $V_{G1} > 0$ , and  $V_{G2} < 0$ ), diode switches in the opposite direction, that is an n-p diode, which rectifies backward current. This NP configuration is shown in Figure 4.5b, violet dots. In the same plot, black curve corresponds to the OFF state, with both gates grounded.

For better understanding of the device configurations and transitions between them, we measure drain current as a function of applied gate voltages at a constant positive bias of  $V_{DS} = +2.5\text{ V}$ . Every corner of the resulting map, which is shown in Figure 4.5c, represents a different device configuration (PN, NN, NP and PP). We can clearly distinguish three well separated conductivity islands, while the fourth corner remains dark together with the center of the map that represents the OFF state. This is expected as the n-p diode prevents current flow under forward bias. Bottom-right corner (NP) appears bright on the conductivity map measured under backward bias, while the opposite one (PN) becomes dark. Again, we can see the effect of hysteresis on the very top line of the current map that corresponds to the first measurement sweep. Each of the device configurations under the forward bias, including PN and NP diodes, NN and PP resistors, is schematically explained in Figure 4.5d. Cartoon positions in the diagram correspond to the corners of the current

map. When the flake is n-doped (NN), the device behaves as a resistor with bias voltage causing electron drift along the channel. Similarly, the opposite corner, which is the PP-regime, corresponds to the p-doped channel, so that the device operates as a resistor with holes playing a role of charge carriers. In the case of heterogeneous electrostatic doping, for instance in the PN-configuration, the device behaves as a p-n diode with the forward bias decreasing the built-in potential that results in electron and hole injection in the junction region with recombination and light emission. In contrast, positive bias applied to the device in the NP-regime increases the potential barrier, preventing current flow.

### Multiple junctions

A big advantage of the demonstrated device is its tunability and reconfigurability. For instance, by employing an electrode array (shown in the inset of Figure 4.6a) instead of a single pair of gate electrodes, we can controllably establish p-n junctions in different locations. The junction position will solely depend on the voltage distribution over the multiple stripes of backgates. We demonstrate it by fabricating and characterizing such a device in Figure 4.6. Interestingly, the device shows similar performance for different junction positions. We can clearly see that  $I - V$  curves measured for different gate voltage resemble each other. Schematics in Figure 4.6b illustrates device performance for p-n junctions established in various locations.

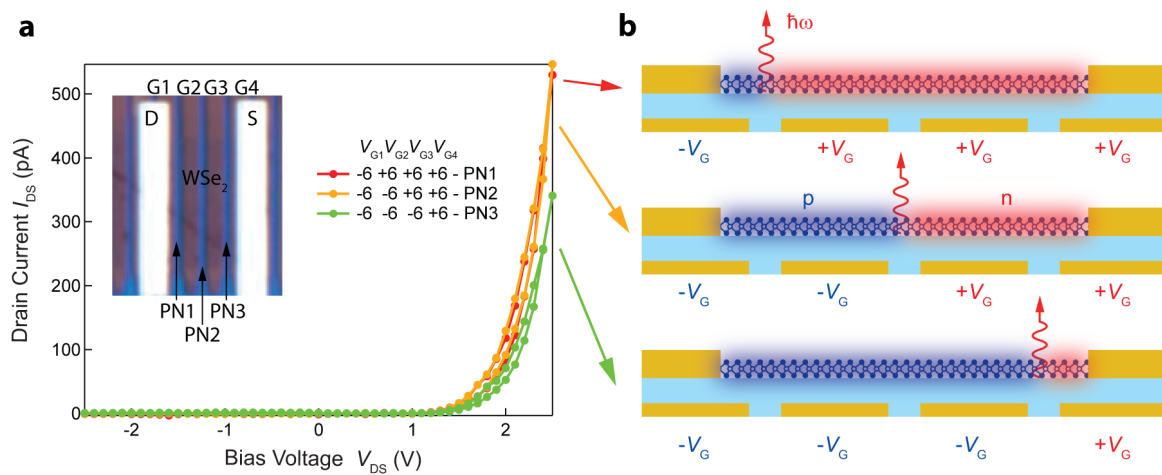


**Figure 4.6** – Device with multiple junctions. (a)  $I_{DS} - V_{DS}$  curves measured for the device in the PN configuration. Different colors corresponds to the p-n junction established in different positions determined by gate voltages. Inset shows optical image of the measured device (b) Schematic illustrations of the device states corresponding to measurements in (a). Blue and red shaded areas represents p- and n-doped regions respectively.

As we said above, switching gate voltages discretely moves the region of electron-hole



recombination, as well as the light emitting area. Therefore, this device architecture can be employed as a "dispenser"-like electrical-to-optical interface. Depending on the applied bias and gate voltages, light can be coupled into one out of several optical waveguides patterned underneath the gate gaps.

### Device disadvantages

The obtained results prove the device architecture to be promising. Nevertheless, we notice some drawbacks in device performance. Namely, as we have already mentioned, transfer characteristic of devices in the FET-configuration demonstrates that  $\text{WSe}_2$  is slightly n-doped. Also, we notice hysteresis in transport curves. Both of these effects could originate from contamination related to the monolayer transfer process. Therefore, we test thermal annealing in high vacuum that is known to improve electrical transport and optical properties in graphene and monolayer TMDCs [160]. However, after annealing, the situation is worsened as the flake becomes strongly n-doped. We can no longer observe hole conductivity within a reasonable gate voltage range. We assign this large doping to the charge transfer from the substrate to the monolayer as thermal annealing improves the coupling between them. We also notice in Figure 4.7a a large hysteresis, which we attribute to the charges trapped at the interface between  $\text{Al}_2\text{O}_3$  and  $\text{WSe}_2$ . Additional temperature-dependent measurements indicates charge traps freezing at low temperatures, reducing hysteresis of the transfer characteristic[161].

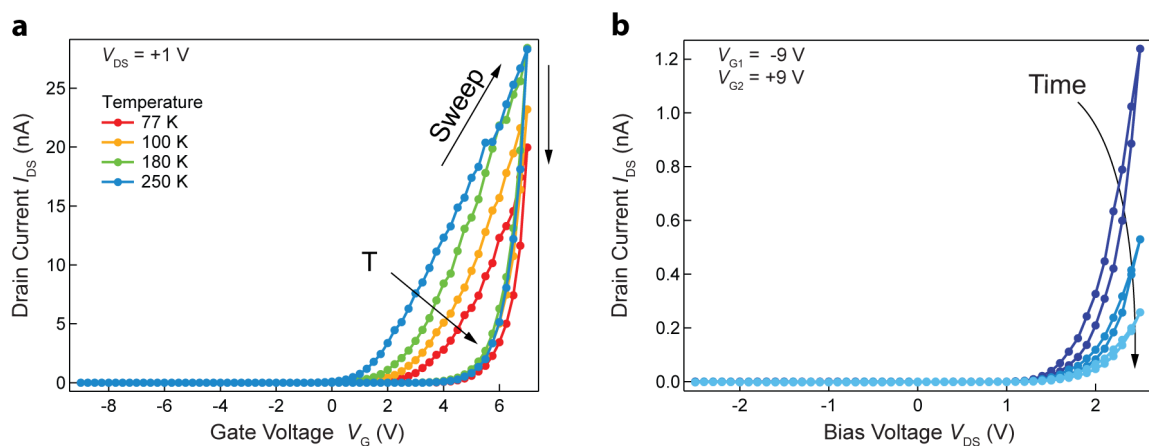


**Figure 4.7** – Degradation of the lateral LED with  $\text{Al}_2\text{O}_3$  dielectric layer. (a)  $I_{DS} - V_G$  Transport characteristic of thermally annealed device in the FET configuration when gates are connected and swept together, measured for a set of temperatures. Only the n-side can be observed within the studied gate region indicating strong n-doping of the  $\text{WSe}_2$  channel after annealing. (b) Progressive electron doping with time degrades the characteristics of the device in the p-n diode configuration.

Interestingly, even without a specific thermal annealing we observe a shift in the threshold voltage when operating the device. That can be explained by a high current flow that effectively anneals the device. Since the  $WSe_2$  channel appears more and more n-doped with time, the p-n junction becomes difficult to establish, thereby degrading the performance of the LED, as seen in Figure 4.7b.

#### 4.2.4 LED based on a lateral p-n junction with an h-BN gate dielectric

In this section we employ a two-dimensional h-BN crystal as the gate dielectric layer instead of ALD grown  $Al_2O_3$ . We demonstrate that the atomically flat dielectric, which is free of dangling bonds, trap states and charge inhomogeneities, improves device performance and long-term stability. Indeed, the h-BN substrate has been already employed for realization of high quality structures based on graphene [130, 161] and TMDCs [94, 162, 163, 164].

##### Fabrication

The fabrication procedure is similar to the one presented before. However instead of ALD growth of a dielectric layer we now deposit h-BN crystal. For this we exfoliate the h-BN flakes on a PDMS stamp for further transfer on a pre-patterned 8 nm thick chrome-platinum backgates. We aim at 10- to 20-nm thick hBN crystals, which have a capacitance similar to the 20-nm  $Al_2O_3$  layer.

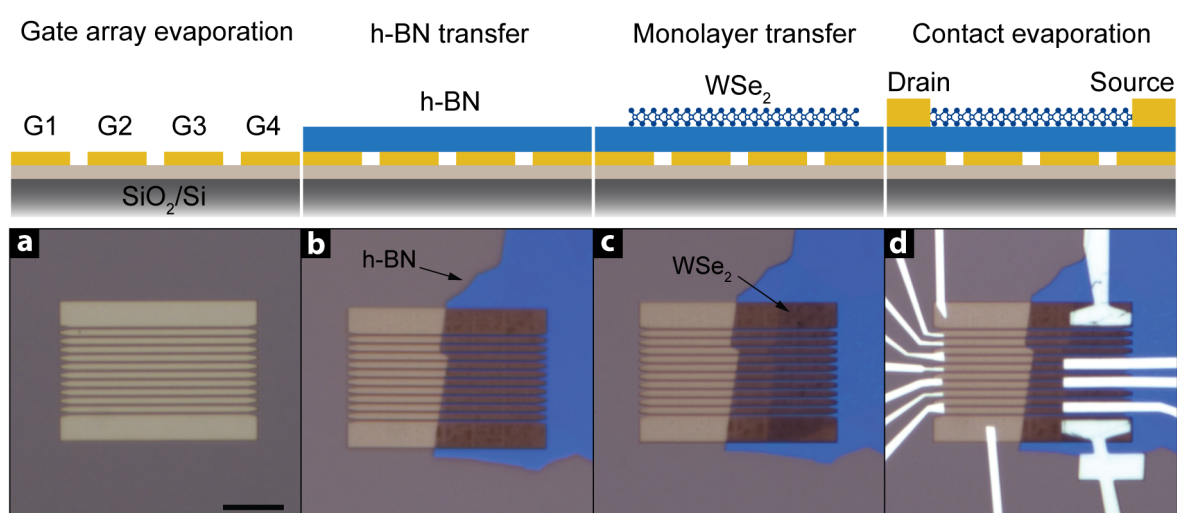


**Figure 4.8** – Fabrication process of the lateral LED with h-BN dielectric layer. Schematics on the top corresponds to the optical images on the bottom. They demonstrate deposition of the thin platinum gate array (a), transfer of a 20-nm h-BN flake (b), transfer of a monolayer  $WSe_2$  flake (c) and deposition of source and drain contacts (d). Scale bar is 10  $\mu m$ .

After the h-BN transfer we anneal the stack in air at 300°C for 8 h in order to burn and evaporate from the surface all possible residues. After the surface quality check carried out by AFM, we transfer a WSe<sub>2</sub> monolayer flake of suitable size and shape pre-exfoliated on another PDMS stamp. We anneal then the final stack in high vacuum at 240°C for 6 h. The fabrication procedure is completed by patterning, evaporation and liftoff of contact leads made of 50-nm thick palladium. Optical images of different fabrication steps and of the finished device are presented in Figure 4.4.

### Electrical characterization

By introducing the h-BN layer, we immediately see an improvement in the transfer characteristic, as shown in Figure 4.9a, measured on a fabricated device biased by a positive drain-source voltage ( $V_{DS} = +1V$ ). We observe two symmetrical branches of conductivity with no or little hysteresis. From the semi-log plot, shown in the inset of Figure 4.9a, we conclude that WSe<sub>2</sub> on h-BN is intrinsic as both threshold voltages have the same absolute value of 4 V. We also observe similar electron and hole mobilities of 0.2 cm<sup>2</sup>/V·s. However, inefficient gating of the region between gates leads to underestimation of the extracted value by factor of 40, according to numerical simulations. Therefore the estimated two-probe mobility is about 10 cm<sup>2</sup>/V·s at room temperature.

Following the measurement of transfer characteristics, we focus our attention on the device output at different regimes. We plot  $I - V$  curves of the device in the NN, PN and NP regimes in the inset of Figure 4.9b. While PN (blue) and NP (violet) configurations reveal expected diode-like rectifying behaviour, the NN regime now appears to deviate from the linear resistor-like curve. We associate this non-linearity at zero bias with the large undoped region and with Schottky barriers at the interface with metal [156]. The later one was absent due to electron doping from the Al<sub>2</sub>O<sub>3</sub> substrate that is missing now.

We gain more insight into the p-n junction by plotting  $I - V$  curves in semi-log scale for the device in PN and PP configurations, as shown in Figure 4.9b. We model the device output by the following equation that describes an ideal diode:

$$I = I_0 \left( e^{\frac{qV}{nk_B T}} - 1 \right) \quad (4.1)$$

where  $I_0$  is the saturation current at negative bias,  $q$  the elementary charge,  $k_B T$  the thermal energy of the system and  $n$  is the diode ideality factor. We fit our data with this exponential relationship (dashed line in the plot) and extract ideality factors of 2.3 and 2.4 for NP and PN configurations correspondingly. An ideality factor above 2 implies that the recombination is limited by both types of carriers and not just by minority ones. Moreover,

## Chapter 4. Optoelectronic devices

recombination current dominates over the diffusion current [158], which we attribute to a large space charge zone. Deviation from exponential growth at higher bias voltages can be explained by a series resistance that can be accounted for in a more sophisticated model [165]. Figure 4.9 shows current through the device acquired under positive (c) and negative (d) biases. We observe symmetrical, hysteresis-free, well separated conductivity islands, which were already extensively discussed and explained by the schematics in Figure 4.5d.

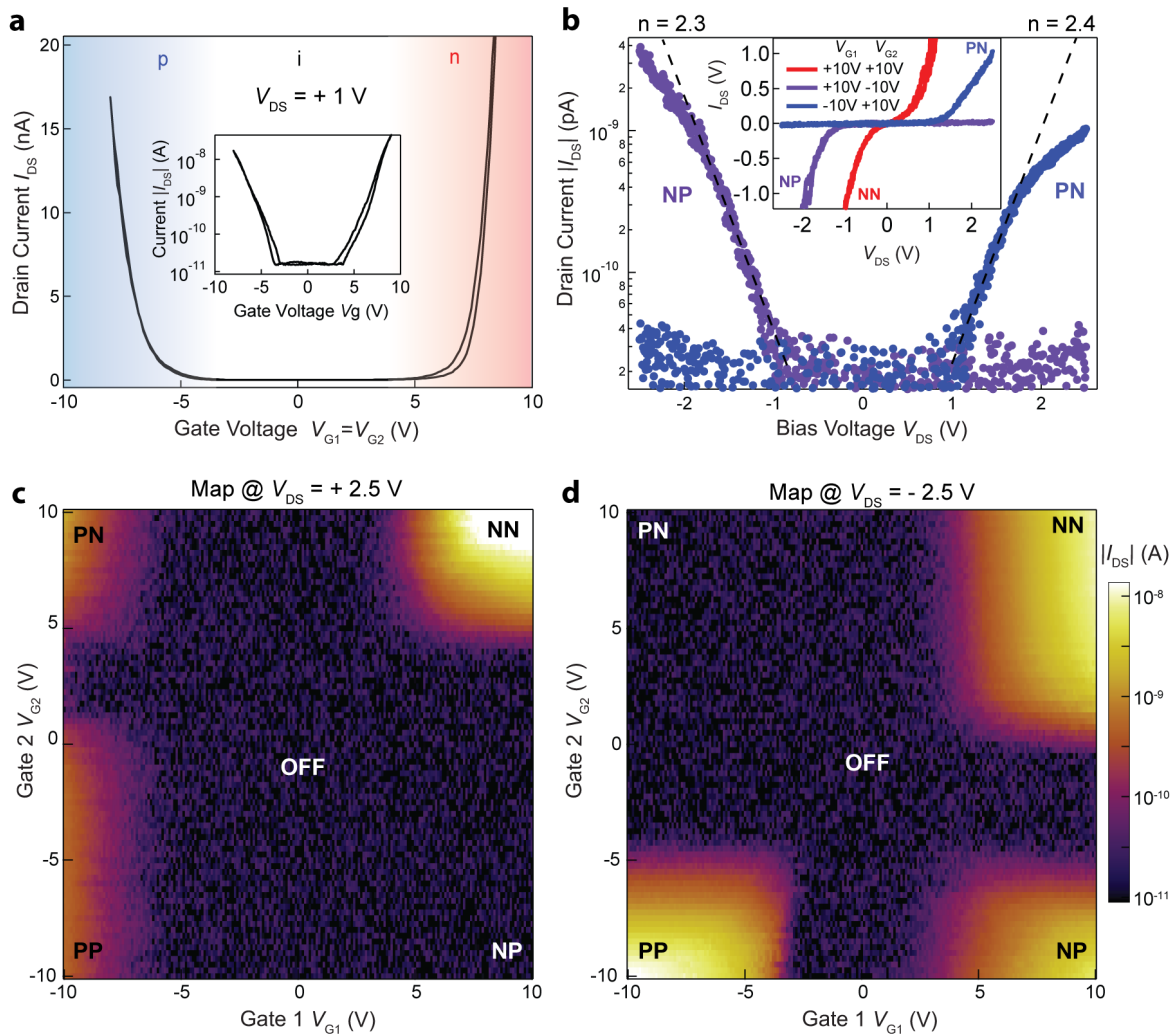


**Figure 4.9** – Electrical characterization of the lateral LED with the h-BN dielectric layer. (a)  $I_{DS} - V_G$  transfer characteristic of the device in the FET configuration when the gates are connected and swept together, measured under a forward bias of  $V_{DS} = +1$  V. Blue and red shading represents p- and n-type transport. Inset displays the gating curve in logarithmic scale. (b)  $I_{DS} - V_{DS}$  curves of the device in p-n (blue) and n-p (violet) diode configurations in logarithmic scale. Dashed line shows the exponential fit for ideality factor extraction. Inset graph demonstrates  $I - V$  curves for n-n resistor, p-n and n-p diode regimes in linear scale. (c, d) 2D map of the drain current as function of applied gate voltages measured at positive ( $V_{DS} = +2.5$  V) and negative ( $V_{DS} = -2.5$  V) bias.

### Light emission

Being confident of the electrical performance of fabricated devices, we now investigate optical aspects of the LED based on a lateral p-n junction with an h-BN dielectric layer. We start with configuring the device into the PN-regime. We confirm that a p-n junction has been established by measuring the output characteristic, demonstrating current rectifying behaviour, shown in Figure 4.10a. Under stronger bias and therefore higher drain current, we obtain bright electroluminescence from the junction region, shown in the plot inset. Indeed, we can observe EL at current densities below  $1 \text{ nA}/\mu\text{m}$  that makes it promising for implementation of electrically pumped laser based on a 2D semiconductor.

At room temperature (300 K), electroluminescence spectra bears a resemblance to the photoluminescence acquired on the very same  $\text{WSe}_2$  monolayer channel. Though, from the spectra we can conclude that the EL process goes through the neutral exciton recombination (750 nm), while both neutral and charged (790 nm) species participate in the PL process.

We now study the power dependency of the electroluminescence. Figure 4.10c shows EL spectrum evolution with the increase of current through the junction. We see that the emitted light preserves its shape. In addition, we plot EL intensity as a function of current in Figure 4.10e, that shows slightly sub-linear dependency  $I_{\text{EL}} \sim I_{\text{DS}}^\alpha$ , with extracted  $\alpha = 0.92$ .

Finally, we investigate the temperature dependence of the electroluminescence. We plot normalized EL spectra for a set of temperatures from 300 K all the way down to 4 K. First of all, we observe energy blue-shift and narrowing of the line corresponding to the neutral exciton emission, that we extract and represent in Figure 4.10f. These effects go in line with bandgap shrinkage and excitonic emission broadening due to the phonon-exciton interaction at elevated temperatures. Similar energy shift and bandwidth change of the neutral exciton emission were also observed in temperature dependent PL studies [166].

Furthermore, similar to low temperature photoluminescence, at 4 K we observe multiple lines beyond neutral excitons. These are different kinds of exciton species including charged excitons, dark excitons, (charged) (dark) biexcitons, defect-bound excitons and others. Because of this huge variety of excitonic states, there was a long debate in the community regarding the exact origin of each emission peak [59, 61, 62, 63, 167, 168, 169, 170]. We would like to notice here, that their occurrence is due to the electron band structure of  $\text{WSe}_2$  monolayer, which reveals lowest possible transition to be spin-forbidden. Therefore all secondary recombination pathways becomes similarly efficient and thereby they appear strong in PL spectra at low temperature.

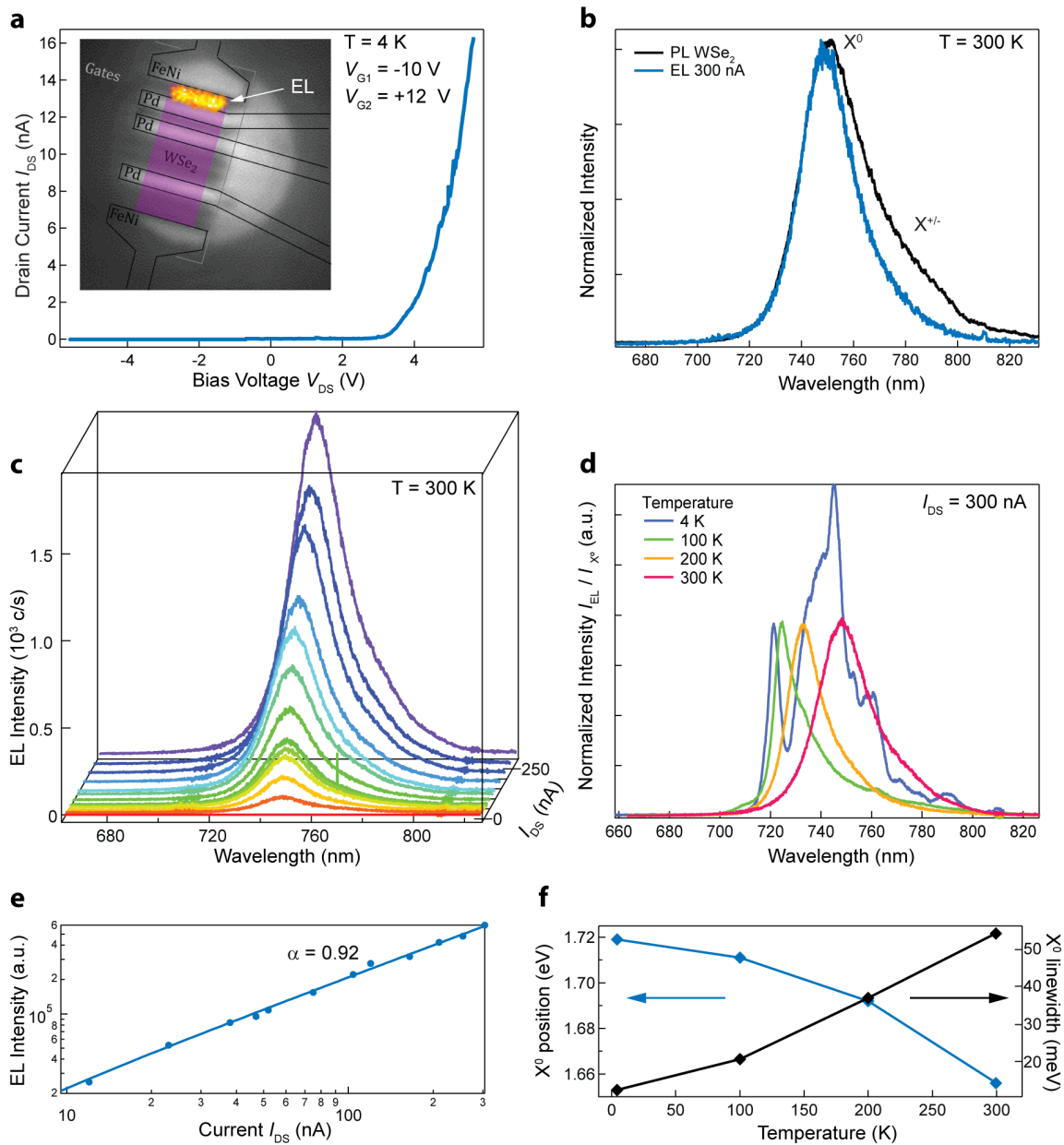


**Figure 4.10** – Optical characterization of the lateral LED with the h-BN dielectric layer. (a)  $I_{DS} - V_{DS}$  curves of the device in the p-n diode configuration that generates electroluminescence in the forward bias. Inset shows EL map superimposed on the reflection image of the device with outlined contacts. Both gating curve and EL map are observed at low temperature (4 K). (b) Electroluminescence and photoluminescence spectra measured at room temperature. EL emission happens at the energy corresponding to the neutral exciton, while charged species are distinguishable in the PL spectrum, taken from the semiconducting channel of the same device as the EL spectra. (c) EL spectra at different injection currents. (e) Extracted from (c): EL intensity versus injected current showing near-linear dependency. Solid line corresponds to the fit to the power-law. (d) EL spectra normalized by the intensity at the neutral exciton wavelength measured at various temperatures. (f) Extracted from (d): position (blue) and linewidth (black) of the neutral exciton as a function of temperature.

## Photocurrent generation

We demonstrated above, that the device based on the  $\text{WSe}_2$  monolayer configured as a lateral p-n junction can efficiently emit light. Indeed, despite the light emission, this device in the PN/NP configurations can also serve as a light detector, which we prove below.

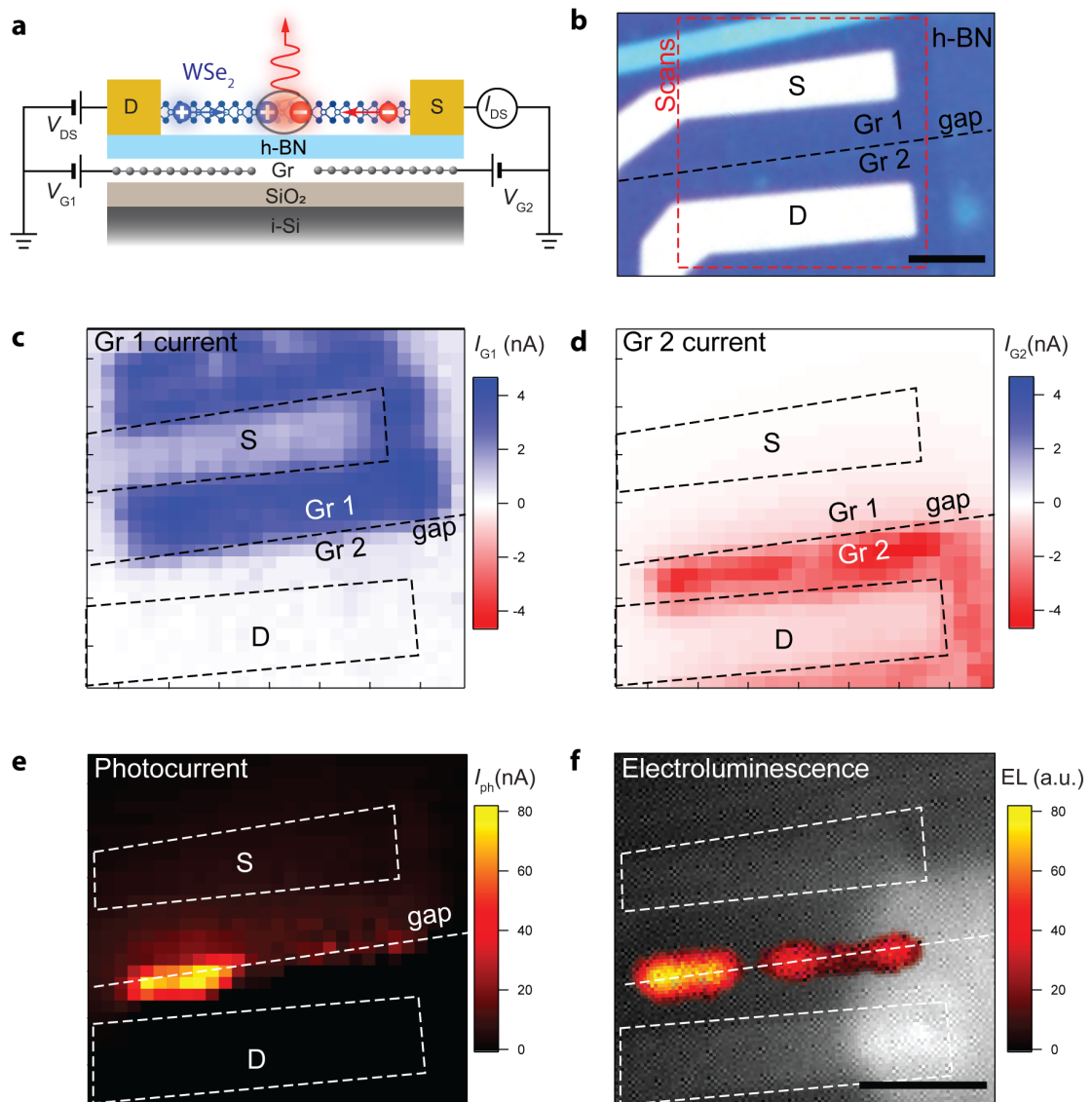


**Figure 4.11** – Photocurrent generation in the lateral p-n junction. (a) Schematic of a device, based on  $\text{WSe}_2$ /h-BN/Gr stack. (b) Optical image of the device. Red square indicate area used for spatial mapping in c-f. (c,d) Photocurrent generated on the oppositely biased graphene gates ( $V_{G1} = 10$  V,  $V_{G2} = -10$  V). Blue and red areas therefore represent p- and n-doped regions of the  $\text{WSe}_2$  flake. (e) Photocurrent map as a function of laser spot position. (f) Electroluminescence image overlaid on the reflection image of the device. EL obtained under the same gate configuration, at  $I_{DS} = 240$  nA and  $V_{DS} = 4$  V. Dashed lines outline contacts and the gap between graphene contacts. All scale bars are 5  $\mu\text{m}$ .

For this we fabricated another device with thin graphene layer serving as a transparent gate. We etch narrow lines within the graphene flake to realize independent local gates. Similarly to the previous devices, by application of opposite gate voltages on the local gates, we can establish a p-n junction above the gate area. This is schematically represented in Figure 4.11a, and an optical image of the fabricated device is shown in Figure 4.11b.

First, we investigate our device in the PN configuration ( $V_{G1} = 10$  V,  $V_{G2} = -10$  V) with scanning photocurrent microscopy, by measuring generated current while focusing laser light (250  $\mu$ W, 488 nm) on a different areas of the device. First we measure leakage current of the biased graphene flakes. We plot corresponding results in Figure 4.11c,d. Interestingly, oppositely biased graphene gates act as a phototransistor, so that we observe two current maps which coincide with gate positions. Graphene crystals electrostatically dope a WSe<sub>2</sub> monolayer, therefore observed regions of positive and negative current respectively represent n- and p-doped regions of the semiconducting channel. And the border thereby corresponds to the formed p-n junction.

We now measure the photocurrent generated between source and drain contacts at zero bias ( $V_{DS} = 0$  V) under the same gate configuration. The corresponding map is shown in Figure 4.11e. We see that the position of the measured signal coincides with the gap between graphene gates. We therefore assign the generated current to the separation of the photogenerated carriers by a strong electric field in the depletion region of the lateral p-n junction.

We note in Figure 4.11e the absence of the photocurrent signal on the WSe<sub>2</sub>/metal interface. We therefore conclude that photocurrent generation in the depletion region of the lateral p-n junction dominates over other effects like photothermoelectric effect as well as photocurrent generation on the Schottky barrier. Indeed, when biasing the device with  $V_{DS} = 4$  V, we observe electroluminescence of the same spatial shape as photogenerated current (Figure 4.11f).

### 4.2.5 Conclusion

In this section, we studied different architectures of a transceiver, the device that transforms electrical signal into an optical, which is an essential element for interconnect applications. We have demonstrated that lateral device based on WSe<sub>2</sub> monolayer holds promise for this purpose. In the following section, we therefore focus our attention on the development of the transceiver counterpart: a receiver, which would efficiently generate electrical signal out of optical signal.



## 4.3 MoS<sub>2</sub> Photodetector integrated with a photonic circuit

### 4.3.1 Introduction

In recent years, two-dimensional materials have risen as an attractive platform for integrated optoelectronics, due to their atomic scale thickness, favorable electrical, mechanical and optical properties. In particular, graphene has been exploited as an ultrafast light modulator and photodetector, operating at telecommunication wavelengths. However, materials with larger bandgap are required for light detection in the visible range of the spectrum, with wide applications in space communication, industrial quality controls, light sensing, etc. Even though TMDC-based light emitting and detecting devices in the visible spectrum have already been realized, efficient light absorption and photocurrent generation on integrated devices has not been achieved yet. In this section, we demonstrate the integration of an ultrasensitive MoS<sub>2</sub> photodetector with a silicon nitride photonic circuit, schematically shown in Figure 4.12. The general idea of the device operation principle is that light traveling inside the high-index contrast waveguide (WG) couples "laterally" *via* the evanescent field of the optical mode to MoS<sub>2</sub>, which is directly deposited on top of the photonic structure. In contrast to the limited vertical light absorption, we observe near-unity lateral absorption, which results in even higher responsivity. In the second part of this section, we fabricate an alternative device where the MoS<sub>2</sub> semiconducting channel is combined with hexagonal boron nitride substrate. With this we significantly improve the speed of the photodetector. In the last part, we further achieve low power operation by employing a third device with graphene local gates.

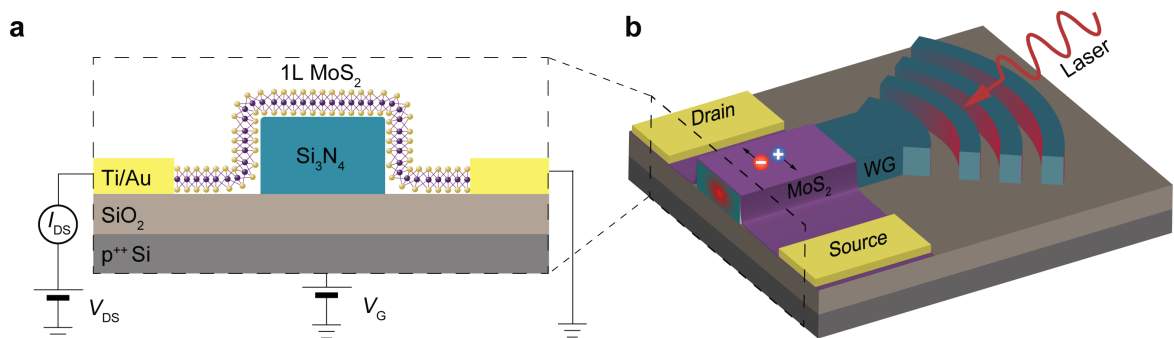


**Figure 4.12** – MoS<sub>2</sub>-based photodetector integrated in a photonic circuit. (a) Cross sectional schematics of the photodetector, with monolayer MoS<sub>2</sub> directly exfoliated on top of the waveguide. (b) Schematics of light coupling by focusing a 647 nm CW laser on the diffraction grating. Light propagates through the Si<sub>3</sub>N<sub>4</sub> waveguide (WG) and generates e-h pairs in MoS<sub>2</sub>, which leads to photocurrent generation in the biased semiconducting monolayer.

### 4.3.2 Fabrication and optimization of photonic structures

We first develop the core of our devices, namely photonic structures composed of several elements. The first one is a low-loss waveguide that will be defined by lithography and then etching directly on the substrate. The second required element is a diffraction grating, which will allow us to couple external light into the waveguide. This is schematically represented in Figure 4.12b.

#### Numerical simulations

Prior to structure fabrication we perform numerical simulations, which allow us to determine parameters essential for the processflow including required thickness of different layers of substrate. The substrate itself is degenerately doped silicon, which will be employed as a global back gate. Photonic structures will be then patterned in the top layer made of higher refractive index top layer ( $\text{Si}_3\text{N}_4$ ), which should be decoupled from the silicon substrate. For this we employ a spacing layer of lower refractive index material. 1- $\mu\text{m}$   $\text{SiO}_2$  layer is thick enough to decouple waveguide modes from the substrate, but is thin enough to gate the photodetector using the global back gate.

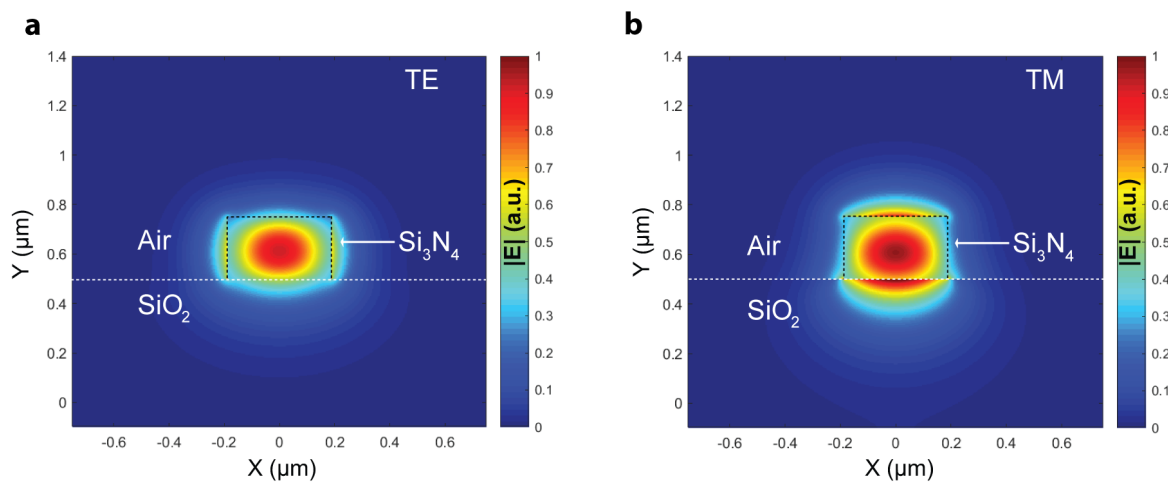


**Figure 4.13** – Fundamental modes of the waveguide. Calculated spatial distribution of the electric field amplitude  $|E|$  for fundamental quasi-TE (a) and quasi-TM (b) modes of the designed  $\text{Si}_3\text{N}_4$  waveguide at 647 nm.

The thickness of the top nitride layer is also a compromise between high optical contrast of exfoliated  $\text{MoS}_2$  flake and optical mode composition in the future waveguide. Using the transfer-matrix method that we implemented in *Wolfram Mathematica*, we found that 250-nm  $\text{Si}_3\text{N}_4$  film on thick  $\text{SiO}_2$  layer gives optimal optical contrast for monolayer  $\text{MoS}_2$  identification.

### 4.3. MoS<sub>2</sub> Photodetector integrated with a photonic circuit

Dimensions of photonic circuits were optimized for wavelengths at the MoS<sub>2</sub> excitonic resonance, so that it can also be used for transmission of light emitted by MoS<sub>2</sub>-based devices. The waveguide is designed so that only the first fundamental quasi-transverse electric (TE) and quasi-transverse magnetic (TM) modes propagate at a wavelength of 647 nm, while higher order modes are radiative. Calculated in *Lumerical* electric field profile for fundamental TE and TM modes based on Finite-Difference Time-Domain (FDTD) simulations is plotted in Figure 4.13. The evanescent field extends through a large area over the waveguide, which allows optical excitation of the attached monolayer. We also verify that guided modes are decoupled from the silicon substrate by the SiO<sub>2</sub> spacer. In addition, we perform numerical calculations for optimization of the final structure including verification of parameters such as gap size between WG and the substrate, and WG - electrical contacts separation distance, that will be presented later in Figures 4.15 and 4.17.

#### Waveguide fabrication

Knowing optimal parameters we fabricate our photonic structures. Process flow starts with dicing of the degenerately doped silicon wafers with 250 nm nitride on top of 1 μm oxide layers grown by low pressure chemical vapor deposition (LPCVD). Photonic structures were patterned using electron beam lithography after spin coating of ZEP. This resist is coated on the chip surface, freshly exposed to a mild oxygen plasma for better adhesion. Following step is a reactive ion etching with CHF<sub>3</sub>/SF<sub>6</sub> plasma. The polymer was then removed using O<sub>2</sub> plasma and the resulting structure was submerged in KOH to smooth the waveguide sidewalls. We further confirmed resulted dimensions of fabricated structures by focused ion beam (Figure 4.14a), scanning electron microscopy (Figure 4.14b) and atomic force microscopy (Figure 4.14c).

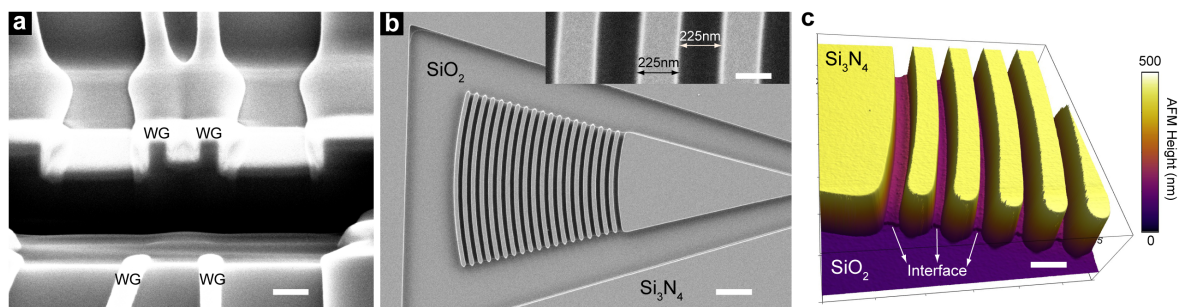


**Figure 4.14** – Structural characterization of fabricated photonic structures. (a) SEM image of a FIB cross section through a double waveguide structure. Scale bar is 500 nm. (b) SEM image of diffraction grating. Scale bar is 2 μm. Inset shows a closer image of grating lines. Scale bar is 200 nm. (c) AFM height profile of grating lines, where the Si<sub>3</sub>N<sub>4</sub>/SiO<sub>2</sub> interface is visible. Scale bar is 500 nm.

**Determination of waveguide losses**

As part of the process-flow optimization we characterize the fabricated photonic structure. This includes estimation of waveguide losses associated with surface roughness and the environment. We also characterize the efficiency of the grating coupler in the next section.

We use the following measurement scheme for determination of waveguide losses and MoS<sub>2</sub> absorption, which will be presented later. Laser light with a wavelength of 647 nm is focused on the input grating, and light emission from the output grating is quantified with the number of counts measured in the CCD camera. By comparing counts measured for a reference structure, waveguide losses and MoS<sub>2</sub> absorption can be extracted. In order to remove the reflected light, a cross-polarization scheme was used. Laser light is first polarized along the grating coupler lines, and the waveguide makes a turn so that the light emitted in the output grating is polarized perpendicularly to incident light. Since the polarization of reflected light is the same as for incident light, we can remove laser reflection without affecting detection of light emitted from the output grating.

Figure 4.15a shows the relative transmission as a function of cladding size  $d$  for 200  $\mu\text{m}$  long waveguides. Below 1.5  $\mu\text{m}$ , a significant drop in transmission occurs due to evanescent coupling of the mode in the waveguide to the surrounding Si<sub>3</sub>N<sub>4</sub> layer. The cladding size is therefore designed to be  $d = 2 \mu\text{m}$ . Intrinsic losses of the waveguide, mainly due to scattering on its surface, are shown in Figure 4.15b. From the linear fit we can extract an attenuation coefficient  $\alpha = 14 \pm 1 \text{ mm}$ , which is sufficiently good for our purposes.

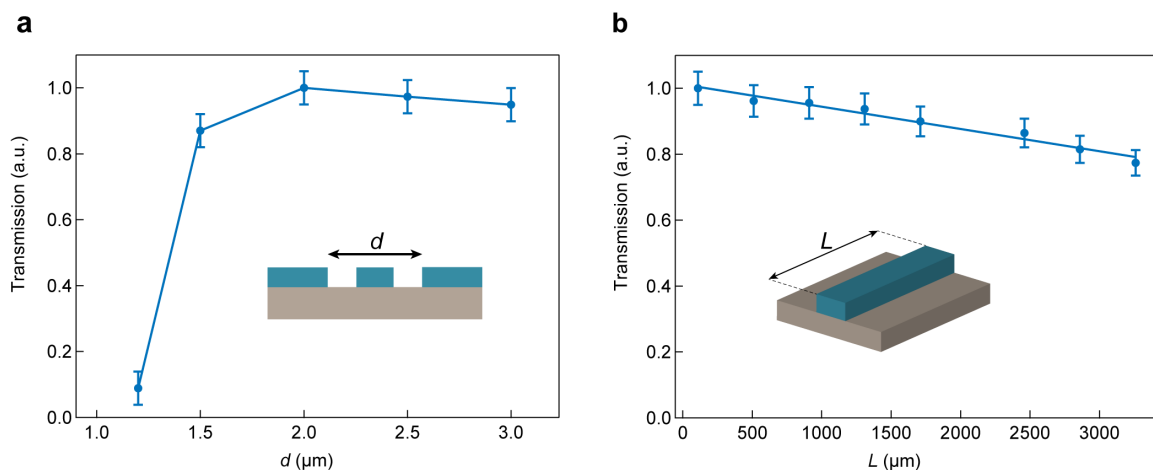


**Figure 4.15** – Optical characterization of photonic structures. (a) Relative transmission as a function of cladding size  $d$ . Losses due to coupling of the evanescent field in the waveguide with the surrounding Si<sub>3</sub>N<sub>4</sub> layer become significant for cladding sizes below 1.5  $\mu\text{m}$ . (b) Relative transmission as a function of the waveguide length. Losses appear mainly due to light scattering at the surface of the waveguide.

#### Coupling efficiency of the diffraction grating

In order to evaluate the coupling efficiency of the diffraction grating, it is necessary to quantify the power transmitted through the waveguide and emitted back by the output grating. For this, we first establish a relation between the number of counts and power arriving in the CCD camera, using a mirror with known reflectivity as a reference. Once this relation is measured, we can derive the grating coupling efficiency knowing the relation between input and output powers,  $P_{\text{out}} = \eta_{\text{GC}}^2 t_{\text{WG}} P_{\text{in}}$ , where  $\eta_{\text{GC}}$  is the grating coupler efficiency and  $t_{\text{WG}}$  the transmission of the waveguide. For a wavelength of 647 nm, the relative transmission is calculated to be  $t_{\text{WG}} = e^{-L/\alpha} \sim 0.99$ , where  $L = 130 \mu\text{m}$  is the length of the waveguide, and  $\alpha$  is the measured attenuation coefficient. The estimated coupling efficiency at this wavelength is then  $\eta_{\text{GC}} \sim 3.4\%$ . This value constitutes a lower limit, since not all the emitted light is collected by the objective  $P_{\text{out}}^{\text{meas}} < P_{\text{out}}^{\text{emit}}$ .

#### 4.3.3 Photodetector integrated with waveguide

In this section we discuss fabrication and characterization of a photodetector integrated with the optimized photonic structures.

##### Device fabrication

Device fabrication starts with micromechanical cleavage of MoS<sub>2</sub> with low residue tape. Thin crystals on the tape are then deposited on visco-elastic PDMS stamp and peeled-off slowly. Example of a monolayer flake attached to a thicker crystal on the polymer substrate is shown in Figure 4.16a. Monolayers are then identified under the microscope using optical contrast, confirmed by atomic force microscopy and photoluminescence measurements. Finally, polymer stamp is placed on a glass slide and a monolayer is transferred onto a photonic structure using the dry transfer method. An optical image in Figure 4.16b shows a transfer results with MoS<sub>2</sub> monolayer deposited on top of the waveguide. Same flake in bigger magnification is clearly visible when PL imaging is employed, Figure 4.16c, top.

Post-transfer thermal annealing was done at 250°C under high vacuum for 6 h. This step improves coupling between the MoS<sub>2</sub> flake and the photonic structure. We note that PL emission is enhanced in the region above the waveguide, indicating efficient coupling of the flake with the photonic circuit, discussed more in the following Section 4.3.4. Note that PL is strongly quenched over the flake surface (Figure 4.16c, bottom) after annealing due to the charge transfer from the nitride substrate. The resulting structure is then spin coated with PMMA-MMA bilayer resist and patterned by electron beam lithography, followed by electron beam evaporation of 10 nm Ti and 60 nm Au. Standard lift-off process in acetone

bath completes contact deposition on the structure. An optical image of the fabricated device is shown in Figure 4.16d.

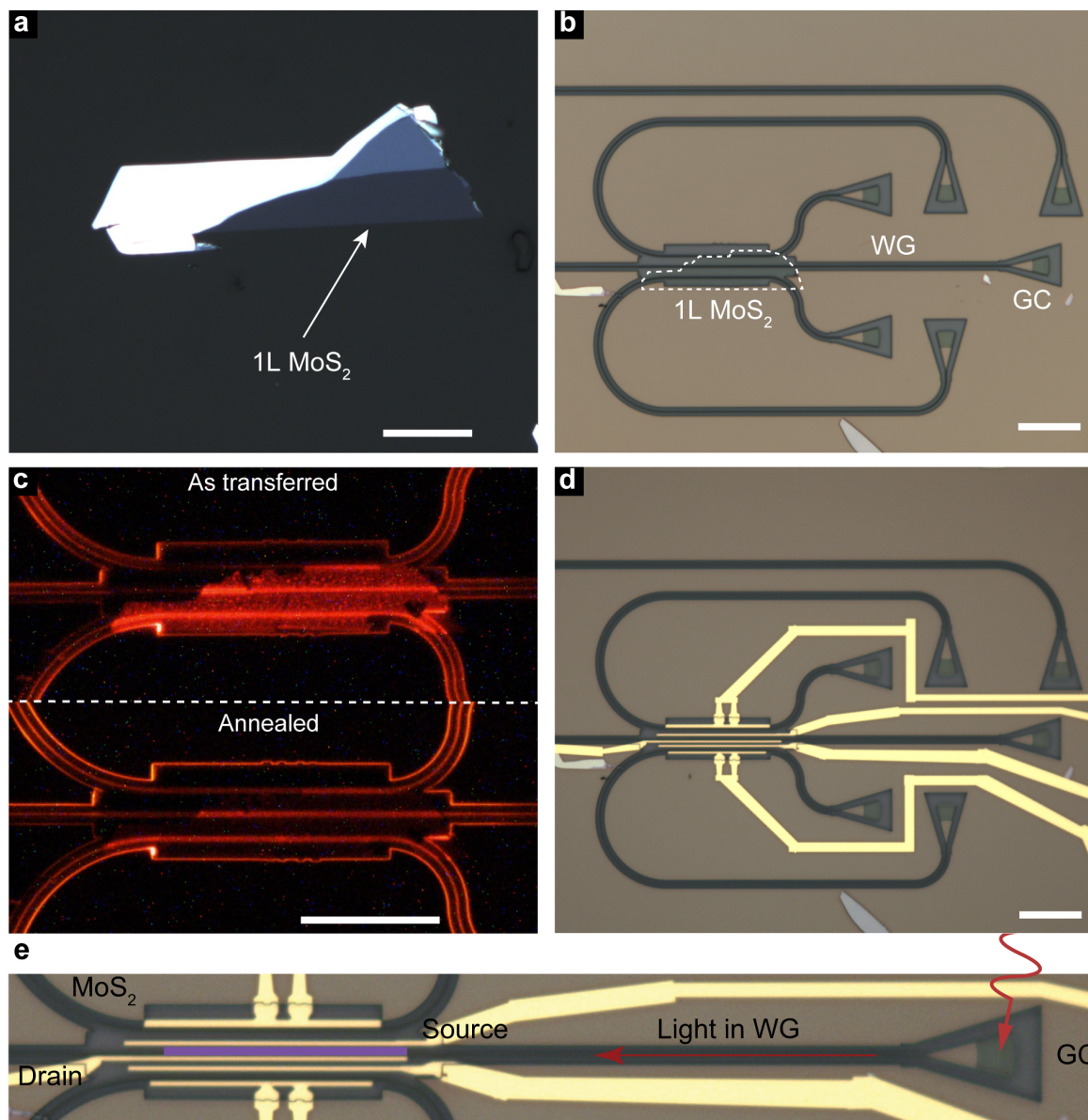


**Figure 4.16** – Fabrication of integrated photodetector. (a) Optical image of the MoS<sub>2</sub> flake exfoliated onto a PDMS stamp. Large monolayer area is clearly visible. (b) Optical image after dry transfer of monolayer MoS<sub>2</sub> on the photonic structure, indicated by the dashed line. (c) Photoluminescence image of the flake before (top) and after (bottom) thermal annealing. (d) Optical image after deposition of metallic contacts. Scale bar for every image is 30 μm. (e) Optical image of the fabricated MoS<sub>2</sub> photodetector integrated in the photonic structure. This image is the same as (d), acquired with higher magnification. MoS<sub>2</sub> channel is highlighted in violet. The diffraction grating coupler (GC) used for light coupling, waveguide (WG) source and drain are also indicated. Scale bar is 20 μm.

### 4.3. MoS<sub>2</sub> Photodetector integrated with a photonic circuit

Figure 4.16e presents the operation of the fabricated photodetector. Incident laser light at 647 nm is focused on the diffraction grating coupler (GC), which redirects light for propagation through the waveguide. Light is linearly polarized perpendicularly to the propagation direction, which leads to excitation of the TE mode in the waveguide, that is known for a stronger absorption by the MoS<sub>2</sub> film than the TM mode [171]. Part of the light is then absorbed and converted into an electrical signal in the biased MoS<sub>2</sub> flake.

#### Device optimization

Similarly to waveguide optimization, in order to improve final structure we characterize here how free parameters affect device performance. Namely, we determine optimal length of the MoS<sub>2</sub> flake. It should be long enough for efficient light absorption in the lateral configuration. However, a channel which is too large results in a large OFF-current and therefore decreases device performance. Also, we estimate optimal waveguide to contact separation, as deposited metal close to the waveguide might alter modes propagation

Limited absorption of normally incident light in 2D materials due to their atomic-scale thickness [172] can be overcome by lateral excitation *via* the waveguide. In order to demonstrate this experimentally, we measure the lateral absorption of MoS<sub>2</sub> as a function of the flake length. Figure 4.17a shows how lateral absorption overcomes the vertical one (taken from ref [51]) and approaches unity. From an exponential fit of transmission ( $T = e^{-L/\alpha}$ ), the absorption coefficient is found to be  $\alpha = 7.7 \pm 1.1 \mu\text{m}$ . It is clear that lateral absorption can be fine-tuned by modifying the length of the flake, which could be defined by an extra etching step after transfer.

For the optoelectronic characterization of the waveguide-integrated photodetector, the amount of light incident on the device needs to be quantified. While we have demonstrated above that optical losses due to scattering in the waveguide surface and coupling to the surrounding Si<sub>3</sub>N<sub>4</sub> layer can be neglected, interaction of light with the evaporated metal contacts can alter its propagation. In order to maximize the photocurrent in the fabricated photodetector, contacts should be as close as possible to the waveguide so as to reduce the device resistance. However, this can modify light propagation if the evanescent field couples to the metallic contacts, leading to optical losses in the waveguide. To find the minimum distance between source and drain for which TE and TM mode profiles are not altered, we perform FDTD simulations for different positions of contacts with respect to the waveguide. Relative transmission for both TE and TM modes after deposition of 10 nm Ti, 60 nm Au is shown in Figure 4.17b. The inset presents propagation losses on a logarithmic scale. Long contacts ( $L = 65 \mu\text{m}$ ) are chosen in order to maximize the channel length after the transfer of large MoS<sub>2</sub> monolayers onto the waveguide. For edge-to-edge distances larger than 600 nm, the influence of metal contacts on light propagation is

negligible. Therefore, we design contacts with 700 nm separation to exclude the effect of light coupling to the metal.

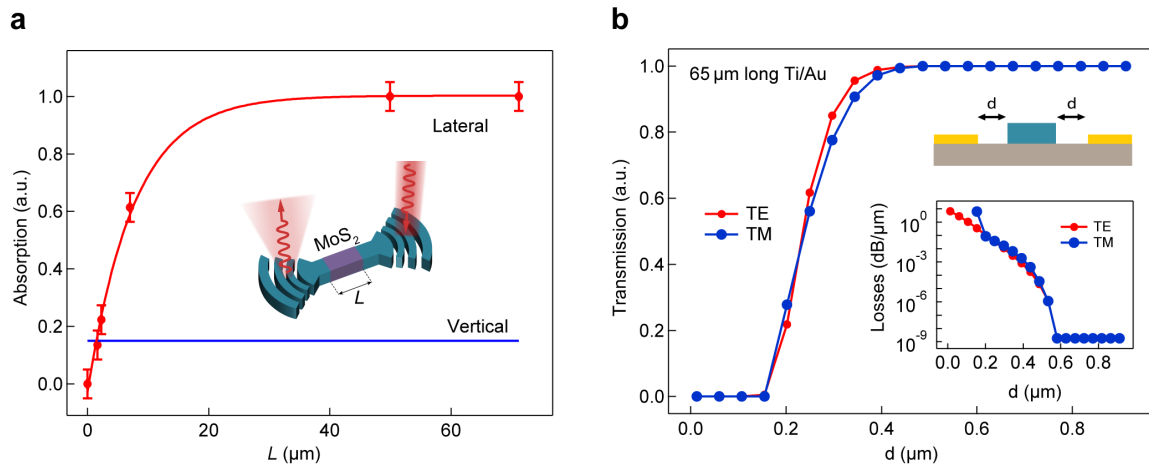


**Figure 4.17** – Effect of monolayer MoS<sub>2</sub> and metal contacts on light propagation in the waveguide. (a) Comparison between MoS<sub>2</sub> lateral (experimental data points) and vertical absorption (taken from reference [51]) as a function of the flake length. Error bars represent the standard deviation of the measurements. (b) Calculated relative transmission for TE (red) and TM (blue) modes after deposition of 65  $\mu\text{m}$  long metal contacts at a distance  $d$  from the waveguide. Inset shows calculated losses per micrometer in log scale.

### Device characterization

We now focus our attention on the device characterization. Optoelectronic measurements are performed in vacuum ( $10^{-6}$  mbar) at room temperature, under continuous-wave (cw) laser illumination at a wavelength  $\lambda = 647$  nm, unless stated otherwise. The three main mechanisms for photocurrent generation in MoS<sub>2</sub> are photogating, photoconductive and photothermoelectric effects [173, 174]. In our case, photogating is dominant, leading to a slow photocurrent, 80 times higher than the fast photocurrent associated with the photoconductive effect [174] (see the next section and Figure 4.21a).

Drain-source current characteristic of the device for different gate voltages is shown in Figure 4.18a, while Figure 4.18b presents the corresponding  $I_{\text{DS}} - V_{\text{DS}}$  curves for different illumination intensities on the grating coupler at  $V_{\text{G}} = 0$  V. The behavior is similar to the one found in previous reports for monolayer MoS<sub>2</sub> photodetectors [175]. No appreciable current is measured at zero bias, even for large illumination intensities up to 8  $\mu\text{W}$ . This excludes the photothermoelectric (PTE) effect as origin of photocurrent.[174, 176]



### 4.3. MoS<sub>2</sub> Photodetector integrated with a photonic circuit

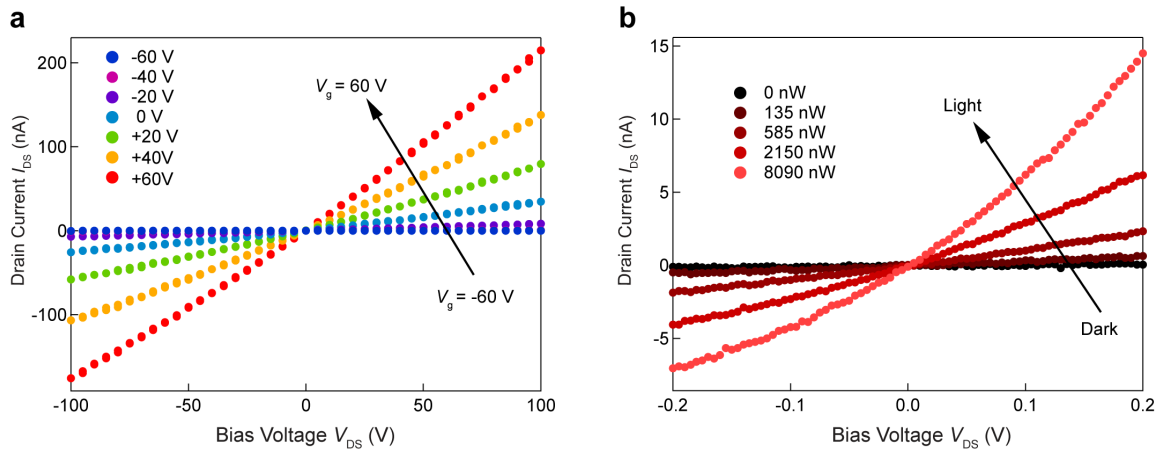


**Figure 4.18** – Drain-source  $I_{DS} - V_{DS}$  characteristics of the photodetector under different back-gate voltages (a) and vertical illumination intensities for  $V_G = 0$  V (b).

Figure 4.19a shows the schematics of the device band alignment in three different conditions: dark (1), vertical illumination (2) and lateral illumination via the waveguide (3), leading to the corresponding  $I_{DS} - V_G$  curves in Figure 3b. In the dark, current follows the characteristic behavior of an MoS<sub>2</sub> transistor [177], with a threshold voltage  $V_G^{\text{th}} = -11$  V and an on/off ratio above  $10^5$  limited by the noise level of the measurement setup.

When focusing the laser light onto the flake, electron-hole (e-h) pairs are generated across the channel. The device stays in the on-state for the entire range of back-gate voltages, with trapped holes shifting the Fermi level, effectively gating the flake. Since the lifetime of trapped holes is much larger than that of the electrons, many carriers can flow for each generated e-h pair, resulting in a large photogain. The ratio of photocurrents under vertical illumination and in dark reaches values as high as  $I_{\text{flake}}/I_{\text{dark}} > 6 \cdot 10^3$  at  $V_G = -12$  V and is again limited by the noise level. When the flake is excited through the waveguide by focusing the laser on the grating coupler, creation of e-h pairs occurs only in the overlapping region between the waveguide and the flake, creating a potential profile for electrons which allows turning off the photocurrent. The off-state for lateral illumination is found at a new threshold voltage  $V_G^{\text{th}} = -37.5$  V.

From the  $I_{DS} - V_G$  curves, we can further derive the external responsivity of the photodetector, defined as the ratio between the generated photocurrent  $I_{\text{ph}} = I_{\text{light}} - I_{\text{dark}}$  and optical power  $P_{\text{in}}$  incident to the flake. Figure 4.19c shows the dependence of the photoreponse on the gate voltage for a fixed laser power of 25 nW. Due to the characteristic band alignment, in the case of lateral coupling the gate modulation of photoresponsivity is three orders of magnitude larger compared to vertical illumination, with responsivity dropping to zero for back-gate voltages below the threshold voltage.

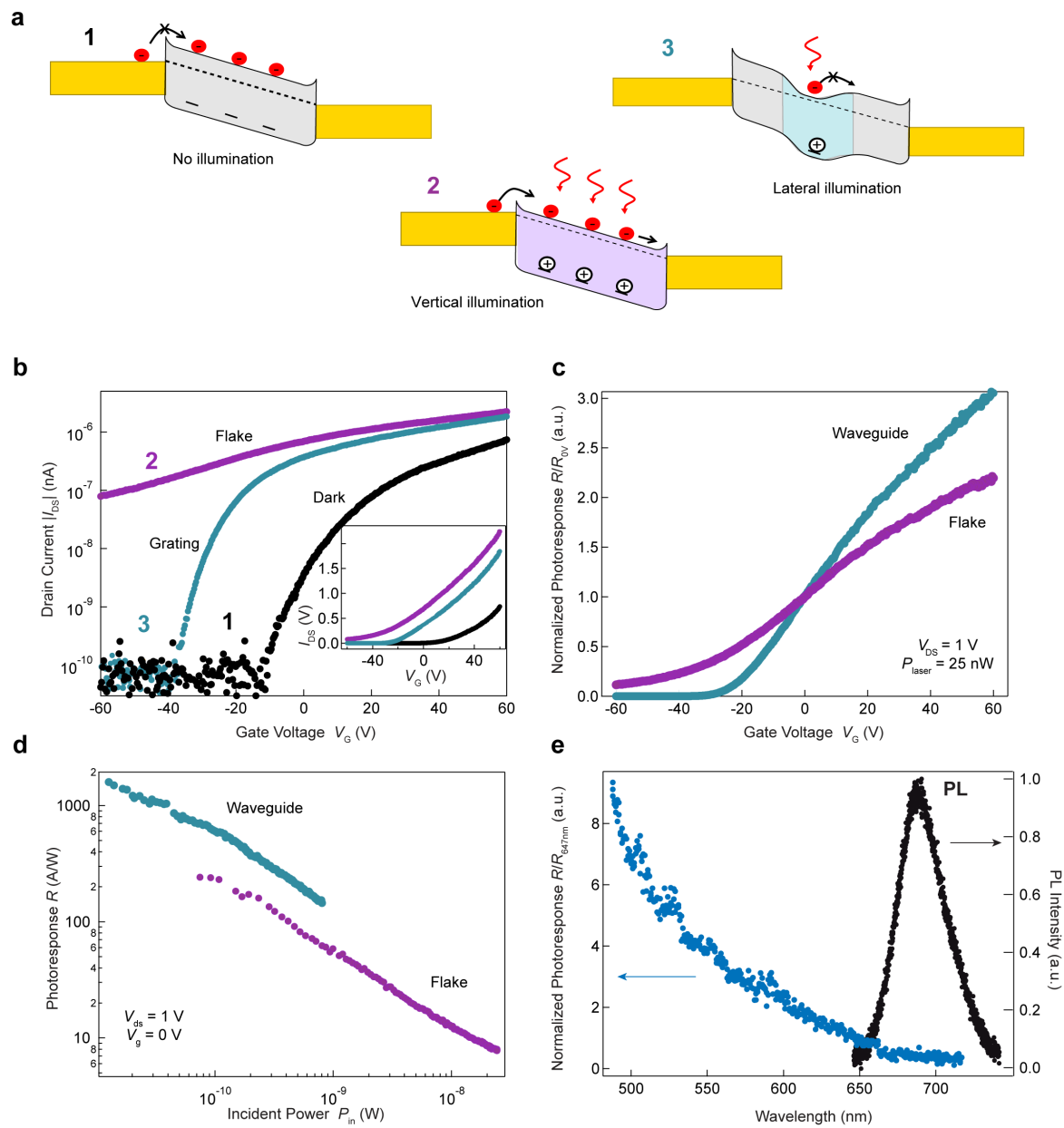


**Figure 4.19** – Optoelectronic properties of the photodetector. (a) Schematics of band alignment for device under applied bias in different conditions: dark (1), vertical (2) and lateral illumination (3). (b) Drain-source current ( $I_{DS}$ ) dependence on the applied back gate voltage ( $V_G$ ) for the three regimes represented in (a), obtained at bias voltage  $V_{DS} = 1$  V and laser power  $P_{laser} = 25$  nW. (c) Modulation of the photoresponse with back-gate voltage for lateral and vertical illumination at  $V_{DS} = 1$  V and  $P_{laser} = 25$  nW. Responsivity is normalized by its value at zero gate voltage. (d) Measured photoresponsivity  $R$  as a function of incident power  $P_{in}$  at  $V_G = 0$  V and  $V_{DS} = 1$  V. (e) Responsivity dependence on the excitation wavelength, normalized by its value at 647 nm (wavelength used for measurements shown in (b-d)), and photoluminescence spectra from  $\text{MoS}_2$  on  $\text{Si}_3\text{N}_4$ .

### 4.3. MoS<sub>2</sub> Photodetector integrated with a photonic circuit

---

Dependence of responsivity on incident optical power at  $V_G = 0$  V is shown in Figure 4.19d. The responsivity for the waveguide is calculated by taking into account that the grating coupler efficiency is 3.4 % at the 647 nm wavelength, as was found previously. Therefore,  $P_{in} \sim 0.34 \times P_{laser}$ . For low incident power we obtain an extremely high photoresponse above 1000 A/W, which is the result of higher lateral absorption compared to vertical illumination. Flake responsivity depends strongly on the excitation wavelength, as shown in Figure 4.19e, and can be further enhanced by increasing the energy of incident photons. Photoresponse for wavelengths below the optical bandgap vanishes, as photons cannot be absorbed by the 2D material. It should be noted that photoresponse depends directly on the conductivity of the channel, and therefore slightly varies with time since MoS<sub>2</sub> is known to experience Fermi level shifts on substrates such as SiO<sub>2</sub> and S<sub>3</sub>N<sub>4</sub> upon thermal, light or current annealing [178]. We also observed this effect in the first part of the chapter with LEDs fabricated on Al<sub>2</sub>O<sub>3</sub>.

#### Photocurrent mapping

The realization of chip-integrated devices with TMDCs requires precise alignment of light sources such as optical fibers or lasers, on the material. However, relaxed alignment conditions can be achieved with the usage of grating couplers. Figure 4.20 presents photocurrent maps for vertical illumination on MoS<sub>2</sub> and the grating coupler when a DC bias is applied to MoS<sub>2</sub>. For the latter, the map represents the spatial distribution of the coupling efficiency since it shows the photocurrent generated in the MoS<sub>2</sub> when the light from the laser is focused onto the diffraction grating then coupled to the waveguide and finally absorbed in the MoS<sub>2</sub> layer.

Since the response time associated with photogating is on the order of seconds, to have accurate photocurrent maps, it is necessary to access the fast component of the photoresponse, originating from the photoconductive mechanism. In order to do that, a chopper is placed in front of the laser for periodical interruption of the light incident to the photodetector. Photocurrent is then measured using a lock-in amplifier whose reference frequency is locked to the rotation frequency of the chopper. This allows us to measure only the component of the current at the chopper frequency.

For the diffraction grating in Figure 4.20b, significant photoresponse ( $>1/2 I_{max}$ ) can be obtained over a larger area compared to the flake. In addition, response is homogeneous around the grating lines, which indicates that alignment could be greatly facilitated by simply increasing the diffraction grating area.

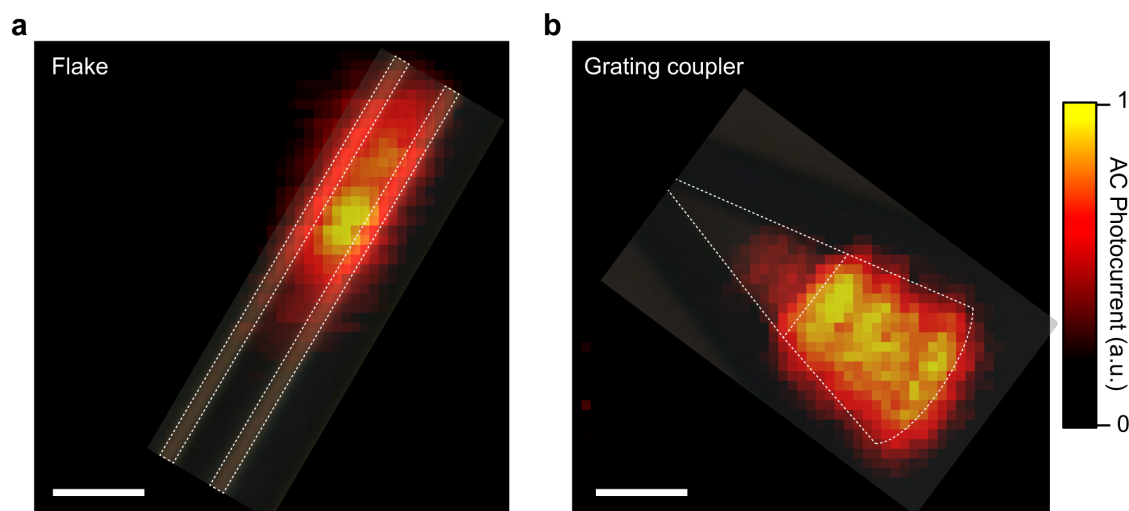


**Figure 4.20** – Normalized photocurrent maps for the case of direct vertical excitation on the flake (a), and excitation through the grating coupler (b), at  $V_{DS} = 2$  V,  $V_G = 0$  V and laser power of  $1 \mu\text{W}$  and  $110 \mu\text{W}$ , respectively. Laser light is modulated by the chopper with a frequency of 30 Hz. The value of alternating current (AC) at the modulation frequency of light is obtained by a lock-in amplifier. Scale bar is  $5 \mu\text{m}$ . Dashed lines denote the contacts in (a) and the outline of the grating coupler in (b).

The flake photocurrent map in Figure 4.20a reveals an active channel length  $L \sim 14 \mu\text{m}$ , which corresponds to a lateral absorption of 84%, according to measurements presented in Figure 4.17a. This allows us to estimate external quantum efficiency for photons traveling in the waveguide with absorption coefficient of  $\eta = 0.84$ . It can be calculated as  $EQE = R \times hv / q\eta_{\text{ext}} > 2300$ , indicating large photogain for low incident powers, where  $hv$  is incident photon energy and  $q$  is the elementary charge.

### Time-dependent photoresponse

The slow but large photoresponse is associated with the photogating mechanism which manifests itself as a change in the threshold voltage due to charge transfer to adjacent molecules, in particular when transferred onto  $\text{SiO}_2$  [174] or  $\text{Si}_3\text{N}_4$ , as in our case. This effect can be eliminated if h-BN serves as a substrate for the fabricated photodetector that we will present in the following section. On the contrary, fast response is related to photoconductive and photoelectric effects [174].

Time-dependent photoresponse is represented in Figure 4.21a. In order to accurately fit rise and decay of photocurrent after switching on and off the laser, we need to fit the data with double exponential functions. This indicates that photocurrent generation in  $\text{MoS}_2$  is mediated by several processes. The corresponding rise time constants are  $\tau_{1,\text{rise}} = 0.45 \pm 0.05$  s and  $\tau_{2,\text{rise}} = 13 \pm 2$  s. For the decay time, we found  $\tau_{1,\text{decay}} = 0.90 \pm 0.04$

### 4.3. MoS<sub>2</sub> Photodetector integrated with a photonic circuit

s and  $\tau_{1,\text{decay}} = 11.4 \pm 0.5$  s.

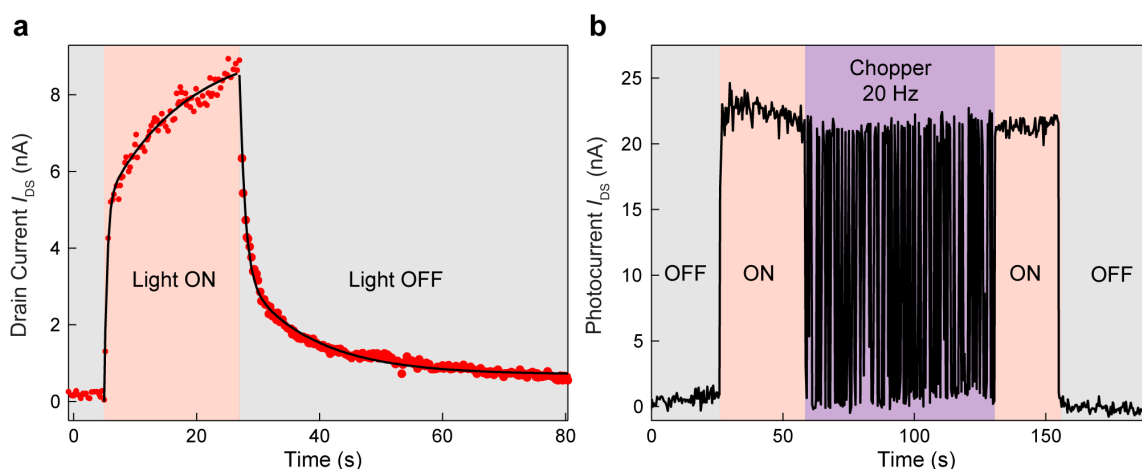


**Figure 4.21** – Time dependency of the photoresponse. (a) Time response of the photocurrent at gate voltage  $V_G = 0$  V, applied bias  $V_{DS} = 1$  V, and incident power  $P_{in} = 200$  nW. Black solid lines represent double exponential fits for rise and decay times. (b) Fast operation of the MoS<sub>2</sub>/h-BN photodetector: photocurrent under different illumination conditions (laser off and on as well as with and without chopper) at  $P_{in} = 7$  mW and  $V_{DS} = 1$  V. Chopper frequency is fixed to 20 Hz.

As was already discussed above, we can access the fast photoresponse by employing an optical chopper with lock-in amplifier. By comparing measured values with this approach and conventional DC measurements we found the current associated with photogating to be 80 times larger than the one assigned to the photoconductive effect, in the case when the MoS<sub>2</sub> channel is in direct contact with the nitride waveguide.

#### 4.3.4 Improved architectures of the integrated photodetector

The main limitation of MoS<sub>2</sub>-based photodetectors is the low speed of operation, which in our case is restricted by the photocurrent rise and decay times of  $\tau_{\text{rise}} > 13$  s and  $\tau_{\text{decay}} > 11$  s, respectively (Figure 4.21a). In order to avoid photogating and realize a device with a fast response, a device with an alternative architecture is fabricated.

#### Fabrication

Here we first transfer a multilayer h-BN flake with a thickness of  $\sim 10$  nm on top of the waveguide. This h-BN layer serves as a charge-traps-free, atomically-flat van der Waals substrate for the MoS<sub>2</sub> channel, as shown in Figure 4.22. Note that in this case the flake remains flat and does not conform to the waveguide. Before the transfer of monolayer

MoS<sub>2</sub>, we deposit Ti-Au contacts on top of h-BN. This configuration is chosen to increase the fabrication yield, since the metal contacts act as anchors by keeping the suspended h-BN in place after dry transfer of MoS<sub>2</sub> monolayer. In addition, the monolayer remains pristine clean by avoiding its interaction with any polymer such as the e-beam resist.

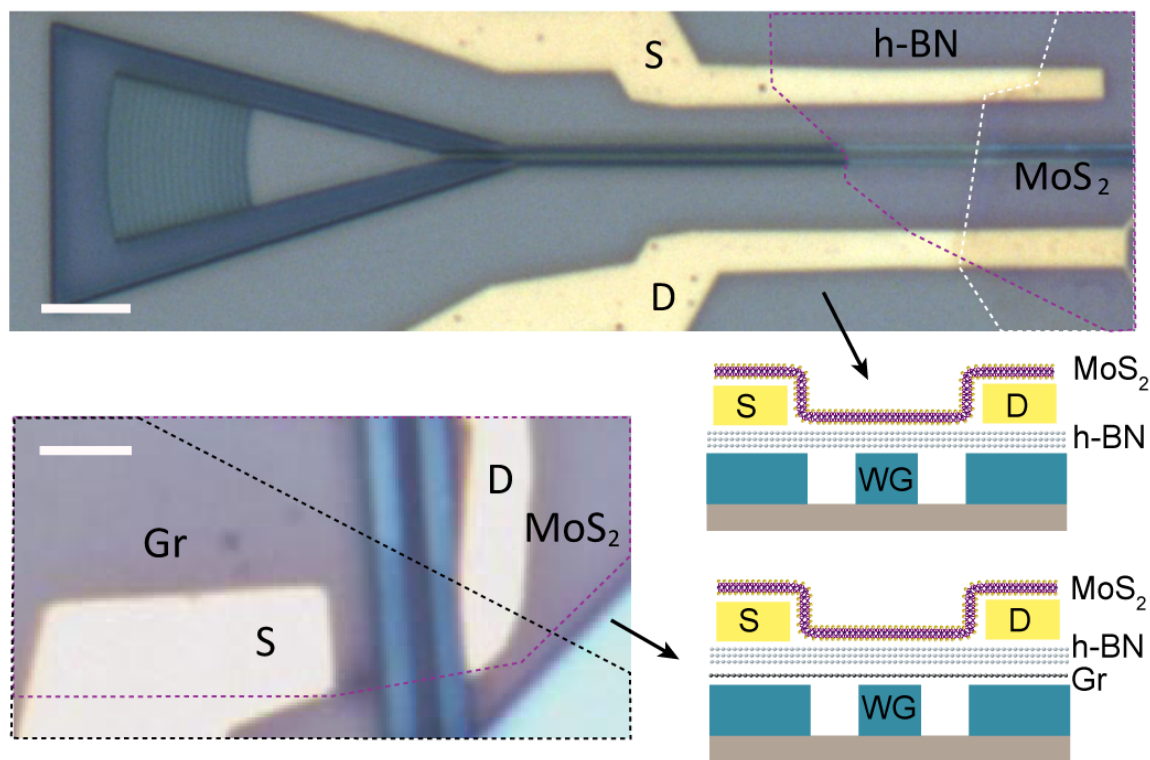


**Figure 4.22** – Fabrication of photodetectors with alternative architecture. Top: optical image of the MoS<sub>2</sub>/h-BN photodetector. Dashed lines highlight monolayer MoS<sub>2</sub> and 10-nm thick h-BN crystals. Bottom left: Optical image of MoS<sub>2</sub>/h-BN/Gr photodetector. Dashed lines highlight monolayer MoS<sub>2</sub> and few-layer graphene. The surface of h-BN with thickness  $t$  of 11 nm extends over the entire area shown in the image. Bottom right: Schematic depiction of device structures. Scale bar is 5  $\mu\text{m}$  (top) and 2  $\mu\text{m}$  (bottom)

### Fast and low power operation

The combination of an atomically flat, charge-free substrate and a pristine monolayer allows us to significantly reduce charge trapping leading to photogating current. In this case, all the photocurrent is associated with the fast photoresponse, as seen in Figure 4.21b, where photocurrent caused by the chopped light is directly compared to dark current and the continuous light illumination case. Even when light is modulated by the 20 Hz chopper, the response of the device is still fast enough to reach maximum (constant illumination) and minimum (dark) values of photocurrent, which demonstrates the photoconductive origin of the photoresponse.

### 4.3. MoS<sub>2</sub> Photodetector integrated with a photonic circuit

We expect similar response time for vertical and lateral illumination via the waveguide, since the response time is associated with the mechanism responsible for photocurrent generation. This mechanism is the same regardless of whether we excite locally (waveguide coupling) or over the entire active area (vertical illumination), since the MoS<sub>2</sub> flake is supported by a flat and homogeneous h-BN layer. When illuminating with a continuous wave laser, a constant photocurrent is generated. After adding a chopper rotating at 20 Hz at the output of the laser, the response of the device is still fast enough to reach maximum (constant illumination) and minimum (dark) values of photocurrent, which demonstrates that all the response is faster than 20 Hz, Figure 4.21b. To determine more precisely the speed of the response, photocurrent is measured as a function of the chopper rotation frequency. Figure 4.23a shows the ratio between DC photocurrent ( $I_{DC}$ ) obtained for constant illumination, and oscillating photocurrent ( $I_{AC}$ ) at the frequency of the chopper, measured by the lock-in amplifier. The oscillating (fast) photocurrent is constant for frequencies up to 1 kHz, the limit of the measurement setup. The response time of the monolayer MoS<sub>2</sub>/h-BN photodetector is therefore shorter than 1 ms, overcoming the performance of previously reported MoS<sub>2</sub> photodetectors [179]. Similar results are obtained when exciting via the waveguide, with lower photocurrents due to weaker coupling after the addition of thick h-BN, leading to a fast responsivity of 1.5  $\mu\text{A}/\text{W}$  at  $P_{in}=7$  mW (Figure 4.23a, inset).

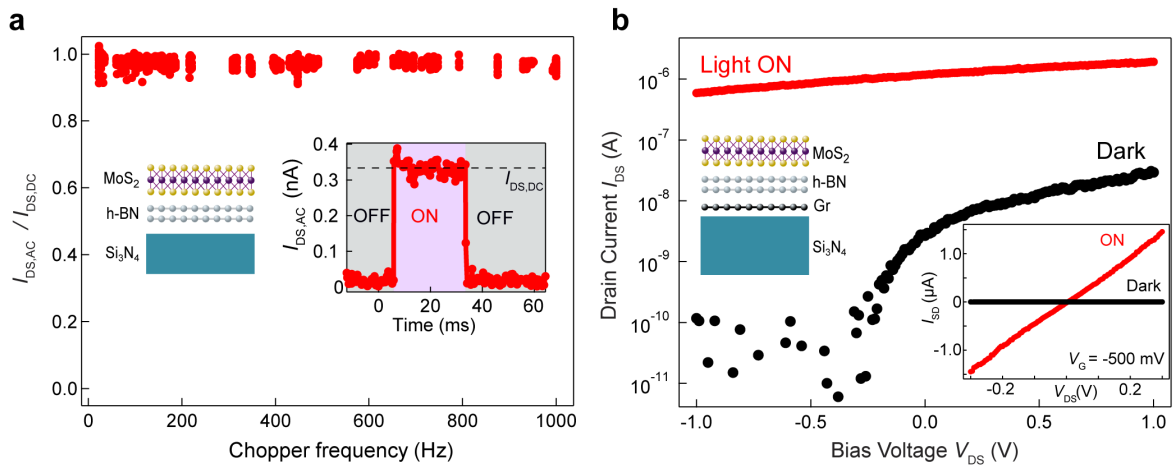


**Figure 4.23** – Fast response and low-power operation of MoS<sub>2</sub>-based photodetectors. (a) Fast operation of the MoS<sub>2</sub>/h-BN photodetector: Lock-in amplifier measurements of AC photocurrent dependence on chopper frequency at  $P_{in} = 7$  mW,  $V_G = 0$  V and  $V_{DS} = 1$  V, under vertical illumination. Inset shows schematic structure of the photodetector and operation under dark (OFF) and chopped illumination at 1 kHz (ON) on the grating coupler with  $P_{in} = 7$  mW,  $V_G = 0$  V and  $V_{DS} = 1$  V. (b) Low voltage operation of the MoS<sub>2</sub>/h-BN/Gr photodetector. Main graph shows transfer characteristics under dark and illumination at  $P_{in} = 11$  mW and  $V_{DS} = 250$  mV, showing low threshold voltage  $V_{th} = -250$  mV without illumination. Inset graph shows  $I_{DS} - V_{DS}$  curves with and without illumination for  $P_{in} = 11$  mW,  $V_G = -500$  mV. Inset schematic depicts the structure of the photodetector.

For low-power applications of integrated optoelectronic devices, operation voltages need to be decreased. In order to have more efficient electrostatic control over the charge carrier density in the MoS<sub>2</sub> flake, we fabricate a third device where multilayer graphene is used as a back gate, with an 11 nm thick h-BN dielectric layer.

Resulting  $I_{DS} - V_G$  curves for the device in the dark and under vertical illumination are shown in Figure 4.23b. The off state is reached at a back gate voltage as low as  $V_G = -250$  mV, due to the higher capacitance ( $C = 2.8 \cdot 10^{-7} \mu\text{F}/\text{cm}^2$ ) of the thin h-BN dielectric compared to the 1  $\mu\text{m}$  thick SiO<sub>2</sub> ( $C = 3.4 \cdot 10^{-9} \mu\text{F}/\text{cm}^2$ ). High values of photocurrent on the order of  $\mu\text{A}$  can be measured for the complete range of back gate voltages. Figure 4.23b inset presents measured  $I_{DS} - V_{DS}$  curves in the off state, with gate voltage below the threshold. Photocurrent to dark current ratio over  $10^5$  is achieved at  $V_{DS} = 300$  mV and incident power of 11 mW.

### Additional characterization

The fabricated structure (MoS<sub>2</sub>/h-BN/WG) allows us to study how the coupling between MoS<sub>2</sub> and the waveguide affects monolayer photoluminescence. Even though we have observed PL enhancement in the proximity of the waveguide in the first generation of devices, it could not be directly attributed to the coupling with the waveguide (enhancement of spontaneous emission rate by an environment with higher density of final states). Induced strain and change of substrate (Si<sub>3</sub>N<sub>4</sub>, SiO<sub>2</sub> or suspended) may also alter emission energy and intensity.

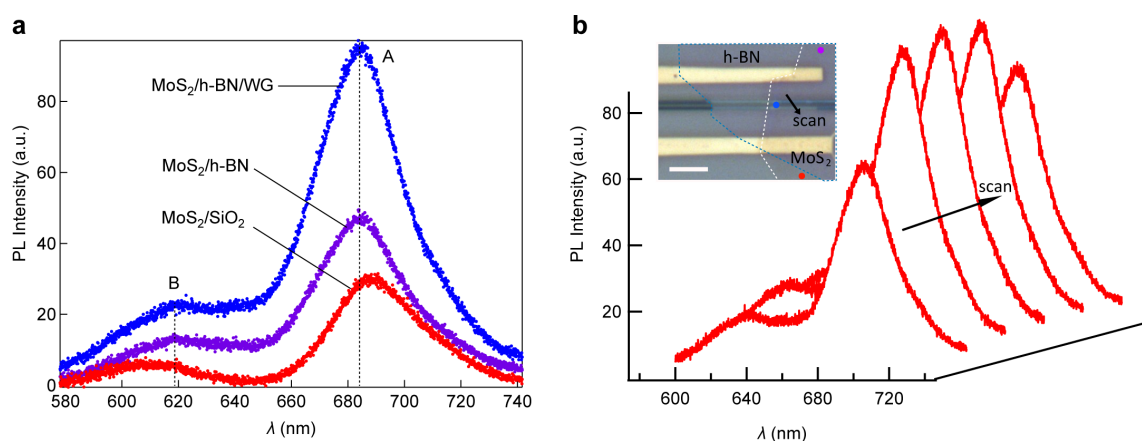


**Figure 4.24** – MoS<sub>2</sub> photoluminescence on different substrates. MoS<sub>2</sub> photoluminescence spectra for 488 nm excitation wavelength and 6 mW incident power. (a) PL spectra measured on different substrates. (b) Measurement of PL intensity across the waveguide (WG).



### 4.3. MoS<sub>2</sub> Photodetector integrated with a photonic circuit

---

On the other hand, the monolayer in Figure 4.22(top) is supported by an h-BN crystal and thereby stays in pristine conditions even on the waveguide. We measure PL spectra of MoS<sub>2</sub> across the heterostructure, and show it in Figure 4.24. These PL intensity measurements confirms photoluminescence enhancement due to the coupling with the waveguide. Even for an h-BN thickness of 10 nm, the field mode can overlap with the flake transferred on top, leading to a PL enhancement by a factor of 2.

### 4.4 Conclusion and outlook

In the first part of the chapter, we have realized tunable and versatile device based on the monolayer WSe<sub>2</sub> channel. We demonstrated that in the PN-configuration, this device appears to be a practical light emitter. Our results prove that this approach is more reliable than the one based on vertical p-n junctions in MoS<sub>2</sub>/WSe<sub>2</sub> heterostructures. We have also shown the importance of the h-BN layer as a gate dielectric environment for efficiency and stability of the fabricated LED.

In the second part, we demonstrated the integration of MoS<sub>2</sub> photodetectors with photonic structures and presented device architectures for practical optoelectronic circuits. The first figure of merit is the large responsivity of the photodetector for lateral illumination at wavelengths close to the optical bandgap. In addition, photocurrent can also be suppressed for gate voltages below a given threshold, leading to three different regimes in photoresponse. Homogeneous and large coupling area in the diffraction gratings facilitates alignment for future optical interconnects. Furthermore, by realizing more complex structures we demonstrate the potential of this device as a platform for the development of MoS<sub>2</sub>-based integrated photodetectors aiming at various applications. In a second device, photoresponse times below 1 ms were achieved by adding an h-BN layer between MoS<sub>2</sub> and Si<sub>3</sub>N<sub>4</sub>. The use of a graphene back gate with thin h-BN as the dielectric in a third device reduced the voltage range needed to operate the phototransistor.

Altogether, these results raise the prospects of TMDC monolayers as a promising materials for future integrated optoelectronic circuits. Moreover, as we already presented here monolayer-based LEDs, a platform for integrated light emission and detection could be potentially realized. Therefore we believe that these results pave the way for future TMDC-based integrated optoelectronic devices.

We would like to note here that during the final stage of this work we became aware of another work from the group of Pablo Jarillo-Herrero that demonstrates a waveguide-integrated LED and PD, which rely on a p-n junction established in bilayer MoTe<sub>2</sub>. This material is another member of the big TMDC family with bandgap lying in the infrared range. We encourage the reader to get acquainted with this work [180].

# 5 Optospintronic devices

## 5.1 Introduction

Spintronics has been proposed for applications in logic devices as a complement or even an alternative to devices based on the charge degree of freedom [4, 181]. Searching for the ideal material that can transport spin-dependent currents beyond micron size distances (e.g. spin interconnects) has been one of the main focuses of spintronics research [181, 182]. In this respect, graphene is a promising (unique) material due to its low spin-orbit coupling [21], negligible hyperfine interaction [22], large Fermi velocity [20] and very high electronic mobility [130]. Indeed, it exhibits the longest spin relaxation length at room temperature probed by magnetoresistance electrical measurements using ferromagnetic electrodes [24, 26]. However even these record values are still orders of magnitude smaller than its intrinsic limit [20]. The origin of this striking difference between theoretically predicted and experimentally observed spin relaxation lengths could still be spin-dependent scatterings at the graphene-ferromagnetic electrode interfaces despite the recent advances in creating high quality tunnel barriers [76, 183, 184]. Nondestructive optical spin injection schemes could be an appealing alternative. However, the absence of sufficient spin-orbit coupling and weak optical absorption of graphene poses challenges for their implementation [185]. The absence of optospintronics functionality in graphene is also a serious limitation for the prospect of potential graphene spintronics applications.

In contrast, transition metal dichalcogenides exhibit strong light absorption even in their monolayers [54, 186]. Monolayer TMDCs also have (unique) spin-valley physics which has captured the interest of the solid state physics community [71, 72, 133]. Due to the broken spin degeneracy and the time-reversal symmetry, the spin and valley degrees of freedom are coupled in such a way that excitation by opposite handedness leads to preferential population of the K or K' valley with a defined spin orientation. Among TMDCs, tungsten diselenide gets special attention due to the achievement of a valley polarization value close

to unity and large external quantum efficiency [187, 188]. More importantly, WSe<sub>2</sub> has also the strongest spin-orbit induced splitting among TMDCs (~450 meV [189]), making it more suitable for spin-injection compared to its molybdenum-based counterparts.

In this chapter we demonstrate indirect optical spin injection into graphene by bringing it in a close proximity with a WSe<sub>2</sub> monolayer. This device architecture was previously proposed by M. Gmitra & J. Fabian [185]. The generation of spin polarized charge carriers by using its spin coupled valley selective absorption property [190] allows inducing spin dependent currents in the superjacent graphene layer through a tunneling process, without the need for a ferromagnetic spin injector. In the second part of the chapter we focus our attention on another challenging aspect of spintronics: manipulation of the spin current. As for the case of a Datta-Das spin transistor, one need to require efficient control over the spin current transport. Here we demonstrate our initial efforts on a control in all electrical configuration and also by means of optics. For this we again harvest complementary properties of graphene and WSe<sub>2</sub> monolayer in their heterostructure.

This work was performed in a close and fruitful collaboration between Dmitrii Unuchek and Ahmet Avsar, who are the equally contributed authors of the article "Optospintronics in Graphene *via* Proximity Coupling", which was published in *ACS Nano*, **2017**, 11 (11), pp: 11678–11686 (DOI: 10.1021/acsnano.7b06800). We note that there is a considerable overlap between this article [191] and the first part of the current chapter that discuss optical spin injection into graphene.

## 5.2 Optical spin injection in graphene *via* proximity coupling with WSe<sub>2</sub>

The observation of micron size spin relaxation makes graphene a promising material for applications in spintronics requiring long-distance spin communication. However, spin dependent scatterings at the contact/graphene interfaces affect the spin injection efficiencies and hence prevent the material from achieving its full potential. While this major issue could be eliminated by nondestructive direct optical spin injection schemes, graphene's intrinsically low spin-orbit coupling strength and optical absorption place an obstacle in their realization. We overcome this challenge by creating a hybrid device based on sharp artificial interfaces between graphene and WSe<sub>2</sub> monolayers. Such a device is schematically depicted in Figure 5.1. This cartoon presents graphene/WSe<sub>2</sub> heterostructure under the application of incident circularly polarized light that activates the spin-polarized charge carriers in the WSe<sub>2</sub> layer due to its spin-coupled valley-selective absorption. These carriers diffuse into the neighboring graphene layer, transport over a 3.5  $\mu\text{m}$  distance, and are finally detected electrically using h-BN/Co contacts in a non-local geometry. In this section we will demonstrate such an optical injection and confirm the spin origin of the non-local signal by polarization-dependent measurements and a set of control experiments. We also will demonstrate that such signal is absent if graphene is contacted to bilayer WSe<sub>2</sub> where the inversion symmetry is restored.

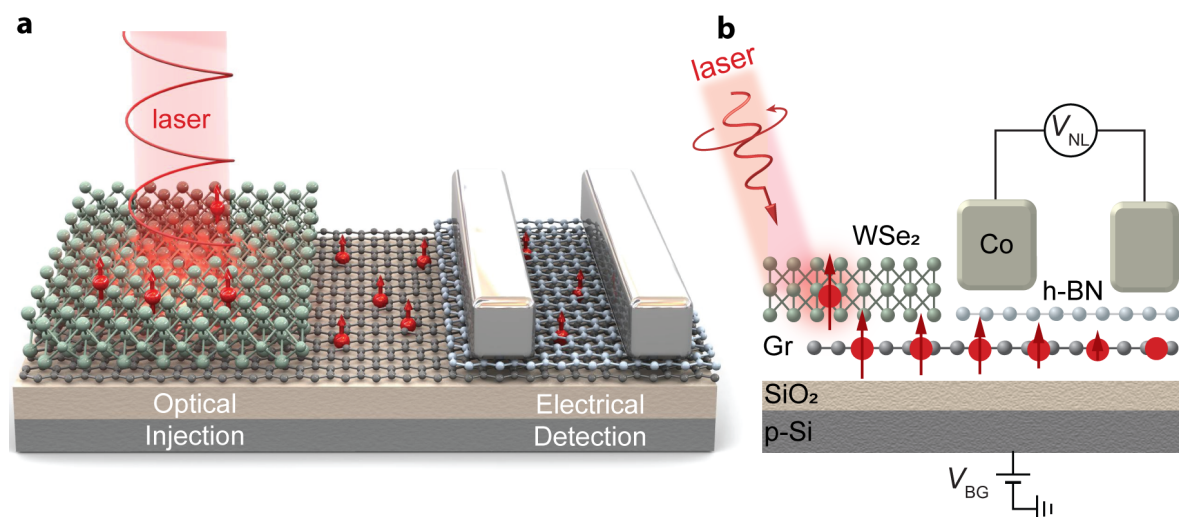


**Figure 5.1** – Schematics of the device. 3-dimensional (a) and cross sectional (b) representation of the device during its operation. Incident beam is focused on WSe<sub>2</sub>, close to the region at the graphene side. The red spheres with arrows represent the spin generation and diffusion during a non-local spin valve measurement.

### 5.2.1 Device fabrication

Towards realization of optical spin injection, we fabricate heterostructure devices consisting of monolayer WSe<sub>2</sub>, monolayer graphene and h-BN crystals. Our fabrication process starts with the mechanical exfoliation of monolayer graphene on a conventional SiO<sub>2</sub> (270 nm)/Si wafer, and followed by the graphene transfer to partially cover monolayer WSe<sub>2</sub>. Finally, a three-layer h-BN crystal is similarly transferred by targeting the uncovered region of graphene. In order to ensure clean interfaces in graphene/WSe<sub>2</sub>/h-BN heterostructure, we utilize the dry transfer method described in Chapter 3 and anneal samples under high vacuum conditions. This process results in a cleaner interface between two-dimensional materials by removing the transfer-related residues. Electrode masks are prepared by utilizing the standard electron beam lithography technique discussed in the Chapter 3. Device fabrication is completed by forming the Ti / Co (10 nm / 35 nm) electrodes. Deposition rate for both materials is  $\sim 0.5 \text{ \AA/s}$  and the Ti layer serves as a capping layer to prevent the oxidation of ferromagnetic Co electrodes.

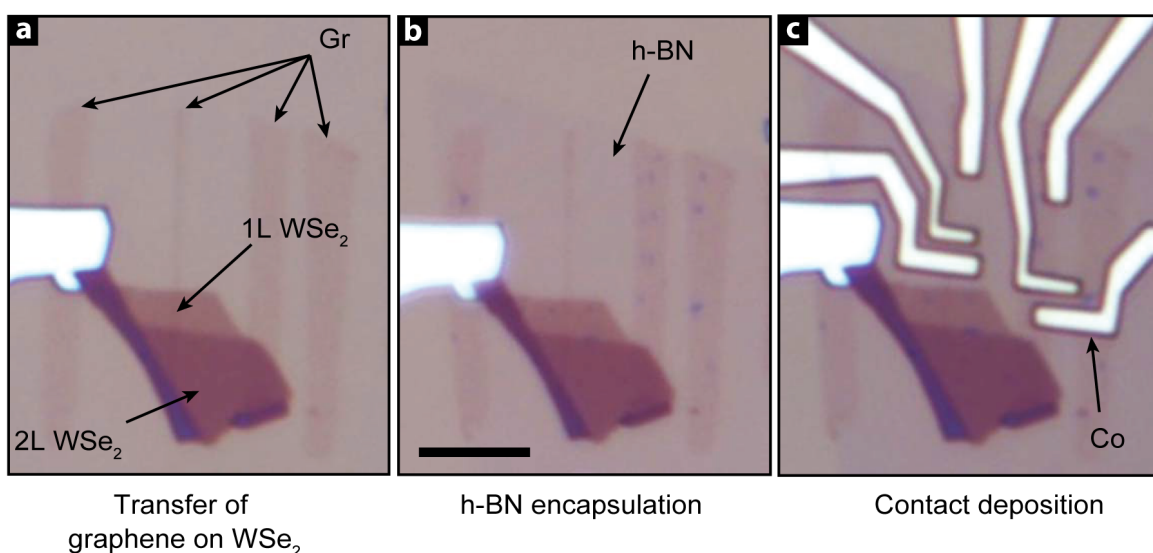


**Figure 5.2** – Device fabrication. Optical images present a typical device at various fabrication stages. (a) WSe<sub>2</sub> is transferred onto an initially exfoliated graphene stripe. Then, the h-BN layer is transferred (b) which is followed by the evaporation of ferromagnetic Co electrodes (c). Scale bar is 5  $\mu\text{m}$ .

Figure 5.2b shows the optical images for one of our typical heterostructure devices at different fabrication steps. The final structure has an additional Co/h-BN/graphene region which is crucial for the electrical detection of the generated spin signal. We note that such a stack could also host tunable magnetic proximity effects and hence allow the possibility of additional control of spin transport by gating, that we will exploit in the last section of this chapter. In total, we have characterized more than five different devices. Here,

we represent results obtained in two optospintronic devices, labelled as device A and device B. Unless otherwise stated, the results shown are from device A. In order to achieve the highest signal to noise ratio for a clearer signal, we performed measurements at low temperature (4 K).

### 5.2.2 Graphene spin channel characterization

Prior to any optical measurements, we first characterize a graphene-based spin valve device with trilayer h-BN used as a tunnel barrier. Figure 5.3b shows the device conductivity as a function of back-gate voltage ( $V_{BG}$ ). Our device characteristic shows the typical ambipolar field effect behavior. The charge neutrality point is observed at negative  $V_{BG}$  values which indicates the weak n-doped nature of graphene. Such doping is common for spin valve devices [192]. From four-terminal measurement configuration, we extract an electron mobility of  $\sim 5.500 \text{ cm}^2/\text{V}\cdot\text{s}$  at  $\sim 1 \cdot 10^{12} \text{ cm}^{-2}$  carrier concentration. At low bias range, we observe a nearly linear  $I - V$  relation (Figure 5.3b-Inset).

As the next step, we perform all-electrical spin injection, transport and detection measurement in a four-terminal non-local geometry [193]. This measurement scheme is shown in Figure 5.3a. We apply a fixed current of  $5 \mu\text{A}$  between electrodes 1 & 2 and record the non-local voltage between electrodes 3 & 4 while applying the in-plane magnetic field  $B_{\parallel}$ . By passing charge current through a magnetized cobalt, current is becoming spin-polarized, which effectively creates spin accumulation in the graphene channel. As a result, there is a net charge and spin transport between contacts 1 & 2, while there is a pure spin diffusion (zero net charge current) towards probes 3 & 4. We intentionally fabricate ferromagnetic contacts of different width in order to introduce shape anisotropy that results in different coercive fields of injector and probe. This changes the relative polarization orientations of the injector (2) and detector (3) electrodes and induces a non-local spin signal of  $\sim 0.2 \Omega$  when sweeping the in-plane magnetic field (Figure 5.3c).

In order to determine the spin polarization ( $P$ ) of electrodes (Co/3 layers of h-BN) which will be later employed for detecting the optically generated spin signal, we perform conventional Hanle precession measurements [193, 194]. Here, the non-local signal is recorded while the out-of-plane magnetic field  $B_{\perp}$  is swept in the range of  $\pm 150 \text{ mT}$  (Figure 5.3d). Since the spin-dependent current precesses along the field (schematically depicted in Figure 5.3a), the signal decreases (increases) for the parallel (anti-parallel) configuration as the strength of the  $B_{\perp}$  is increased. The resulting signal can be fitted with the solution of the Bloch equation [23]:

$$R_{NL} \sim \int_0^{\infty} \frac{1}{\sqrt{4\pi D_S t}} \exp\left(-\frac{L^2}{4D_S t}\right) \exp\left(-\frac{t}{\tau_S}\right) \cos(\Omega_L t) dt \quad (5.1)$$

## Chapter 5. Optospintronic devices

where  $L \simeq 4 \mu\text{m}$  is the center-to-center separation between the injector and detector electrodes and  $\Omega_L = g\mu_B B/\hbar$  is the Larmor frequency. This gives a spin relaxation time of  $\tau_S \simeq 131 \pm 1 \text{ ps}$ , a spin diffusion constant of  $D_S \simeq 0.123 \text{ m}^2/\text{s}$ , and hence, a spin relaxation length of  $\lambda_S \simeq 4 \mu\text{m}$  at  $V_{\text{BG}} = 0 \text{ V}$ . These spin transport properties are comparable with those of typical graphene spin valves [23, 192, 195] but lower than the state-of-the-art graphene spin valves [26]. In our device structure, h-BN layer also acts as an encapsulation layer. This excludes polymer residues as the source of spin scattering in the devices [196]. The limiting factor could be contact-induced spin scattering. We believe that spin transport parameters in our device architecture could be enhanced by carefully engineering the number of h-BN layers to completely suppress the conductivity mismatch issue [183].

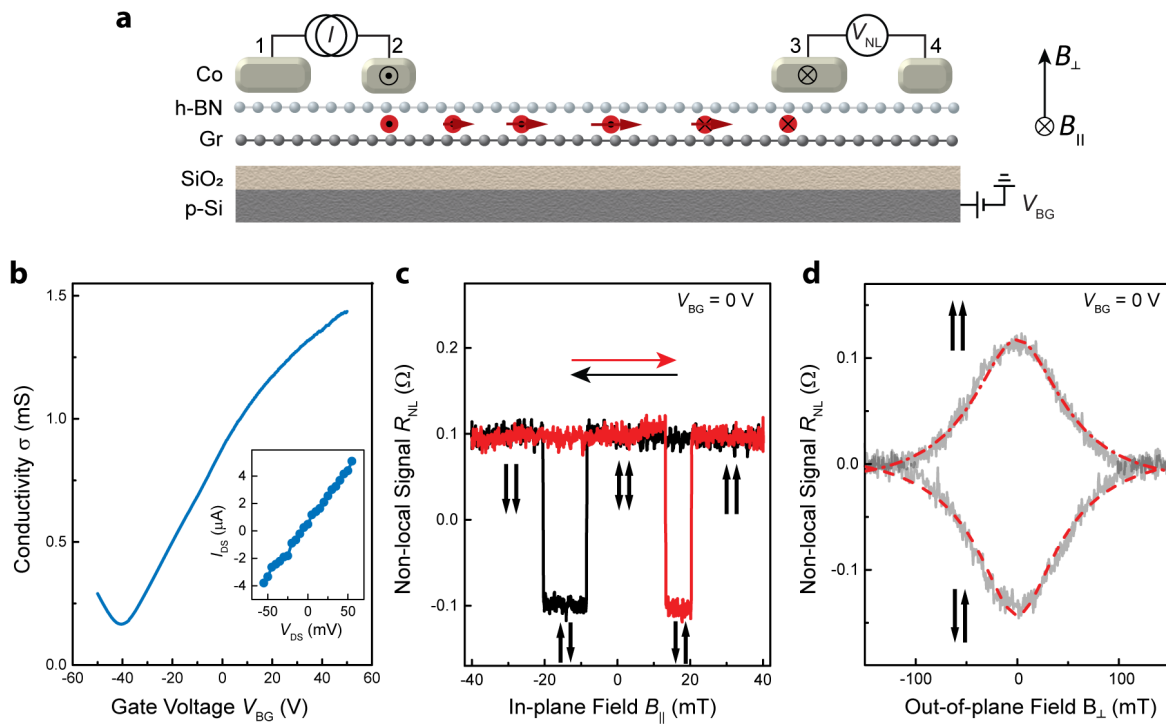


**Figure 5.3** – Electrical characterization of the graphene spin valve with a 3L h-BN tunnel barrier. (a) Schematic depiction of a non-local configuration for spin-valve characterization and Hanle spin precession measurements. A charge current of  $5 \mu\text{A}$  is applied from electrode 1 to 2 and the generated spin current is detected by probing the electrochemical potential differences between electrodes 3 and 4. (b) Back-gate voltage dependence of graphene conductivity. Inset shows the  $I - V$  dependence of injector and detector electrodes. They are represented as 2 and 3, respectively in the schematics shown in (a). (c) Non-local signal as a function of in-plane magnetic field  $B_{\parallel}$ . Black and red horizontal arrows represent the magnetic field sweeping directions. Vertical arrows represent the relative magnetization directions of the injector and detector electrodes. (d) Hanle precession of the non-local signal as a function of the perpendicularly applied magnetic field. Measurements are performed at  $V_{\text{BG}} = 0 \text{ V}$ .



## 5.2. Optical spin injection in graphene *via* proximity coupling with WSe<sub>2</sub>

Spin polarization value can be calculated by following formula, explained in details in reference [197]:

$$P = \sqrt{\frac{2\Delta R w \sigma}{\lambda_S} \exp\left(\frac{L}{\lambda_S}\right)} \quad (5.2)$$

where,  $w$  and  $\sigma$  are the width and conductivity of graphene, respectively. By inserting the  $\lambda_S$  extracted from spin precession measurements, we calculate  $P$  to be  $\sim 0.6\%$ .

### Gate dependency of spin transport

Next, we repeat spin Hanle precession measurements as a function of gate voltage  $V_{BG}$  under both parallel and anti-parallel polarization configurations and we extract spin transport parameters as described. We plot results in Figure 5.4 as a function of carrier concentration  $n$ , which is calculated as  $n = C_{BG} V_{BG} / e$ , where  $C_{BG}$  is the gate oxide capacitance and  $e$  is elementary charge. We observe that extracted spin relaxation time, spin diffusion constant and spin relaxation length values are highest near the charge neutrality point and decrease as we increase the carrier concentration and therefore are highest near the Dirac point. The maximum extracted spin relaxation time (length) value is  $\sim 225$  ps ( $6.1 \mu\text{m}$ ).

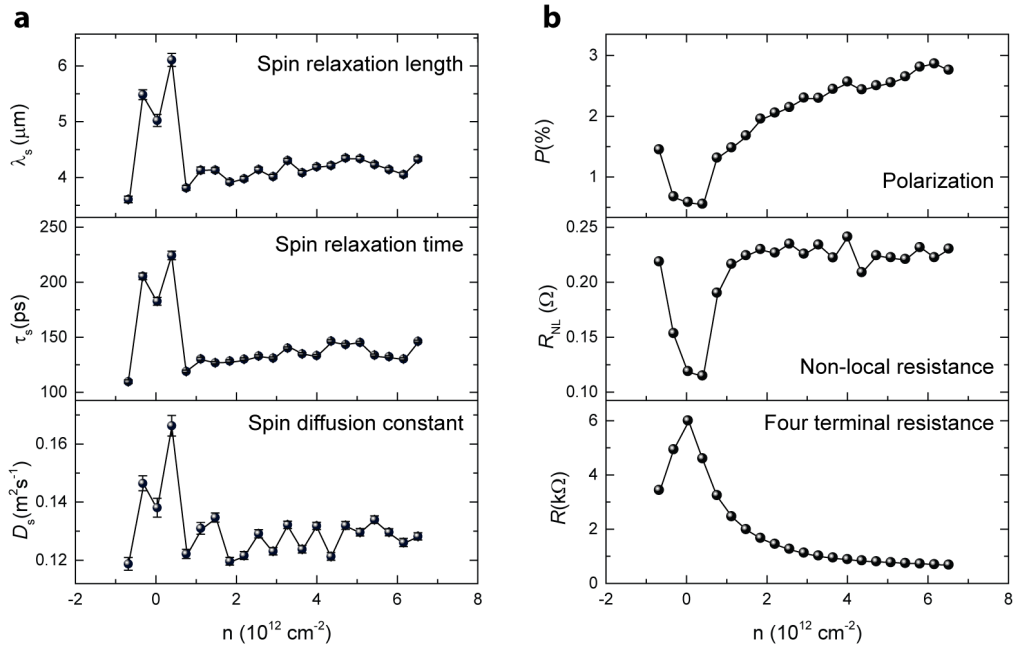


**Figure 5.4** – Characterization of graphene spin transport. Carrier concentration dependence of (a) spin relaxation length ( $\lambda$ ), spin relaxation time ( $\tau_s$ ), spin diffusion constant ( $D_s$ ) and (b) carrier's spin polarization ( $P$ ), non-local resistance ( $R^{\text{NL}}$ ), local four-probe resistance ( $R$ ).

Meanwhile, calculated polarization values have opposite back-gate dependence. Extracted  $P$  value is smallest near the Dirac point and increases up to 2.85 % at high carrier concentration. We consistently observe a very similar response in all measured junctions within this device which indicates the large size uniformity of three-layer thick h-BN. Note that these spin polarization values are an order of magnitude smaller than for the best tunnel barriers ever created for graphene[184]. However, they are comparable to the values obtained using oxide based tunnel barriers [196] and reliable enough for detecting optically injected spin currents.

### 5.2.3 Optospintronics device characterization

Next, we characterize our h-BN/Gr/WSe<sub>2</sub> heterostructure device. Figure 5.5a shows the gate dependence of graphene conductivity for device A which is similarly measured by using Co/3L h-BN electrodes. We observe ambipolar characteristic with a weak n-type doping. The corresponding  $I - V$  characteristic is also linear at low bias range. These results are consistent with the device performance shown in Figure 5.3b. This suggests that our electrode could serve as a spin detector.

In order to determine how monolayer WSe<sub>2</sub> affects electrical transport of the graphene channel when the former is transferred on top of the latter, we have fabricated another device, that will be presented in details in Section 5.3.2. The design of this device allows us to perform four-terminal measurements independently on the pristine graphene as well as on the same graphene flake with monolayer WSe<sub>2</sub> on top. Sheet resistance shown in Figure 5.12c reveals similar behavior of both regions in a reasonable proximity to the Dirac point. We extract an electron mobility of  $\sim 5.200 \text{ cm}^2/\text{V}\cdot\text{s}$  and  $\sim 5.800 \text{ cm}^2/\text{V}\cdot\text{s}$  at  $\sim 1 \cdot 10^{12} \text{ cm}^{-2}$  carrier concentration for pristine graphene and WSe<sub>2</sub>-graphene heterostructure respectively. This result indicates the absence of any obvious effect of large band gap material WSe<sub>2</sub> on graphene transport properties while the Fermi level is kept in the band gap of the former material.

Prior to optical spin injection, we also optically characterize the WSe<sub>2</sub> flake in our device. In addition to the flake optical contrast, we confirm the monolayer nature of WSe<sub>2</sub> by photoluminescence measurements using a 488 nm blue laser diode with low incident power of 40  $\mu\text{W}$ . As shown in Figure 5.5b, we observe a strong peak X° near 1.72 eV corresponding to the excitonic resonance in a monolayer flake. In future experiments we will resonantly excite WSe<sub>2</sub> at this energy (indicated by black arrow in Figure 5.5b) in order to minimize spin decoherence of optically pumped carriers. In the PL spectrum we can also distinguish the lower energy X' peak that could be associated with the trion or localized exciton emission [167].

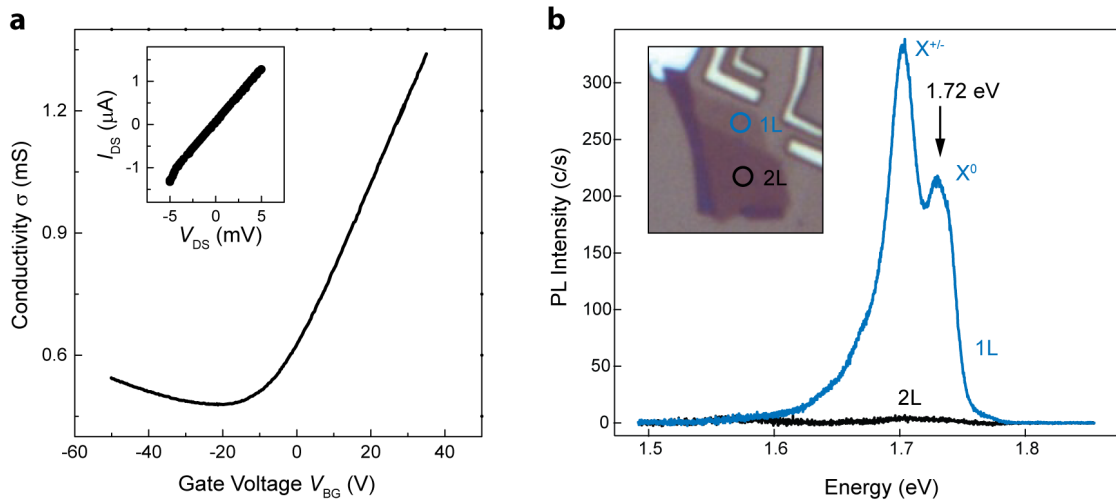


**Figure 5.5** – Electrical and optical characterization of optospintronic devices. (a) Back-gate voltage dependence of graphene conductivity. Inset shows the two-probe  $I$ – $V$  dependence of detector electrodes of the optospintronic device, shown in the inset of (b). (b) Low-temperature photoluminescence measurements of monolayer (blue) and bilayer (black) WSe<sub>2</sub> obtained at 488 nm excitation wavelength with 40  $\mu$ W incident power in the areas indicated by circles on the device optical image (inset).

### 5.2.4 Optical spin injection into graphene

Now we turn our attention to the optical spin injection aspect of our study. The schematic of the device set-up is shown in Figure 5.6a. We polarize the initially unpolarized 720-nm light beam using a linear polarizer oriented 45° to the optical axis of the photoelastic modulator (PEM). This orientation of the incident light provides the highest degree of modulated light circularity. PEM acts as a variable birefringent plate providing time-dependent retardation along one of the axes at a frequency of 50 kHz (1f). In the case of  $\lambda/4$  modulation, applied retardation has maximal (minimal) value of  $\lambda/4$  ( $-\lambda/4$ ) with the PEM acting as a quarter wave plate at these moments, thus generating the right (left) circularly polarized light. Lock-in amplification of the non-local signal with the PEM (1f) fundamental frequency (50 kHz, gray dashed line) results in a signal that corresponds to the difference of the non-local signals caused by the right and left-handed light. Therefore, the resulting light modulation is right-to-left (left-to-right) in the case of 45° ( $-45^\circ$ ) incidence angle. This measurement configuration minimizes the background-related artificial signals. In order to assure the full out-of-plane direction magnetization of Co electrodes, we first apply  $B_{\perp} = 2$  T [198] and then set the field to  $B = 0$  T. By keeping  $B = 0$  T, we exclude any contribution from the valley-Zeeman effect [199]. We note that the remaining out-of-plane magnetization of Co is sufficient enough for contacts to be used as spin signal detectors.

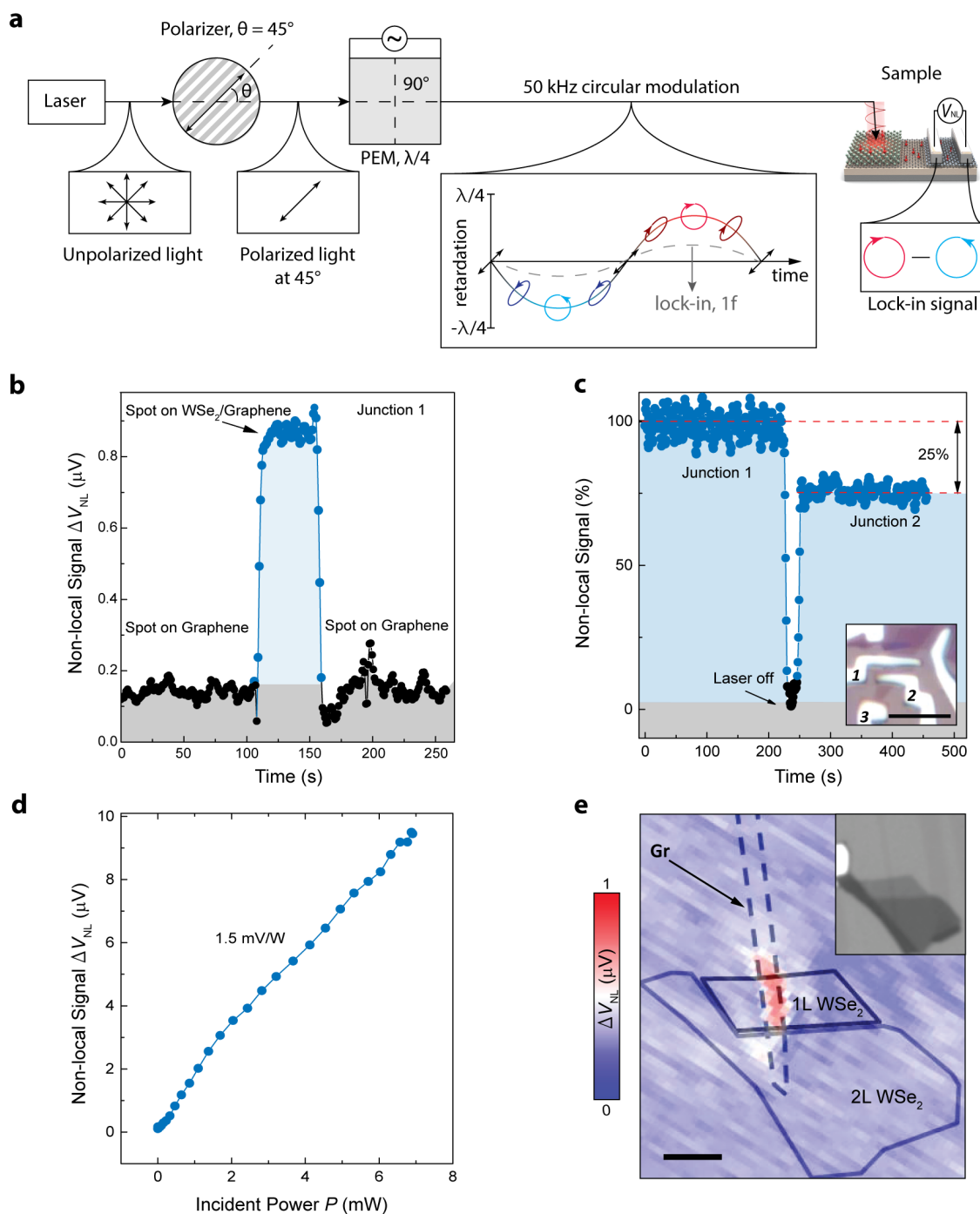


**Figure 5.6** – Optical spin injection into graphene. (a) Measurement schematics for achieving quarter-wave modulation and electrical detection of the non-local signal. (b) Time dependence of the non-local signal while the laser spot is moved from graphene to WSe<sub>2</sub> and then back to graphene. A photoelastic modulator is used for enhancing the signal quality. (c) Non-local signal measured at junction 1 and 2. Junction 1(2) refers to the non-local voltage measured between electrodes 1 (2) and 3. Inset shows the optical image of the device. Scale bar is 3  $\mu m$ . (d) Laser power dependence of the non-local signal generated under quarter wave modulation. (e) Spatial map of the non-local voltage signal. The dotted line represents monolayer graphene, while black and blue solid lines outlines the WSe<sub>2</sub> regions.

## 5.2. Optical spin injection in graphene *via* proximity coupling with WSe<sub>2</sub>

Next, we focus the laser beam under quarter-wave modulation onto the device and detect the generated non-local signal electrically in a non-local geometry by employing a lock-in amplifier with a reference signal from the PEM controller unit. As shown in Figure 5.6b, we do not observe any significant non-local signal while the light spot is parked on graphene. In contrast, once the spot is placed on the graphene/WSe<sub>2</sub> heterostructure, we observe a sudden increase in the non-local voltage reaching 1  $\mu\text{V}$ , even though the laser beam is much further away from the detector electrodes compared to the initial case with the laser spot on graphene. The signal returns back to its initial value of  $\sim 0.1 \mu\text{V}$  when the spot is placed back on top of the graphene region. This measurement suggests that the measured signal is not due to spurious effects such as laser heating or others.

The non-local origin of the signal is confirmed by the length-dependent measurement. As shown in Figure 5.6c, the magnitude of the signal decreases  $\sim 25\%$  from the initial value if the electrode 2 is utilized as the detector which is  $\sim 3.7 \mu\text{m}$  away from the Gr/WSe<sub>2</sub> interface. This is expected within the spin transport theory as the spin dephases more while it travels a longer distance and therefore the measured signal amplitude decreases [200]. It is also worth mentioning that the measured signal has only a very weak dependence on the location of the laser spot. This indicates the homogeneous interface between 2D crystals.

In Figure 5.8d we plot the power dependency measurement. Importantly, the non-local signal under  $\lambda/4$  modulation changes linearly with the laser power with a slope close to  $\sim 1.5 \text{ mV/W}$ . We obtain the non-local signal as large as  $\sim 9.5 \mu\text{V}$  under 6.2 mW laser power.

In order to confirm that the origin of the signal is the spin-coupled, valley-selective absorption by monolayer WSe<sub>2</sub>, we compare the non-local signals generated at the monolayer WSe<sub>2</sub>-graphene and bilayer WSe<sub>2</sub>-graphene interfaces. Note that optical spin injection is not expected in the latter interface case as the inversion symmetry is restored in bilayer devices [71]. Figure 5.6e shows the spatial map of the non-local voltage signal measured in device B at  $V_{\text{BG}} = 0 \text{ V}$ . For the purpose of direct comparison, an optical image of the device is shown in Inset of Figure 5.6e. Similarly to the device A (Figure 5.6b), we detect the non-local voltage only if the laser spot is parked on monolayer WSe<sub>2</sub>. As we move the spot onto the bilayer WSe<sub>2</sub> region, we observe a sudden suppression of the non-local voltage and it is undetectable. This unequivocally proves the valley-selective origin of the signal.

### Gate dependency of optical spin injection

We also compare the gate dependence of the non-local signal generated by electrical and optical injection techniques. Figure 5.7a shows the  $V_{\text{BG}}$  dependence of both charge resistance and the amplitude of the non-local resistance obtained by all-electrical measurements. We observe the inverse relation between local and non-local resistances. The

non-local signal is  $\sim 0.12 \Omega$  near the Dirac point and as the carrier concentration increases, the non-local signal increases two-fold. Based on the 1D diffusion spin transport theory [197], such inverse scaling indicates that our contacts are not tunneling, in good agreement with the observation of linear  $I - V$  as shown in Figure 5.3b-Inset. For the optical spin injection case, the scaling between device resistance and the non-local signal is completely different. The electrostatic doping decreases both the channel resistance and the non-local signal. We observe the maximum non-local signal at  $V_{BG} = -20$  V that matches the Dirac point of graphene (Figure 5.7b). Such direct scaling has previously been observed in graphene [184] and black phosphorus [201] spin valve devices and discussed to be the direct signature of tunneling spin injection [197]. Here, note that the non-local signal at the hole conduction region decreases slightly faster than the electron conduction region which could be due to enhanced barrier height between graphene and TMDC layers at lower gate values [45, 202, 203].

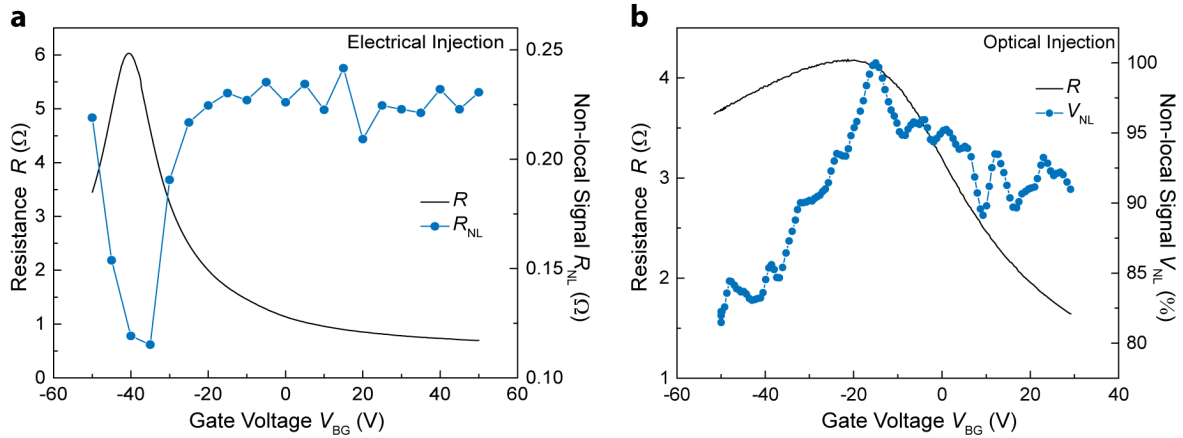


**Figure 5.7** – Non-local signal as a function of back-gate voltage. Back gate voltage dependence of local device resistance and non-local signal generated through electrical (a) and optical (b) injection.

### 5.2.5 Control experiment — half-wave modulation

In order to prove spin origin of the measured non-local signal, we perform a set of control experiments, including measurements under half-wave ( $\lambda/2$ ) modulations of incident light. In this case, applied retardation has maximal (minimal) value of  $\lambda/2$  ( $-\lambda/2$ ) with PEM acting as a half-wave plate at these moments, thus rotating the incident polarization by  $2\theta$  ( $90^\circ$  in the case of  $45^\circ$  incidence), while preserving its linearity. Lock-in amplification of the sample electrical response with the reference signal (gray dashed line) at double the PEM operating frequency (100 kHz,  $2f$ ) results in a signal that corresponds to the variation in the non-local signal caused by the original and rotated linearly polarized light. Therefore, the resulting light modulation is linear-to-linear. The corresponding measurement set-up is

## 5.2. Optical spin injection in graphene *via* proximity coupling with WSe<sub>2</sub>

shown in Figure 5.8a. The activation of a specific valley is only possible with the circularly polarized light, while the half-wave modulation does not meet this requirement. Therefore only  $\lambda/4$  modulations should result in the spin-dependent signal, and we are not expecting to observe a signal in the case of  $\lambda/2$  modulation.

If the origin of the signal was not spin dependent, we would observe the same response under both modulations. Figure 5.8b shows the time dependence of the non-local voltage measured under  $\lambda/4$ , followed by  $\lambda/2$  modulation. We observe a non-local signal of  $\sim 0.62$   $\mu\text{V}$  for the case of  $\lambda/4$  modulation and the signal drops significantly for the  $\lambda/2$  modulation case. Unlike  $\lambda/4$  modulation case, the signal is nearly independent of the incident laser power for the  $\lambda/2$  modulation case as shown in Figure 5.8c.

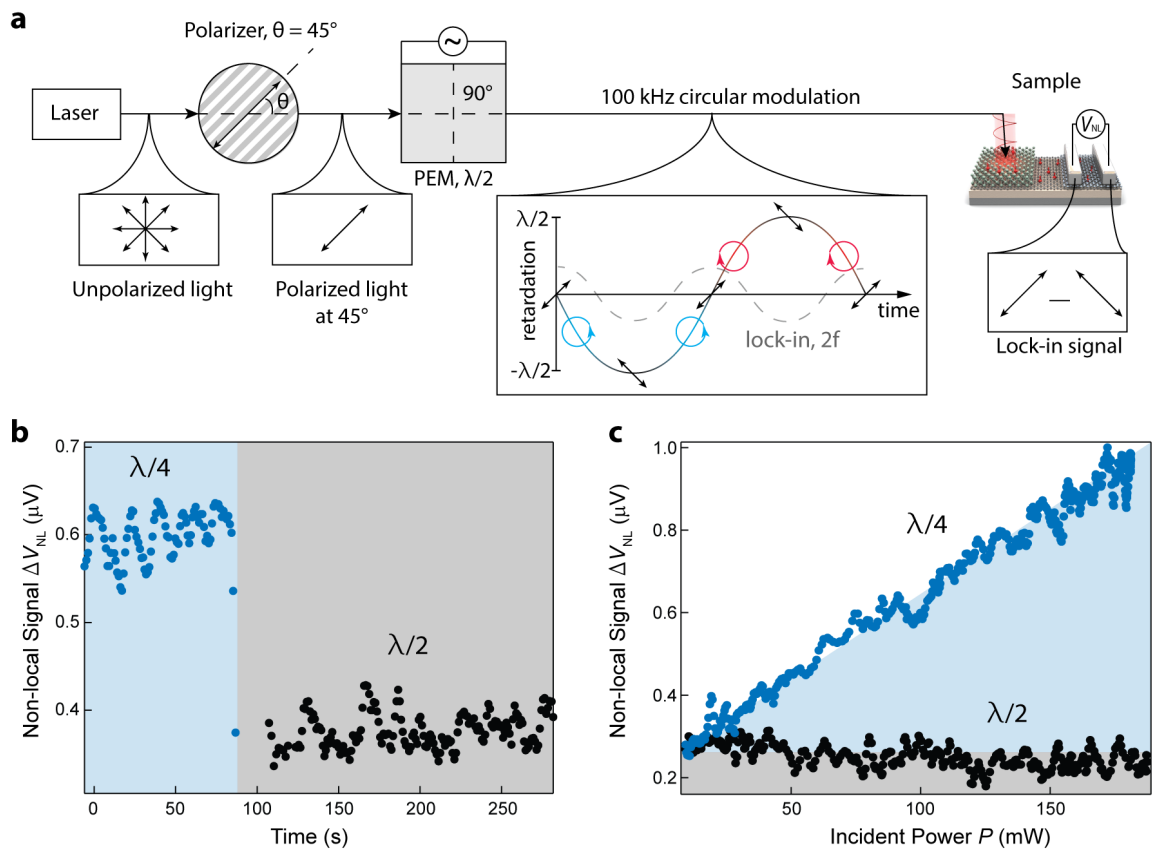


**Figure 5.8** – Non-local signal at half-wave modulation. (a) Measurement schematics for achieving half-wave modulation and electrical detection of the non-local signal. (b) Non-local signal recorded with the incident light under quarter-wave and half-wave modulations. (c) The dependence of the non-local signal on the power of incident light.

It is important to note that  $\lambda/2$  modulation signal is observed at 100 kHz, which is considerably higher than 50 kHz frequency of  $\lambda/4$  modulation. Acting as a long pass RC-filter, silicon global gate might therefore attenuates higher frequency signal assigned

to the  $\lambda/2$  modulation case. However, even considering the worst case scenario when cut-off frequency is below the modulation frequency, the obtained attenuation value is -4 dB, meaning  $\lambda/2$  signal to be 1.6 times smaller than the lower frequency  $\lambda/4$  signal. Instead, we observe the  $\lambda/4$  signal to be 5 times higher, beyond what is expected from simple attenuation due to the capacitive coupling. Moreover, the  $\lambda/2$  signal is nearly independent to the incident power ramp. We believe that this constant signal constitutes the background-related portion of our non-local signal. Its origin could be the finite resistance of graphene rather than any laser heating-related artifacts as the signal does not change with increasing laser power.

### 5.2.6 Control experiment — ellipticity dependence

We further prove the spin-valley coupling origin of the non-local signal by measuring its dependence on the ellipticity of the modulated light by modifying the incident angle ( $\theta$ ) of light to the optical axis of the photoelastic modulator in quarter-wave and half-wave regimes.

The sketch shown in Figure 5.9a schematically represents results of light modulation for three particular angles of incidence ( $\theta = 45^\circ, 22^\circ, 0^\circ$  from the top to the bottom) in the cases of quarter-wave and half-wave modulation (left and right parts respectively). Since the PEM operated in a  $\lambda/4$  mode acts as a time-dependent quarter-wave plate, it results in the modulation of the circular handedness of the light if incident at  $45^\circ$  angle to the PEM axis (upper left drawing).

Deviating incident angle by a half-wave plate  $\theta$  from the  $45^\circ$ , results in the components of light parallel and perpendicular to the PEM optical axis being taken out of balance, thereby increasing ellipticity of the modulated light (middle left). Light incident at  $\theta = 0^\circ$  (bottom left schematic) is not influenced by the PEM since it is oriented along its optical axis while only the component across this axis gets retarded. In other words, the angle  $\theta$  has a direct impact on the ellipticity degree of the light modulated by the PEM operating in  $\lambda/4$  mode and thus on the signal amplified by the lock-in. On the other hand, half-wave modulation (right part) is fundamentally different from the quarter-wave case, since light is modulated linearly between  $\theta$  and  $-\theta$  at twice the frequency of PEM operation. Importantly, changing the incidence angle  $\theta$  under the half-wave modulation does not change the resulting modulation, keeping it linear-to-linear (L-L).



## 5.2. Optical spin injection in graphene *via* proximity coupling with WSe<sub>2</sub>

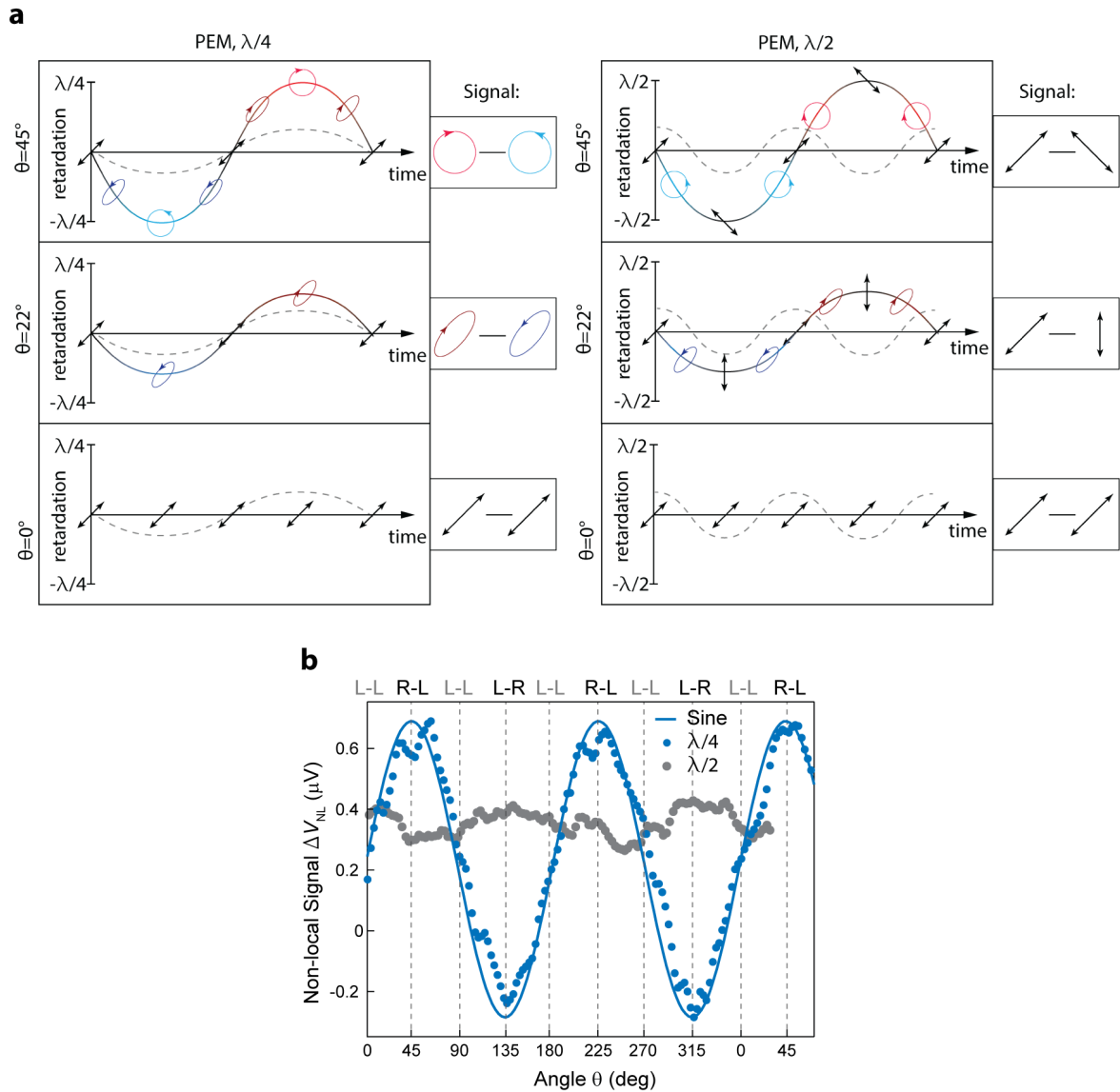


**Figure 5.9** – Ellipticity dependence of the non-local signal. (a) Schematics of the resulting light modulation for three particular angles of incidence ( $\theta = 45^\circ$ ,  $22^\circ$ ,  $0^\circ$  from the top to the bottom) in cases of quarter-wave and half-wave modulation (left and right parts respectively). (b) Non-local signal as a function of the incident light angle  $\theta$  at half-wave modulation (gray dots) and quarter-wave modulation (blue dots) fitted with the sine function (solid line). During the measurements, ellipticity of the light is modified by changing the incident angle  $\theta$  that is controlled by the rotation of a permanent half-wave retarding plate. Deviation from  $\theta = 45^\circ$  decreases the signal amplitude, reaching the lock-in noise floor when incident light polarization is parallel to the PEM optical axis. For the experiment with linear light modulation, half-wave configuration of PEM was used with double frequency (100 kHz) as a reference signal. We observe high non-local signal and ellipticity dependence only for quarter-wave modulation.

We now study experimentally how the non-local signal depends on incident light angle  $\theta$  at half-wave modulation (red dots) and quarter-wave modulation (blue dots). As shown in Figure 5.9b with blue markers, the non-local signal in  $\lambda/4$  mode demonstrates very strong dependence on the  $\theta$ . This dependence follows sine function of twice the angle of incidence ( $2\theta$ ) as a representation of the ellipticity degree of the modulated light, in good agreement with schemes in Figure 5.9a. We observe a maximum signal of  $0.6 \mu\text{V}$  under  $\theta = +45^\circ$ , which refers to R-L modulation of polarization. The signal decreases and remarkably even changes its sign as  $\theta$  is changed. We observe a minimum signal of  $-0.2 \mu\text{V}$  at  $\theta = -45^\circ$  ( $135^\circ$ ), under L-R modulation. We therefore confirm that sign of the non-local signal depends on the light helicity as expected for the spin-dependent signal.

The signal for the linear-linear case is  $\sim 0.3 \mu\text{V}$  and matches the value obtained for the  $\lambda/2$  case which was attributed to the background signal. As shown in Figure 5.9b in gray, incident angle dependence is absent for  $\lambda/2$  modulation which additionally indicates the opto-valleytronic origin of the spin injection process.

### 5.2.7 Control experiment — constant polarization

In the experiment above we have demonstrated that sign of the measured signal depends on the light helicity while magnetization of the detector electrode is kept constant. This is expected since spin orientation (up-down) is locked to the valley index (K/-K) that is addressed by the light helicity (right/left). However the signal should also depend on the magnetization direction of the detector, that we demonstrate is the final control experiment. By changing the experiment design we also exclude possibility of the signal to be originated from a spurious effect associated with photoelastic modulation. Here, instead of time-dependent light modulation we constantly polarize light incident to the sample.

Figure 5.10a schematically shows the measurement scheme of this control experiment. Light transmitted through a fixed linear polarizer is incident to the birefringent plate that introduces quarter-wave retardation along the slow axis compared to the fast one. The resulted polarization is therefore dependent on the plate orientation  $\theta$ .  $\theta = 45^\circ$  ( $-45^\circ$ ) generates light which is circularly right (left) polarized, while light polarized along the optical axis of the plate preserves its linear polarization. All the intermediate positions result in the elliptically polarized light.

We now focus light on the Gr/WSe<sub>2</sub> heterostructure and measure the non-local signal. As we expect it to be in order of  $\mu\text{V}$ , we modulate the intensity of the incident light by an optical chopper that periodically interrupts light transmission. The signal is then measured by a lock-in amplifier with a reference signal from the chopper controlling unit.

## 5.2. Optical spin injection in graphene *via* proximity coupling with WSe<sub>2</sub>

This significantly improves the signal-to-noise ratio.

We measure the non-local signal when ferromagnetic detector is polarized up and down, while slowly rotating the quarter-wave plate in order to modify light polarization. Results of such measurements are shown in Figure 5.10b. We observe a large background signal originating from the photovoltaic effect, thermoelectric effect, etc. It was absent in all previous measurements as the result of PEM light modulation, which cancels out all spurious signals independent on the polarization of light.

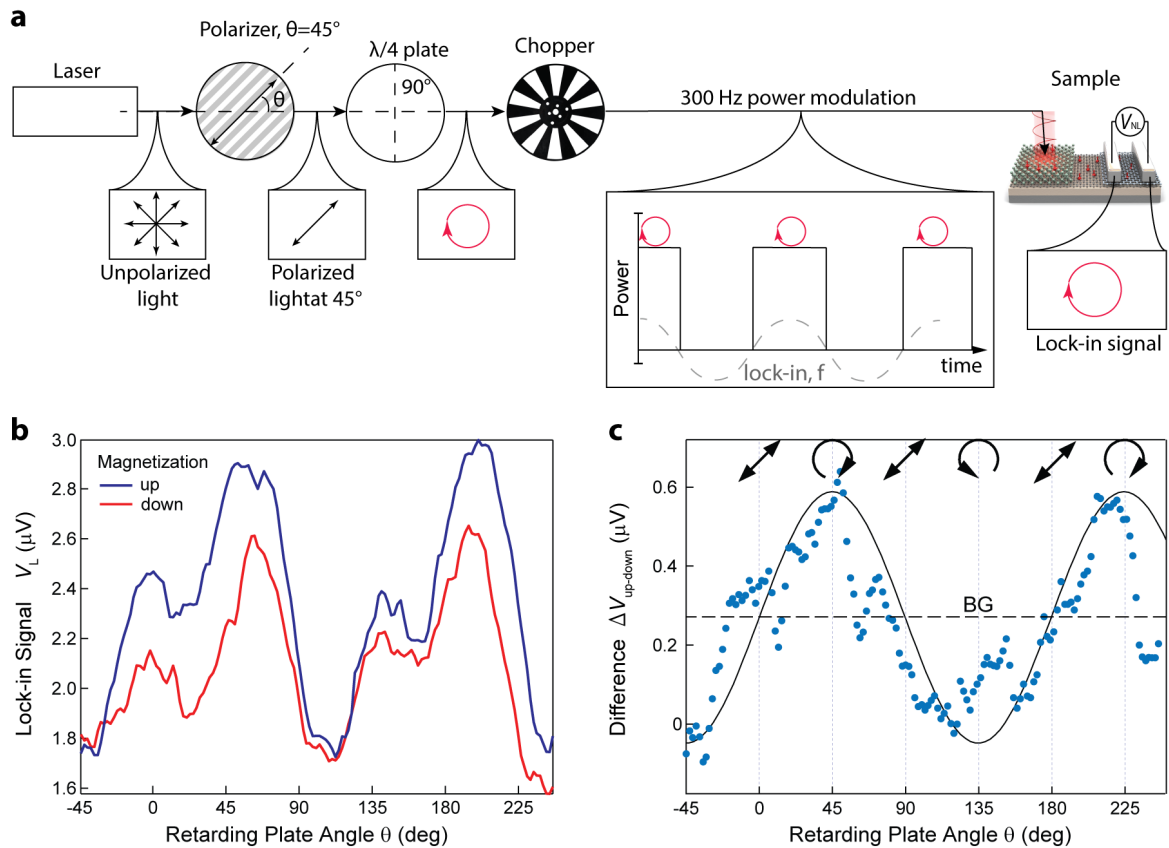


**Figure 5.10** – Non-local signal at constant polarization. (a) Measurement schematics for achieving electrical detection of non-local signal at a constant polarization of light. For better signal-to-noise level, we modulate light intensity by means of optical chopper. (b) Polarization dependence of the non-local signal recorded for up (blue) and down (red) magnetization of contacts. (c) Extracted dependence of magnetization dependent non-local signal on polarization of incident light. BG refers to the background signal

Subtractions of two curves corresponding to up and down magnetization should remove any spin-independent background. The result of such an operation is shown in Figure 5.10c. We can clearly see that the measured signal as a function of the quarter-wave plate orientation follows a sinusoidal function, expected for the signal that solely depends on the light helicity. The signal reaches its maximum at  $\theta = 45^\circ$ , when WSe<sub>2</sub> is pumped with

right-handed circularly polarized light, and corresponding minimum for left-handed light at  $\theta = -45^\circ$ . It even changes the sign. However the difference is not centered at  $R_{\text{NL}}$  due to the background signal as mentioned previously.

### 5.2.8 Conclusion

In this section we have demonstrated optical spin injection into graphene by benefiting from the spin-valley properties of monolayer  $\text{WSe}_2$ , including valley-dependent optical selection rules. We activate the spin polarized charge carriers in the  $\text{WSe}_2$  layer by illuminating the crystal with circularly polarized light. The generated spin current tunnels into the graphene layer and transports over  $3.5 \mu\text{m}$  before its electrical detection through a three layer thick h-BN tunnel barrier. A recent optical experiment in a graphene/TMDCs based heterostructure suggests that induced charge carriers are electrons [204].

We exclude any spurious effects by prudently studying the separation, power intensity, incident light polarization and detector magnetization dependence on the non-local signal. This proves that the measured signal is in agreement with the orientation of the injected spins that depends on the incident light helicity, but also on the orientation of the contact magnetization relative to injected spins. We also compare non-local signals generated at the monolayer  $\text{WSe}_2$ /graphene and bilayer  $\text{WSe}_2$ /graphene interfaces in order to prove its spin-coupled, valley selective absorption origin.

Our findings go in line with very recent Hanle precession measurements in similar structures based on  $\text{MoS}_2$ /graphene heterostructures performed in the group of Roland Kawakami. Indeed these independent observations of optical spin injection in a hybrid graphene-TMDC device additionally confirm our findings and therefore we strongly encourage reader to get acquainted with this work [205].

## 5.3 Modulation of spin transport in a graphene-WSe<sub>2</sub> heterostructure

### 5.3.1 Introduction

Having demonstrated successful optical spin injection, we continue taking advantage of complementary properties of graphene and TMDCs in their artificial heterostructures. Now we focus our attention onto another challenge of spintronics, namely on achievement of control over the spin currents in a device. This is required for the realization of a spin transistor and for further development of the field. We will demonstrate that all-electrical as well as optical modulation of spin transport in graphene is possible via the proximity effects induced by neighboring TMDC monolayer.

Similarly to the previous section, we fabricate devices based on graphene with superlattice spin properties and WSe<sub>2</sub> monolayer with strong spin-orbit coupling, valley dependent optical selection rules and spin-valley locked physics. The fabrication steps are analogous to the ones described in Section 5.2.1. Schematically device is presented in Figure 5.11. We employ graphene as a channel for spin transport, with TMDC placed on it for spin current modulation and Co/h-BN contacts for electrical injection and detection of spin currents. All measurements presented in this section are performed at low temperature (4 K).

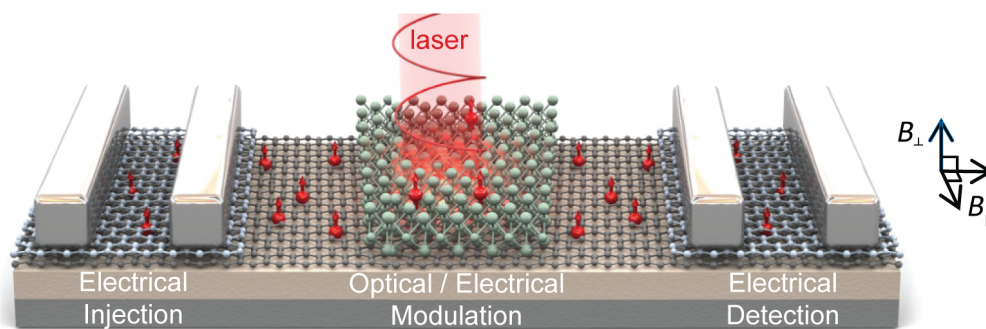


**Figure 5.11** – Schematic of the spin switch device. We employ graphene as a channel for spin transport with Co/h-BN probes for electrical spin injection and detection. For optical an electrical spin transport modulation, we employ a WSe<sub>2</sub> monolayer deposited on graphene that acts as a spin sink.

## 5.3.2 Heterostructure characterization

Optical image of a device based on a WSe<sub>2</sub>-graphene heterostructure is presented in Figure 5.12a. This device is designed in a way to perform four-terminal charge and spin transport measurements on regions with and without WSe<sub>2</sub> monolayer of the same graphene channel.

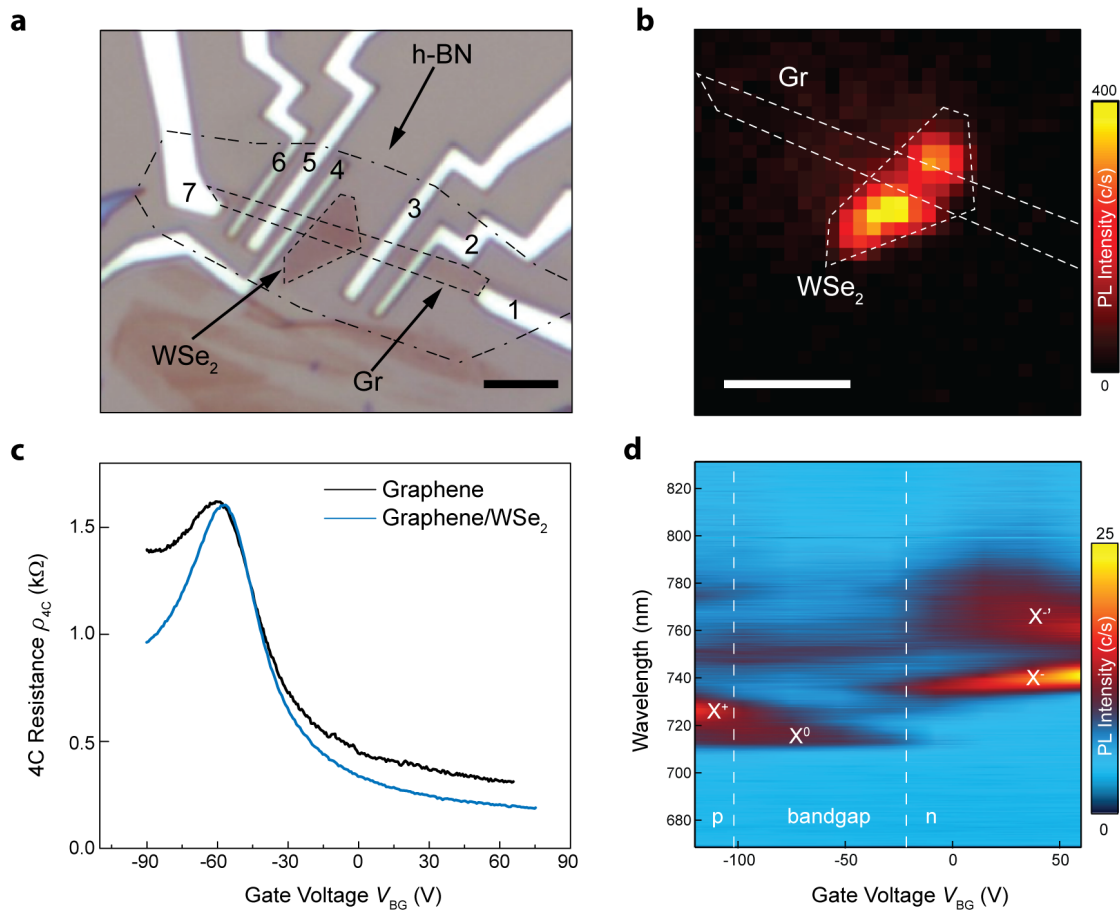


**Figure 5.12** – Device characterization. (a) Optical image of the fabricated device. Compound crystals are outlined by black dashed lines. Co probes are numbered for the future measurements. Scale bar is 5  $\mu\text{m}$ . (b) Photoluminescence spatial map. Graphene and WSe<sub>2</sub> flakes are indicated by dashed outlines. PL intensity drop in the heterostructure region indicates strong coupling between graphene and the semiconducting monolayer. Scale bar is 5  $\mu\text{m}$ . (c) Back-gate voltage dependence of the four-terminal resistivity of pristine graphene (black) and of the WSe<sub>2</sub>/graphene heterostructure (blue), measured between probes 2&3 and 3&4. (d) Back gate voltage dependence of PL spectrum. Neutral exciton ( $X^0$ ) appears when the Fermi level is located well in the bandgap. Charged excitons or trions are observed when the flake is doped with holes or electrons.

Prior to spin-transport measurements we first characterize the device electrically and optically. We start with four-probe resistance measurements of the device between differ-

### 5.3. Modulation of spin transport in a graphene-WSe<sub>2</sub> heterostructure

ent probes, in order to determine how monolayer WSe<sub>2</sub> affects electrical transport of the graphene channel when the former is transferred on top of the latter. Graphene resistance shown in Figure 5.12a reveals similar behavior of both regions (pristine graphene and covered with WSe<sub>2</sub> monolayer) in a reasonable proximity to the Dirac point. We extract an electron mobility of 5.200 cm<sup>2</sup>/V·s for graphene and 5.800 cm<sup>2</sup>/V·s for heterostructure at 10<sup>12</sup> cm<sup>-2</sup> carrier concentration. The observed difference in the resistivity away from charge neutrality point indicates that the semiconducting monolayer acts as a parallel pathway for charges when doped with holes (negative) or electrons (positive gate voltages).

We further study optical properties of the fabricated heterostructure by performing photoluminescence measurements. For this we record PL intensity as a function of the laser spot position. Resulting map is shown in Figure 5.12b. As expected, a high intensity region is well correlated with WSe<sub>2</sub> monolayer flake. In addition, we observe an intensity drop of the PL signal in the region of the WSe<sub>2</sub>/graphene heterostructure due to the fast transfer of photoexcited carriers between compound layers. This indicates strong coupling between graphene and WSe<sub>2</sub>, which is a required condition for further measurements. Additionally we study how PL spectra depends on the carrier concentration in the system. On the map presented in Figure 5.12d we can differentiate three regions. Highest energy emission at 715 nm correspond to the neutral excitons X<sup>0</sup>. This type of emission we can observe in the gate range between -100 V and -30 V that corresponds to the Fermi level in the band gap of WSe<sub>2</sub> with low carrier density. This gate range also coincides with high resistivity of graphene flake near the Dirac point, Figure 5.12c, indicating similar doping levels of compound monolayers. By shifting the Fermi level towards conduction (valence) band, we introduce more electrons (holes) into the system, making it n-(p-)doped. In the same time, we observe suppression of neutral exciton intensity and an appearance of charged trions X<sup>-</sup> (X<sup>+</sup>).

#### 5.3.3 Spin transport characterization

Now we focus our attention on the spin transport in the fabricated device. Unfortunately, used optical cryostat allows application of vertical magnetic field only, while we aim to investigate the in-plane spin transport. Therefore we improvised with device mounting in order to get both components of the field. Figure 5.13d shows a chip with a device wired-bonded to a chip carrier mounted in the cryostat with an intentional tilt of 8°. This tilt provides necessary  $B$  field components. Namely, the application of a vertical field  $\mathbf{B}$  produces in-plane  $B_{\parallel}$  and out-of plane  $B_{\perp}$  components with following amplitudes:

$$B_{\parallel} = 0.14 \cdot B, \quad B_{\perp} \simeq B \quad (5.3)$$

Strong anisotropy of thin Co contacts allows us to polarize probes in-plane even with such a small portion of the magnetic field.

We start with characterization of a spin valve based on the pristine graphene region. Results and schematic of the measurement scheme are presented in Figure 5.13a. The shape of the measured non-local signal versus the applied field is more complex than in a simple device. This is due to the application of both in-plane field which switches direction of electrodes and out-of-plane field which forces spins to undergo precession. Therefore, the measured signal is a mixture of a spin-valve (shadowed region) and Hanle precession (small field) signals. We have already discussed these two effects in the Section 5.2.2. Comparing forward (red) and backward (black) sweeps, we extract a spin valve signal of  $-7 \Omega$ . However this value is reduced due to the spin precession in the 150 mT out-of-plane field. From the shape of the non-local signal we conclude that the pure signal is more than an order of magnitude higher than extracted one.

Indeed, even in a such configuration we can perform Hanle spin precession measurements. For this, we sweep the magnetic field in a forward direction. Measured curve (red line in Figure 5.13c) represents Hanle precession in a case of parallel injector and detector contacts. We keep sweeping until the switch of the magnetization occurs on one of the magnetic contacts, meaning anti-parallel magnetization of probes. Starting from this point, we ramp the field down preserving polarization of contacts. Detected non-local signal (black in Figure 5.13c) is negative now since it represents anti-parallel magnetization of injector and detector.

Finally, we compare these results with spin-transport measured in the heterostructure region. We observe a similar shape of non-local signal as a function of the applied field, which is again the spin valve signal hindered by spin precession in the out-of-plane  $B$  field. Extracted non-local signal  $\Delta R_{NL}$  associated with a spin valve is around  $-0.2 \Omega$ , an order of magnitude lower compared to junction with a pristine graphene. First of all it is the result of a longer channel in the case of the heterostructure ( $5 \mu\text{m}$ ) compared to the pristine graphene ( $2 \mu\text{m}$ ). The small signal also indicates large spin-orbit coupling induced by  $\text{WSe}_2$  monolayer *via* proximity into the underlying graphene layer[202]. Indeed, it has been recently shown that induced SOC in graphene leads to a strong anisotropy of spin relaxation and lifetime [97, 206]. Particularly it shortens in-plane spin lifetimes by an order of magnitude. Similar proximity effect was also demonstrated to cause spin Hall effect in a  $\text{WS}_2$ -graphene heterostructure [96]. In the same work, Avsar *et al.* estimated induced SOC to be 17 meV, large compared to the intrinsic spin-orbit coupling of graphene, which is in order of  $25 \mu\text{eV}$  [207].



### 5.3. Modulation of spin transport in a graphene-WSe<sub>2</sub> heterostructure

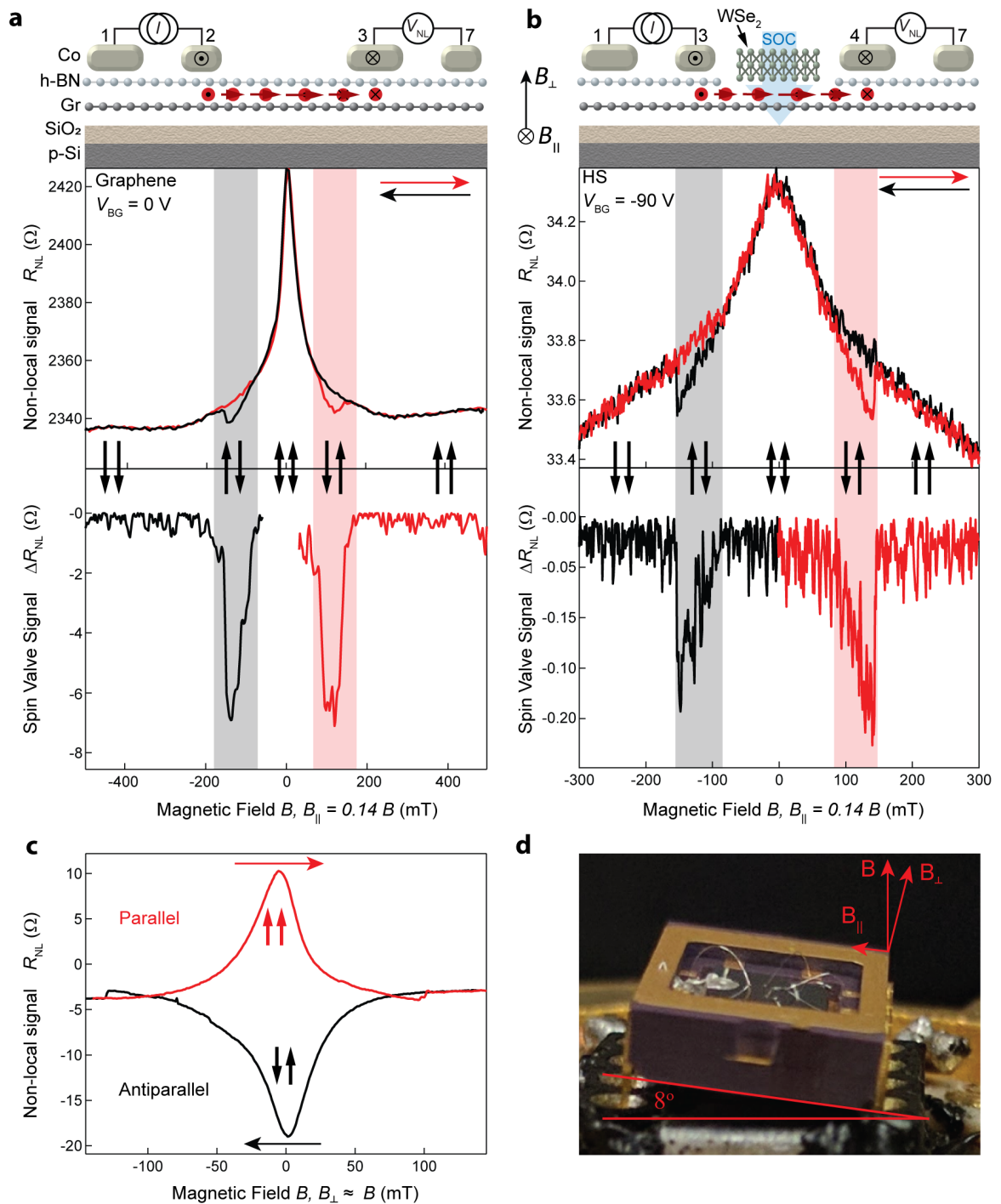


**Figure 5.13** – Non-local measurements of spin transport in pristine graphene (a) and heterostructure (b) regions. Top parts show schematics of measurement schemes with contact numbering according to Figure 5.12a. Central part shows the non-local signal, while the bottom graph shows the extracted spin valve signal as a function of the in-plane magnetic field  $B_{||}$ . Black and red horizontal arrows represent the magnetic field sweeping directions. Vertical arrows represent the relative magnetization directions of the injector and detector electrodes. (c) Hanle precession of the non-local signal as a function of the perpendicularly applied magnetic field. (d) Optical image of a sample mounted with tilt in the cryostat.

### 5.3.4 Field-effect spin switch

In the previous section (Figure 5.3) we have demonstrated that spin transport in graphene is nearly independent on the electrostatic doping of the channel. Here, we perform similar measurements for the  $\text{WSe}_2$ /graphene heterostructure that is between electrodes 3&4 shown in Figure 5.12a. Measurement scheme of spin transport is schematically presented in Figure 5.14a. Red arrow indicates spin transport through graphene, while orange represents the alternative pathway through a monolayer semiconductor.

Main results of the measurements are shown in Figure 5.14b, where we plot magnetic field dependence of the subtracted non-local signals obtained at different gate voltages  $V_{\text{BG}}$  between -110 V and +40 V. Interestingly, we can observe spin signal only for moderately negative gate voltages. In the positive gate range as well as in the case of strongly negative voltages, non-local signal disappears and we cannot differentiate between parallel and anti-parallel magnetization configuration of electrodes.

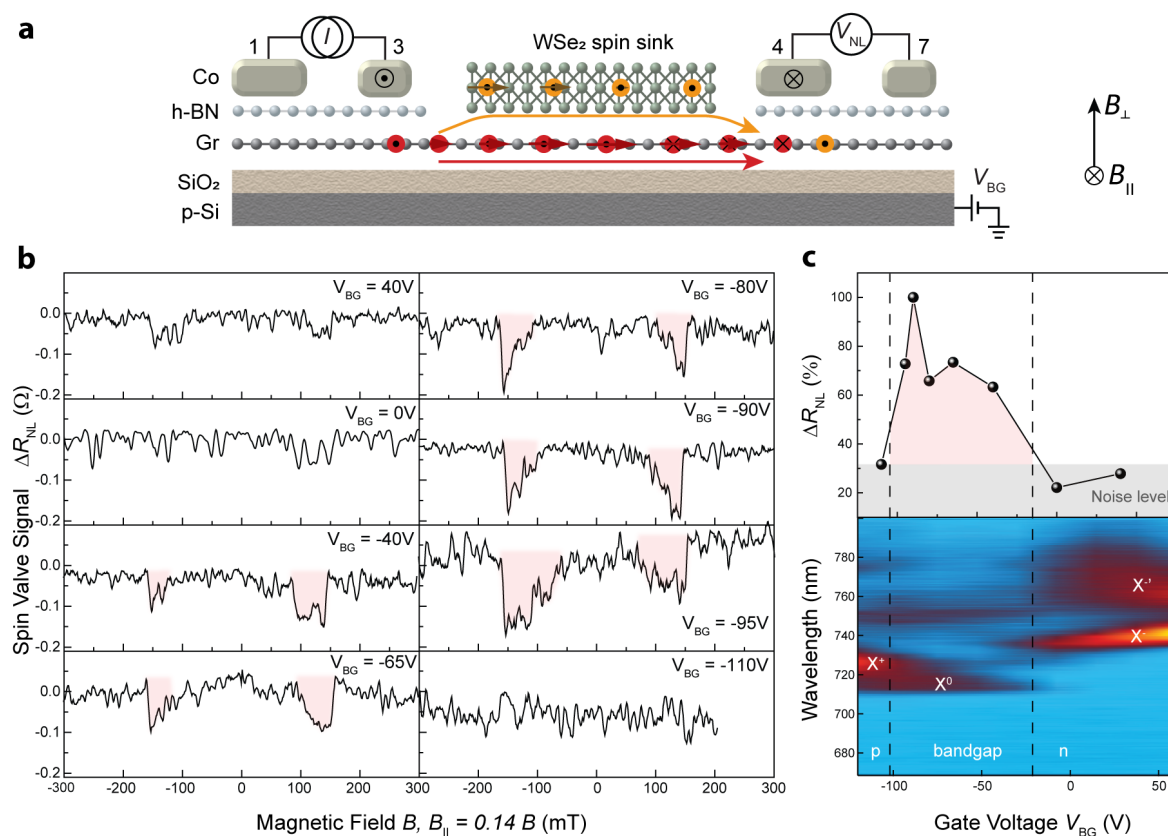


**Figure 5.14** – Field-effect spin switch in  $\text{WSe}_2$ /Gr heterostructure. (a) Schematic depiction of spin-valve measurements with electrodes numbered according to Figure 5.12a. (b) Field dependence of the non-local signal for the set of gate voltages. Observed spin-valve switching is highlighted with red shading. (c) Extracted spin signal as a function of the applied gate voltage (top) compared with PL spectra versus gate voltage map (bottom).

### 5.3. Modulation of spin transport in a graphene-WSe<sub>2</sub> heterostructure

---

We assign this field-effect control of the signal to the influence of the WSe<sub>2</sub> flake. Additional support for this explanation comes from comparison of the extracted non-local signal and PL versus gate map in Figure 5.14c. We can clearly see that the non-zero spin signal (up) coincide with the measured bandgap of WSe<sub>2</sub> (down). As we have already observed in Figure 5.12c, electrostatically doped WSe<sub>2</sub> acts as a parallel channel for carrier transport with much shorter in-plane spin coherence time compared to graphene, mainly due to a large SOC in the monolayer semiconductor. By shifting the Fermi level, we also reduce height of the Schottky barrier between compound layers, making the tunneling process more probable. Therefore, polarized carriers in graphene on their way towards the detector electrode hops to the superjacent WSe<sub>2</sub> where they experience fast decoherence that suppress the non-local signal. In other world, WSe<sub>2</sub> in the ON states (n- or p-doped) operates as a spin sink for the in-plane spins in graphene. This spin absorption process is schematically depicted in Figure 5.14b

We would like to note here that similar behaviour of MoS<sub>2</sub>/graphene spin valve was recently reported by Yan *et al.* [203] and field-effect spin switch behaviour in these structures was later demonstrated at room temperature by Dankert *et al.* [202].

We further investigate the observed field-effect spin switching using a different approach. In the Figure 5.15a we plot the non-local signal in the OFF (top,  $V_{BG} = -70$  V) and ON (bottom,  $V_{BG} = 0$  V) states of the WSe<sub>2</sub> monolayer. The signal was recorded for a large range of applied magnetic fields between -3 T and +3 T, that introduces a large but linear background signal.

In the OFF state, we clearly observe a sharp spike of the non-local signal near zero field, which is associated with the in-plane spin signal, namely Hanle precession of spins in the vertical field similarly to the Figure 5.13b. For clearer representation, we highlight it with blue shading. In contrast, in the OFF state this signal related to the in-plane spin transport vanishes due to absorption of spins in WSe<sub>2</sub>. We record the amplitude of this spike at zero field while sweeping the gate voltage for the parallel and anti-parallel contact magnetization configurations. The difference of these two signals is plotted in Figure 5.15b (up). It represents the non-local signal assigned to the in-plane spin transport. We see that it reproduces the measured signal from Figure 5.14c. Indeed, we obtain similar results when subtracting two curves of the non-local signal obtained at 0 T and 300 mT field, since the later one contains neither the in-plane nor the out-of-plane signal.

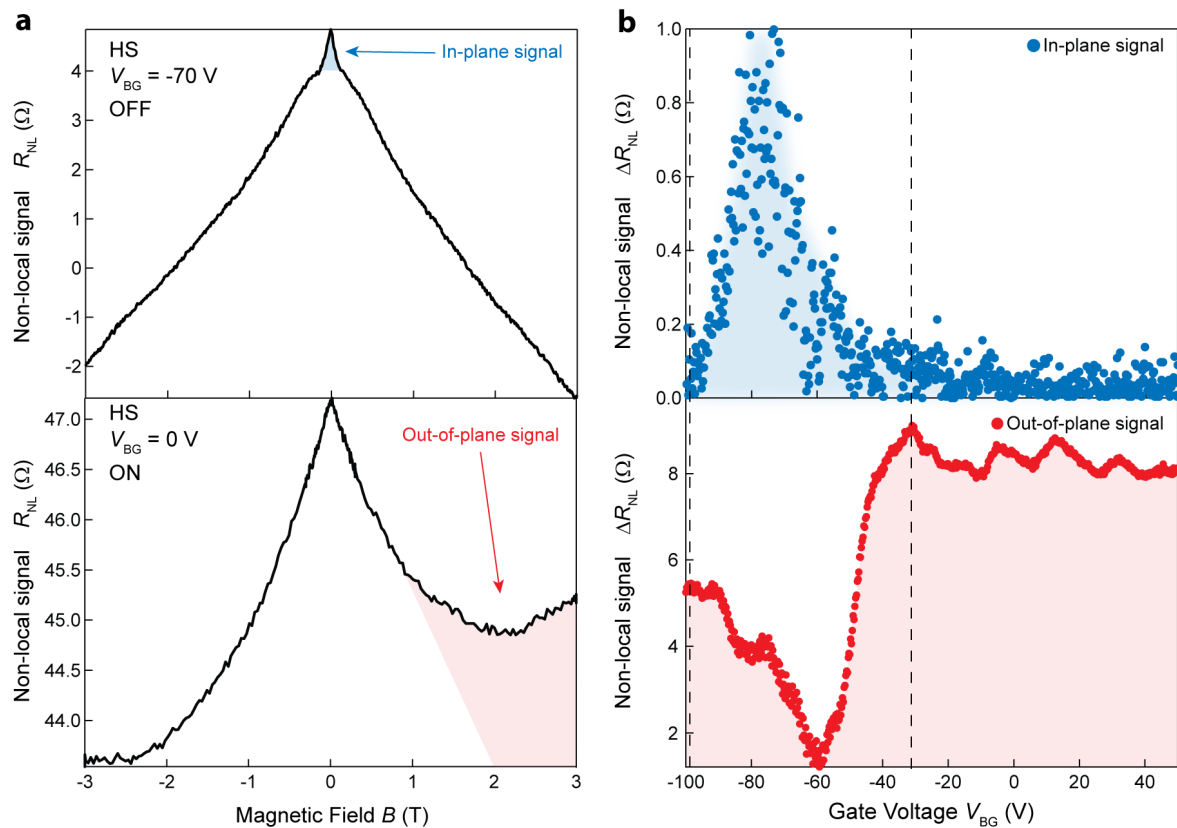


**Figure 5.15** – Gate dependent spin transport. (a) Non-local signal versus the external magnetic field measured at gate voltage of -70 V (top) and 0 V (bottom). (b) Extracted in-plane (top) and out-of-plane (bottom) spin-dependent signals as a function of gate voltage. Region between the two dashed lines represents the bandgap of the WSe<sub>2</sub> monolayer.

We also notice that the observed signal in the ON state of WSe<sub>2</sub> strongly deviates from the linear background at high fields. This is related to the out-of-plane spin transport since the electrodes are magnetized vertically. We highlight this part of the signal with red shading. In order to extract a meaningful value, we record the non-local signal obtained at 3 T and 300 mT while sweeping the gate voltage. As we mentioned above, the later one includes only the background signal, while the former one also contains the spin signal. We plot their difference in Figure 5.15b (bottom) that represents the efficiency of the out-of-plane spin transport. Interestingly, our results state that in case of out-of-plane polarization, the WSe<sub>2</sub> monolayer assists with the spin transport when in the ON state.

### 5.3.5 Optical spin switch

Finally, we perform optical modulation of the spin current in the graphene channel, that is schematically depicted in Figure 5.16a. For this, we circularly polarize light, employing combination of a linear polarizer and a quarter-wave plate. The incident beam is then

### 5.3. Modulation of spin transport in a graphene-WSe<sub>2</sub> heterostructure

focused on the heterostructure region, generating in the WSe<sub>2</sub> monolayer valley-polarized carriers with out-of-plane spins (shown in cartoon as orange bulbs with arrows). Similarly to the device for optical spin injection, photoexcited carriers tunnel into the underlying graphene layer, where in-plane spin polarized carriers are transported from injector to detector (represented as red spheres and arrows).

Figure 5.16b shows results of the measurements. We plot there the extracted spin valve signal from the non-local measurements as a function of the applied magnetic field, swept up. Comparing results obtained in dark measurements, with those, observed under the circularly polarized light, we can clearly see the effect of spin transport modulation. We assign the reduction of the measured signal to two effects. First, the photogating might effectively turn the WSe<sub>2</sub> flake into the ON state, that is known to act as a spin sink. Second reason for this modulation is induced scattering of transported in-plane spins on the optically injected out-of plane polarized carriers.

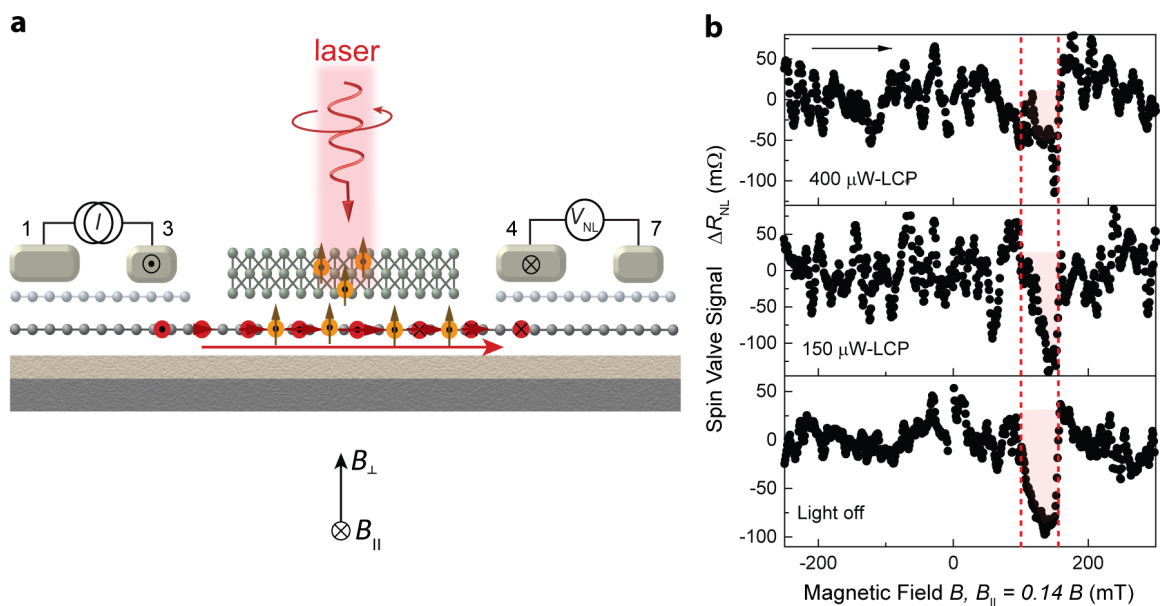


**Figure 5.16** – Optical spin switch. (a) Schematic illustration of the spin transport modulation by application of circularly polarized light. (b) Non local signal extracted for the spin-valve measurements versus applied magnetic field at different light intensities. Black arrow indicates the field sweep direction.

These are encouraging but preliminary results. More profound studies including theoretical calculation are required to further characterize and understand the mechanism involved in optical spin switching.

### 5.4 Conclusion and outlook

In this chapter we have demonstrated several important findings in the field of optospintronics, which include generation and control of spin polarized currents. Our approach was to combine superior spin properties of graphene with rich spin-valley physics of WSe<sub>2</sub> in an artificial heterostructure in order to realize new device concepts which are not possible in the isolated materials.

In the first part of the chapter we demonstrate optical spin injection and prove its valley origin by performing a meticulous set of control experiments. It appears to be a promising, non-destructive and less power consuming alternative to the electrical spin injection, which requires large currents in the range of micro-amperes. We note an independent report of the similar observation [205].

In the second part of the chapter we have realized a field-effect spin switch with a clear ON and OFF states, controlled solely by the gate voltage, with an ON/OFF ratio above 10. We assign it to a spin absorption functionality of a TMDC monolayer. We note reports with similar result [202, 203] and follow-up works [97, 206]. Even more interestingly, we have demonstrated here switching behaviour controlled by the incident light.

These results form the foundation of a newly emerging sub-field of 2D heterostructures which will be the key for the optospintronics functionality in graphene spintronic applications.

## 6 Excitonic devices

### 6.1 Introduction

Excitons, electrically neutral quasi-particles formed by bound electrons and holes, could be manipulated in solid-state systems as an alternative to the charge degree of freedom, providing a direct link between optical data transmission and electronic processing systems. While fast optical switches were already demonstrated [208, 209], the comparably large size [210, 211] of such devices strongly limits packing density. This can be overcome in excitonic devices, whose characteristic size is that of electronic FETs. The development of such excitonic devices has so far been hindered by the absence of a suitable system enabling room-temperature manipulation of excitons, strongly limiting the expansion of the field. Atomically thin semiconductors could open the way for wider studies and applications of excitonic devices in the academic as well as in the industrial sector [7].

Owing to their finite binding energy  $E_b$ , excitons can exist up to temperatures on the order of  $T \sim E_b/k_B$ , where  $k_B$  is the Boltzmann constant. In a conventional III-V semiconductor coupled quantum well (CQW) with a size of a few nanometres, a relatively small binding energy around 10 meV allows exciton observation only at cryogenic temperatures ( $<100$  K, ref. [9]). To reach higher temperatures, different materials are required. Towards this, systems with higher  $E_b$  (in the range of tens of meV) have more recently been explored, such as (Al,Ga)N/GaN [212] or ZnO [213].

Two-dimensional semiconductors such as transition metal dichalcogenides possess even larger exciton binding energies, which can exceed 500 meV in some cases due to strong quantum confinement and reduced dielectric screening [56, 214, 215]. This constitutes a considerable advantage over the systems based on III-V semiconductor and could allow the realization of excitonic devices operating at room temperature. While intralayer excitons in TMDCs have relatively small lifetimes ( $\tau \sim 10$  ps) [216, 217], the spatial separation of holes and electrons in interlayer excitons (IX) results in more than two orders of magnitude

longer lifetimes, well in the nanosecond-range [111, 112], that ensures long distance exciton diffusion. Moreover, the spatial separation of charges expands lifetime and creates a permanent dipole moment, enabling the manipulation of excitons by electric fields.

Valleytronics is another appealing alternative to conventional charge-based electronics which aims at encoding data in the valley degree of freedom [40], i.e. the information over which extreme of the conduction or valence band carriers are occupying. The ability to create and control valley-currents in solid state devices could therefore enable new paradigms for information processing. TMDCs are a promising platform for valleytronics, due to the presence of two inequivalent valleys with spin-valley locking [6] and a direct band gap[50, 51], which allows optical initialization and readout of the valley-state [71]. Potential progresses on the control of interlayer excitons in these materials could also offer an effective way to realize optoelectronic devices based on the valley degree of freedom.

In the first part of this chapter (Section 6.3), we employ the peculiar physics of TMDC monolayers to demonstrate a polarization switch based on interlayer excitons in a well-aligned van der Waals heterostructure. This device allows manipulating the helicity of light, as well as its wavelength and intensity, by application of electric and magnetic fields, which is very promising for future valleytronics applications. Our experimental results suggest formation of a moiré pattern that brightens spin-forbidden optical transition.

In the second part of the chapter (Section 6.4), we show the generation and transport over mesoscopic distances of valley-polarized excitons in a similar vdW system. Engineering of the interlayer coupling results in enhanced diffusion of valley-polarized excitons, which can be controlled and switched electrically. Furthermore, using electrostatic traps, we can increase exciton concentration by an order of magnitude, reaching densities on the order of  $10^{12} \text{ cm}^{-2}$ , opening the route to achieving a coherent quantum state of valley-polarized excitons via Bose-Einstein condensation.

In the last part of the chapter (Section 6.5), we exploit large binding energies and long lifetimes of interlayer excitons hosted in van der Waals heterostructures in order to demonstrate the ability to manipulate exciton dynamics at room temperature.

We note that the order in which results are presented in this chapter does not follow the chronological order of the performed experiments, which can be tracked by the publication dates of the articles mentioned below. Instead, we present here our results in a way to have a clear and effective pedagogical output, starting with an introduction to the rich physics of interlayer excitons, followed by their employment in practical devices at low- and room-temperatures.



This work was performed in a close and extremely fruitful collaboration between Dmitrii Unuchek and Alberto Ciarrocchi, who are equally contributing authors of the letter "Room-temperature electrical control of exciton flux in a van der Waals heterostructure" published in *Nature*, **2018**, volume 560, pp: 340–344 (DOI:10.1038/s41586-018-0357-y); of the article "Polarization switching and electrical control of interlayer excitons in two-dimensional van der Waals heterostructures", published in *Nature Photonics*, **2019**, volume 13, pp: 131–136 (DOI:10.1038/s41566-018-0325-y); and of the submitted yet unpublished manuscript titled as "Valley polarized exciton currents in a van der Waals heterostructure". We note that there is a considerable overlap between these works [113, 163] and the current chapter.

## 6.2 State-of-the-art

Before going into the details of the experiments and their results, we would like to briefly introduce the reader to the pre-existing works on excitonic devices. Indeed there was a significant progress achieved by the research groups of A. C. Gossard, L. V. Butov and others, who extensively studied interlayer excitons in the coupled quantum wells based on epitaxially grown III-V semiconductors.

Electrostatic control of interlayer excitons, as well as the realization of excitonic integrated circuit was first demonstrated at cryogenic temperatures by A. High *et al.* [8, 218]. The excitonic device in an ON and OFF states is presented in Figure 6.1a, showing clear modulation of the exciton propagation with application of a control gate voltage. The potential difference between source and drain contacts promotes exciton diffusion, similarly to a conventional FET device. Further improvement of the semiconductor heterostructure allowed them to achieve device operation temperatures as high as 100 K [9], limited by the binding energy of the interlayer excitons.

Interestingly, the same group also demonstrated proof of concept devices, where an excitonic switch was not only pumped but also controlled by the incident light, showing promise for all-optical excitonic routers. Another important achievement was done by directing exciton propagation through ramp potential profiles [219, 220, 221], as well as in moving lattices by employing surface acoustic waves created by a set of AC voltages [222]. Operation of the latter device is shown in Figure 6.1b. In contrast to the static potentials, here excitons remains in a local energy minima, which propagates away from the excitation spot, providing constant velocity to the excitons and ensuring their transport over long distances.

For more examples of different excitonic devices and potential applications for interlayer excitons, the reader might refer to the review article by L. V. Butov [7].

## Chapter 6. Excitonic devices

As we mentioned before, the small binding energy of interlayer excitons in conventional bulk semiconductor systems limiting their practical application appears to be the major motivation for developing similar devices based on van der Waals heterostructures with tightly-bounded excitons. Consequentially, interlayer excitons in different TMDC-based heterobilayers attracted a lot of attention and were extensively studied in recent years [111, 223, 224, 225]. Even more, creation and observation of the diffusion of valley-polarized excitons was recently reported by P. Rivera *et al.* [114], as shown in Figure 6.1c. However no progress has been made so far in controlling the transport of these quasi-particles, which is a crucial point for excitonic and valleytronic implementations. In this chapter we will try to address the lack of progress in this direction.

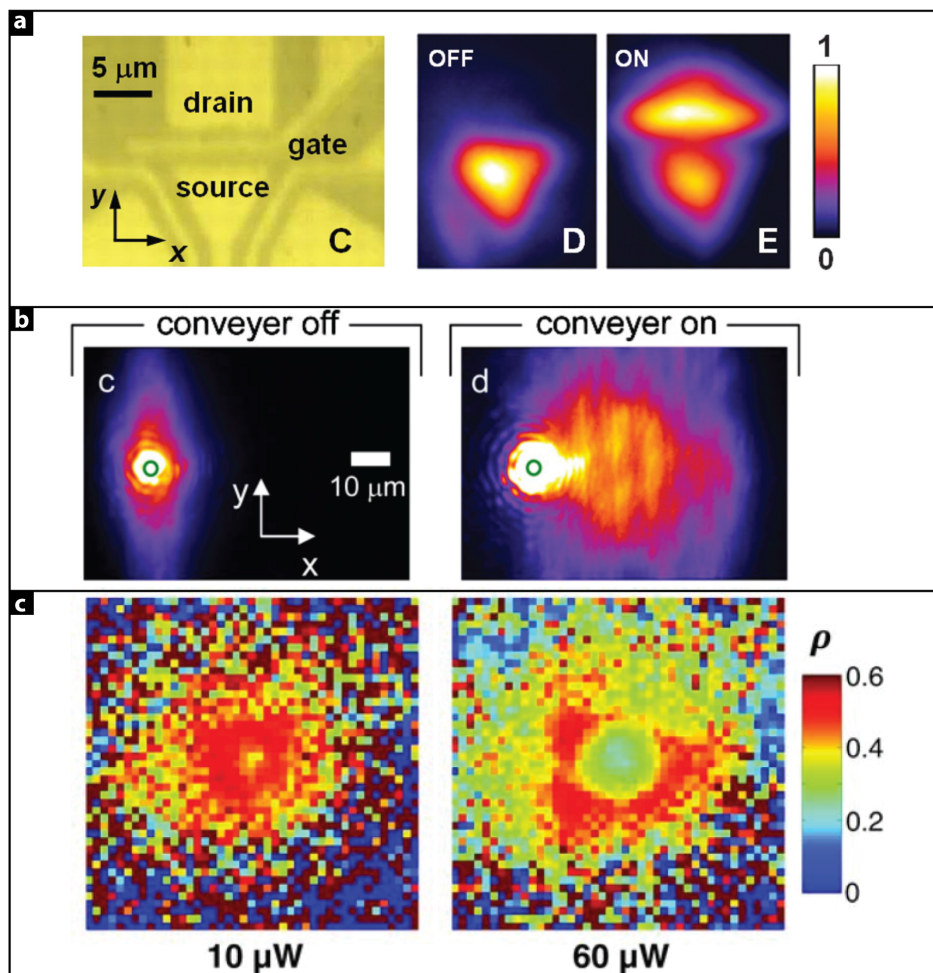


**Figure 6.1** – State-of-the-art excitonic devices. (a) Operation of an excitonic transistor based on III-V semiconductor system. Adapted from ref.[8] with permission of AAAS. (b) Realization of electrostatic conveyers for interlayer excitons in a coupled quantum wells. Adapted from ref.[222] with permission of APS. (c) Diffusion of valley-polarized interlayer exciton gas in a MoSe<sub>2</sub>/WSe<sub>2</sub> heterostructure. Adapted from ref.[114] with permission of AAAS.

## 6.3 Electrical control of interlayer excitons

### 6.3.1 Introduction

Long-living interlayer excitons in van der Waals heterostructures based on transition metal dichalcogenides, together with unique spin-valley physics, make them promising for next-generation photonic and valleytronic devices. While the emission characteristics of interlayer excitons have been already studied [111, 114], efficient manipulation of their valley-state, a necessary requirement for information encoding, is still lacking.

For a full control of such manipulation, different strategies could be employed, including the creation of a moiré potential. 2D van der Waals heterostructures possess unique physics which arises from the moiré patterns that form when different crystals with lattice mismatch are brought in contact. This opens an entirely new direction for research because the moiré pattern can dramatically change the material properties, as experimentally demonstrated for graphene on h-BN [103, 106]. This approach has also been recently considered for exciton-moiré interactions. In particular, the prediction of a moiré potential-induced brightening of forbidden optical transitions [120, 121] and its electrostatic tunability could enable complete switching of the helicity state (i.e. realization of a logic NOT gate), crucial for logic operations.

In this section, we demonstrate comprehensive electrical control of interlayer excitons in a WSe<sub>2</sub>/MoSe<sub>2</sub> heterostructure. Encapsulation of our well-aligned stack with hexagonal boron nitride allows us to resolve two separate narrow interlayer transitions with opposite helicities under circularly polarized excitation, either preserving or reversing the polarization of incoming light. By electrically controlling their relative intensities, we realize a polarization switch with tunable emission intensity and wavelength. Finally, we demonstrate large Zeeman shifts of these two transitions upon application of an external magnetic field. These results are interpreted within the picture of moiré-induced brightening of forbidden optical transitions. The ability to control the polarization of interlayer excitons is a step forward towards the manipulation of the valley degree-of-freedom in realistic device applications.

### 6.3.2 Optical characterization of interlayer excitons

Prior to the demonstration of the device operation we first characterize a fabricated heterostructure based on single layers of MoSe<sub>2</sub> and WSe<sub>2</sub>, encapsulated in atomically flat h-BN. We choose these semiconducting materials as they pose superior optical properties and a relatively small lattice mismatch of  $\sim 0.1\%$  [120]. We note that all the measurements presented here were carried out at 4.2 K, unless stated otherwise.

Micro-photoluminescence spectra

As we have already discussed in the previous chapters, encapsulating 2D materials in h-BN crystals using dry method technique with consecutive annealing at high vacuum results in structures of a very high quality. Such h-BN-encapsulation of the heterostructure allows us to observe bright and sharp photoluminescence peaks from individual monolayers, with full-width half maxima (FWHM) between 7 and 15 meV. We can see it in Figures 6.2a,b, where photoluminescence spectra of h-BN-encapsulated monolayers are plotted.

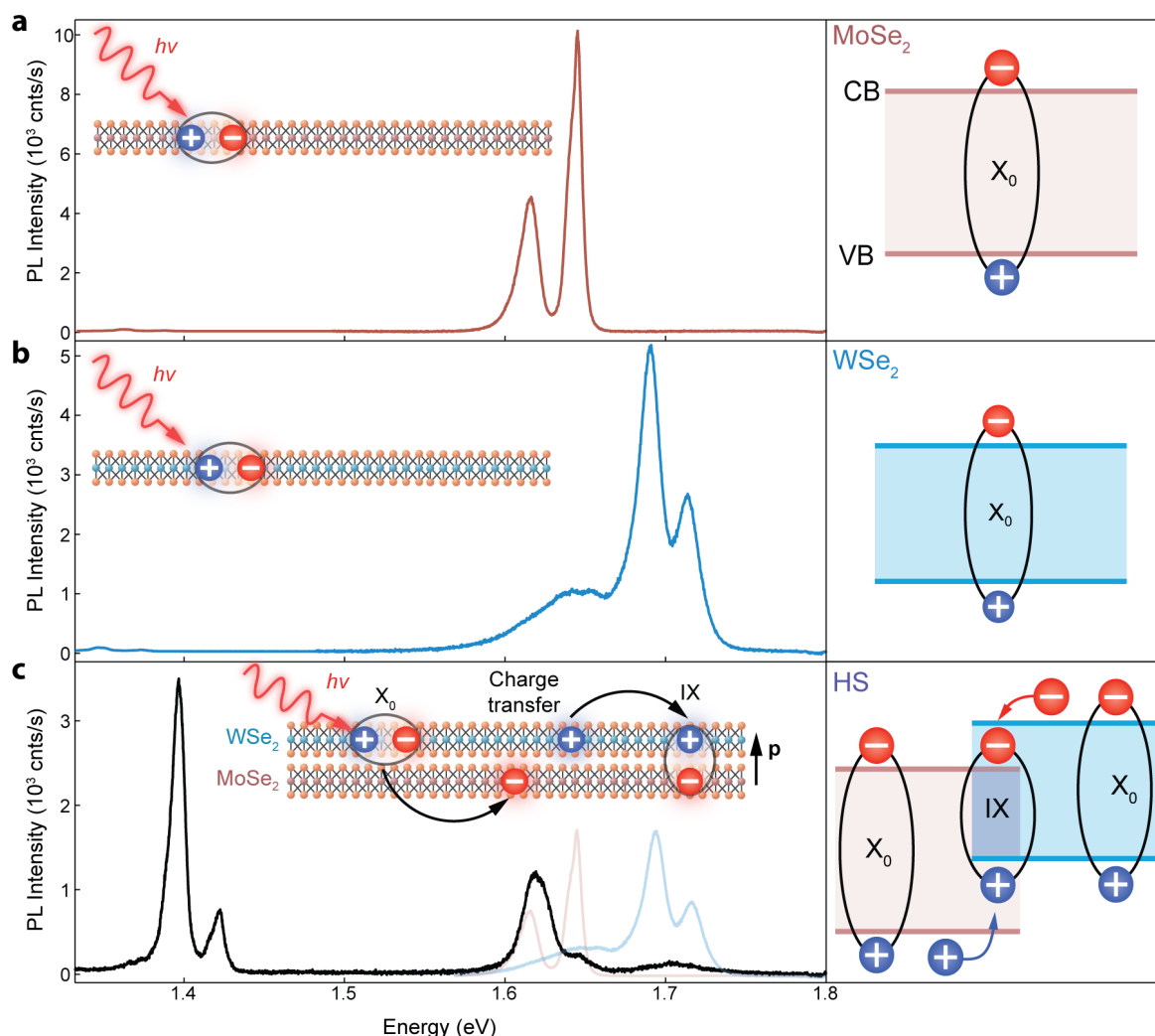


**Figure 6.2** – Optical characterization of a WSe<sub>2</sub>/MoSe<sub>2</sub> heterostructure. PL spectra obtained from individual monolayers of MoSe<sub>2</sub> (a) and WSe<sub>2</sub> (b), and their heterostructure (c). PL spectrum from the heterostructure shows quenched emission from MoSe<sub>2</sub> and WSe<sub>2</sub>, but also a lower energy interlayer feature. Insets show intralayer excitons and interlayer exciton formation, which includes ultrafast charge transfer between constituent layers. Right panels show band diagrams of monolayers and their heterostructure with type-II band alignment.

### 6.3. Electrical control of interlayer excitons

Figure 6.2a shows bright emission of MoSe<sub>2</sub> monolayer at low temperature since lowest energy transition is allowed by optical selection rules. Two optical resonances observed in the plot are related to the neutral and charged excitons, that we will study later in more details. Compared to MoSe<sub>2</sub>, spin splitting of the conduction band in monolayer WSe<sub>2</sub> has opposite sign. Therefore, the lowest energy transition requires a spin flip and thereby is forbidden, resulting in a less intense PL emission at low temperature (Figure 6.2b). This is also why we start observing the whole zoo of optical resonances in WSe<sub>2</sub>, including neutral exciton, charged excitons, biexcitons and defect-bound excitons.

We now turn our attention from individual monolayers to their heterostructure, Figure 6.2c. In the heterobilayer region, we observe strong quenching of the intralayer excitonic peaks, together with the appearance of low-energy emission around 1.4 eV. We attribute this optical transition to interlayer exciton formation, which is schematically represented in the inset of Figure 6.2c. Due to the relative band alignment of constituent semiconductors [108], stacking MoSe<sub>2</sub> and WSe<sub>2</sub> on top of each other results in the creation of a type-II heterostructure, represented in the right part of Figure 6.2c. The conduction band minimum of the resulting structure is in MoSe<sub>2</sub>, while the valence band maximum corresponds to WSe<sub>2</sub>. Thus, the effective band gap of such a structure is slightly reduced compared to the isolated monolayers, and we observe light emission at lower energy. Upon the photon absorption, photoexcited carriers experience ultrafast charge transfer and the resulting interlayer exciton extends over the two layers with electrons in MoSe<sub>2</sub> and holes in WSe<sub>2</sub>.

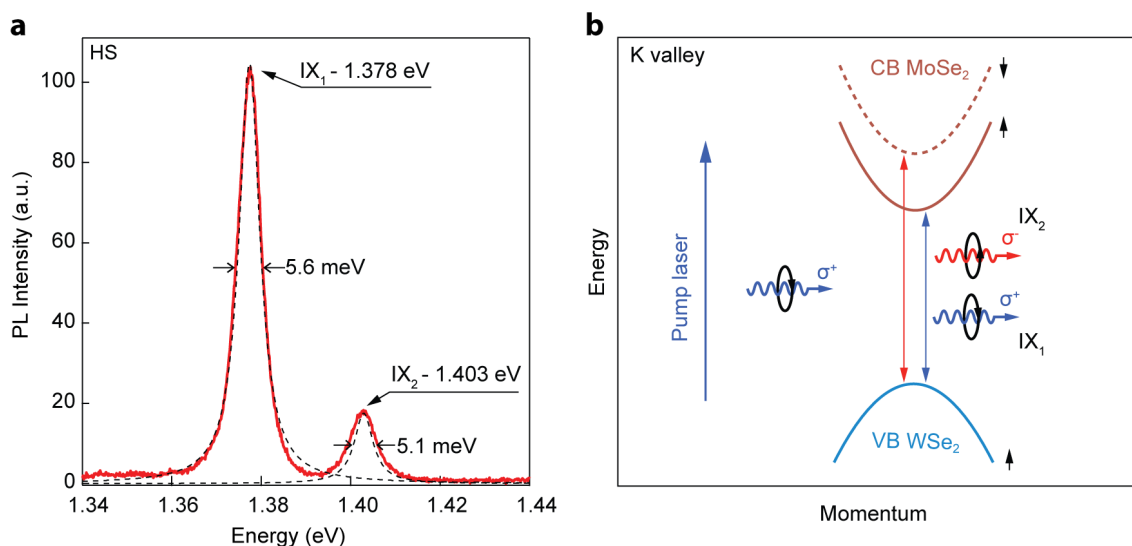


**Figure 6.3** – Interlayer exciton doublet. (a) Detail of the PL spectrum from a typical heterobilayer, with numerical fits for the emission peaks. (b) Schematic of the spin-conserving (IX<sub>1</sub>) and spin-flipping (IX<sub>2</sub>) transitions in the K valley for the structure under consideration and their coupling with circularly-polarized light.

While low energy emission is expected for a system with type-II band alignment, closer look at the interlayer emission reveals novel and unforeseen observations. In Figure 6.3a we clearly resolve two distinct emission peaks, with FWHM around 5 meV and an energy separation of 25 meV between them. We will refer to these lower- and higher-energy features as  $IX_1$  and  $IX_2$  respectively. Interestingly, separation value corresponds to the  $MoSe_2$  conduction band spin-splitting [226]. Therefore, as we will be discussing in details later, we attribute this doublet to a spin-conserving and a spin-flipping transition (Figure 6.3b). The latter is normally dark (forbidden) in monolayers, but can be brightened by the moiré pattern in our heterobilayer [121] due to selection rules dictated by the local atomic registry. Searching for a confirmation to such doublet explanation, we perform following power and temperature dependent studies.

### Power dependency

Figure 6.4 shows the measured dependence of the PL emission intensity on the incident laser power. We note that at low incident powers both peaks show linear power dependency, with no change in their spectral profiles down to 5 nW. At higher power (above 200  $\mu W$ ), the lower energy peak  $IX_2$  shows saturation. Also, both peaks broaden and experience blue shift which we assign to the sample heating and exciton repulsion, respectively. Excitation power higher than 1 mW was not used to avoid potential damage to the sample.

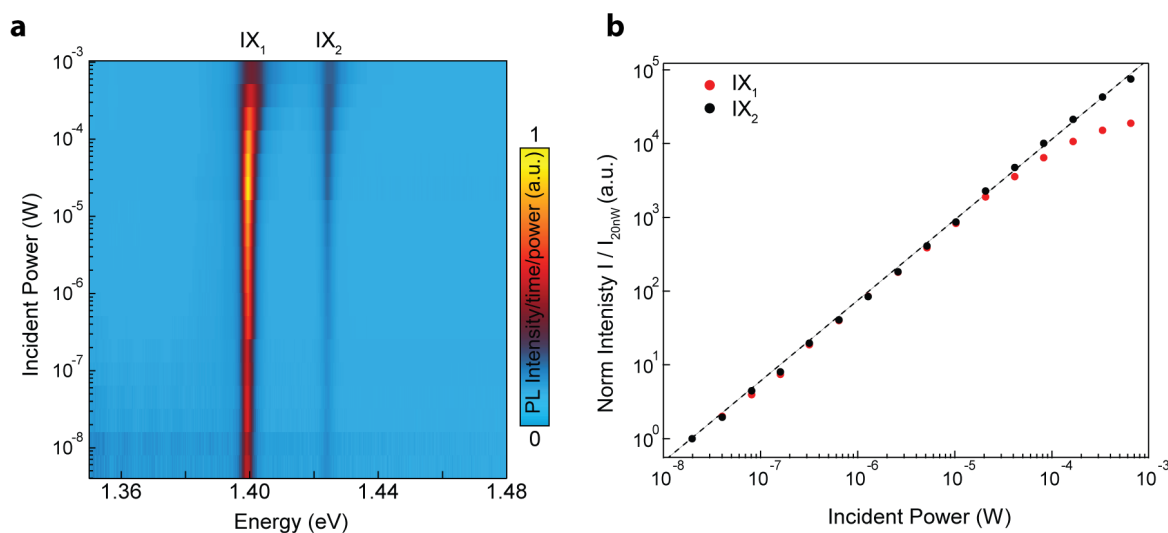


**Figure 6.4** – Excitation power dependence of interlayer exciton emission. (a) Power dependency of the PL spectra intensity normalized by acquisition time and incident power. (b) Emission intensity of  $IX_1$  (red) and  $IX_2$  (black) as a function of the excitation power of the 647 nm laser used. The normalized intensity is the number of counts per second normalized by the emission intensity at 20 nW excitation power.

We note that while the earliest reports on this type of heterostructures showed saturating PL with power as low as  $0.5 \mu\text{W}$  [111], in recent reports of encapsulated  $\text{WSe}_2/\text{MoSe}_2$  higher values are reported, as in ref. [227] The enhanced efficiency could be related to the reduced linewidth, indication of clean and homogeneous interfaces.

### Temperature dependency

The evolution of the doublet spectra with increasing temperature is shown in Figure 6.5a. We clearly observe, a transfer of intensity from  $\text{IX}_1$  to  $\text{IX}_2$  and then suppression of both peaks, together with red shift and broadening of their emission. The two peaks eventually merge, so that we cannot distinguish between them above 200 K. This behaviour is similar to the  $\text{MoSe}_2$  neutral-charged exciton doublet [58] and resembles what one would expect from a three-level system with thermal suppression of lower energy emission. Extracted values of peaks intensities and positions are shown in Figures 6.5 b,c.

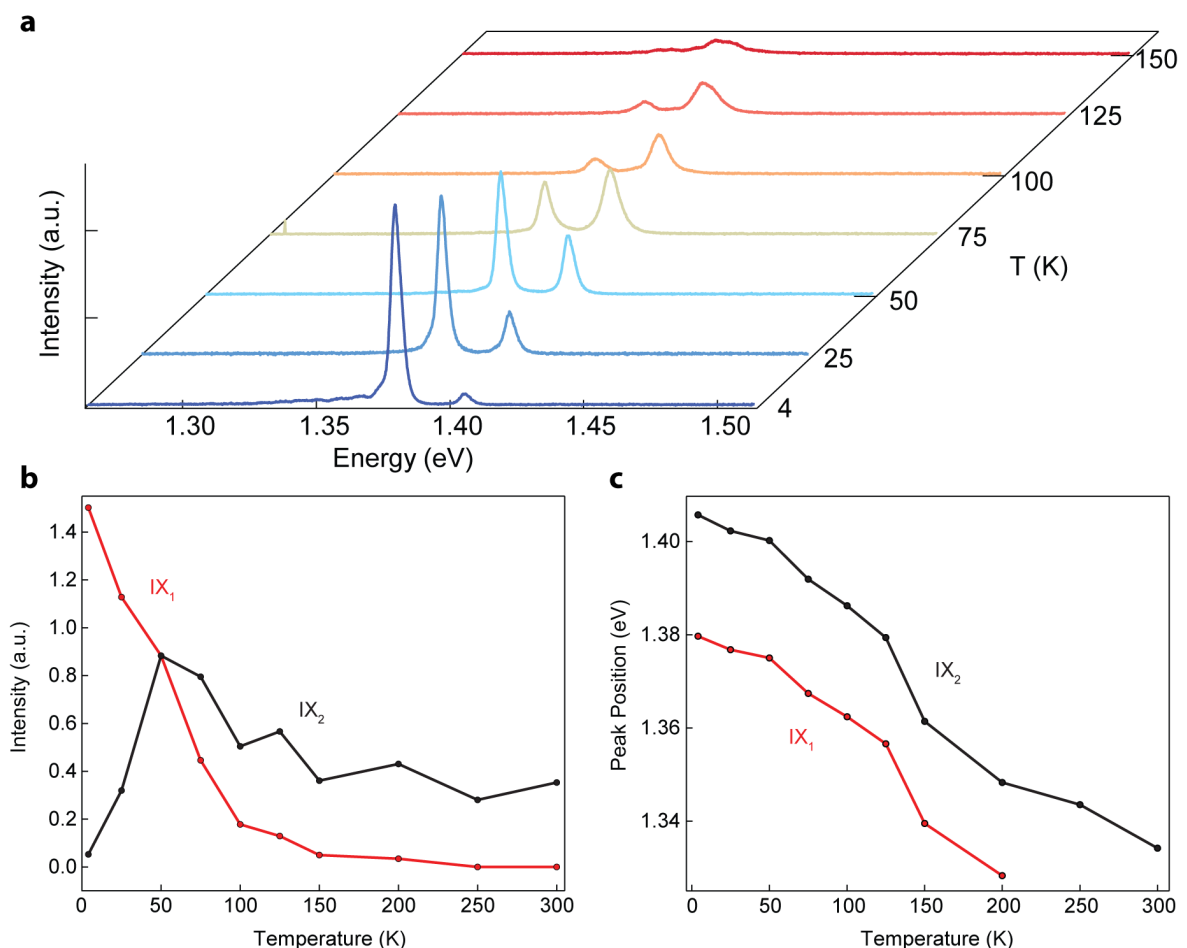


**Figure 6.5** – Temperature dependence of interlayer exciton emission. (a) Interlayer exciton emission spectra as a function of temperature. Plots of the emission intensity (b) and energy (c) of  $\text{IX}_1$  (red) and  $\text{IX}_2$  (black) for different temperatures.

### Structure quality

Indeed, the observation of interlayer excitons relies on strong coupling between layers and therefore requires structures of a high quality. Importantly, we could observe interlayer emission only in a well-aligned heterostructures, which complicates device fabrication even further. We therefore take this opportunity to express our gratitude to Alberto Ciarrocchi for his hard work. We appreciate his efforts in optimization of transfer recipes and in fabrication of structures of excellent quality, without which none of the presented results would be possible. We note that we were among the first groups to resolve and report the interlayer exciton doublet. We believe that such high resolution is achieved as a result of improved heterostructure quality, in agreement with Hanbicki *et al.* [227].

### 6.3.3 Electrical tuning of interlayer excitons

We now focus our attention to the electrostatic tuning of interlayer exciton properties. For this, we first need a device which would allow us to independently control electric field and carrier concentration with optical access to the structure. Such a device is schematically presented in Figure 6.6a.

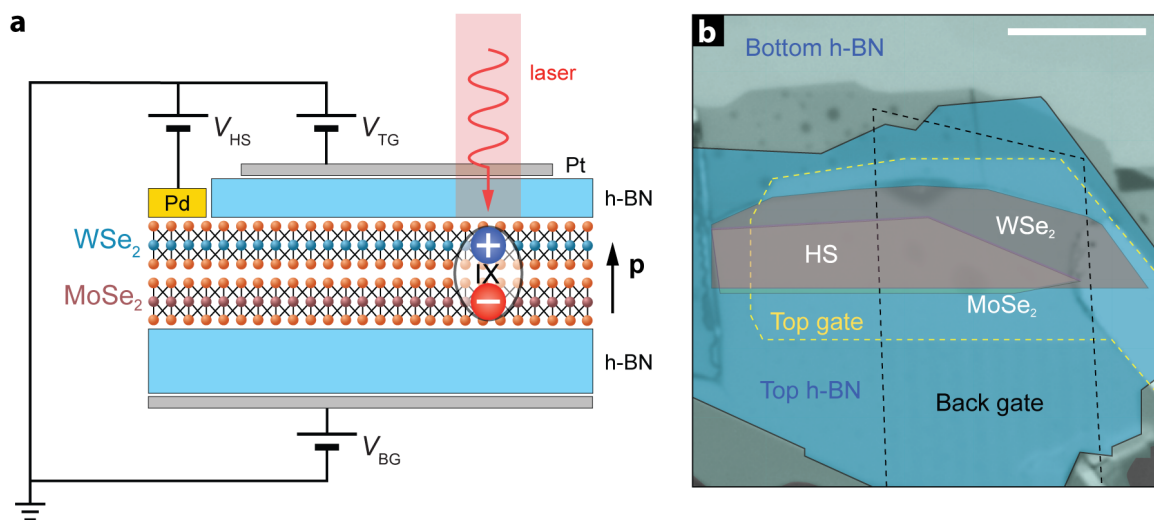


**Figure 6.6** – Dual-gate device. (a) Schematic depiction of the device structure and artistic representation of the interlayer exciton with its dipole moment **p**. (b) Optical image of the device. The pink area indicates the heterobilayer area, yellow region is MoSe<sub>2</sub> and violet represents the WSe<sub>2</sub> monolayer. The cyan areas show top and bottom h-BN crystals. Yellow dashed line outline the top gate made of 8-nm-thick platinum layer. Scale bar is 10  $\mu\text{m}$ .



#### Device Fabrication and Characterization

Our device consists of a contacted  $\text{WSe}_2/\text{MoSe}_2$  heterobilayer encapsulated in h-BN, with a graphene bottom gate and a top transparent Pt gate. Few-layer graphene flakes for the bottom gate were obtained by exfoliation from graphite (*NGS*) on Si/SiO<sub>2</sub> substrates and patterned in the desired shape by e-beam lithography and oxygen plasma etching. The heterostructure was then fabricated using polymer-assisted transfer of mono- and few-layer flakes of h-BN,  $\text{WSe}_2$  and  $\text{MoSe}_2$  (*HQ Graphene*). The stack was realized using the dry-transfer technique described in Chapter 3, with an additional attention to the minimization of the stacking angle between monolayers. For this, a homemade software was used to measure the angle between the flake edges, with a precision limited by the resolution of optical images ( $< 1^\circ$ ). The alignment angle is later confirmed with measurements of second harmonic generation (SHG) which shows strong anisotropy and therefore can be linked to the crystal orientation. Device fabrication continued with evaporation of 8 nm Pt that forms the transparent top gate and is completed with evaporation of 80 nm Pd for contacting the heterostructure and top/bottom gates.

This device architecture allows us to perform optical measurements on the sample while applying different voltages at the top and bottom gates, as well as at the global Si back-gate, and gives us the possibility to independently control the doping level and the transverse electric field. Figure 6.6b shows the optical microscopy image of one of our completed heterostructure devices.

We start device characterization with performing angle-dependent second harmonic generation measurements (Figure 6.7a) and carrying out photoluminescence scans (6.7b-d). Comparing SHG signals obtained from  $\text{MoSe}_2$  and  $\text{WSe}_2$  monolayers, we conclude that they have similar crystal orientation (within experimental error). Spatial distribution of emission at 1.62 eV (intralayer exciton of  $\text{MoSe}_2$ ) coincide with the exposed area of the  $\text{MoSe}_2$  monolayer. Similarly, tracking light at 1.67 eV, we observe emission at the exposed  $\text{WSe}_2$  layer. Meanwhile, in the heterobilayer area we detect several orders of magnitude quenching of intralayer  $\text{MoSe}_2$  and  $\text{WSe}_2$  emission, indicating efficient interlayer coupling with ultrafast charge hopping of a time scale comparable or lower than intralayer exciton recombination ( $\sim 10$ ps) [216, 217].

Instead, in the heterostructure area we observe quite a uniform emission at the energies associated with interlayer exciton (1.32-1.48 eV). We observe dark spots in the PL map, which coincide with transfer-related bubbles seen in the optical image. These areas with trapped polymer residuals prevent coupling between layers, and therefore interlayer excitons are not forming there.

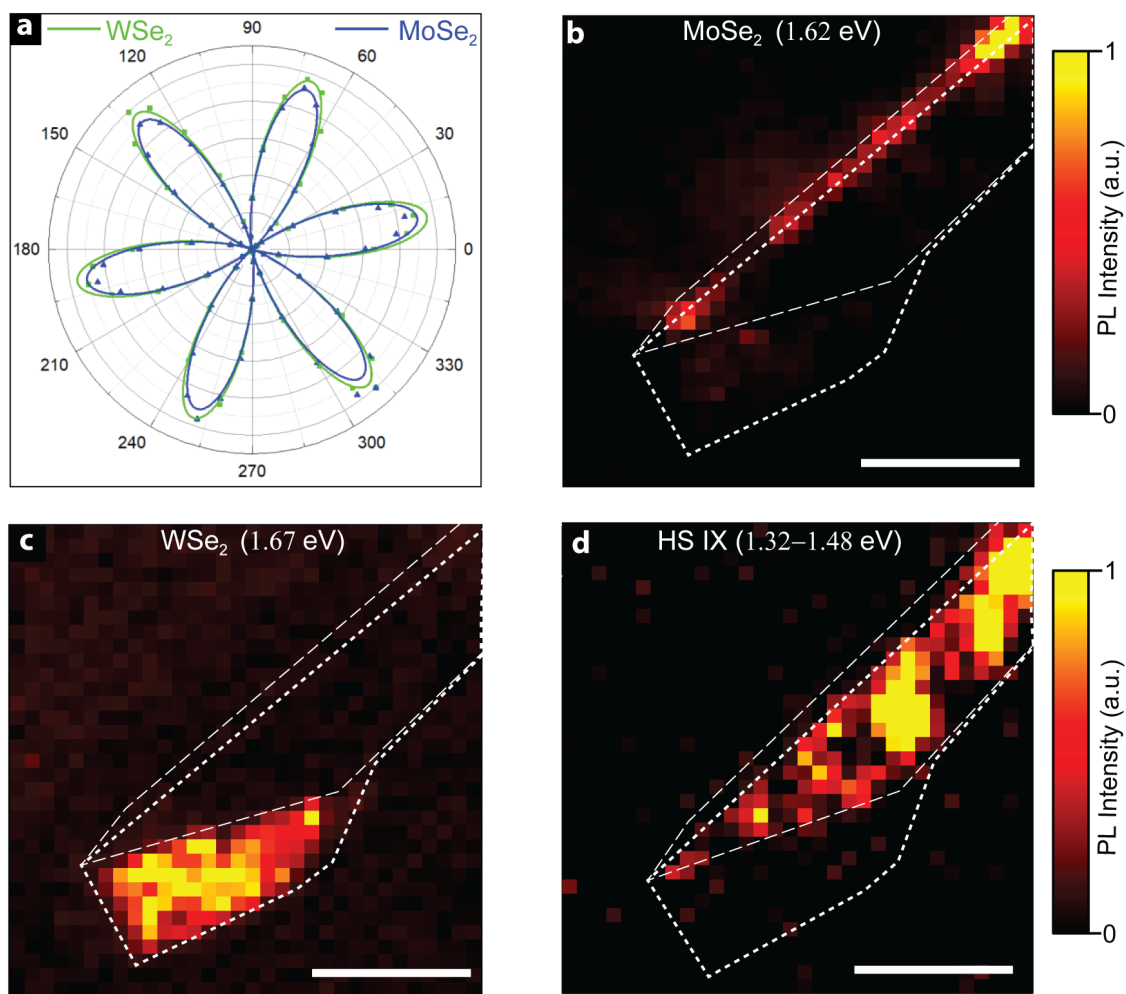


**Figure 6.7** – Device characterization. (a) Angle-dependent second harmonic generation signal. (b,c) Spatial maps of photoluminescence intensity at 765 nm (1.62 eV), 740 nm (1.67 eV) emission wavelengths, corresponding to MoSe<sub>2</sub>, WSe<sub>2</sub> intralayer excitonic resonances. Photoluminescence is quenched in the HS area due to efficient charge transfer. (d) Spatial distribution of the interlayer exciton, integrated in the 840-940 nm wavelength range (1.32-1.48 eV). White dashed lines represent edges of constituent crystals. Scale bar is 5 μm for every panel.

### Stark Effect

Prior to manipulating the polarization of the two transitions, we first characterize our device and demonstrate intensity and energy manipulation, which will enable the polarization switching in future. As we already mentioned, stacking MoSe<sub>2</sub> and WSe<sub>2</sub> on top of each other results in the creation of a van der Waals heterostructure with type-II band alignment. Since electrons and holes are confined in separate layers, interlayer excitons have a defined dipole moment  $\mathbf{p}$  perpendicular to the heterostructure plane. This allows us to linearly tune their energy with an external electric field  $\mathbf{E}$  along the dipole axis:  $\delta\mathcal{E} \sim -\mathbf{p} \cdot \mathbf{E}$ . To this

### 6.3. Electrical control of interlayer excitons

end, we apply a vertical field at constant carrier concentration. As shown in Figure 6.8, a modulation of the IX emission position  $\delta\mathcal{E} \sim 138$  meV is obtained, from 1.34 to 1.47 eV. A linear fit of the energy shift yields a tuning rate of  $\sim 500$  meV $\cdot$ nm $\cdot$ V $^{-1}$ , from which we obtain a qualitative estimation of the dipole size  $d \sim \delta\mathcal{E}/qE \sim 0.5$  nm (where  $q$  is the elementary charge). Indeed we have characterized other structures with more careful electric field estimation, which revealed a dipole size of 0.6 nm, compatible with the expected interlayer spacing [228].

While this semiclassical dipole picture is oversimplified, it captures the main observations. Indeed, we also observe second order effects in the Stark shift. For positive electric fields, the decrease in energy of the dipole (charges are more separated) results in reduced recombination rate and a slightly larger Stark effect. On the contrary, when the exciton energy is increased, and the overlap between the electron and the hole is larger, we observe a brighter PL and smaller energy shift.

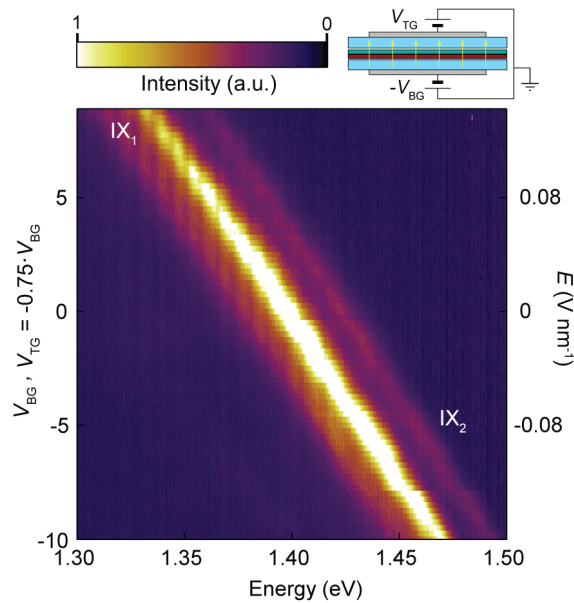


**Figure 6.8** – Linear Stark effect. Map of PL emission as a function of applied gate voltages  $V_{BG}$  when sweeping at constant doping,  $V_{TG} = -V_{BG}$ . Calculated electric field in the vertical direction is indicated in the right axis. Schematics on the top demonstrates measurement scheme where the electric field is applied *via* symmetric biasing of top and bottom gates.

The energy shift presented here is due to the linear Stark effect, which plays a crucial role in next sections where we will realize excitonic switches which rely on the modulation of energy landscape of interlayer excitons diffusing in the sample.

### Gating

If we ground the heterobilayer while applying voltage to the top gate, we can achieve control over the relative intensities of the two peaks by changing the charge carrier concentration. We show the results of this electrostatic doping in Figure 6.9a. For negative values of  $V_{TG}$ , the intensity of the  $IX_2$  peak is first reduced, then suppressed around -4 V. At the same time,  $IX_1$  becomes broader and starts to dominate the spectrum. On the contrary, at high positive voltages, we observe that  $IX_2$  becomes the dominant emission feature, while  $IX_1$  decreases in intensity and becomes quenched at higher electron density.

In contrast with previous reports [111], our dual-gated configuration allows us to independently control exciton energy or relative peak intensity, while keeping the other property fixed. Using the dual gating geometry we can also achieve a much higher carrier concentration without damaging a gate dielectric by electrostatic breakdown. Figure 6.9b shows PL spectra evolution at very high electron concentration, where we can observe inversion of the doublet and complete suppression of the lower energy emission  $IX_1$ .

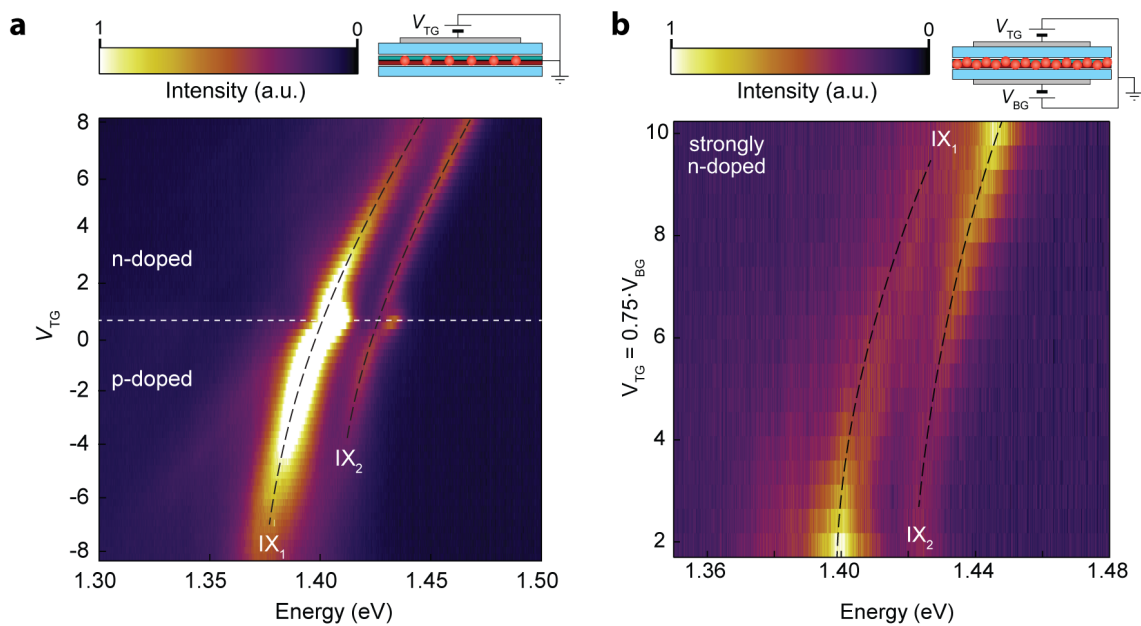


**Figure 6.9** – Effect of electron concentration on interlayer exciton emission. (a) Map of PL emission as a function of gate voltage when electrostatically doping the device. (b) PL map as a function of the applied voltages to the top and bottom gates in the dual-gate configuration. Here  $V_{TG} = 0.75 \cdot V_{BG}$  to minimize the displacement field

Observation of the inversion supports the proposed picture of the double transition, that we believe originates from the conduction band splitting. An increase of the electron doping level leads to filling of the lower conduction band and therefore more optically excited transitions involve the higher energy band, thus increasing the intensity of  $IX_2$ . This

interpretation is also supported by the observation of a faster increase in the intensity of  $IX_2$  with increasing laser power in the absence of electrostatic doping. Further confirmation of this filling mechanism is the temperature dependence of the two transitions, with  $IX_2$  becoming stronger as the bands are thermally populated.

#### **Charged interlayer excitons**

In the center of Figure 6.9a we observe an increase in the emission intensity accompanied with a sudden blueshift. To further elucidate the origin of this feature, we carry out additional experiments.

The device geometry allows precise control over the doping of individual layers within the heterobilayer, and therefore we can perform gate dependent measurements of the  $WSe_2$  monolayer (Figure 6.10a),  $MoSe_2$  monolayer (Figure 6.10c) and HS independently (Figure 6.10e). For each of the monolayers we can determine the charge neutrality point. In case of the  $WSe_2$  layer, we observe the strongest intensity of the neutral exciton emission at  $V_{BG} = V_{TG} = 0.5 V$  (Figure 6.10b), implying slight p-doping of the source crystal. On the contrary, the neutral exciton of the  $MoSe_2$  reaches a maximum when all the gates are grounded, as seen in Figure 6.10d. Therefore, the  $MoSe_2$  crystal is an intrinsic semiconductor with the Fermi level positioned at the center of the bandgap. Relative doping of the constituent layers supports the picture of the type-II band alignment of the heterostructure.

Knowing the positions of the exciton resonances, we perform differential reflectance measurements on the heterobilayer area. The resulting map of the reflectance spectra as a function of the applied gate voltage is presented in Figure 6.10f. In the center part of map, with gate voltage in the range between 0 V and +1 V, we observe two features associated with the monolayers. Now, if we dope our structure with electrons, the  $MoSe_2$  feature disappears, and we observe only one line. We assign this effect to the filling of  $MoSe_2$  with electrons due to charge transfer (electrons are preferably hosted in  $MoSe_2$ ). Similarly, by p-doping we switch off the reflectance feature of  $WSe_2$  (bottom part of map in Figure 6.10f).

Therefore we assign the central region ( $0 V < V_G < +1 V$ ) to the intrinsic heterostructure. This gate range coincides with the observation of the narrow, bright and blue shifted interlayer doublet in Figures 6.10e and 6.9a, which we attribute to the "neutral" interlayer exciton. Introduction of free charges to the system either reduces interaction between excitons and therefore redshifts emission, or leads to formation of charged excitonic species with a binding energy of  $\sim 10$  meV.

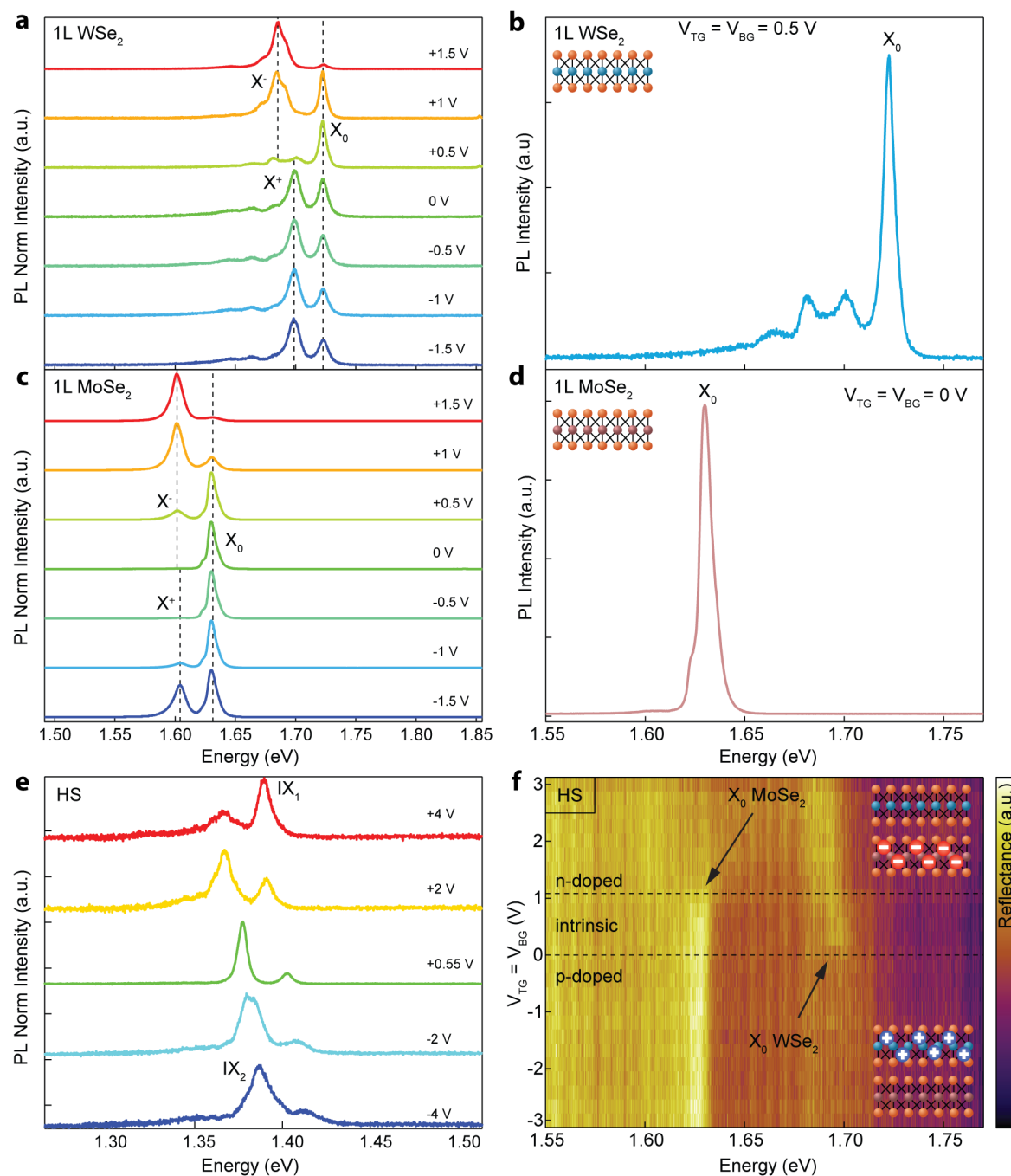


**Figure 6.10** – Effect of gating on the device optical properties. Gate dependence of the PL spectra acquired on WSe<sub>2</sub> (a), MoSe<sub>2</sub> monolayers (c), and on heterostructure (e). Lowest charge carrier concentration reveals strongest neutral exciton emission in WSe<sub>2</sub> (b) and MoSe<sub>2</sub> (d) monolayers. (f) Gate dependency map of differential reflection spectra from the heterobilayer region. P-doped (n-doped) sample shows only the reflection feature associated with the neutral exciton of MoSe<sub>2</sub> (WSe<sub>2</sub>), while intrinsic region demonstrates both. This is the direct consequence of the charge transfer associated with type-II band alignment. Symmetrical dual-gating is used:  $V_{BG} = V_{TG}$ .

### 6.3.4 Electrical control of polarization state

Excitonic valleytronic devices should have an optical input and output, with the information encoded in the polarization of light. Consequently, selectively addressing the valley degree of freedom of excitons with polarized light is critically important. To this end, we characterize the polarization-resolved photoluminescence from our heterostructure.

#### Polarization response

Similarly to the previous sections, we start with the characterization of isolated monolayers. In Figure 6.11 we compare PL spectra associated with circularly polarized left ( $\sigma^-$ , red) and right ( $\sigma^+$ , blue) emitted light under different excitation. As expected, the emission intensity for positive and negative helicity are the same in the case of linear excitation. The situation changes with circularly polarized excitation.

As have been reported by other groups [229], the degree of circular polarization (DCP) is virtually zero in the case of the MoSe<sub>2</sub> neutral exciton, Figure 6.11a. Poor valley index preservation by MoSe<sub>2</sub> is normally explained by the phonon-assisted intervalley scattering [230, 231]. We can observe that polarization conservation of the charged exciton is slightly higher than neutral, but still on the order of few percents.

In contrast to MoSe<sub>2</sub>, in Figure 6.11b we observe robust conservation of the incident polarization from monolayer WSe<sub>2</sub>, which demonstrates a degree of polarization exceeding 20 % [232]. Indeed, using resonant excitation at 720 nm we can surpass 60% polarization of the emitted light. We calculate the degree of circular polarization using the following equation:

$$\rho = \frac{I(\sigma^+) - I(\sigma^-)}{I(\sigma^+) + I(\sigma^-)} \quad (6.1)$$

where  $I(\sigma^+)$  and  $I(\sigma^-)$  are emission intensities of right- and left-circularly polarized light.

We now turn our attention to the heterobilayer region. As shown earlier, our clean interfaces in h-BN-encapsulated heterostructures allow us to resolve the two different optical transitions, IX<sub>1</sub> and IX<sub>2</sub>. In Figure 6.11c, we observe that IX<sub>1</sub> and IX<sub>2</sub> have opposite behaviour under circularly polarized excitation, with polarization values up to 27% and -25% respectively, in agreement with a recent report [227]. Such behaviour agrees with what is expected from a spin-conserving (-flipping) transition between the WSe<sub>2</sub> VB maximum and the lower (upper) CB minimum of MoSe<sub>2</sub>. As we discuss later in the text, in WSe<sub>2</sub>/MoSe<sub>2</sub> both these transitions are allowed, with opposite polarizations and comparable intensities, for excitons localized in some energy minima of the moiré pattern.

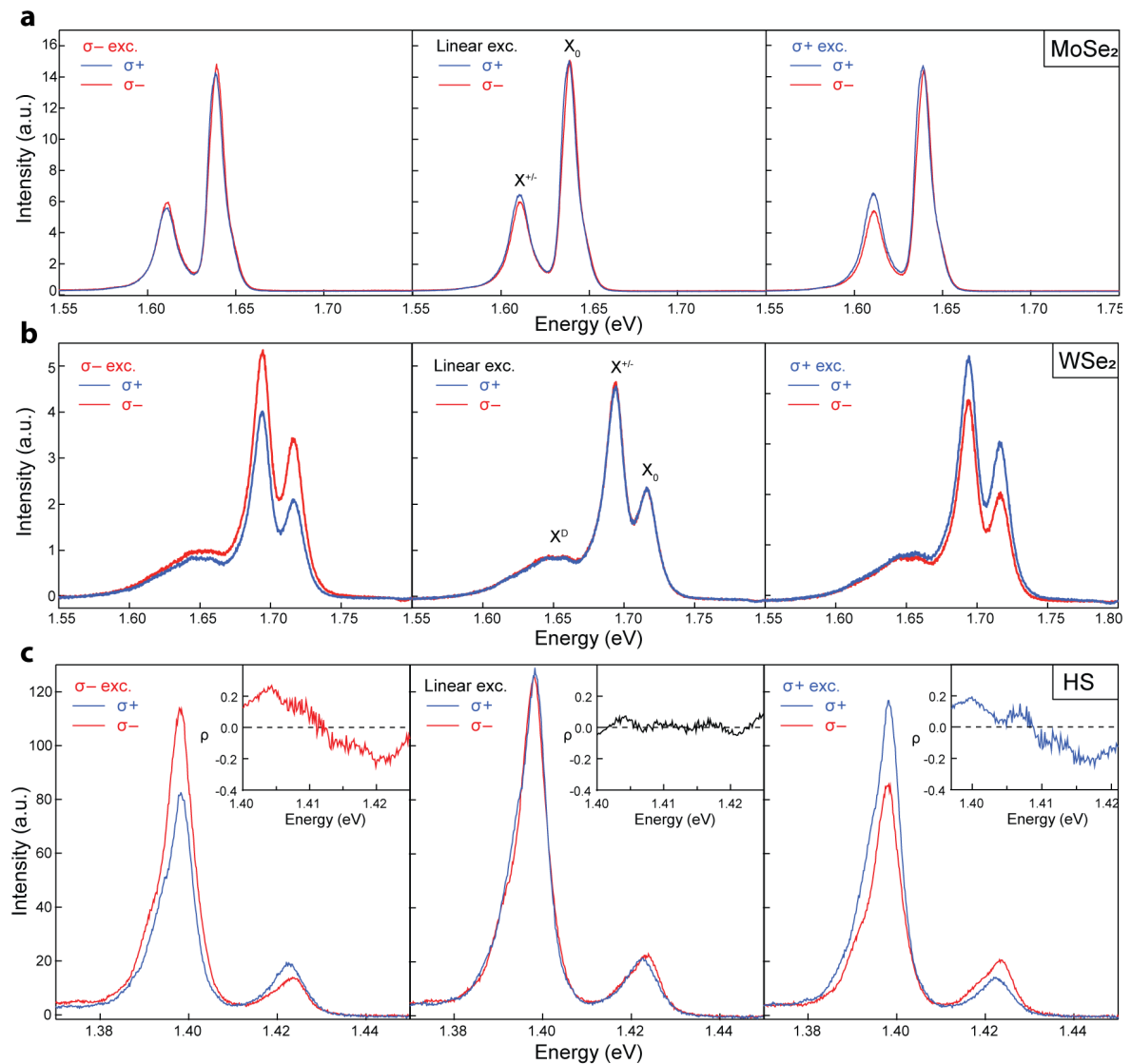


**Figure 6.11** – Polarization-resolved PL from monolayer MoSe<sub>2</sub> and WSe<sub>2</sub>, and from their heterostructure. PL spectra showing left- and right-circularly polarized emission components (red and blue respectively) for the case of linear, left- and right-polarized excitation in monolayer MoSe<sub>2</sub> (a) and WSe<sub>2</sub> (b). (c)  $\mu$ PL spectra for left and right emission from the heterobilayer in the case of the same excitation polarization as in (a) and (b). Insets show the calculated polarization degree  $\rho = (I(\sigma^+) - I(\sigma^-)) / (I(\sigma^+) + I(\sigma^-))$ . We note that the use of excitation wavelength at resonance with the monolayer excitonic peaks could increase this figure considerably.

### Electrostatic tuning of polarization

We now focus on the central point of our experiment, by combining the gate modulation of the two excitonic peaks with their unique polarization dependence. As we have seen, strong electron doping enhances IX<sub>2</sub>, while at small or negative gate voltages IX<sub>1</sub> dominates.



### 6.3. Electrical control of interlayer excitons

Thanks to the opposite polarization of the two peaks, this allows us to change the device operation between a polarization-inverting and polarization-preserving regime.

First, we simultaneously record two maps of photoluminescence as a function of the applied gate voltage for the left and right emission light, as shown in Figure 6.12. We then deduce polarization from these maps, and present the corresponding results in Figure 6.13a: both excitonic peaks are clearly visible in the upper (positive) half of the map, with opposite helicity. In Figure 6.13c (left), the spectra corresponding to  $V_{TG} = 0$  V is presented. Due to the higher intensity of the  $IX_1$  peak, the total polarization of the signal  $\Delta I_{RL}$  (net polarization  $\delta I_{RL} = I_R - I_L$  integrated over the frequency spectrum) is positive (i.e., of the same sign as the excitation). This is even more clearly visible in the right panel of Figure 6.13c, where the spatial image of the exciton polarization acquired on the CCD is shown. For strong electron doping the situation is reversed, as seen on Figure 6.13b. In this configuration,  $IX_2$  emission is stronger, resulting in an overall negative value of  $\Delta I_{RL}$ , and our device operates here as a polarization inverter.

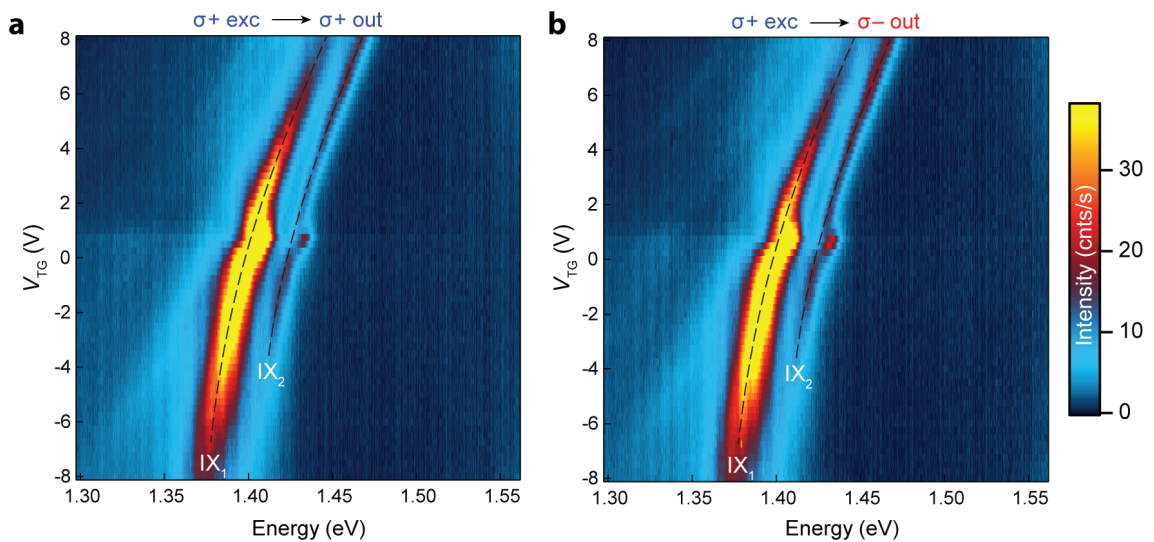


**Figure 6.12** – Polarization resolved PL gate maps. PL spectra showing right (a) and left (b) circularly polarized emission components as a function of applied top-gate voltage, when heterostructure is pumped with right-circularly-polarized light.

Even more interesting is the behaviour in the p-doped region (i.e. for the application of negative gate voltage). As seen before, the higher energy  $IX_2$  peak is suppressed at negative gate voltages, so one would expect the device to strongly preserve the helicity when electrostatically p-doped. On the contrary,  $IX_1$  polarization behaviour is now completely reversed, while  $IX_2$  shows a vanishing circular polarization (see lower half of Figure 6.13 a). This is a result of the alteration of the moiré potential induced by electrostatic doping, which shifts the exciton localization from one to another type of local minima in the moiré pattern,

with a different local symmetry and thus different light coupling rules (see later). In Figure 6.13d we show the spectra recorded for a strong hole-doped case, demonstrating that the polarization-inverting emission is indeed coming from the lower-energy  $IX_1$ . Just as in the case of positive gate voltage, we obtain a globally negative polarization (right panel).

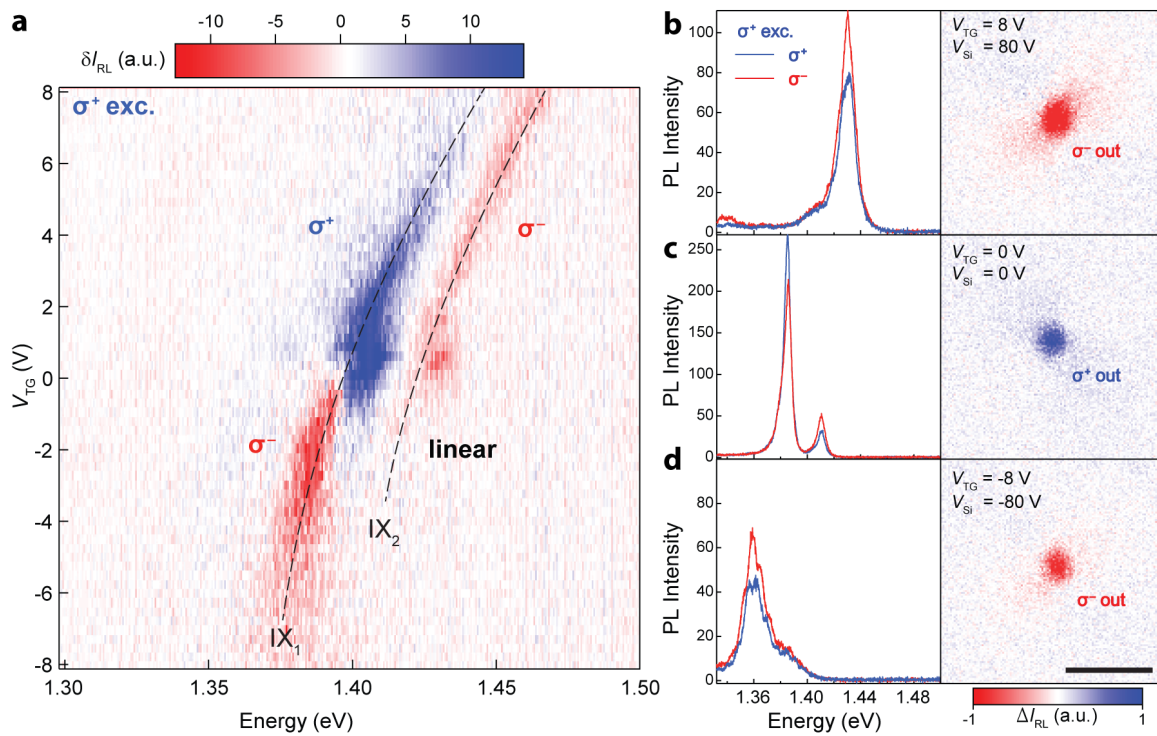


**Figure 6.13** – Electrical control of polarization. (a)  $\mu$ PL map of the difference between right- and left-circularly polarized (CP) emission intensities when the device is pumped with right-CP light:  $\delta I_{RL}(\lambda) = I_R(\lambda) - I_L(\lambda)$  as a function of the gate voltage  $V_{TG}$  in single-gate configuration. The dashed lines serve as guides for the eye, and are the same as in Figures 6.12a,b and 6.9. (b-d) Details of device operation in dual-gating mode. Left panel: PL spectra for  $V_{TG} = +8$  V, 0 V and -8 V. Right panel: spatial imaging of  $\Delta I_{RL}$  in the corresponding gate configurations. The silicon back-gate is kept at  $V_{Si} = 10 \cdot V_{TG}$  to reach higher doping densities and further enhance the effect. Scale bar is 5  $\mu$ m.

Based on our results, we can conclude that the contrasting reports in recent literature on the polarization dependence of PL in this system (observation of conservation [233], reversal [234] or both [227] for the light helicity) could be due to different levels of natural doping occurring in the samples, over which there was previously no full control, as well as to variable amounts of disorder. Indeed, using the same device structure we could reliably reproduce our observations in multiple successive devices, obtaining qualitatively similar results.

### Polarization switch

To characterize the switching operation in more detail, we study the evolution of  $\Delta I_{RL}$  (polarization  $\delta I_{RL}(\lambda)$  integrated over the spectrum) as a function of the applied gate voltage, as shown in 6.14. For top gate voltages higher than 5 V, we have negative  $\Delta I_{RL}$ , as a result of  $IX_2$  being the strongest transition (as in Figure 6.9). For gate values between 5 V and 0 V, the lower energy interlayer transition dominates, giving positive  $\Delta I_{RL}$ , i.e. preserving the input polarization.

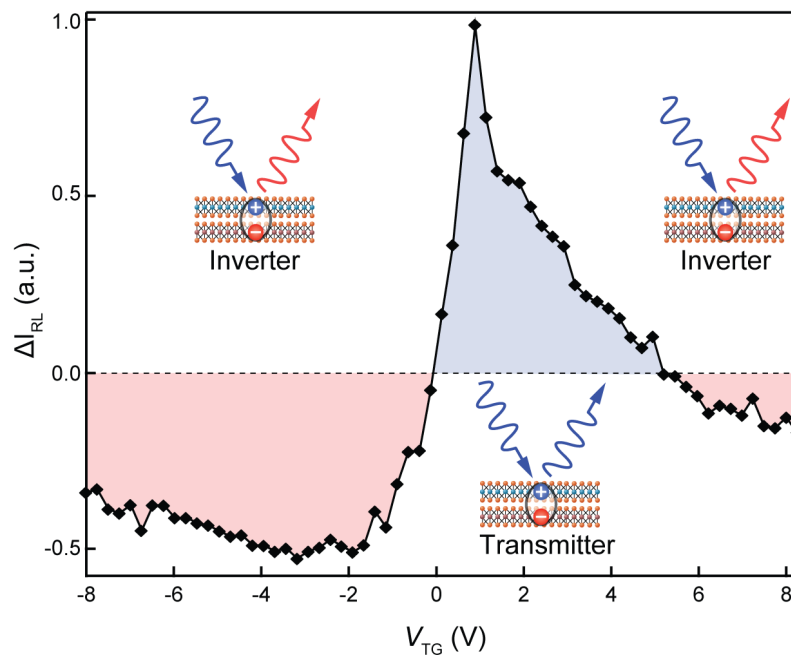


**Figure 6.14** – Polarization switching action. Plot of the difference between right- and left-circularly polarized (CP) emission intensities when the device is pumped with right-CP light:  $\Delta I_{RL} = I_R - I_L$  as a function of the gate voltage  $V_{TG}$ . The resulting polarization is obtained by integrating over the entire measured emission spectrum.

It is interesting to note that within this region, application of gate voltage also allows us to modulate the amplitude of the effect, with a maximum around  $V_{TG} = 1$  V. We then see a sharp transition between the two logic states happening around zero gate voltage, with a small required switching voltage around  $\pm 1$  V. This threshold value depends on the gate capacitance, and could thus be considerably reduced by engineering thinner dielectric layers to obtain even higher efficiency. For  $V_{TG}$  below 0 V, we have an inverting action, due to the polarization reversal of  $IX_1$ .

### 6.3.5 Interlayer excitons in magnetic field

Since the valley pseudospin is associated with the magnetic moment, it is also possible to manipulate it with an external magnetic field [232].

#### Observation of Zeeman splitting

For better understanding of magnetic field interaction with the band structure of TMDCs, we first consider isolated monolayers in a vertical magnetic field.

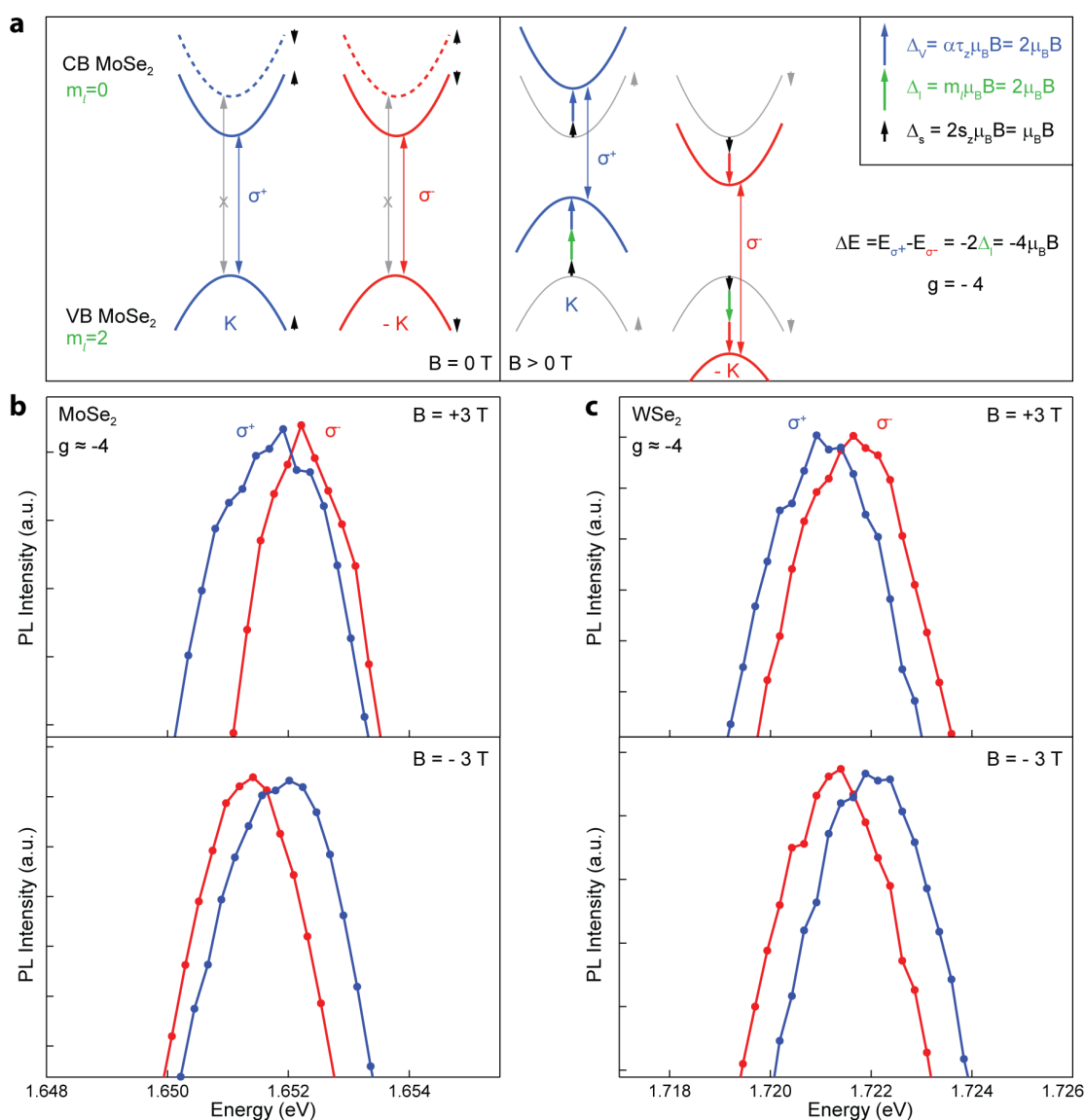


**Figure 6.15** – Effect of magnetic field on intralayer excitons. (a) Schematic explanation of energy shifts revealing a g-factor of -4. (b) and (c) PL spectra splitting of monolayer MoSe<sub>2</sub> and WSe<sub>2</sub> in a magnetic field.

Generally speaking, energy shift in a magnetic field appears due to the interaction of the field with the magnetic moment of carriers. Since electronic bands can be characterized with their spin, valley (which acts as a pseudospin) and orbital moment, we can deduce corresponding contributions to the energy shifts, including spin, valley and orbital Zeeman shifts (indicated as black, blue and green arrows in the Figure 6.15a). However, as optical transitions are allowed only within the same valley (momentum conservation) and between bands with the same spin orientation (spin conservation), contributions of spin and valley Zeeman effects cancel out. In contrast, conduction ( $m_l = 0$ ) and valence ( $m_l = 2$ ) bands have different values of orbital magnetic moment  $m_l$ , and therefore the orbital component of the Zeeman shift ( $\Delta_l = 2\mu_B B$ ) is the only contribution that modifies the energy of optical transitions in the case of the TMDC monolayer. Moreover, this contribution has different signs in K and -K valleys, which couple to  $\sigma^+$  and  $\sigma^-$  correspondingly. Namely, the transitions in K valley shrink by  $2\mu_B B$ , while in -K their energy increases by the the same value. Thereby, upon application of magnetic field, one would observe splitting of the PL emission for the two opposite light helicities by  $\Delta E = -4\mu_B B$ . This splitting efficiently reveals a g-factor of -4, that we experimentally observe in Figure 6.15b,c.

Indeed, to gain more insight into our doublet transition of interlayer exciton, the extraction of the effective g-factor could prove useful. Towards this, we perform polarization-resolved photoluminescence measurements in a magnetic field  $B$ , between -3 T and +3 T. The results are shown in Figure 6.16. Similarly to the monolayer case shown above, the  $\sigma^-$  and  $\sigma^+$  components of the PL peaks experience opposite energy shifts, with a splitting  $\Delta E^{IX} = E_{\sigma^+}^{IX} - E_{\sigma^-}^{IX}$  proportional to applied field  $B$ . Interestingly, the same polarization component for each peak undergoes energy shifts slightly different in amplitude (see Figure 6.16). For a more quantitative analysis of the data, we extract peak positions using a similar technique as in ref. [232]. In Figure 6.16b we show the calculated shift for  $IX_1$  and  $IX_2$ :  $\Delta E^{IX1} = E_{\sigma^+}^{IX1} - E_{\sigma^-}^{IX1}$ ,  $\Delta E^{IX2} = E_{\sigma^+}^{IX2} - E_{\sigma^-}^{IX2}$ , together with their linear fit. Using the Zeeman energy shift  $\Delta E = g_{\text{eff}}\mu_B B$ , where  $\mu_B$  is the Bohr magneton and  $B$  is the applied field, we calculate effective g-factors  $g_{\text{eff}}^{IX1} = -8.5 \pm 1.5$  and  $g_{\text{eff}}^{IX2} = 7.1 \pm 1.6$ . Our result is considerably larger than what observed above and previously reported for monolayer TMDCs (normally around -4), in line with recent results on similar heterostructures [224]. However, in the latter case, larger g-factors were reported for a single interlayer transition and attributed to a large valley magnetic moment contribution caused by the AB-stacking of layers. Even within a relatively small magnetic field range, thanks to the large g-factor, we can clearly see that the two peaks show a different behaviour. The opposite sign of g-factors comes from the fact that, for the same valley, the emission is  $\sigma^+$ - or  $\sigma^-$ -polarized for  $IX_1$  and  $IX_2$ . Therefore, the measured shift  $\Delta E^{IX} = E_{\sigma^+}^{IX} - E_{\sigma^-}^{IX}$  will have opposite sign for the two transitions, even if the valley shifts are in the same direction. In addition to this, one would expect two different g-factors, as a transition between spin-up and spin-down bands ( $IX_2$ ) will have non-zero contribution to the Zeeman shift from the spin magnetic

moment:  $\Delta_s = 2s_z\mu_B B$ , while the spin-conserving transition ( $IX_1$ ) will not, as we explain in details below.

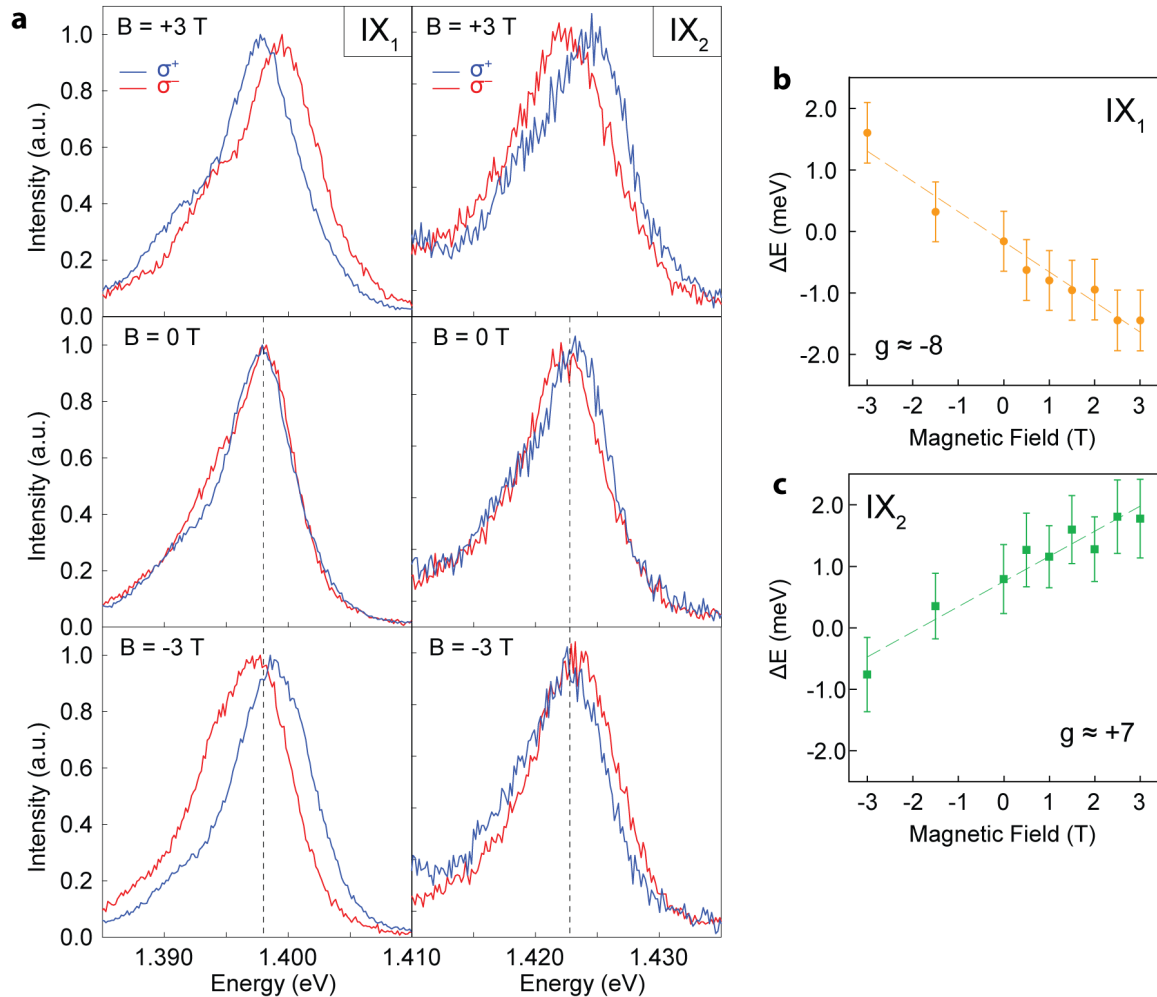


**Figure 6.16** – Effect of magnetic field on interlayer excitons. (a) PL spectra for applied magnetic fields between +3 T and -3 T for left- and right-circularly polarized emission for  $IX_1$  (left column) and  $IX_2$  (right column). (b,c), energy shift  $\Delta E$  between right- and left-CP peaks for  $IX_1$  (b) and  $IX_2$  (c). Error bars are calculated from the statistical error on the fitting procedure used to determine the peak position.

### Explanation of Zeeman splitting

In order to explain large and opposite splitting of interlayer doublet, we now consider an R-type (also referred as AA-stacking)  $WSe_2/MoSe_2$  heterostructure in an external magnetic field. Figure 6.17 schematically depicts how an applied magnetic field  $B$  lifts the valley degeneracy of the optical transitions between the valence band of  $WSe_2$  and the spin-split conduction band of  $MoSe_2$ . The simplified model we describe here accounts for the three main contributions to the interaction with magnetic field: spin, orbital and valley.

### 6.3. Electrical control of interlayer excitons

Spin-Zeeman shift ( $\Delta_s$ , black arrows in Figure 6.17) arises due to the interaction of the field  $B$  with the magnetic moment of the spin, and is proportional to the  $g$ -factor of the electron  $g_s$  and its spin  $s_z$ , as  $\Delta_s = g_s s_z \mu_B B$ , which is roughly equal to the  $\mu_B B$ , where  $\mu_B$  is the Bohr magneton. The low-energy  $IX_1$  interlayer exciton corresponds to the spin-singlet transition between the conduction and valence bands with the same spin. Therefore, the spin Zeeman effect does not affect  $IX_1$  resonance in any of the valleys, as its effect on the initial and final states is equal and thus the total contribution is zero. In contrast, the higher-energy spin-triplet  $IX_2$  exciton corresponds to the transition between bands with opposite spins (forbidden in monolayers but brightened in the moiré potential), and therefore gets a non-zero spin contribution to the Zeeman splitting of  $-4\mu_B B$ .

Atomic orbitals contribute only to the Zeeman shift of the valence band, since it has an orbital magnetic moment  $m_l = 2$ , while the conduction band carries a zero orbital moment. We represent this component  $\Delta_l$  to the Zeeman shift with green arrows in Figure 6.17. Consequently, the orbital part of the field-induced splitting of the transitions in K/-K valleys ( $\Delta E = E_K - E_{-K}$ ) amounts to  $-4\mu_B B$ . For the optical transition in monolayer TMDs, this is the only component that plays a significant role, and consequently a  $g$ -factor of -4 is typically observed in these systems [199, 232].

The valley contribution to the Zeeman shift ( $\Delta_v$ , blue arrows) is due to the interaction between the magnetic field and the valley magnetic momentum  $\tau_z \alpha^{(c,v)} m \mu_B$  of the self-rotating Bloch wavepackets, where  $\tau_z = \pm 1$  is the valley index for  $\pm K$  valley, and  $\alpha^c = m_0/m_e^* \approx 1.8$  ( $\alpha^v = m_0/m_h^* \approx 2.8$ ) takes into account the different effective mass of electrons (holes) in the conduction (valence) band of  $MoSe_2$  ( $WSe_2$ ). Here we use  $m_e^* = 0.57m_0$  and  $m_h^* = 0.36m_0$ , as calculated by Kormányos *et al.* [235]. We note that the use of different values from the literature could affect the final numerical result but does not change the general picture. The non-equivalent effective masses of electrons and holes give an additional term  $\mp(\Delta_v^h - \Delta_v^e)$  in the  $\pm K$  valley. In our case, the valley splitting of both  $IX_1$  and  $IX_2$  acquires an additional term of  $-2(\Delta_v^h - \Delta_v^e)$ . This valley-dependent term can indeed be substantial, as in recent reports of a large  $g$ -factor in AB-type stacked  $WSe_2/MoSe_2$  [224].

Adding up all the components, the total valley splitting induced by the magnetic field  $\Delta E = E_K - E_{-K}$  is expected to be  $-6\mu_B B$  ( $-10\mu_B B$ ) for  $IX_1$  ( $IX_2$ ). However, since the  $IX_2$  transition is associated with light of opposite helicity with respect to  $IX_1$ , the observed PL peak splitting has an opposite sign:  $\Delta E = E_{\sigma^+} - E_{\sigma^-} = -(E_K - E_{-K}) \approx 10\mu_B B$ . This is in agreement with the experimentally observed opposite  $g$ -factors of  $-8.5 \pm 1.5$  for  $IX_1$  and  $7.1 \pm 1.6$  for  $IX_2$  moiré excitons. We note that the estimation of the shift for  $IX_2$  is less precise than what we get for  $IX_1$ , due to the reduced emission intensity, which reduces the signal-to-noise ratio.

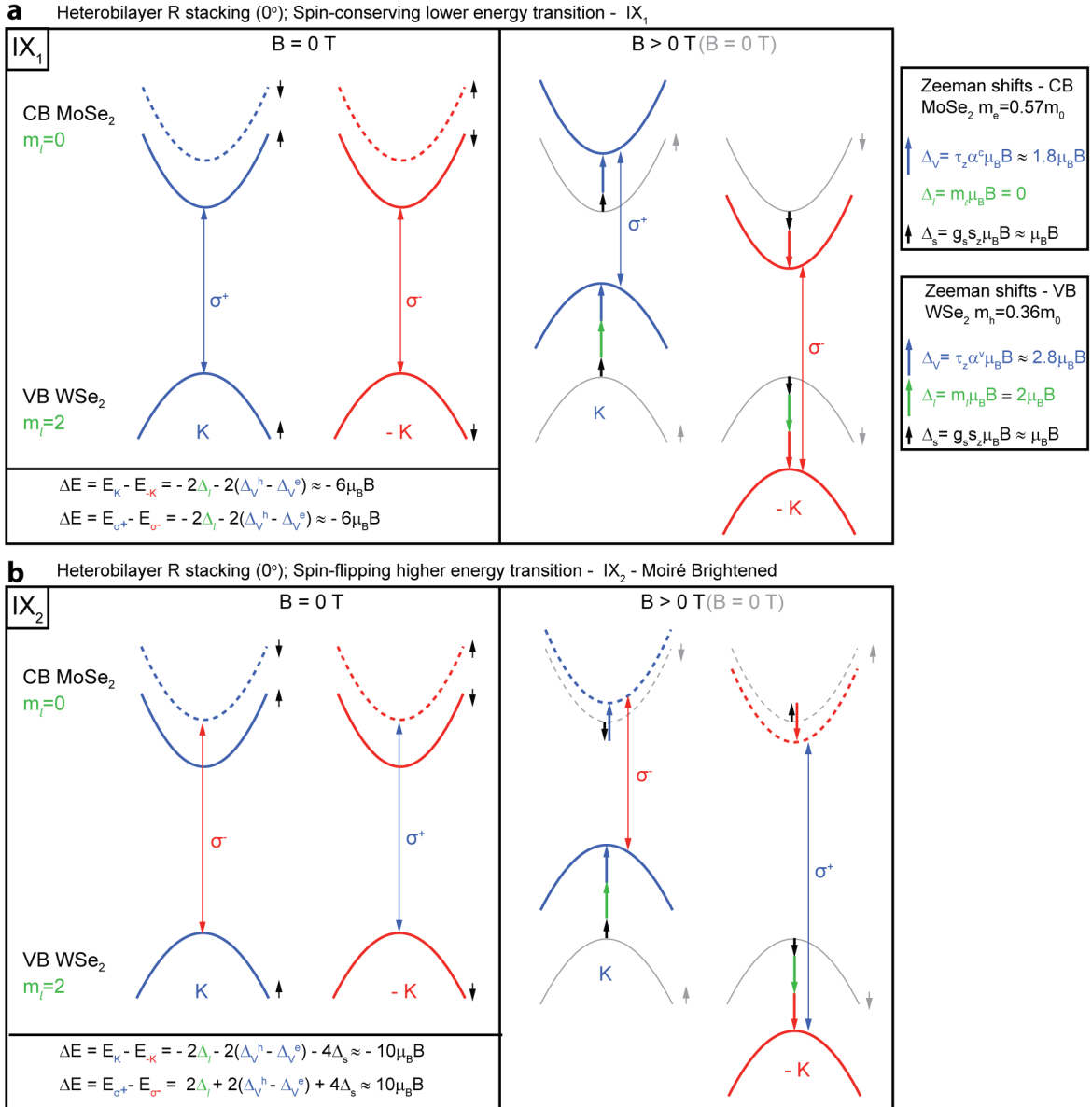


**Figure 6.17** – Zeeman splitting of the interlayer doublet. (a) Left panel: spin-conserving transitions between the conduction band of MoSe<sub>2</sub> and the valence band of WSe<sub>2</sub> in the absence (left) and presence (right) of a magnetic field, yielding an effective g-factor of -6. Right panels: spin- (black), orbital- (green) and valley- (blue/red) magnetic moment contributions to the total Zeeman shift. (b) Higher energy transition between conduction band of MoSe<sub>2</sub> and valence band of WSe<sub>2</sub> with opposite spins in absence (left) and presence (right) of a magnetic field, yielding an effective g-factor of +10.

### 6.3.6 Discussion

Our results can be explained in the frames of several recently proposed theoretical models. In the following we examine and compare them with our experimental data.



#### K-Q transitions

Given the energy difference between  $IX_1$  and  $IX_2$  of 25 meV, it is natural to interpret the doublet feature as a result of the spin splitting in the conduction band of  $MoSe_2$  [226] (roughly one order of magnitude smaller than the  $WSe_2$  valence band splitting). A very recent work interpreted  $IX_1$  and  $IX_2$  as the result of a transition between VBM in  $WSe_2$  at K/-K points and CBM in  $MoSe_2$  at Q/-Q points with relaxed selection rules [227]. The presence of polarization-reversing transitions can then be explained by considering the relaxed selection rules in the case of indirect interlayer excitons. Indeed, DFT calculations of the matrix elements for recombination between spin-orbit-split conduction band at the Q point and valence band at the K point yield similar weights and opposite helicities [227]. Similarly, the gate and power dependence we observe are in principle compatible with this picture. Concerning the switching between positive and negative polarization observed for  $IX_1$ , this may arise from a shift between a Q-K transition to a different one (K-K or K- $\Gamma$ ) because of doping. Calculations for the band structure of two-dimensional materials indeed showed that large shifts and even crossings are possible at high doping levels [236, 237, 238]. However, our observation of the sharp switching and the small doping required to trigger the effect do not match well with this picture. Also, measured temperature dependence contradicts with the indirect transition picture. Moreover, the strong quenching of interlayer emission as a function of temperature (and stacking angle [239]) seems to exclude phonon-assisted indirect transitions as the main channel for IX radiative emission.

#### Direct and indirect transitions

Miller *et al.* [240] proposed that the long-lived IXs in  $WSe_2/MoSe_2$  heterostructures involve two different transitions, one being direct in momentum space and the other being indirect. From our results, we exclude that this could be related to  $IX_1$  and  $IX_2$ , since the transition probability for a direct or phonon-assisted transition should differ by orders of magnitude. The temperature dependence would contradict our observations of  $IX_1$  and  $IX_2$  having similar intensities. Also, the strength of the transition suggests well-aligned layers [239], for which the K-K dipole momentum is much stronger.

#### Moiré-brightening of spin-forbidden transition

A likely explanation for the multiple emission lines and their behaviour could come from taking into account the lattice mismatch between  $MoSe_2$  and  $WSe_2$  that results in the formation of a moiré pattern. In this work, we consider two different approaches to the moiré pattern, namely the one proposed by Yu *et al.* [120, 121] and the one in ref. [118, 241].

Due to the spatially-changing stacking order, a periodic array of different symmetry points is produced, with different selection rules from site to site. Even in a well-aligned ( $\delta\theta \lesssim 1^\circ$ ) WSe<sub>2</sub>/MoSe<sub>2</sub> heterobilayer, the small difference in the lattice constant for the two crystals [242]  $\delta = |a - a'|/a$  will produce a moiré pattern with a period  $\lambda_M \sim a/\sqrt{\delta^2 + \delta\theta^2}$  of a few tens of nanometres. This means that our optical measurements (spot size 1  $\mu\text{m}$ ) probe the behaviour of tens to hundreds of different stacking sites.

We have already mentioned how the prediction of a brightened triplet transition can fit our data well. We now explain this in further detail. As calculated in ref. [121], the exciton energy minima correspond to regions of the moiré pattern with the local  $R_h^X$  atomic registry. Here, both spin-conserving ( $IX_1$ ) and spin-flipping transitions ( $IX_2$ ) are allowed. They couple to opposite circular polarizations of light, with comparable transition dipole strengths (see Figure 6.18). These two optical transitions, coming from sites with the same local registry, are expected to show a similar Stark shift in the electric field, which is in agreement with our observations (Figure 6.8). We rule out the possibility that we observe emission from different moiré sites since they would be associated with different dipole strengths due to variations of interlayer distance within the moiré and thus exhibit significantly different slopes of the Stark effect (and potentially crossing, as in ref. [120]). A different type of local minima, with  $R_h^h$  registry shows an opposite coupling with polarized light for  $IX_1$ , and a coupling with linearly polarized light for  $IX_2$ . This picture matches our data remarkably well: with doping, we alter the moiré potential landscape (by filling some minima or by shifting their energy electrostatically), thus localizing the excitons in sites with a different local symmetry. This is accompanied by a change in the coupling with light for  $IX_1$  (sign change in  $\rho$ ), and in the loss of polarization for  $IX_2$  in the circular basis ( $\rho$  becomes zero as it is now coupled with linearly polarized light).

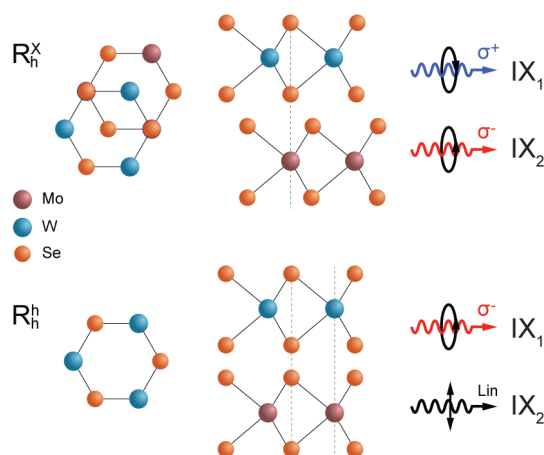


**Figure 6.18** – Atomic registries in the moiré pattern. Graphical representation of the two different local geometries for R-stacked WSe<sub>2</sub> and MoSe<sub>2</sub>:  $R_h^h$  and  $R_h^X$ , (top- and side-view), together with the predicted coupling with light for  $IX_1$  and  $IX_2$  according to ref [121].

### Other explanations

Other studies [118, 241] have explained the doublet feature in terms of ground and excited states of interlayer excitons localized in the moiré potential, where the splitting would result from the moiré potential well. These calculations show multiple transitions with alternating selection rules, with a predicted optical absorption peaks separated by  $\sim 10$  meV. The same authors also report the observation of 4 peaks with opposite polarizations. It is interesting to note that in their case an increase in temperature strongly quenches the high-energy peaks. This alternative moiré-based model cannot be excluded, but the opposite temperature dependence and the reproducible transition doublet we observe suggest a different mechanism in our case.

We should also mention very recent observation of moiré effects in similar heterostructures reported by Alexeev *et al.* [116], Tran *et al.* [243], Seyler *et al.* [117] and Jin *et al.* [119]. Though more studies are required to clarify all experimental observations.

### 6.3.7 Additional structures

While performing this work, we also had other important findings on similar heterostructures. Two of them presented bellow.

#### Heterostructure contacting

We have found that contacting the  $\text{WSe}_2/\text{MoSe}_2$  heterostructure with metallic leads is an important step towards achievements of narrow-lined optical transitions. To prove this point, in Figure 6.19a we present two PL spectra corresponding to the same heterostructure before (black) and after (blue) contact deposition. Using the gating map in Figure 6.9a as a reference, one might conclude that black spectra corresponds to the p-doped regime. By contacting the heterostructure with metal leads, we remove excess charge, inhomogeneously distributed in our structure, which was increasing exciton linewidth. We also found that wider spectra demonstrate strongly sublinear behaviour of power dependency. Nevertheless, both spectra show similar polarization preservation.

#### Heterotrilayer structure

We had another important observation by studying the  $\text{WSe}_2/\text{MoSe}_2$  structure, with  $\text{MoSe}_2$  having both monolayer (1L) and bilayer (2L) regions. Interestingly, in Figure 6.19b, where the PL spectra of this device is presented, we see formation of interlayer exciton not only in the 1L-1L but also in 2L-1L region. The latter one demonstrates a wide single peak emission at lower energy, that is expected as the bilayer crystal has a smaller band gap

compared to a monolayer crystal.

We measure a similar but slightly nonlinear Stark effect in case of the interlayer exciton from the heterotrilaer compared to the heterobilaer region. Interestingly, the 3L region demonstrates fast saturation with increase of power and absence of polarization preservation under any gate conditions. The last finding is expected as bilayer crystal recovers inversion symmetry and is therefore lacking peculiar valley physics.

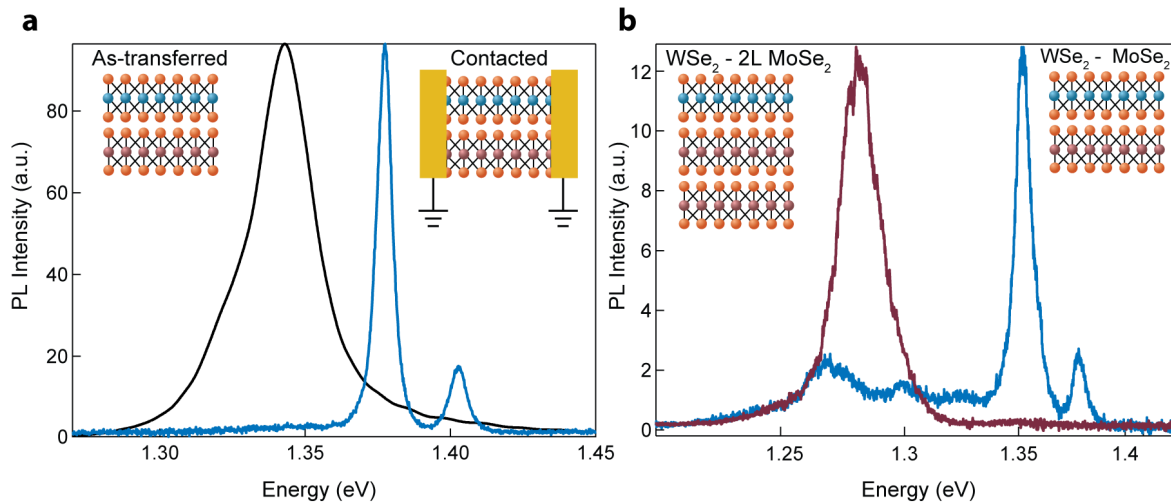


**Figure 6.19** – PL from additional structures. (a)  $\mu$ PL spectra of the interlayer exciton from the  $\text{MoSe}_2/\text{WSe}_2$  heterostructure before (black) and after (blue) contacts deposition. (b)  $\mu$ PL spectra of the interlayer exciton obtained from the 2L  $\text{MoSe}_2/\text{WSe}_2$  (dark red) heterostructure and from the 1L  $\text{MoSe}_2/\text{WSe}_2$  (blue) heterostructure.

### 6.3.8 Conclusion

In this section, we carefully studied interlayer excitons hosted in  $\text{MoSe}_2/\text{WSe}_2$  van der Waals heterostructures. We have demonstrated electrical control over the wavelength, intensity and polarization of emission from these interlayer excitons. The ability to fine-tune the emitted radiation is key to practical optoelectronics and could pave the way for novel applications for excitonic devices. Our encapsulated device allows probing two interlayer transitions with opposite helicities. Even more importantly, polarization conservation or reversal is gate-tunable, enabling for the first time a polarization inverting action. We measure high and opposite g-factors for both  $\text{IX}_1$  and  $\text{IX}_2$  transitions that is explained with the framework of moiré physics. These results are relevant in the context of valleytronic devices since they enable easy manipulation of the information encoded in the polarization of light. The following step would consist in a controllable transport of such quasi-polarized particles, which we demonstrate in the next section.

## 6.4 Valley-polarized excitonic transistor

### 6.4.1 Introduction

In the previous section we have demonstrated that heterostructures of transition metal dichalcogenides such as MoSe<sub>2</sub> and WSe<sub>2</sub> can host interlayer excitons, bound electron-hole pairs where charges are spatially separated in opposite layers and that these quasiparticles can be electrically manipulated. Moreover, the valley-dependent optical selection rules in TMDCs permit to selectively populate the K or -K valleys of WSe<sub>2</sub> and MoSe<sub>2</sub> with circularly polarized light, thus creating interlayer excitons with a certain valley-state.

In addition, the spatial separation of different carriers results in long lifetimes of these quasi-particles which can reach hundreds of nanoseconds in very high quality samples [111, 112]. It also provides interlayer excitons with a permanent out-of-plane electrical dipole moment, that results in the linear Stark effect, as shown in the previous section.

All these features of interlayer excitons can be harnessed in excitonic devices. For instance, long-living interlayer excitons could be used from information transport and storage, making them an attractive medium for generating and manipulating valley-polarized currents in solid state devices.

However, further obstacles arise from the slight lattice mismatch and relative rotation between the two layers, leading to the formation of moiré patterns, which can be as high as 150 meV [121]. Therefore it can effectively trap interlayer excitons in its local minima [116, 117, 119, 243], suppressing their diffusion and impeding the controlled transport of valley-polarized carriers over sizable distances.

To address these issues, we introduce an atomically thin spacer between the constituent monolayers of our heterostructure to further separate the electron- and hole-hosting layers. This tuning of interlayer interaction alters the long-range moiré pattern, while preserving the necessary coupling for hosting interlayer excitons. With this method, we realize an excitonic valley transistor, in which we can electrically control the transport of excitons carrying a certain valley state.

In addition, using a confining electrostatic potential we can collect excitons and increase their concentration, a step towards creation of a valley-polarized exciton superfluid via Bose-Einstein condensation [244, 245, 246]. We reach exciton densities above  $10^{12} \text{ cm}^{-2}$ , which is allowed by removing the limitation associated with increased recombination rate at high density [247].

### 6.4.2 Towards electrical control of exciton diffusion

The final goal of this study is to achieve electrostatic control of long-diffusing excitons. Towards this aim we fabricate a device based on a well-aligned  $\text{WSe}_2/\text{MoSe}_2$  heterostructure, which was characterized before. We deposit the stack encapsulated in h-BN crystals on an array of local back-gates, which allows us to locally modify the electric field, establishing regions with a lower or higher exciton energy. An optical image of the resulting structure is shown in Figure 6.20a, and in future we will refer to it as the heterobilayer or device B.

First we study free diffusion of excitons in this structure. For this, we focus the laser beam on the heterostructure above one of the split gates, and record the spatial image of PL emission that corresponds to the distribution of the exciton cloud. The result is shown in Figure 6.20b, top. We can see that the emission spot is slightly bigger if compared to the excitation profile, shown in Figure 6.20c (red and gray), a consequence of exciton diffusion.

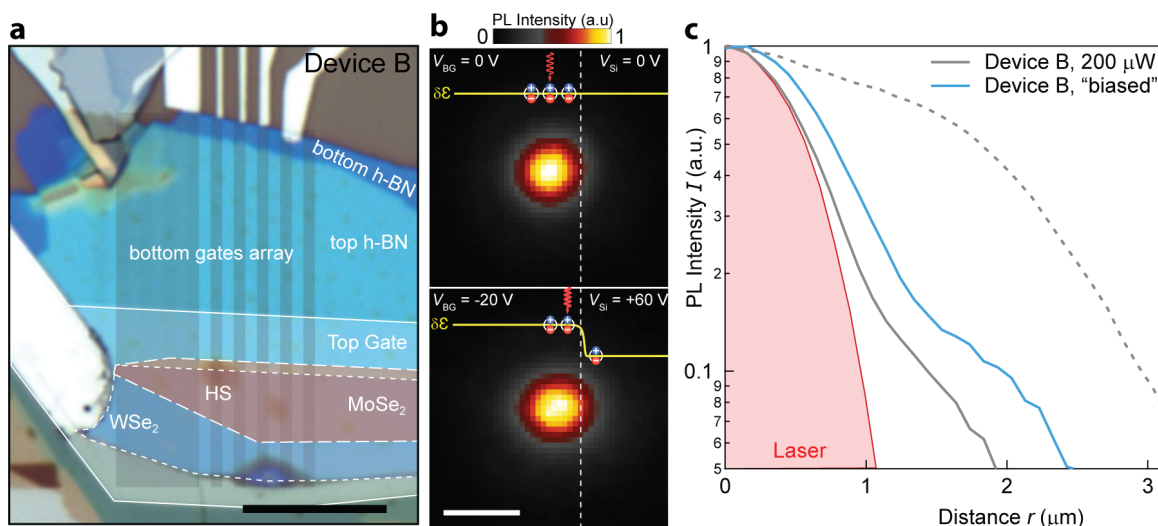


**Figure 6.20** – Exciton transport modulation in the heterobilayer (device B). (a) False colored optical image of the device, highlighting the different materials and local bottom gates. Scale bar is  $10\ \mu\text{m}$ . (b) CCD images of the spatial distribution of the interlayer exciton emission in the absence (top) and presence (bottom) of the applied electric field that promotes IX to diffuse towards the left from the excitation spot upon the application of  $V_{BG}$  and  $V_{Si}$  voltages on the local and global silicon back gate correspondingly. Scale bar is  $1\ \mu\text{m}$ . (c) Normalized PL intensity as a function of distance from the excitation point  $r$  extracted from b. Establishing an electric field clearly promotes exciton diffusion (grey vs blue solid curves), however it is negligible compared to the diffusion in the heterotrilaier (Device A, dashed line) acquired at similar excitation conditions in absence of an electric field. Profile of the laser spot is shown by the red area.

We now apply a positive voltage on the local back gate ( $V_{BG}$ ) and negatively bias on silicon global gate ( $V_{Si}$ ) in order to generate a region with low energy in close proximity to

the excitation spot. As a result, excitons preferentially diffuse towards this region as shown in Figures 6.20 b (bottom) and c (blue). Even though we clearly see some effect of the drift transport, initial diffusion is rather weak and therefore control over the excitonic transport is not efficient. As a matter of comparison we show in Figure 6.20c (dashed curve) what will be achieved in future devices.

We note that the diffusion of interlayer excitons observed here is comparable if not weaker than exciton diffusion in WSe<sub>2</sub> monolayers reported by Cadiz *et al.* [248]. This is despite the fact that interlayer excitons have three orders of magnitude longer lifetimes and are therefore expected to diffuse over longer distances. We assign the weak diffusion of IXs in well-aligned heterobilayers to the trapping of excitons in a moiré-induced potential variation.

### 6.4.3 Heterotrilayer device

In order to suppress effects associated with moiré pattern formation, we fabricate another device, where we introduce an atomically thin h-BN spacer in between WSe<sub>2</sub> and MoSe<sub>2</sub> monolayers. Indeed, this device is the main focus of this chapter section, and in the following we will refer to it as the heterotrilayer or device A.

#### Device fabrication

Figures 6.21a-d show different steps of heterotrilayer device fabrication. We start with the realization of bottom gates by e-beam lithography and evaporation of thin Cr/Pt (2/3 nm) on silicon substrates covered by 270 nm of SiO<sub>2</sub> as shown in Figure 6.21a. The heterostructure is then fabricated using polymer-assisted transfer of mono- and few-layer flakes of h-BN, WSe<sub>2</sub> and MoSe<sub>2</sub> (*HQ Graphene*), described in details in Chapter 3.

We remove the polymer residues with a hot acetone bath and thermally anneal the completed stack under high vacuum conditions. Finally, Figure 6.21d shows electrical contact fabrication using e-beam lithography and metallization (80 nm Pd for contacts, 8 nm Pt for the transparent top-gate).

In order to confirm a similar alignment of heterobilayer and heterotrilayer devices, we perform second harmonic generation measurements on both structures. Figure 6.21e demonstrate good alignment of WSe<sub>2</sub> and MoSe<sub>2</sub> in both stacks. We are very grateful to Sun Zhe for helping with these measurements.

As a matter of probing interlayer coupling strength, we perform photoluminescence spatial mapping of the completed heterostructure by tracking emission intensity at the

wavelength of MoSe<sub>2</sub> and WSe<sub>2</sub> intralayer excitons, as well as of lower-energy interlayer exciton. Corresponding results are presented in Figure 6.21f. First we clearly see that the intensity distribution of intralayer exciton emission coincide with exposed monolayers and is strongly quenched in the heterobilayer region where the interlayer coupling is the strongest.

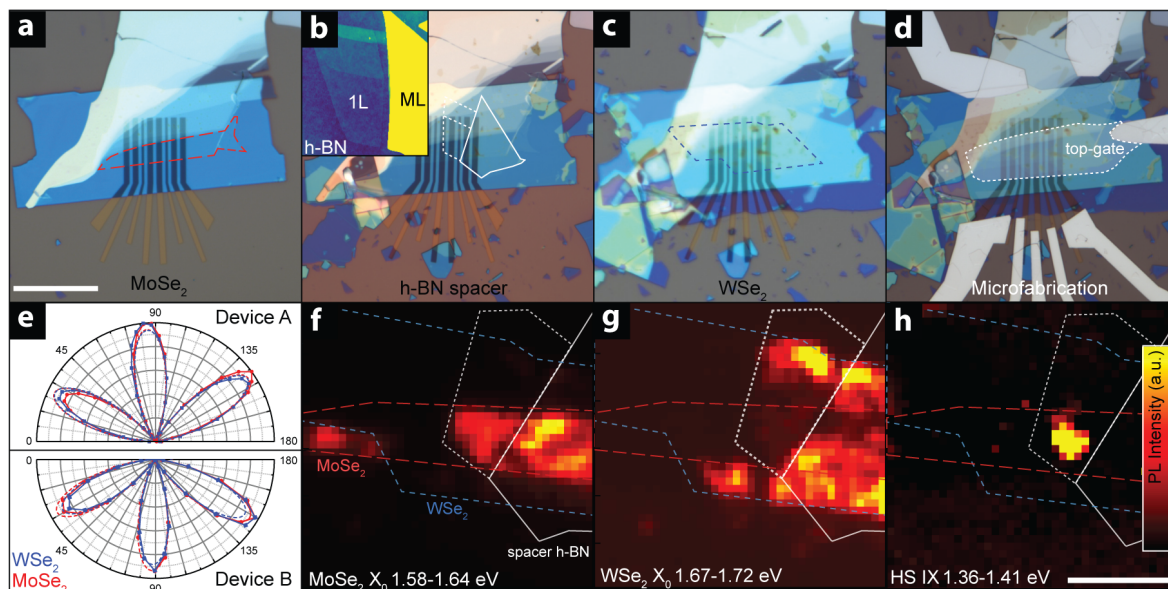


**Figure 6.21** – Heterotrilayer device fabrication and characterization. (a-d) Fabrication steps showing: local back-gate array evaporation; transfer of bottom h-BN and MoSe<sub>2</sub> on the gates; transfer of the h-BN spacer (inset: AFM image of the h-BN flake); transfer of WSe<sub>2</sub> and the top h-BN flake; finished device with contacts and top-gate. Scale bar is 25 μm. (e) Angle-dependent SHG signal acquired from the device A (top) and compared to the device B (bottom). (f) μPL map centered around the emission energy of MoSe<sub>2</sub>. (g) μPL map centered around the emission energy of WSe<sub>2</sub>. (h) μPL map centered around the emission energy of the interlayer exciton (IX). Scale bar is 10 μm.

Compared to the bilayer area, the region with the h-BN spacer clearly demonstrates emission at monolayer energies (intralayer exciton). This indicates a reduction of coupling strength between layers. Nevertheless, the coupling is sufficient for the formation of interlayer exciton in that region as we can see in Figure 6.21h.

### Device structure

As a result of fabrication, we obtain artificial heterostructures based on MoSe<sub>2</sub> and WSe<sub>2</sub> monolayers, with an atomically thin hexagonal boron nitride separator. In Figure 6.22a, we show a schematic depiction of a trilayer stack, fully encapsulated by thick h-BN flakes which serve as a flat and clean dielectric environment between the heterostructure and



the top- and bottom-gates. Multiple transparent gate electrodes allow us to apply laterally-changing vertical electrical fields while performing optical measurements, that will be required in future studies. Figure 6.22b shows an optical image of the trilayer structure or device A.

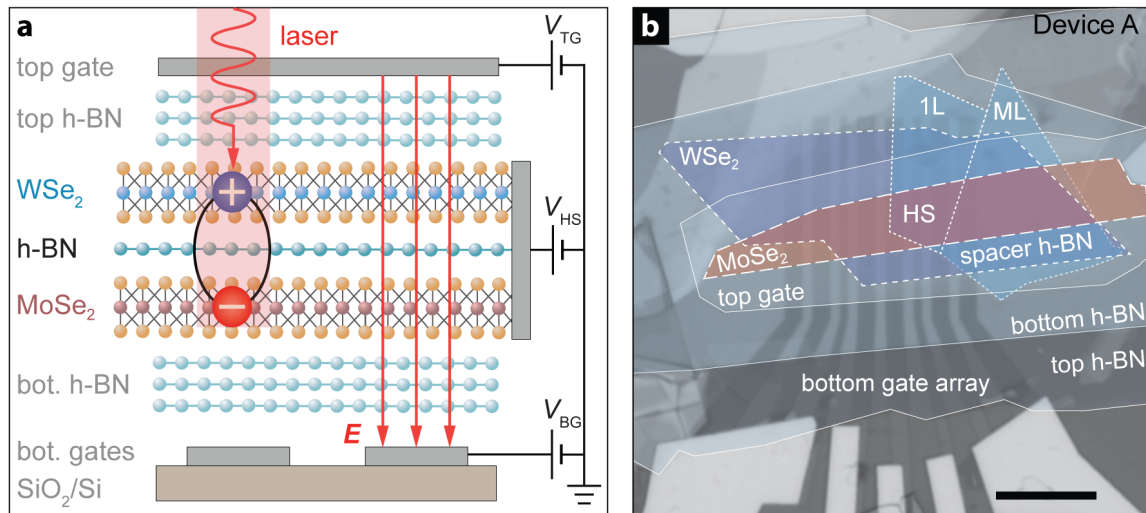


**Figure 6.22** – Heterotrilayer device with h-BN spacer. (a) Schematic of the device structure. (b) False colored optical image of the device, highlighting the different materials. Scale bar is 10  $\mu\text{m}$ .

#### 6.4.4 Optical characterization

Prior to the demonstration of device operation, we first characterize optically our heterotrilayer structure (Device A). As a matter of comparison, we also present results of similar measurements obtained on the different heterostructure without the h-BN spacer (Device B). This way we can directly highlight the effects introduced by the interposed layer.

##### Polarization resolved PL

We start with the acquisition of polarization-resolved micro-photoluminescence spectra by exciting the samples with a 647 nm-laser at 4 K. Upon photon absorption, the type-II band alignment of MoSe<sub>2</sub> and WSe<sub>2</sub> leads to fast charge separation of photo-generated carriers [249], followed by the formation of interlayer excitons from electrons in MoSe<sub>2</sub> and holes in WSe<sub>2</sub>. For device A we observe the appearance of a single low-energy interlayer transition at 1.39 eV which preserves the circular polarization of incoming light (Figure 6.23a, left panel). This is in sharp contrast to bilayer samples without h-BN spacer like device B, where we observe an interlayer doublet, characteristic of aligned heterobilayers [163, 227], with opposite helicities for the two peaks (Figure 6.23a, right panel).

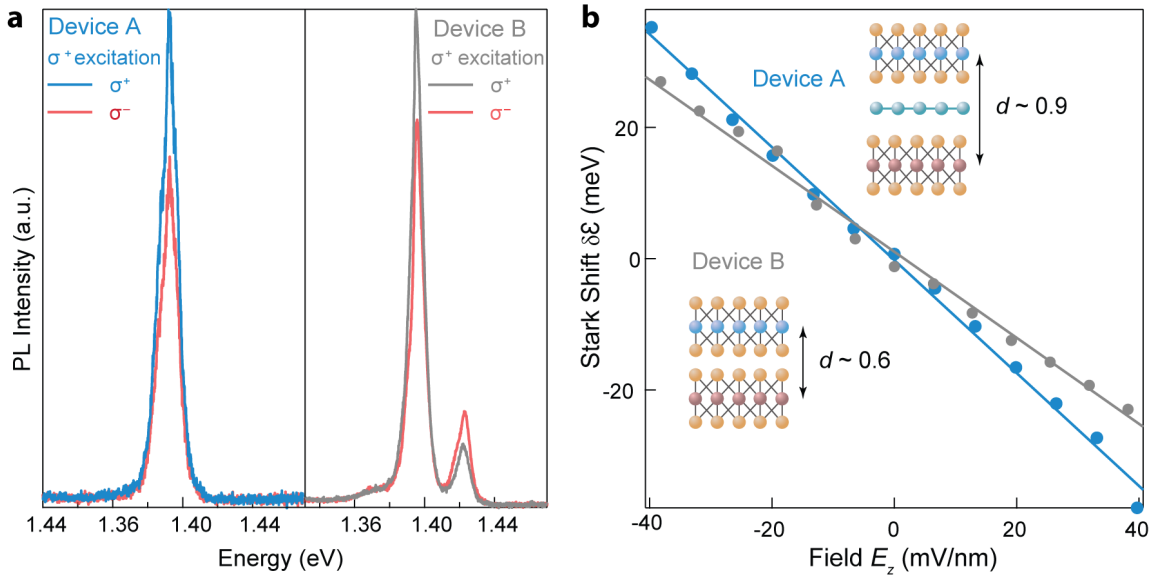


**Figure 6.23** – Optical characterization. (a) Polarization-resolved micro-photoluminescence spectrum from the  $\text{WSe}_2/\text{h-BN}/\text{MoSe}_2$  heterotrilinear (left) and the  $\text{WSe}_2/\text{MoSe}_2$  heterobilayer (right) excited with right circularly polarized light. (b) Energy of interlayer exciton emission as a function of the applied vertical electric field ( $E_z$ ) when sweeping at constant doping the Device A (blue) or Device B (grey). Solid lines correspond to the linear Stark shift of the dipole with a size of 0.9 nm (0.6 nm) extracted for the heterotrilinear (heterobilayer).

### Stark effect

Since the interlayer exciton has a built-in out-of-plane dipole moment  $\mathbf{p}$ , the application of an external electrical field  $\mathbf{E}$  perpendicular to the structure shifts its energy by  $\delta\mathcal{E} = -\mathbf{p} \cdot \mathbf{E}$ . We extract this Stark shift from the  $\mu\text{PL}$  spectra taken as a function of the applied electric field (Figure 6.23b) for both devices. Here the slope of the energy shift is proportional to the size of the IX dipole  $d = \delta\mathcal{E}/eE_z$ , where  $e$  is the elementary charge. We obtain  $d \approx 0.9$  nm for device A, which is considerably larger than what was previously reported for bilayer structures [112] and observed in device B ( $d_B \approx 0.6$  nm), with a difference similar to the thickness of a h-BN monolayer ( $\sim 0.3$  nm).

### Temperature dependence

For device A, we notice that the polarization of the emitted light  $\rho$  (which is a measure of valley-state conservation [40, 71]) has comparable magnitude to device B. Interestingly, temperature-dependent studies presented in Figure 6.24, show a decay of polarization with increasing temperature, due to enhanced inter-valley scattering. Nevertheless, we can detect non-zero polarization at temperatures as high as 150 K, while the interlayer

exciton emission can be observed up to room temperature, making these structures quite promising for applications at elevated temperatures.

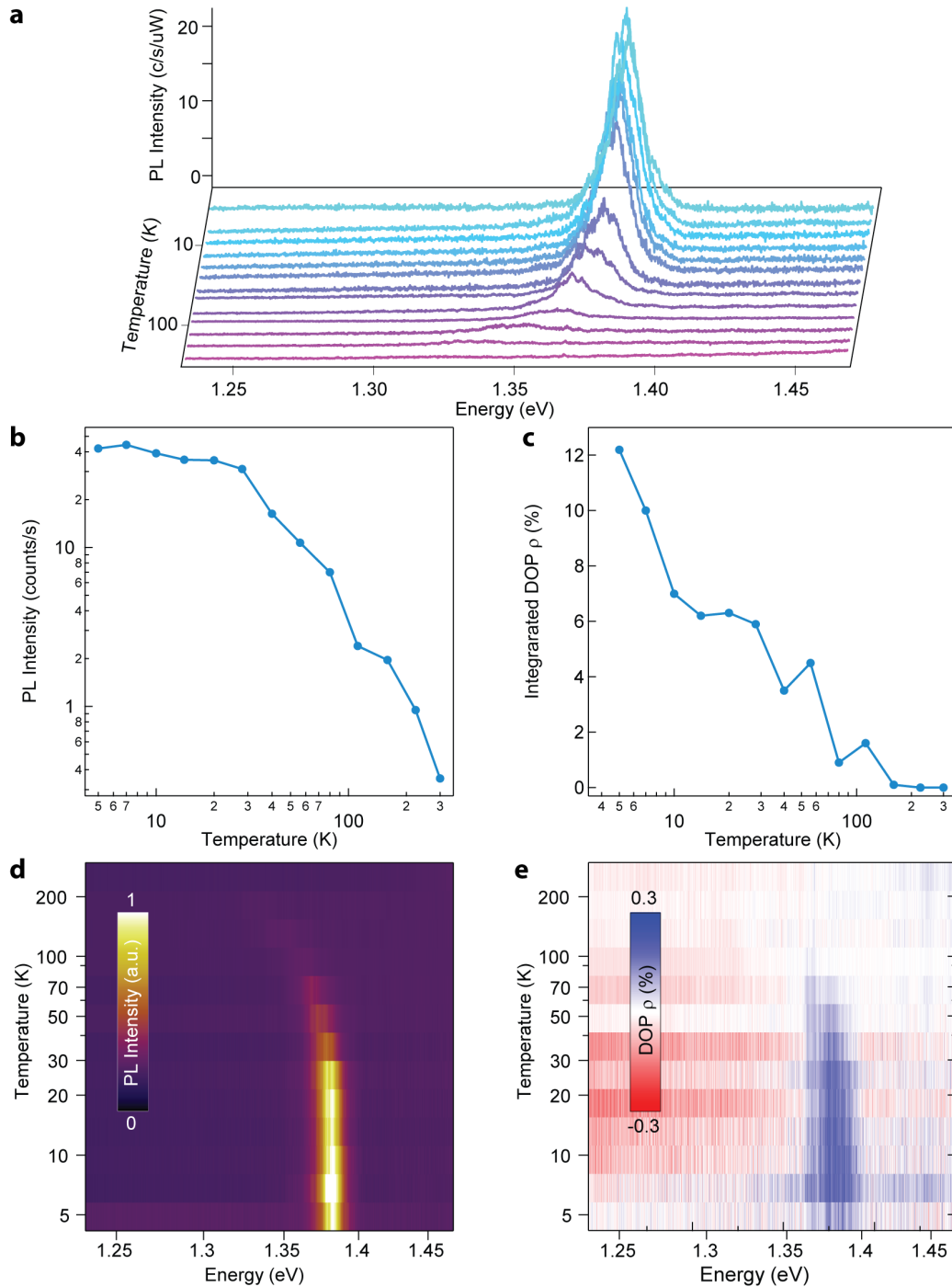


**Figure 6.24** – Temperature dependence of PL intensity and polarization. (a)  $\mu$ PL spectra of the interlayer exciton measured at different temperatures ranging from 4 to 300 K. (b) Intensity of the IX emission as a function of temperature. (c) Temperature dependence of the polarization degree integrated over the complete IX spectra. (d) Maps of  $\mu$ PL intensity (left) and polarization degree (right) as a function of temperature.

### Gate dependence

We further study the dependence of interlayer excitons and their polarization degree on the carrier concentration in the system. Corresponding results are shown in Figure 6.25.

We notice that similarly to the heterobilayer structure, excitons hosted by the heterotrilayer are tunable by gate voltage in terms of emission intensity and degree of circular polarization (Figure 6.25b). Nevertheless, we do not observe a sudden polarization switch as we have reported for the  $WSe_2/MoSe_2$  heterostructure without the h-BN spacer layer (Figure 6.14), further indicating the absence of moiré effects.

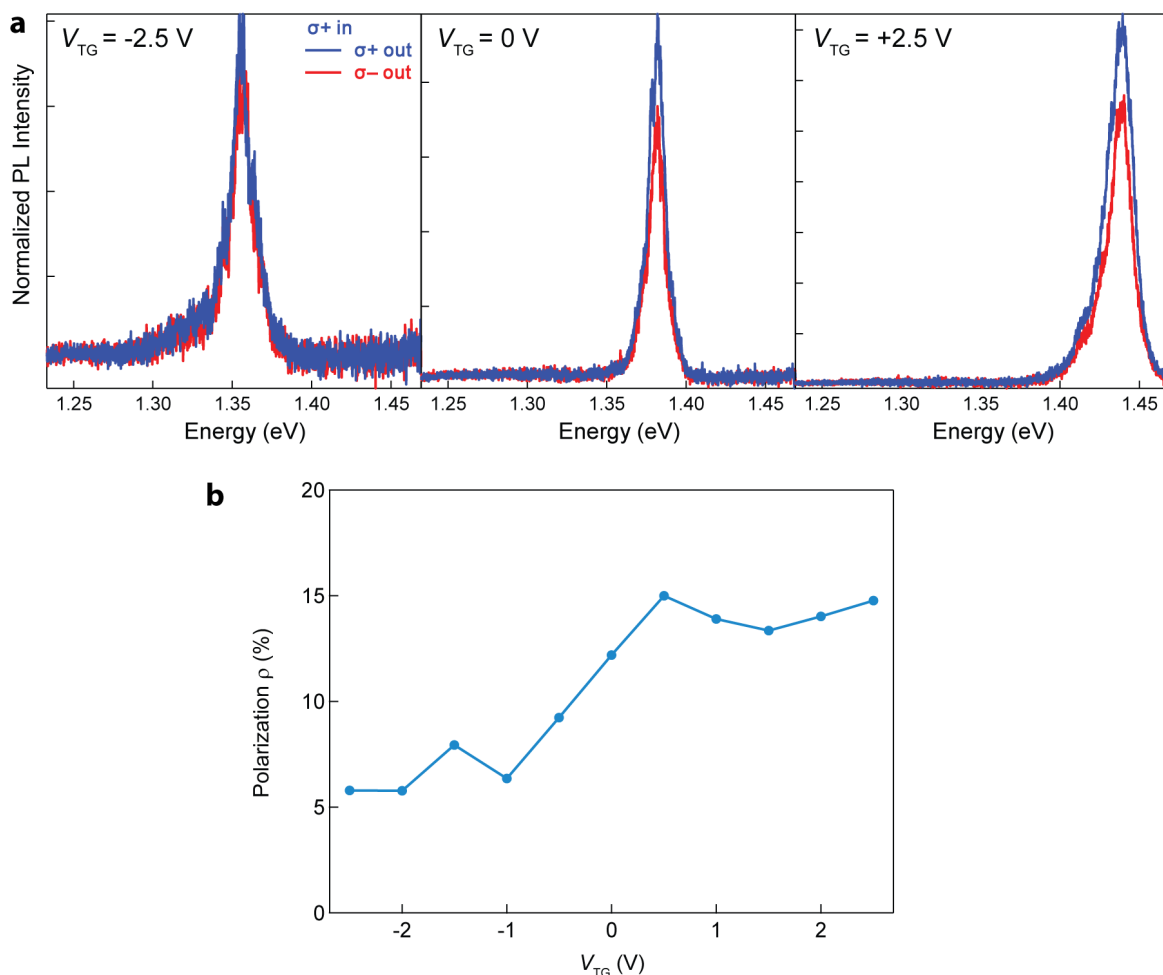


**Figure 6.25** – (a) Set of polarization-resolved  $\mu$ PL spectra acquired for a set of top-gate voltages ( $V_{TG}$ ) when the heterotrilayer is excited with right circularly polarized light. (b) Extracted from a degree of polarization versus applied gate voltage  $V_{TG}$ .

### 6.4.5 Diffusion boosted by high exciton density

#### Interlayer exciton power dependence

Next, we want to study how the interlayer excitons hosted in heterotrilayer change their behaviour at high incident powers. Figure 6.26a shows a linear power dependency, also extracted in Figure 6.26b). We interpret the lack of saturation as a signature of negligible exciton-exciton annihilation effects [247, 248, 250]. Indeed, the h-BN interlayer spacer is expected to reduce density-related recombination processes [251, 252].

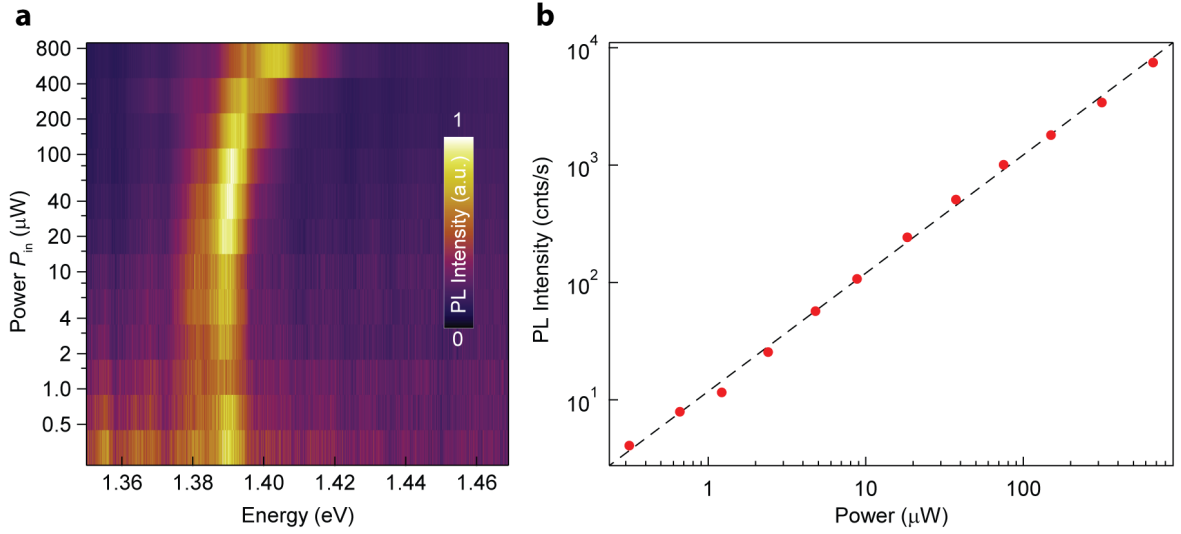


**Figure 6.26** – Power dependence of the PL spectrum. (a) Map of photoluminescence emission as a function of incident laser power  $P_{in}$  normalized by the acquisition time and incident power (counts/s/ $\mu$ W). (b) Extracted from an intensity of IX emission that demonstrates linear power dependency even at high excitation powers.

#### Exciton density

We also notice a spectral broadening and a sudden blue shift at higher incident powers, that we assign to exciton-exciton repulsion at higher density of these quasi-particles. By monitoring the blue-shift of the emitted light, we can estimate a lower bound for the exciton density  $n_{IX}$ , following a simple parallel plate capacitance model [253]:

$$\delta\mathcal{E}_{BS} = n_{IX} \frac{de^2}{\epsilon_{HS}\epsilon_0} \quad (6.2)$$

where the dipole size  $d$  is determined from the Stark shift (Figure 6.23b),  $\epsilon_0$  is the vacuum permittivity and  $\epsilon_{HS} = 6.26$  is the effective permittivity of the fabricated WSe<sub>2</sub>/h-

BN/MoSe<sub>2</sub> heterotrilinear, which was derived by considering the heterostructure as a series of capacitors according to the following calculations:

$$\epsilon_{\text{HS}} = \frac{(2d_{\text{TMD}} + d_{\text{hBN}}^{\text{spacer}}) \cdot \epsilon_{\text{hBN}} \cdot \epsilon_{\text{TMD}}}{2d_{\text{TMD}} \cdot \epsilon_{\text{hBN}} + d_{\text{hBN}}^{\text{spacer}} \cdot \epsilon_{\text{TMD}}} = 6.26 \quad (6.3)$$

where  $\epsilon_{\text{hBN}} = 4$  and  $\epsilon_{\text{TMD}} = 7.2$  are the relative permittivities of h-BN and TMDCs layers,  $d_{\text{TMD}} = 0.65$  and  $d_{\text{hBN}}^{\text{spacer}} = 0.3$  are the thicknesses of monolayer TMDCs and h-BN layers.

As shown in Figure 6.27b, the shift in emission energy grows sub-linearly, however it does not show signs of saturation over the range of incident power we explore. We extract a maximum carrier density of  $n_{\text{IX}} \sim 3 \cdot 10^{11} \text{ cm}^{-2}$  that is only limited by the excitation powers used. We note here that the spectral width of the interlayer exciton emission almost precisely follows its blue shift, as represented by the gray color in the same figure. Therefore, we assign significant broadening of the emission spectra to the exciton density distribution, rather than the photo-heating of the structure.

### Free diffusion of excitons

Knowing that excitons experience strong repulsion at high concentrations, which raises their energy, we now study the free diffusion of excitons as a function of incident power. For this, as shown in Figure 6.27a, we excite our heterotrilinear device near its edge. The laser beam is focused to a near-diffraction-limited spot that follows a Gaussian profile  $e^{-r^2/w^2}$ , with a tail width of  $w = 0.6 \mu\text{m}$ . We show the laser spot profile at low power in Figure 6.27a, top-left panel for comparison.

We now acquire  $\mu\text{PL}$  spectra as well as spatial images of the exciton photoluminescence. Details of optical measurements are described in Chapter 3. As can be seen in Figure 6.27a, when increasing the excitation power  $P_{\text{in}}$ , the size of the exciton cloud grows significantly, diffusing away from the excitation spot for several micrometers, up to the edges of the trilinear area. This is in contrast to what we observed in device B (Figure 6.20).

After characterizing the exciton density we now turn our attention to exciton diffusion. From CCD images, we obtain profiles of emission intensity as a function of the distance  $r$  from the excitation spot, normalized by their intensity at  $r = 0$ , as illustrated in Figure 6.27c. For comparison, we also draw (gray line) the profile from device B, which shows a much shorter diffusion of excitons in the heterobilayer.

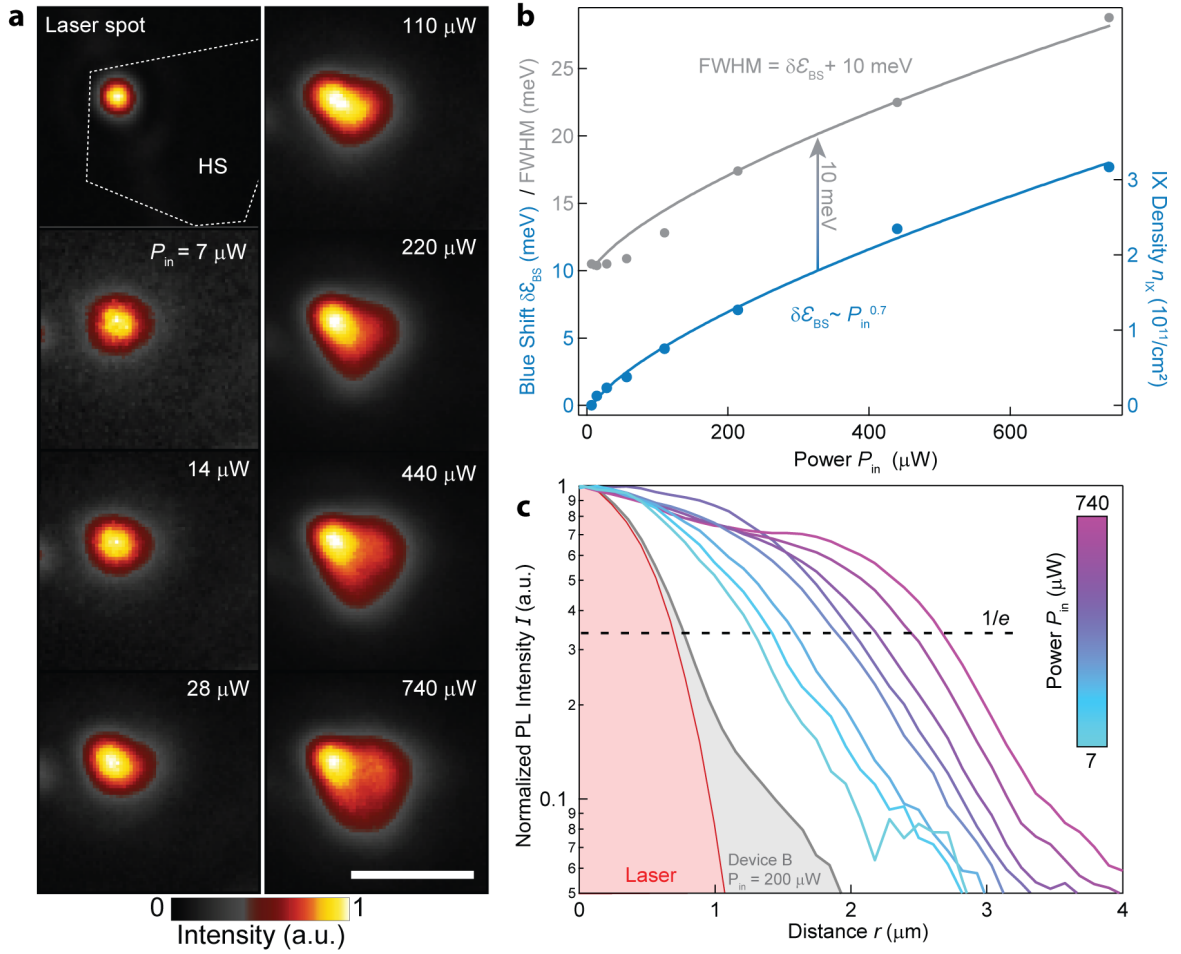


**Figure 6.27** – Exciton diffusion. (a) Leftmost figure: CCD image of the focused laser spot in the corner of the heterostructure, represented by the dashed line. Other figures: CCD images of the IX PL normalized emission intensity, acquired for different incident powers  $P_{in}$ . Scale bar is 4  $\mu\text{m}$ . (b) In blue: extracted blueshift  $\delta\mathcal{E}_{BS}$  dependence on the incident power. The solid curve is a power-law fit  $\delta\mathcal{E}_{BS} \sim P_{in}^{0.7}$ . In gray: full width at half maximum of the interlayer emission spectra at different incident powers resembles the power dependency of the blueshift. (c) Normalized PL intensity versus distance from the excitation point  $r$  extracted from a. The laser profile is shown by the red area. Grey area shows diffusion of excitons in Device B at 200  $\mu\text{W}$  incident power. Dashed line represents  $1/e$  of the maximal emission intensity.

### Fitting of the diffusion curves

At low excitation powers, the density of interlayer excitons follows the solution of the diffusion equation with a Gaussian excitation profile, which is convolution of the laser profile and the modified Bessel function of the second kind  $K_0$  [248]:

$$n_{IX} = n_0 \int_{-\infty}^{+\infty} K_0\left(\frac{r'}{l_D}\right) e^{-\frac{(r-r')^2}{w^2}} dr' \quad (6.4)$$

where  $l_D$  is the diffusion length of interlayer excitons in the heterostructure. However, the PL intensity profiles acquired for higher excitation powers cannot be fitted with Equation 6.4, as they clearly show two distinct regimes. In Figure 6.28 we present two cases, corresponding to low (a) and high (b) incident powers.

While close to the excitation spot we observe a very slow decay with distance ( $l_D$  larger than  $20 \mu\text{m}$ ), further away (roughly after the intensity has dropped by half) the signal starts to decay again with a slope very similar to the one seen at low power ( $l_D \approx 0.9 \mu\text{m}$ ). We interpret this as the result of high exciton density near the laser spot, which augments the diffusion due to dipole-dipole repulsion. However, away from excitation area, their density is much smaller, and thus has little or no effect on the diffusion process.

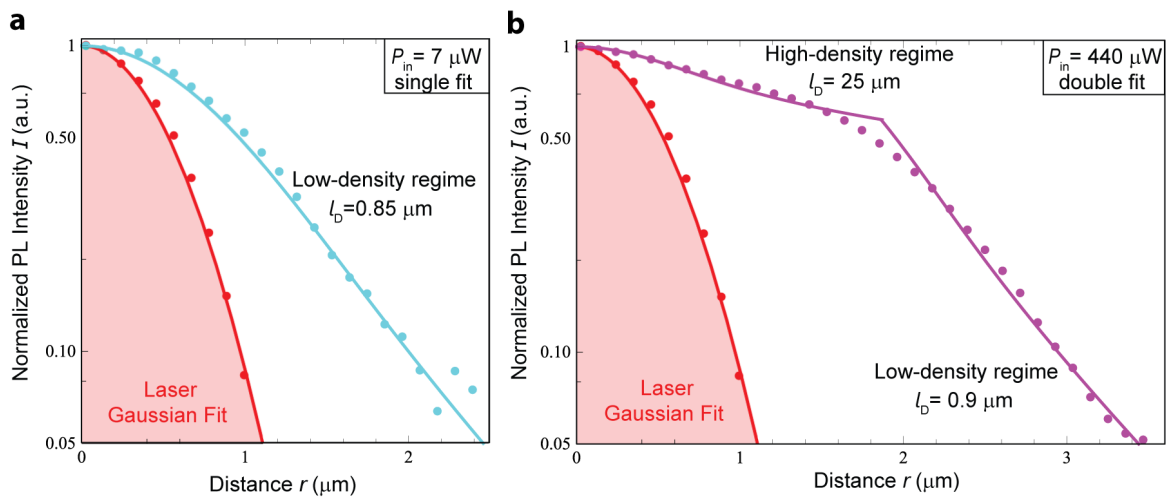


**Figure 6.28** – Fitting of the diffusion curves. (a) Low-density diffusion. PL Intensity as a function of distance from the excitation point  $r$  acquired at  $P_{in} = 7 \mu\text{W}$ . Experimental data (markers) is fitted by Equation 6.4 with a diffusion length of  $l_D = 0.85 \mu\text{m}$ . (b) High-density diffusion. PL intensity versus distance from the excitation point  $r$  acquired at  $P_{in} = 440 \mu\text{W}$ . Two regimes could be distinguished with a diffusion length of  $l_D = 25 \mu\text{m}$  (high exciton density area) and of  $l_D = 0.9 \mu\text{m}$  (low exciton density tail). Profile of the laser spot is shown by the red line, fitted by a Gaussian distribution with  $w = 0.6 \mu\text{m}$ .

### Effective diffusion length

For all excitation powers in Figure 6.27c we can indeed observe parallel tails with a slope corresponding to a diffusion length of  $0.9 \mu\text{m}$ , shown as dashed line in Figure 6.29. In this graph, we plot the extracted effective exciton diffusion length  $l_D^{\text{eff}}$ , defined as the distance where the emission intensity drops to  $1/e$  of its initial value. The extracted value grows with the excitation power  $P_{in}$ , reaching  $l_D^{\text{eff}} = 2.6 \mu\text{m}$  at  $P_{in} = 740 \mu\text{W}$ . We attribute the enhanced diffusion observed in device A to a higher exciton density, thanks to the suppression of recombination processes by the h-BN separator in strong contrast to the heterobilayer



structure of the device A. For this reason, in the following paragraphs we will focus on this trilayer device structure.

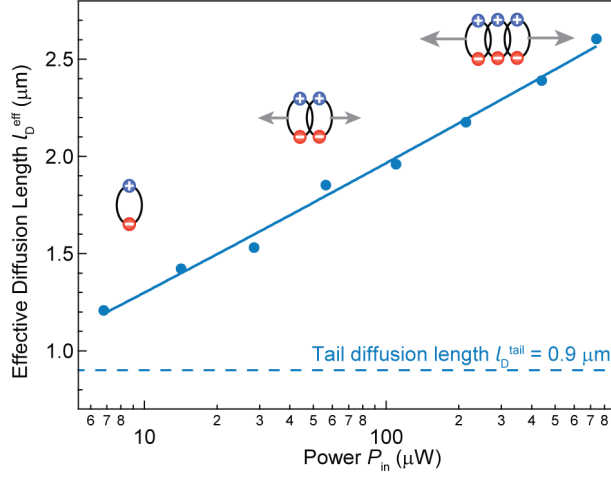


**Figure 6.29** – Extracted effective diffusion length  $l_D^{\text{eff}}$  (a distance from the excitation spot where the emission intensity drops to  $1/e$  of its initial value) as a function of incident power  $P_{\text{in}}$ . The dashed line shows the diffusion length extracted from the tails in Figure 6.27c, fitted by the convolution of the Gaussian-like laser profile with modified Bessel function of the second kind  $K_0$ . Inset schematically demonstrates the density-dependent diffusion driven by exciton-exciton repulsion.

### 6.4.6 Valley excitonic transistor

Long diffusion length at high incident power allows us to realize an electrically-operated excitonic switch device. Using multiple back-gates, we create a laterally-modulated electric field along the  $x$  direction, which in turn produces a spatial variation of the energy profile  $\delta\mathcal{E}(x)$  for the excitons, proportional to the applied electric field :

$$\delta\mathcal{E} = -\mathbf{p} \cdot \mathbf{E} = -p_z E_z \quad (6.5)$$

#### Numerical simulations

In the case of large and uniform top and bottom gates, knowing applied voltages  $V_{\text{BG}}$  and  $V_{\text{TG}}$ , we can easily calculate the vertical electric field:

$$E_z = \frac{V_{\text{BG}} - V_{\text{TG}}}{d_\Sigma} \cdot \frac{\epsilon_{\text{h-BN}}}{\epsilon_{\text{HS}}} \quad (6.6)$$

where the total thickness  $d_\Sigma$  is calculated as  $d_\Sigma = d_{\text{T}} + d_{\text{B}} + d_{\text{HS}}$  taking into account the thicknesses of the top and bottom h-BN  $d_{\text{T}} = 23$  nm,  $d_{\text{B}} = 43$  nm and of HS  $d_{\text{HS}} = 0.65$  nm.

However, this approach cannot be simply applied to the case of narrow metallic stripes which we use as local back gates. In order to estimate the vertical electric field which we apply to our structure in different regimes, we perform numerical simulations using the COMSOL Multiphysics software. Results of the spatial distribution of the electric field inside the heterostructure and corresponding energy of hosted interlayer excitons are shown in Figure 6.30. We use these calculations for better understanding of the following results.

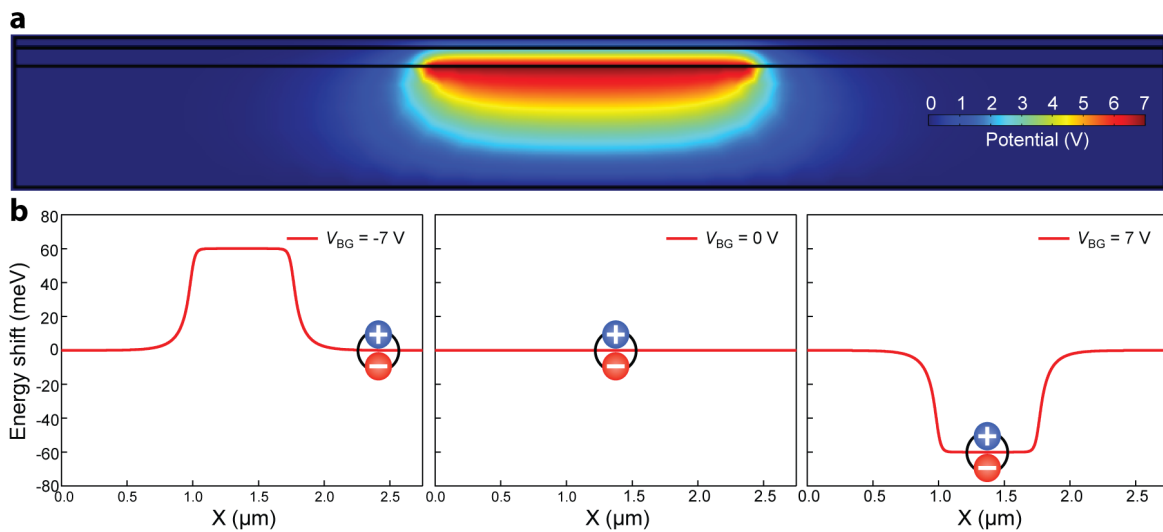


**Figure 6.30** – Numerical simulations. (a) Electrostatic potential in the simulated structure for the case  $V_{BG} = 7$  V. (b) Simulated energy profiles for the interlayer exciton energy for  $V_{BG} = -7$  V, 0 V and +7 V.

### Transistor operation

Here we excite IXs by parking the laser spot ( $P_{in} = 500 \mu W$ ) in the corner of the heterotrilayer, on the left side of a narrow back-gate. By making the gate area higher or lower in energy with respect to its surroundings, we can allow or block exciton diffusion. Figures 6.31a illustrate the spatial extent of PL emission, i.e. the shape of the exciton cloud, for the two cases. In the top part of the images (yellow overlay) we show the calculated interlayer exciton energy modulation  $\delta \mathcal{E} = -\mathbf{p} \cdot \mathbf{E}$  as a function of the lateral position  $x$  for the configurations, together with a schematic depiction of the expected exciton motion. For  $V_{BG} = -7$  V the gated area acts as an energy barrier, effectively blocking the excitons at its edge (OFF-state), as shown in Figure 6.31a. For  $V_{BG} = 0$  V, excitons are instead free to diffuse in a flat potential and move along the “channel” (ON-state), while their emission intensity decays with distance, as in Figure 6.32a where we plot cross-sectional cutlines of the spatial images.

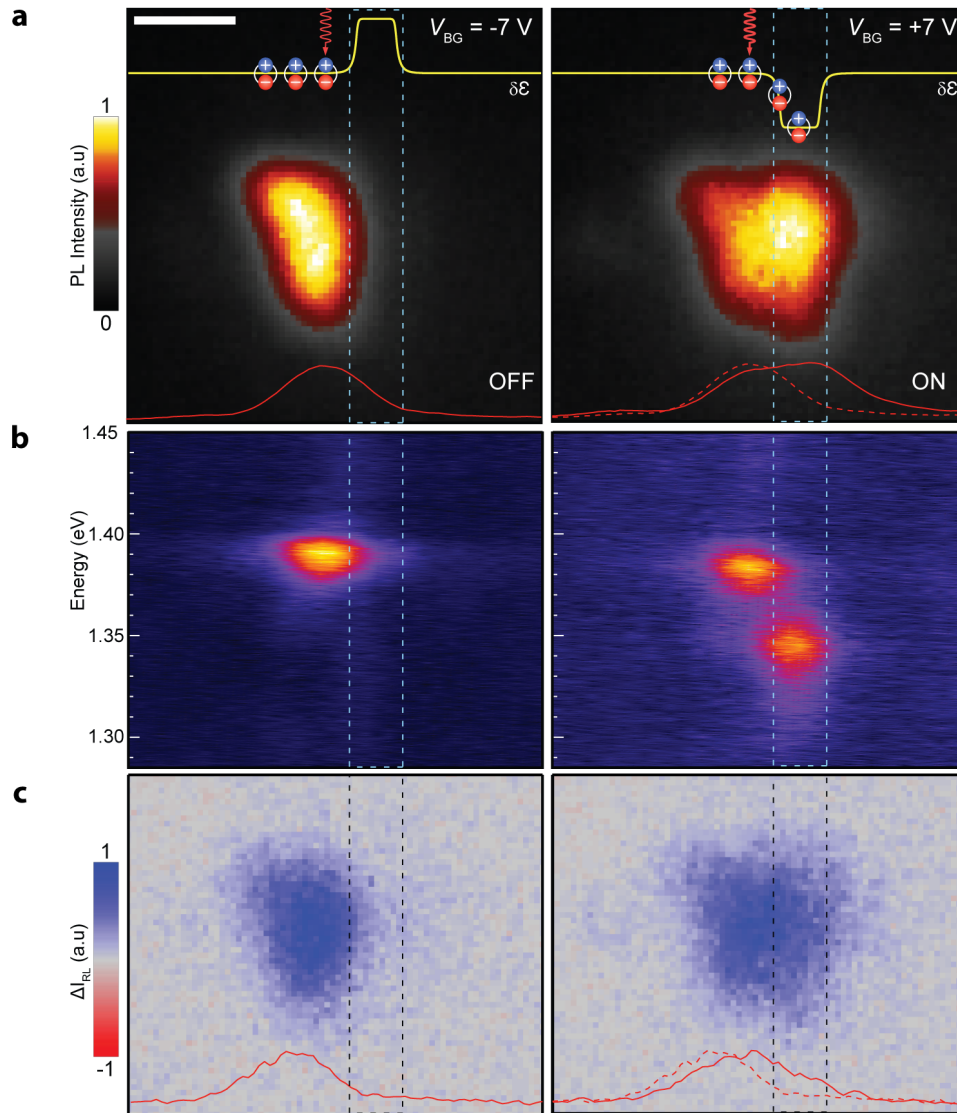


**Figure 6.31** – Excitonic valley switch. (a) Real-space CCD images of the emitted PL intensity corresponding to the ON and OFF configurations observed at high incident powers ( $P_{in} = 500\ \mu\text{W}$ ) for diffusion. The simulated energy shift  $\delta\mathcal{E}$  for the interlayer excitons in the two cases is drawn as a yellow overlay. The red overlay shows the intensity profile along the lateral direction in the middle of the image. As a reference for the eye, the profile in the OFF state is replicated as a dashed line in the panel on the right. (b) “Energy vs x” diagram of the emission energy as a function of the lateral coordinate x observed at low incident powers ( $P_{in} = 65\ \mu\text{W}$ ) for diffusion. (c) Real-space CCD images of the exciton cloud polarization  $\Delta I = I_{\sigma^+} - I_{\sigma^-}$  measured simultaneously with a. The red overlay shows the value of  $\Delta I$  along the lateral direction. The total polarization can be enhanced using resonant excitation at 720 nm. As a reference for the eye, the profile in the OFF state is replicated as a dashed line in the panel on the right. The dashed rectangle in all images corresponds to the gate area, where the vertical electric field is modulated. Scale bars are 2  $\mu\text{m}$ .

In Figure 6.32a we can see that by applying a voltage on the gate electrode the diffusion of excitons is blocked or allowed. We notice that due to the reduced size of the gate, the maximum diffusion is obtained in the case of zero field ( $V_{BG} = 0$  V). Taking the point where the intensity of the emitted light falls to  $1/e$  of its maximum, we obtain a transport over  $\sim 1.4$   $\mu\text{m}$  in the ON state as compared to the OFF state.

### Energy of transported excitons

The bright nature of interlayer excitons in  $\text{WSe}_2/\text{MoSe}_2$  allows us to directly observe their drift/diffusion. To gain further insight in the effective change in exciton energy, we probe the exciton energy spectra as a function of the spatial coordinate while exciting with lower laser power ( $P_{\text{in}} = 66$   $\mu\text{W}$ ) to achieve higher resolution.

The spectrally-resolved PL images were acquired by the following scheme: the light from the heterostructure was transmitted through a Dove prism, an 800-nm long-pass edge filter and a slit, and then was projected on the diffraction grating of the spectrometer. The Dove prism was positioned in such a way that the longitudinal axis of the gate (y-axis) was perpendicular to both the spectrometer slit and the lines of the diffraction grating. This way, spectral cut-lines along x-axis of the device were projected on the CCD camera of the spectrometer. Results of the measurement are shown in Figure 6.31b.

As can be seen in Figure 6.31b (left), in the OFF-state excitons are confined in space by the barrier (green dashed line) and lie around their natural emission energy  $\sim 1.39$  eV. In the absence of any field, we see that the excitons maintain the same energy, but now also occupy the gate area. When we apply positive gate voltage (right panel of Figure 6.31b), the gate area becomes energetically favorable, and we see excitons gradually moving into this region, while progressively going down in energy.

### Valley switch

Combining the excitonic device operation with valley preservation, we can realize a valley switch, effectively controlling the flow of valley-polarized excitons. For this, we optically initialize the exciton valley-state by exciting the device with  $\sigma^+$  circularly-polarized light. The result is displayed in Figure 6.31c, where spatial images of the emitted polarization  $\Delta I = I_{\sigma^+} - I_{\sigma^-}$  are shown for the OFF and ON states. By analyzing the decay of  $\Delta I$  with distance in Figure 6.32b, we see that valley-polarized excitons can either be stopped before the control gate, or travel over an additional  $\sim 1.3$   $\mu\text{m}$ -distance when in the ON-state. While here we are interested in a proof of concept, we notice that the initial degree of polarization (here  $\sim 15\%$ ) could be further improved by resonant excitation[227]. We also note that the measured polarization is slightly higher in the ON state, that we assign to additional

repulsion of majority excitons due to the exchange coulomb interaction [109, 114].

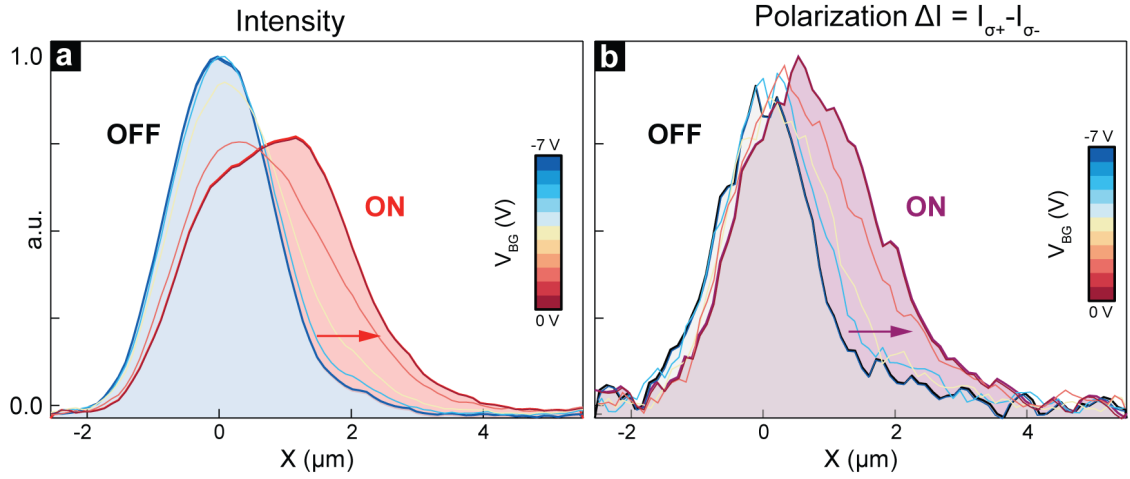


**Figure 6.32** – Cut-lines detailing the operation of the valley transistor device. (a) Intensity profile of the emitted PL for different voltage configurations from  $V_{\text{BG}} = -7$  V to 0 V. (b) Intensity profile of the polarization  $\Delta I = I_{\sigma^+} - I_{\sigma^-}$  for the same voltage configurations.

### 6.4.7 Excitonic trap

We can use the same principle not only to control fluxes of valley-polarized excitons, but also to confine them to achieve higher densities. Indeed, while the emission intensity rises linearly with pumping power, the blueshift increases sub-linearly (Figure 6.27b) due to exciton-exciton repulsion lowering the density. To counteract this, we generate an electrostatically-defined potential well to constrain the valley-polarized excitons and concentrate them further. As we have already mentioned above, the introduction of an h-BN spacer was predicted to suppress such effects like exciton-exciton annihilation, which increases recombination rate with increasing of density, thereby limiting achievable exciton density. Therefore we also expect to achieve higher exciton densities in our structure by employing additional electrostatic trapping.

Toward this, we shine a circularly-polarized laser (720 nm) directly on the area where we apply the electric field. As displayed in Figure 6.33a, anti-confining splits the valley-polarized exciton cloud into two lobes, pushing excitons away from the generation point. On the contrary, when we create a potential well in the lateral direction (Figure 6.33c), excitons are squeezed to a narrower area compared to their natural diffusion length (Figure 6.33b). We notice the same behaviour for the valley polarization of excitons, as shown in the insets of Figure 6.33a-b, where the spatial distribution of the polarization  $\rho = (I_{\sigma^+} - I_{\sigma^-}) / (I_{\sigma^+} + I_{\sigma^-})$  is shown.

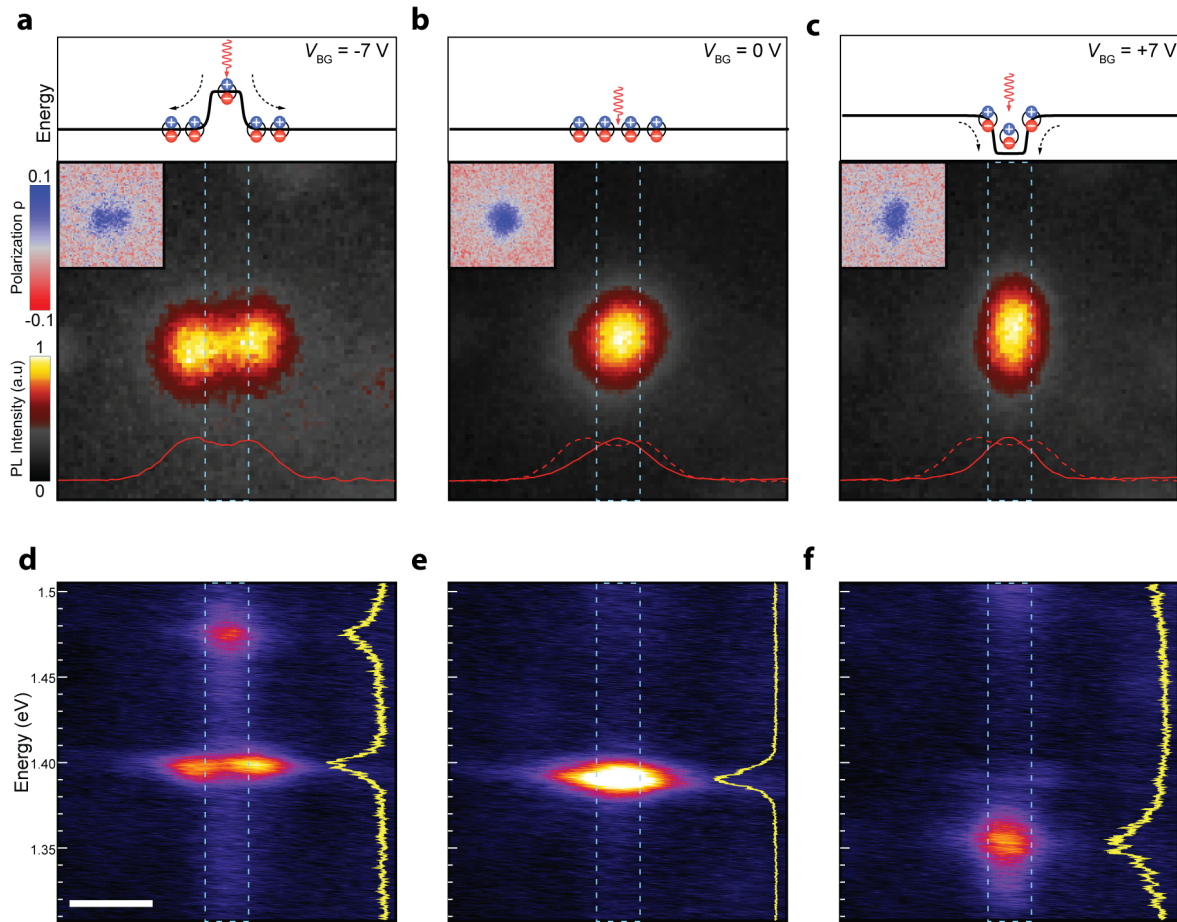


**Figure 6.33** – Electrostatic trap. (a-c) Real-space CCD images of the emitted PL intensity corresponding to the configurations of the repulsive barrier, free diffusion and confinement, observed at 720 nm resonant excitation with incident power of  $P_{in} = 220 \mu\text{W}$  in order to achieve higher degree of polarization  $\rho$  as shown in the insets. The simulated energy shift  $\delta\mathcal{E}$  for the interlayer excitons in the various cases is drawn on top. The red overlay shows the intensity profile along the lateral direction in the middle of the image. As a reference for the eye, the profile in the  $V_{BG} = -7$  V state is replicated as a dashed line in the last two panels. (d-f) “Energy vs  $x$ ” diagram of the emission energy as a function of the lateral coordinate  $x$  observed at the same conditions as Figure 6.31b. The yellow overlay shows the spectra from the central region. Scale bar is  $2 \mu\text{m}$ .

We gain more information by looking at the exciton energy as a function of position. In the barrier case (Figure 6.33d) excitons are separated into two regions spatially and energetically: excitons generated in the gate area have higher energy, hence they diffuse to the sides, where they emit light at the same energy of the zero-field case (Figure 6.33e). This is consistent with the strongest PL emission being localized on the two sides of the barrier, and not at the laser spot.

On the other hand, when we create a well, exciton energy is lowered, producing spatial confinement (Figure 6.33f). Interestingly, the energy shift of excitons is not symmetric with respect to the applied field (as expected from pure Stark effect).

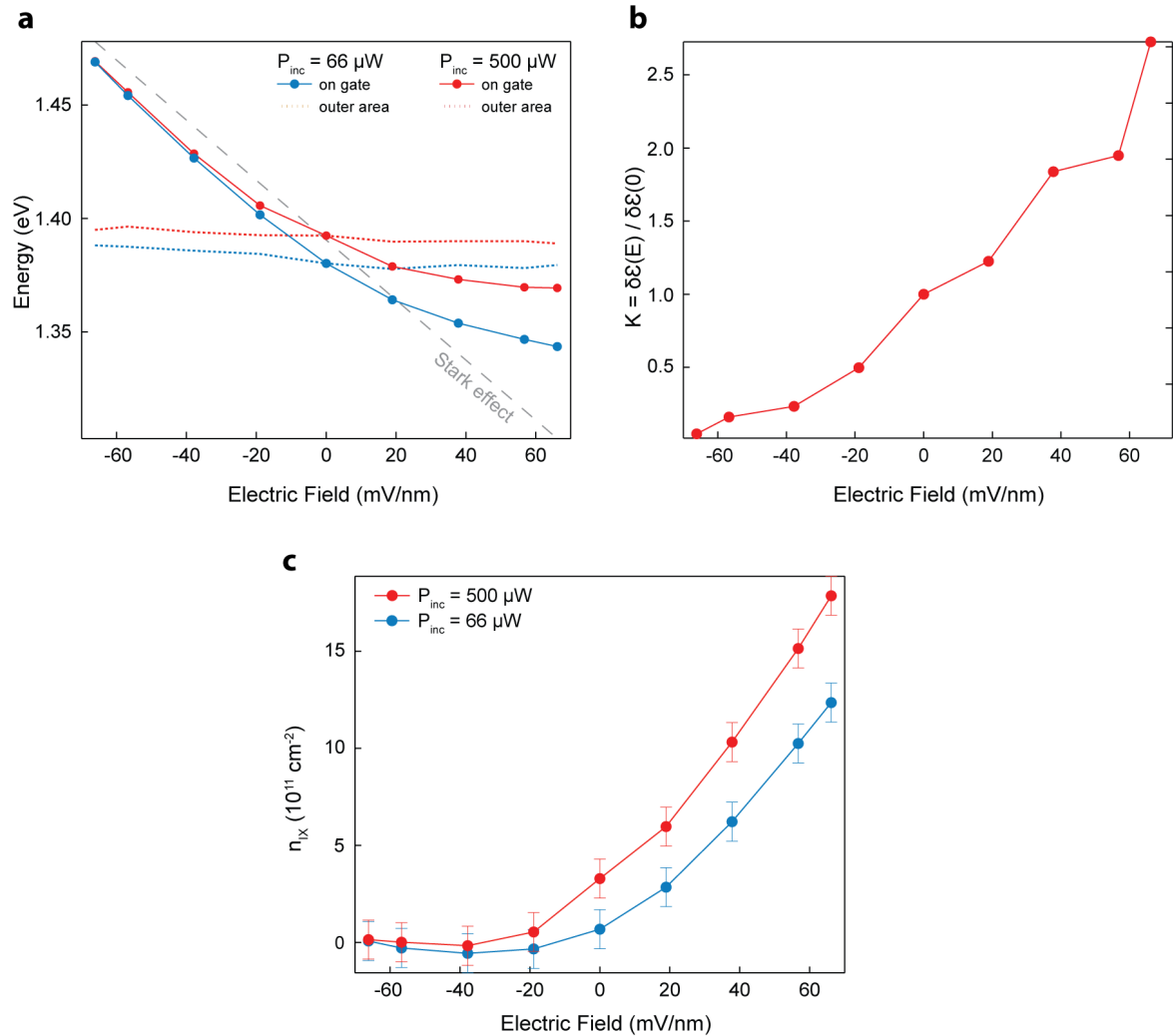


**Figure 6.34** – Electrostatic control of exciton concentration. (a) Peak emission energy in the gate area (solid line) and outside of it (dashed line) as a function of the applied electric field for 500  $\mu\text{W}$  (red) and 66  $\mu\text{W}$  (blue) incident power. In gray, the linear Stark effect extracted from Figure 6.23. (b) Ratio between the blueshift  $\delta\mathcal{E}(E)$  and the blueshift at zero electric field  $\delta\mathcal{E}(0)$ . (c) Density of interlayer excitons as a function of the applied electric field extracted from the non-linear behaviour of the energy shift  $\delta\mathcal{E}$  for 500  $\mu\text{W}$  (red) and 66  $\mu\text{W}$  (blue) incident power. The dashed rectangle in all images corresponds to the gate area, where the vertical electric field is modulated.

In Figure 6.34a we plot the energy of excitons in the region inside (solid) and outside (dotted) of the gate area as a function of electric field for two different excitation powers.

At zero field, increasing the incident power generates a relative blueshift of about  $\sim 12$  meV, in agreement with Figure 6.27b. However, when we disperse excitons (negative field), this blueshift is canceled. Even more strikingly, when we start to confine the excitons, two phenomena appear: first, the magnitude of the blueshift between low- and high-power increases; and second, the exciton energy deviates drastically from a linear behaviour, especially in the high-power case.

We attribute this non-linearity to the changing density inside the electrostatically established potential trap: since excitons are confined, their average energy is not only shifted by the Stark effect, but also has a strong contribution from exciton-exciton interaction depending on local density:

$$\delta\mathcal{E} = -p_z E_z + n_{\text{IX}} \frac{de^2}{\epsilon_{\text{HS}} \epsilon_0} \quad (6.7)$$

Conversely, when we separate them, even at higher power the density is low enough to make interactions negligible. We quantify the resulting modulation of exciton density by two methods. First, we look at how the blueshift  $\delta\mathcal{E}(E) = \delta\mathcal{E}_{500\mu\text{W}}(E) - \delta\mathcal{E}_{66\mu\text{W}}(E)$  is enhanced by the applied electric field  $E$ :  $K(E) = \delta\mathcal{E}(E)/\delta\mathcal{E}(0)$ . This quantifies the increase in exciton density  $\Delta n_{\text{IX}}$  induced by higher power (see Figure 6.34b) as a function of the electric field  $E$ , indicating that the electrostatic confinement can modulate the exciton density.

However, we are mostly interested in estimating the actual exciton density in the trap. For this, we isolate the non-linear contribution to energy shift  $\delta\mathcal{E}(E)$ , proportional to the exciton density, by removing the Stark effect (gray dashed line in Figure 6.34a). We show the result in Figure 6.34c, which allows us to put a lower bound on the concentration of polarized excitons at exciton density of  $n_{\text{IX}} \sim 1.8 \times 10^{12} \text{ cm}^{-2}$ , promising for the production of a degenerate Bose gas [245].

Indeed, the control over the concentration of polarized excitons represents a significant step towards the realization of high-temperature Bose–Einstein condensates of valley-excitons in these systems. Further experimental work to achieve high exciton concentrations in thermal equilibrium could include engineered potential profiles like ramps [220] or optimized traps, enabling the collection of thermalized excitons produced by pulsed excitation at even higher densities.



## 6.4.8 Towards high-temperature operation

As mentioned earlier, relatively large binding energy of interlayer excitons allows us to observe IXs at high temperatures. Indeed, we can operate the valley switch up to a temperature of 100 K, as shown in Figure 6.35. However, polarization conservation becomes negligible above this temperature, as we have shown in Figure 6.24.

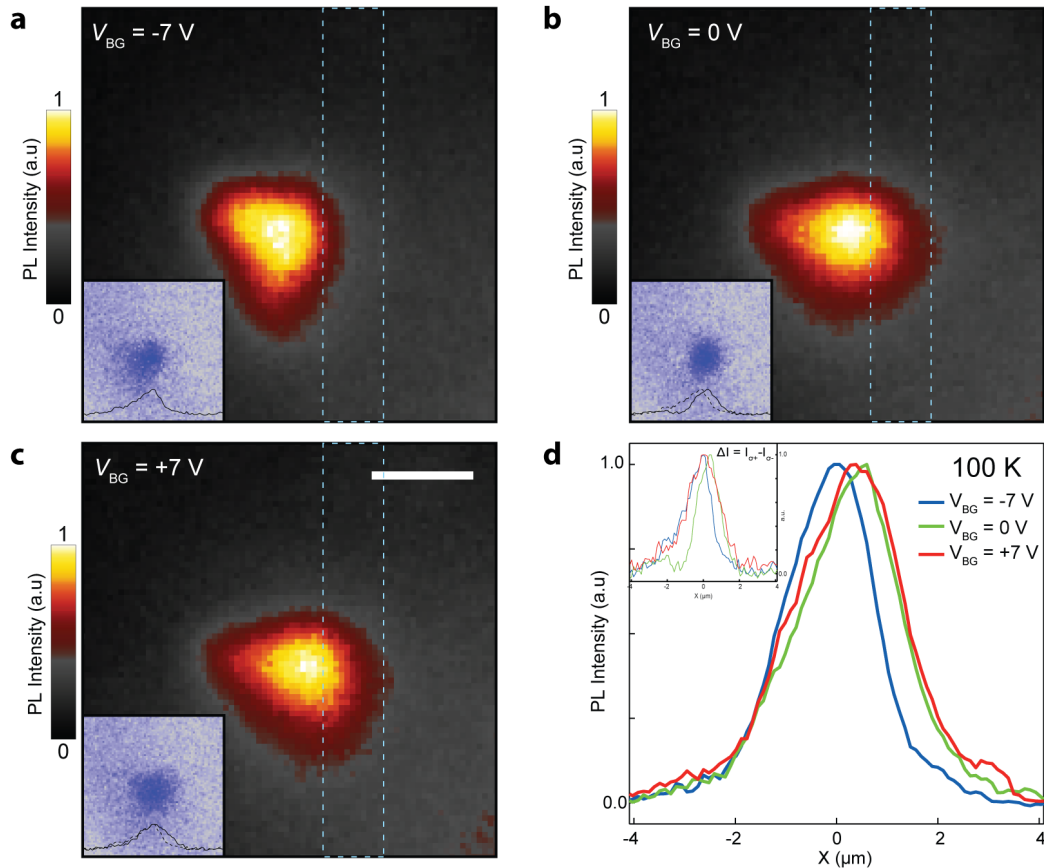


**Figure 6.35** – Valley-exciton switch operation at 100 K. (a-c) Images of the spatial distribution of PL for  $V_{BG} = -7$  V (OFF), 0 V (ON) and +7 V (collection) measured at 100 K. Insets show spatial distribution of  $\Delta I = I_{\sigma^+} - I_{\sigma^-}$  for each configuration, whereas the black overlay is the intensity of  $\Delta I$  along the horizontal direction. The dashed rectangle in all images corresponds to the gate area, where the vertical electric field is modulated. Scale bar is 2  $\mu\text{m}$ . (d) Plot of the intensity along a horizontal cutline in the middle of the images. Inset: intensity of  $\Delta I$  along the same cutline.

Evermore, in Figure 6.36 we prove that a simple excitonic switch can work at temperatures as high as 150 K. These results show the potential of 2D materials in application to excitonic devices. However, the interlayer coupling reduction due to the h-BN spacer applies strong limitation on operation at room temperature.

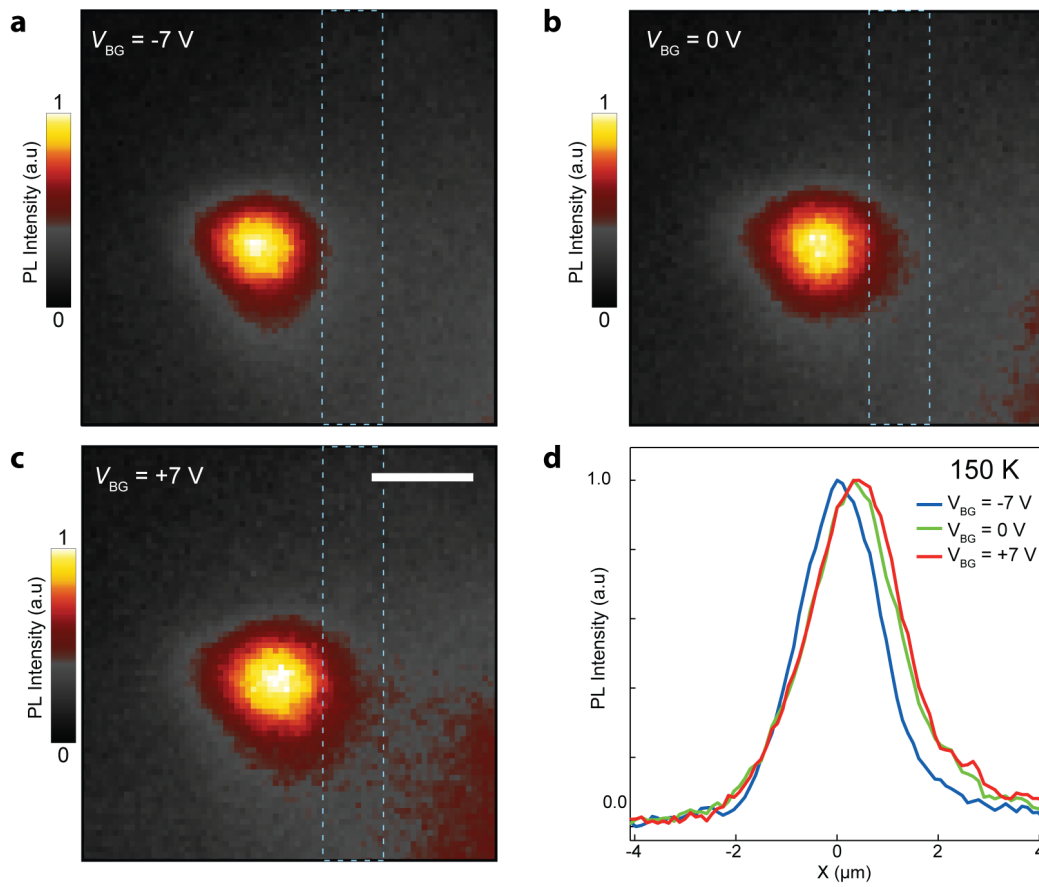


**Figure 6.36** – Exciton switch operation at 150 K. (a-c) Images of the spatial distribution of PL for  $V_{TG} = -7\text{ V}$  (OFF),  $0\text{ V}$  (ON) and  $+7\text{ V}$  (collection) measured at 150 K. The dashed rectangle in all images corresponds to the gate area, where the vertical electric field is modulated. Scale bar is  $2\ \mu\text{m}$ . (d) Plot of the intensity along a horizontal cutline in the middle of the images.

### 6.4.9 Conclusion

In this chapter we have demonstrated several important findings. First, we have suppressed the naturally arising moiré-related potential modulation by introducing a single layer of h-BN as an interlayer spacer that smoothens the interlayer potential on micrometer scale. Careful engineering of interlayer coupling yielded an optically active interlayer exciton with an out-of-plane dipole moment, which can be further manipulated *via* an external electric field. This allowed us to electrostatically define energy traps to confine excitons, increasing their concentration by an order of magnitude and reaching a value of above  $10^{12}$   $\text{cm}^{-2}$ . This is an important step toward the realization of exciton Bose condensation at elevated temperatures.

Second, the reduction of exciton trapping by the moiré potential allowed us to significantly extend the diffusion length of valley-polarized interlayer excitons reaching a regime where manipulation of exciton diffusion via local gates becomes possible. We therefore demonstrate an exciton transistor which can electrically control the flow of valley-polarized excitons over mesoscopic distances. However, the introduction of a spacer between constituent layers of the heterostructure reduces their coupling and the binding energy of the resulting interlayer excitons, thus making it impossible to reach device operation at higher temperatures. In the following section, we therefore apply alternative approaches towards the realization of an excitonic device suitable for room temperature operation.



## 6.5 Room temperature excitonic transistor

### 6.5.1 Introduction

Although we have successfully demonstrated exciton-based transistor actions in the previous section, similar low-temperature devices (excluding valleytronics component) were already reported in bulk semiconductor-based coupled quantum wells [8, 9, 218]. Cryogenic temperatures required for operation limit their promise for practical applications. In this sense, two-dimensional semiconductors with large exciton binding energies provide new prospects for the realization of excitonic devices and circuits operating at room temperature.

Long diffusion of interlayer excitons in a well-aligned  $\text{WSe}_2/\text{MoSe}_2$  van der Waals heterostructures requires an atomically thin spacing layer, which flattens the moiré-related potential profile, but also decreases the binding energy of interlayer excitons. With increase of lattice mismatch  $\delta a$  and misalignment angle  $\delta\theta$ , the moiré period  $\lambda_M \sim a/\sqrt{\delta a^2 + \delta\theta^2}$  is reduced and eventually becomes comparable to the interlayer exciton radius, so that potential fluctuations effectively vanish without the need of an intermediate h-BN layer. However, the recombination rate of interlayer excitons in  $\text{WSe}_2/\text{MoSe}_2$  drops significantly if the stacking angle deviates from zero degree. Therefore we look into another heterobilayer system with much higher lattice mismatch [120], where interlayer transitions can be observed virtually regardless on the alignment angle [225, 254].

In this section, we will demonstrate room temperature excitonic devices made of atomically thin  $\text{WSe}_2/\text{MoS}_2$  van der Waals heterostructures that demonstrate gate-controlled transistor actions. Long-lived interlayer excitons together with the long diffusion constant in our boron nitride-encapsulated stack result in excitons diffusing over a 5  $\mu\text{m}$  distance. Within this stack combination, we further demonstrate the ability to manipulate exciton dynamics by creating electrically reconfigurable confining and repulsive potentials for the exciton cloud.

### 6.5.2 $\text{MoS}_2/\text{WSe}_2$ interlayer excitons

For the device presented here, we take advantage of interlayer excitons hosted in an atomically thin  $\text{MoS}_2/\text{WSe}_2$  heterostructure. Similarly to  $\text{MoSe}_2/\text{WSe}_2$ , this heterostructure exhibits type-II band alignment [108, 255], which results in charge separation between the constituent materials, with electrons and holes residing in  $\text{MoS}_2$  and  $\text{WSe}_2$ , respectively. This is schematically shown in Figure 6.37.

The formation of indirect excitons is marked by the appearance of a new photolumines-

cence emission peak [223], red-shifted by 75 meV with respect to the intralayer A exciton of the WSe<sub>2</sub> monolayer. In Figure 6.37c we present a typical PL spectrum obtained from such a heterostructure on SiO<sub>2</sub>, where the spectral signature of the interlayer exciton is clearly visible (blue line), together with the individual WSe<sub>2</sub> and MoS<sub>2</sub> monolayers (blue and red line respectively).

Interestingly, the alignment has been shown not to be critical for the observation of interlayer excitons in this system with large lattice mismatch. Furthermore, recent reports [225] suggest that excitons in the MoS<sub>2</sub>/WSe<sub>2</sub> system are not only spatial-, but also momentum-indirect. The phonon-assisted nature of the emission process further reduces the exciton recombination rate, yielding a longer lifetime [256]. Such strongly extended lifetime can be exploited to obtain interlayer exciton diffusion in the micrometer scale range, even at room temperature.

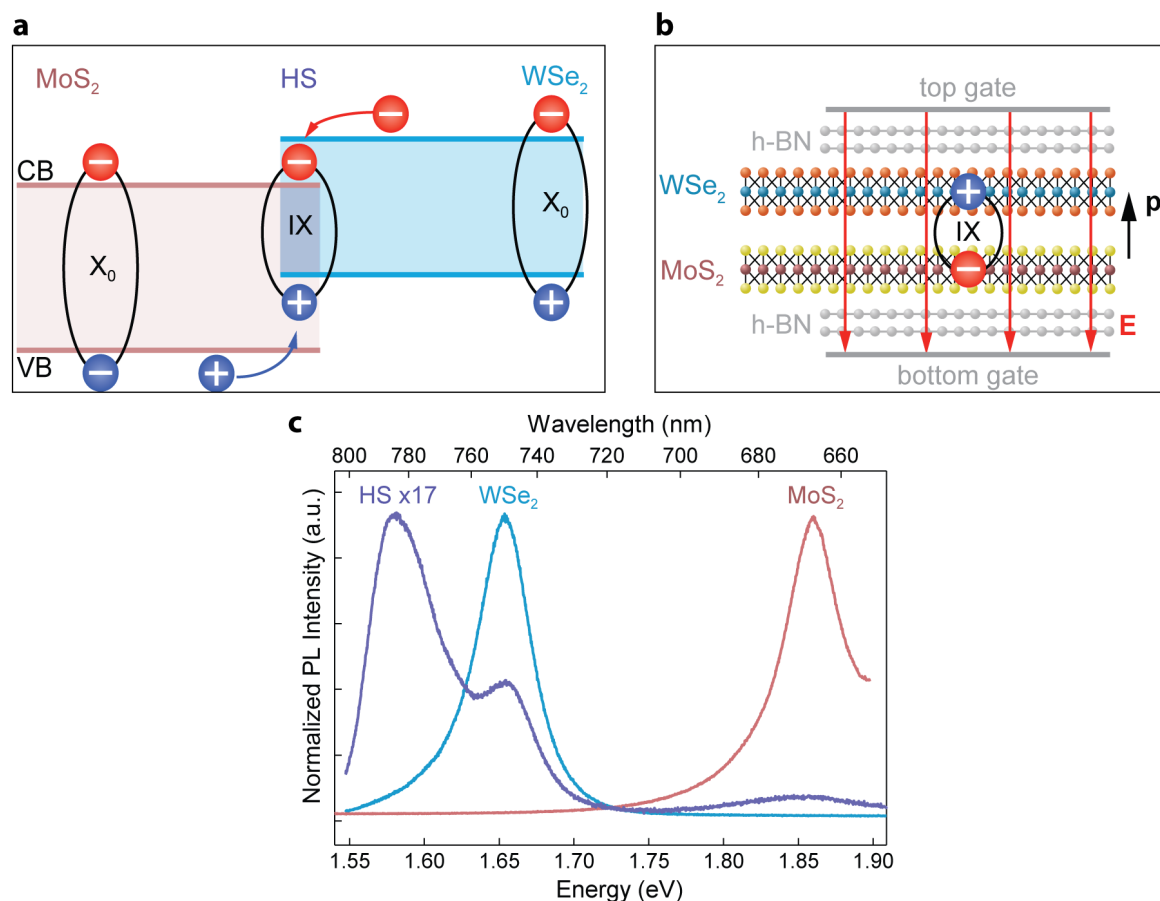


**Figure 6.37** – Interlayer excitons in the WSe<sub>2</sub>/MoS<sub>2</sub> vdW heterostructure. (a), Type-II band alignment in the WSe<sub>2</sub>/MoS<sub>2</sub> heterostructure (HS) with intralayer (X<sub>0</sub>) and interlayer (IX) excitons. (b) Schematic depiction of the WSe<sub>2</sub>/MoS<sub>2</sub> heterostructure. The interlayer exciton has a permanent out-of-plane dipole moment **p** allowing manipulation *via* the electric field. (c) PL spectra of individual monolayers and their HS fabricated on SiO<sub>2</sub>.

### 6.5.3 Excitonic switch

#### Device structure

Although explained in the previous sections, we briefly repeat operation principles of an excitonic device. Given that excitons do not carry a net electric charge, one would not expect that their flow could be influenced by the direct application of an electric field. However, the confinement of oppositely charged carriers in different layers results in a well-defined interlayer exciton dipole moment  $\mathbf{p}$  with an out-of-plane direction (Figure 6.37b) along  $z$  axis of the device. An electric field perpendicular to the crystal plane can then be used to shift the exciton energy by  $\delta\mathcal{E} = -\mathbf{p}\cdot\mathbf{E} = -p_z E_z$ , while a laterally modulated electric field  $E_z(x, y)$  will create an energy landscape, driving the exciton motion along  $x$  axis towards regions of lower energy. In Figure 6.38 we schematically present operation principles of such device.

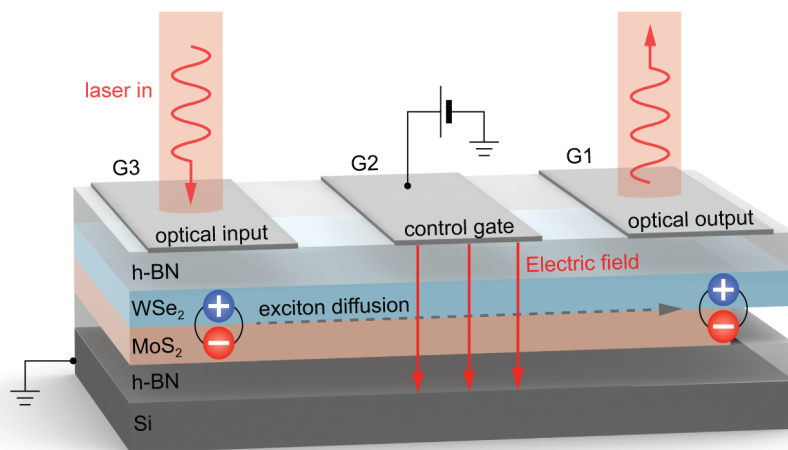


**Figure 6.38** – Schematic of the excitonic switch operation. Application of voltages to transparent graphene electrodes (1-3) can engineer a potential landscape for the diffusion of excitons, controlling their flux through the device.

#### Device fabrication

Figure 6.39 shows optical images of the device fabrication process. The high quality heterostructure was fabricated using polymer-assisted transfer of h-BN and of monolayer flakes  $WSe_2$  (*HQ Graphene*) and  $MoS_2$  (*SPI*). Flakes were first exfoliated on a polymer double layer, as described in Chapter 3. Once monolayers were optically identified, the bottom layer was dissolved with a solvent and free-floating films with flakes were obtained for further transfer.

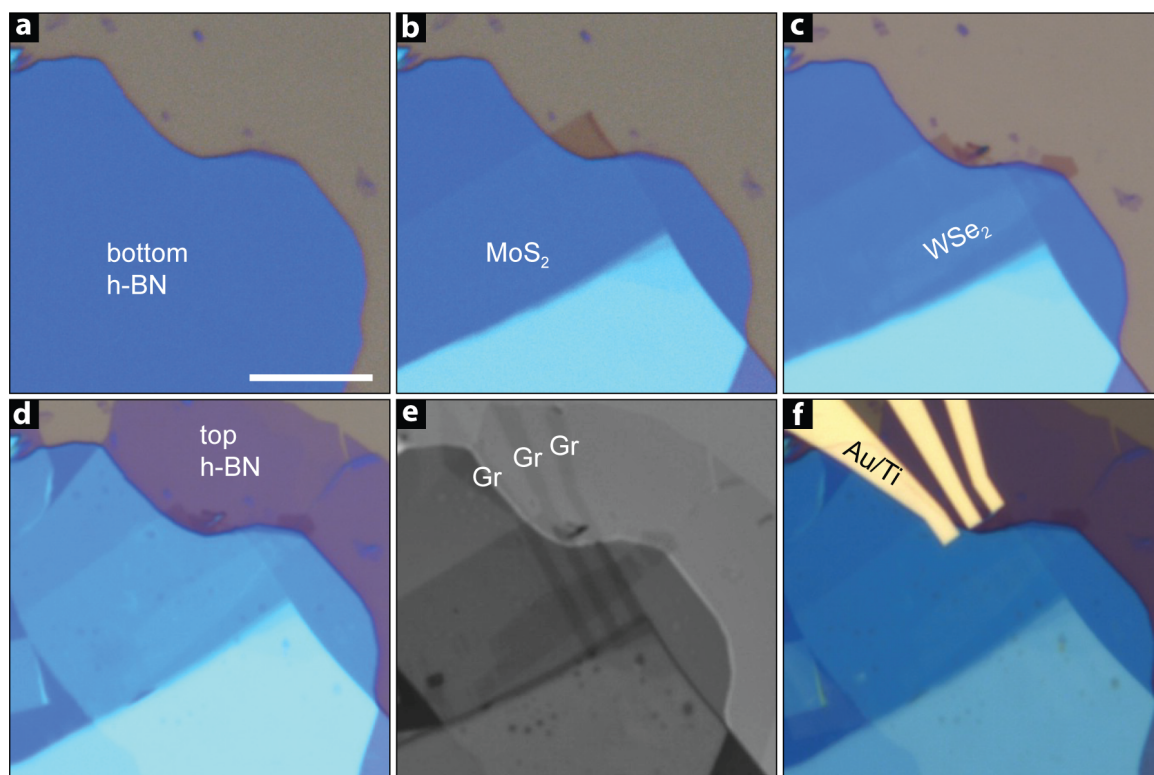


**Figure 6.39** – Heterostructure fabrication. Optical images taken during different fabrication steps: (a) exfoliation of the bottom h-BN; (b) transfer of monolayer MoS<sub>2</sub> flake; (c) transfer of monolayer WSe<sub>2</sub> flake; (d) encapsulation with top h-BN; (e) transfer of pre-patterned few-layer graphene stripes (Gr); (f) metallization of Au/Ti contacts. Optical image (e) is shown in black and white for better visibility of the final structure. Scale bar is 10 μm for every picture.

Multiple transparent top gates are fabricated out of few-layer graphene. This double-gate configuration allows us to apply a vertical electric field without changing the carrier concentration in the MoS<sub>2</sub>/WSe<sub>2</sub> heterostructure. Few-layer graphene flakes were obtained by exfoliation from graphite (NGS) on Si/SiO<sub>2</sub> substrates and patterned in the desired shape by e-beam lithography and oxygen plasma etching. After thermal annealing, the patterned flakes were transferred on top of the van der Waals stack using a polymer-assisted transfer and the entire structure was annealed again in high vacuum. Finally, electrical contacts were fabricated by electron beam lithography and metallization of 60/2-nm thick Au/Ti layer.

Figure 6.40a shows a false-color optical micrograph of the resulting stack. We characterize the structure by PL mapping at room temperature, under 647 nm-excitation. Figures 6.40b-d show the intralayer emission distribution at the wavelengths characteristic of MoS<sub>2</sub> (670 nm), WSe<sub>2</sub> (750 nm) and the interlayer exciton (785 nm). While individual monolayers



appear to be homogeneously bright, emission from the heterostructure region is uniformly quenched by more than three orders of magnitude due to the efficient charge transfer between layers. Even with such strong quenching, we are able to detect the interlayer peak in the PL spectra, confirming the generation of interlayer excitons. Since this effect is playing a central role in our work, we have fabricated three more heterostructures encapsulated in h-BN, confirming the reproducibility of weak interlayer signal from the heterostructures encapsulated in h-BN compared to the ones fabricated on SiO<sub>2</sub> like the one presented in Figure 6.37c. We also note that a similar result was observed in an earlier report [257].

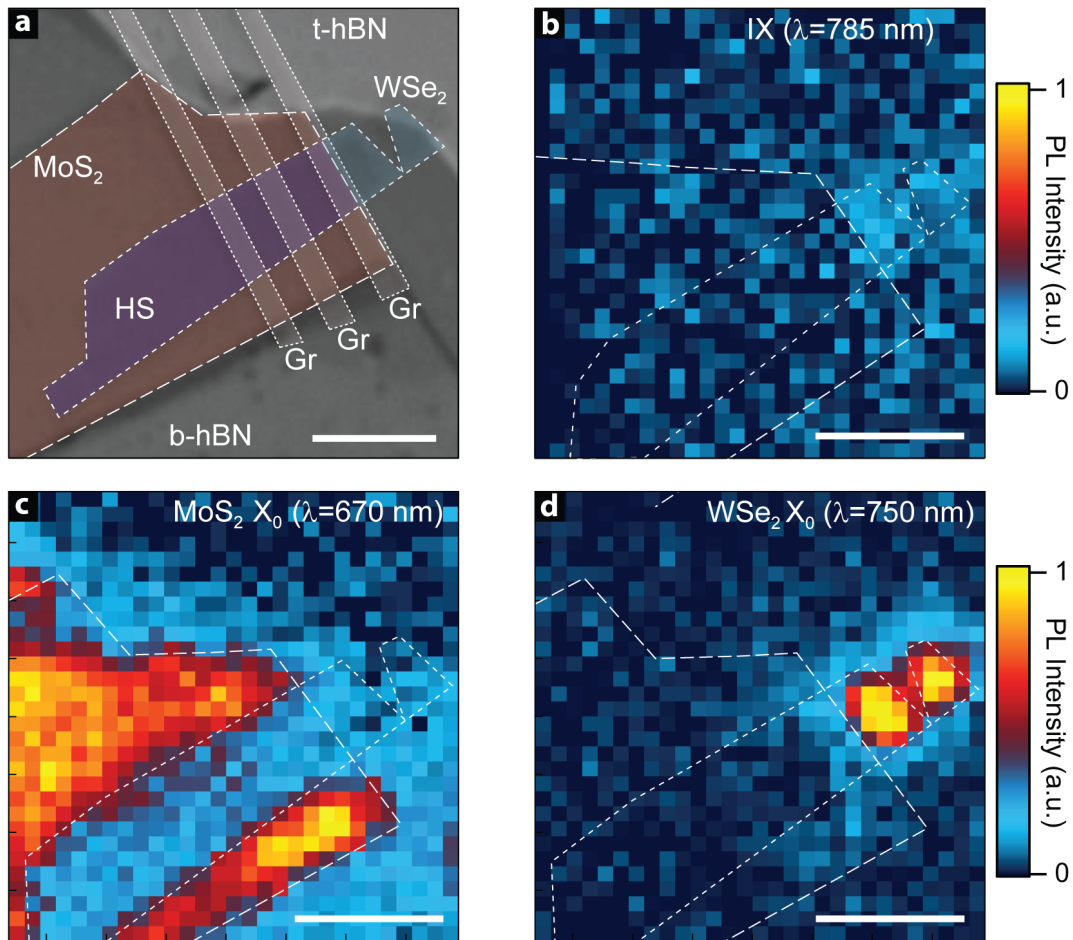


**Figure 6.40** – Device optical characterization. (a) Optical image of the device with false colors highlighting the different materials. (b-d) Spatial maps of photoluminescence at 785 nm, 670 nm and 750 nm, corresponding to the interlayer exciton, MoS<sub>2</sub> and WSe<sub>2</sub> intralayer excitonic resonances correspondingly. Intralayer photoluminescence is quenched in the bilayer area due to efficient charge transfer in the high quality heterostructure. Interlayer exciton is weak in the structures encapsulated with boron nitride. Scale bar is 5  $\mu\text{m}$  for every panel.

Due to the small separation between the interlayer and the intralayer WSe<sub>2</sub> exciton peaks,

it is not possible to completely distinguish them in the images acquired on the CCD. In fact, the tail of the WSe<sub>2</sub> monolayer peak normally has a considerable overlap with the spectral line of the interlayer exciton, meaning that weak luminescence around 785 nm can be observed even on monolayer WSe<sub>2</sub> (Figure 6.40b), which is not due to interlayer excitons.

### Numerical simulations

Prior to electrostatic manipulation of exciton transport, we first calculate the electrical field distribution in our system using COMSOL Multiphysics simulation software. All calculations were performed considering the dimensions of the device as follows: the graphene top gates are around 1.1  $\mu\text{m}$ -wide and spaced  $\sim 0.8 \mu\text{m}$  apart. The heterostructure is encapsulated between two h-BN crystals ( $\sim 10 \text{ nm}$  on the top and  $\sim 20 \text{ nm}$  at the bottom), and the substrate is heavily doped Si with 270 nm of SiO<sub>2</sub> on top.

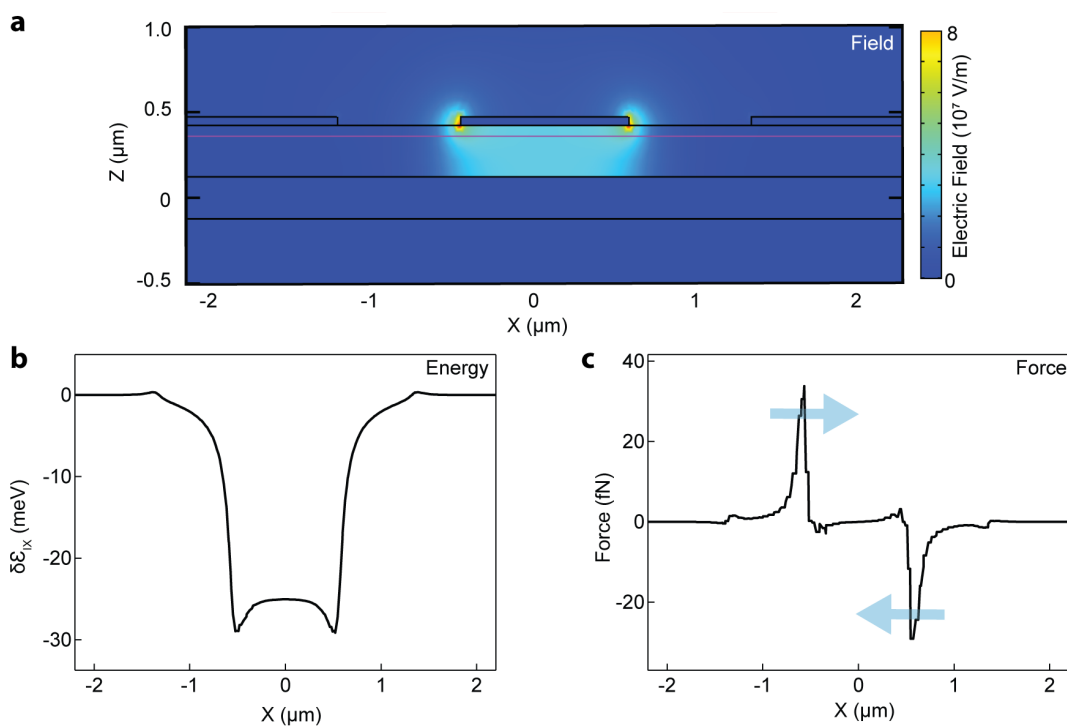


**Figure 6.41** – Numerical simulation of the interlayer exciton in the external field. (a) 2D cross-sectional map of the electric field amplitude distribution calculated for the device in the "exciton confinement" configuration, with -10 V applied to central gate, and side gates grounded. (b) Corresponding amplitude of the vertical electric field (black) and electrostatic potential (red) along the heterobilayer. (c) Energy shift experienced by an interlayer exciton (black) and a single hole (red) along the same cross-section. (d), Projection along the  $x$  axis of the confinement force experienced by the interlayer exciton due to the presence of the electric field. Blue arrows show the direction of the force.

We plot spatial distribution of the electric field in Figure 6.41a for the system in the confinement configuration, with -10 V applied to the central gate and side gates grounded. Interlayer excitons have a built-in out-of-plane dipole moment directed upwards, with an absolute value  $p = ed = e \times 7.5 \cdot 10^{-10} \text{ m}$ , where  $e$  is the elementary charge and  $d = 7.5 \text{ \AA}$  is the layer separation in our heterostructure. They thus experience an energy shift of  $\delta\mathcal{E}_{\text{IX}} = -p_z E_z$  in the presence of a vertical electric field  $E_z$ , which we plot in Figure 6.41b. Energy gradient causes force applied on the exciton in the longitudinal direction (along  $x$  axis). We plot Force amplitude in Figure 6.41c, which is proportional to the first derivative of the vertical electric field  $E_z$  with respect to the channel  $x$  axis,

$$F_x = -\frac{\partial}{\partial x} \delta\mathcal{E}_{\text{IX}} = ed \frac{\partial E_z}{\partial x} \quad (6.8)$$

Applied to the system electric field significantly alters diffusion of interlayer excitons, which we attempt to describe in the following paragraph.

### Diffusion modeling

Dynamics of the exciton in the channel of our device can be modeled with one-dimensional diffusion in the presence of an external potential  $\varphi(x)$ . This potential includes electrostatic potential, dipole-dipole interaction, local temperature of the system and others. The gradient of exciton concentration  $n(x)$  drives diffusion current  $j_{\text{diff}}$  while the potential gradient causes drift  $j_{\text{drift}}$  as following:

$$j_{\text{diff}} = -D \frac{\partial n}{\partial x} \quad j_{\text{drift}} = -\mu \frac{\partial \varphi}{\partial x} n \quad (6.9)$$

where  $\mu$  is exciton mobility related to the diffusion coefficient  $D$  and the thermal energy  $k_B T$  by the Einstein relation  $D = \mu k_B T$ .

In order to derive the exciton diffusion equation, we should also include exciton generation  $G$  as well as recombination  $R$  rate. From the exciton flux conservation equation we then obtain:

$$D \frac{\partial^2 n}{\partial x^2} + \frac{D}{k_B T} \frac{\partial}{\partial x} \left( n \frac{\partial \varphi}{\partial x} \right) + G - R = \frac{\partial n}{\partial \tau} \quad (6.10)$$

In our system, where excitons have a built-in vertical dipole moment  $p_z$ , the electrostatic potential induced by the vertical electric field is  $\varphi_{\text{el}} = -E_z p_z$ . Another important contribution comes from the dipole-dipole repulsion of the excitons, which we estimate from the parallel plate capacitor model as  $\varphi_{\text{rep}} = n \cdot d e^2 / \epsilon_{\text{HS}} \epsilon_0$ .

Excitons are generated by means of optical pumping with a laser spot of Gaussian profile, and the generation rate is therefore  $G \propto \exp(-x^2/w^2)$ . We also take into account two main contributions to the exciton recombination rate. The first one is related to the limited lifetimes of excitons  $-n/\tau$ , and the second one originates from exciton-exciton annihilation at higher concentrations  $-\gamma n^2$ . Combining all these terms together, we obtain the general equation of one-dimensional exciton transport in our system:

$$D \frac{\partial^2 n}{\partial x^2} + \frac{D}{k_B T} \frac{\partial}{\partial x} \left( n \frac{de^2}{\epsilon_{HS} \epsilon_0} \frac{\partial n}{\partial x} - n p_z \frac{\partial E_z}{\partial x} \right) + G_0 e^{-x^2/w^2} - n/\tau - \gamma n^2 = \frac{\partial n}{\partial \tau} \quad (6.11)$$

We now simplify our model to obtain an analytical solution. First of all, we assume a steady-state case ( $\partial n / \partial \tau = 0$ ), since we use continuous wave excitation. We can also neglect such second-order terms as dipole-dipole repulsion and exciton-exciton annihilation, because we will perform measurement far away from the excitation spot, in the region with low concentration of interlayer exciton. Taking this into account, diffusion equation can be described as following:

$$D \frac{\partial^2 n}{\partial x^2} - \frac{D p_z}{k_B T} \frac{\partial}{\partial x} \left( n \frac{\partial E_z}{\partial x} \right) - n/\tau = 0 \quad (6.12)$$

The case of diffusion in the absence of an external field can be solved analytically, revealing exponential decay of exciton density from the pumping region with a characteristic distance corresponding to the diffusion length  $l_{\text{diff}} = \sqrt{D\tau}$ :

$$n_{\text{free}}(x) = n_0 e^{-x/l_{\text{diff}}} \quad (6.13)$$

which is schematically shown in Figure 6.42, where we consider region with homogeneous distribution of generation rate, and region where excitons are free to diffuse.

Application of a non-homogeneous vertical electric field can alter the diffusion length (as will demonstrated experimentally), which can be modeled as a change in the effective diffusion length.

We note that although this simplified model qualitatively explains results of further measurements, for modeling exciton diffusion near the pumping area, one should consider the laser spot profile and exciton-exciton repulsion as in equation 6.4.

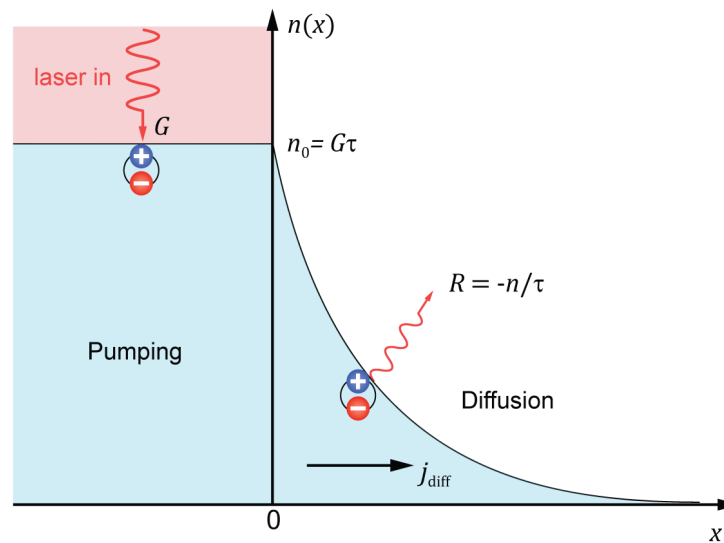


**Figure 6.42** – Modelling of exciton diffusion. Schematic depiction of exciton generation in the pumping area ( $x < 0$ ), and diffusion outside for  $x > 0$  represented by exciton concentration  $n(x)$ . Continuous and homogeneous pumping by the laser (red area) is determined by the generation rate  $G$ . Together with the recombination rate  $R$ , they establish exciton concentration  $n_0$ . Concentration gradient outside the pumping area generates exciton flux  $j_{\text{diff}}$  that drives diffusion and leads to the exponential decay of exciton concentration along the  $x$  axis.

### Device operation

We start with demonstration of an electrically controlled excitonic switch, which was schematically represented in Figure 6.37. Laser light is focused in a diffraction-limited spot inside the heterostructure area which we refer as an input region. It generates interlayer excitons, which diffuse along the channel of the heterostructure according to the transport Equation 6.11.

However, the low brightness of interlayer emission makes monitoring the device operation challenging. For this reason, we use the exposed  $\text{WSe}_2$  layer, which extends out of the heterostructure as a bright emitter. Here, interlayer excitons diffuse towards the edge of the heterostructure. During this diffusion process, interlayer excitons are expected to dissociate into single carriers in a non-radiative pathway. In turn, these charge carriers are allowed to diffuse inside monolayer  $\text{MoS}_2$  and  $\text{WSe}_2$ , where they experience recombination with native charges, resulting in bright emission. The emitted radiation is recorded simultaneously using a CCD camera and a spectrometer to have both spatial and spectral emission profiles. This allows us to further confirm the presence and diffusion of interlayer excitons inside the heterobilayer.

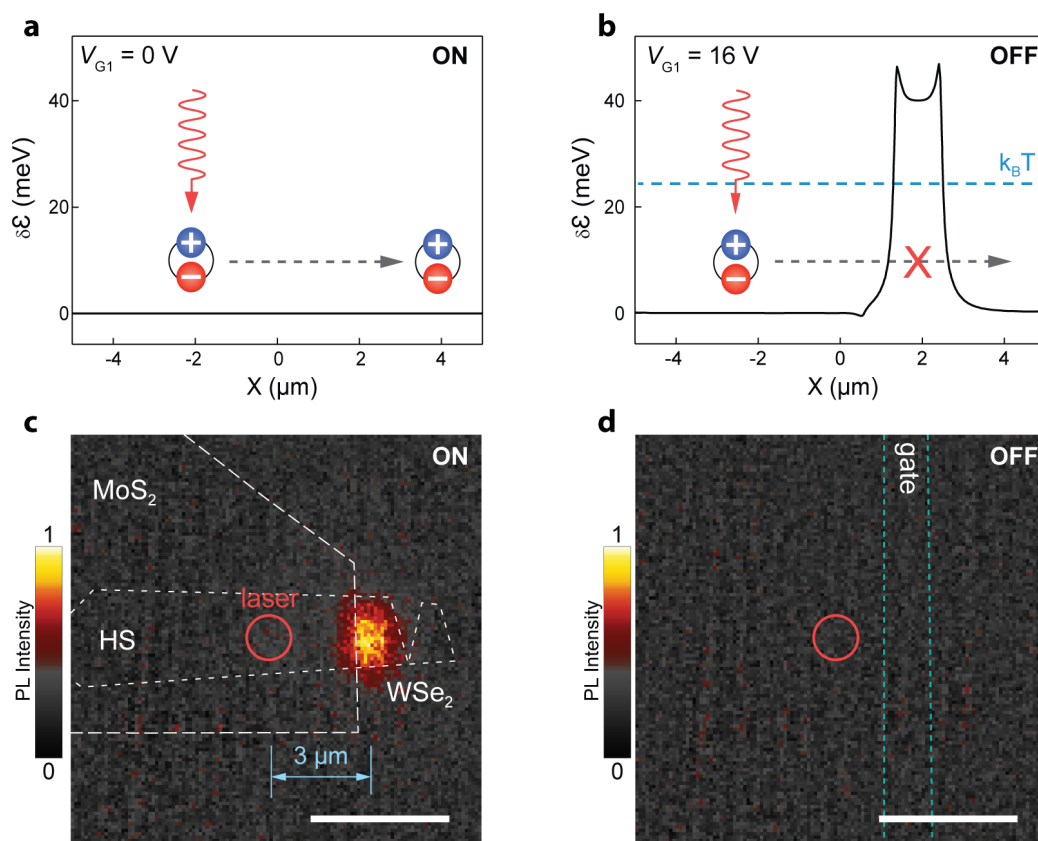


**Figure 6.43** – Excitonic transistor operation at room temperature. (a,b) Calculated energy variation  $\delta\mathcal{E}$  for the excitons in the ON (free diffusion) and OFF (potential barrier) states. (c,d) Corresponding images of exciton emission. Dashed lines indicate positions of the different layers forming the heterostructure and the graphene top gate 1. Scale bar is  $5\ \mu\text{m}$ .

In the absence of applied electric fields (Figure 6.43a), excitons diffuse away from the pumping area (red circle in Figure 6.43c) due to temperature and concentration gradients [248, 250, 258], and reach the recombination site, approximately  $3\ \mu\text{m}$  away, where we detect their emission. Careful comparison of pumping and emission profiles shown in Figure 6.44 lets us exclude the possibility of a direct excitation of monolayer  $\text{WSe}_2$  by the low-intensity tail of the laser spot. We refer to this configuration of exciton free diffusion as a ON state of the excitonic transistor. This situation with bright output is shown in the emission image in Figure 6.43c.

Figure 6.43b shows the contrary case, when introducing a potential barrier higher than  $k_B T$  on the path of the diffusing excitons impedes their motion. This results in the suppression of light emission, as shown in Figure 6.43d.

In Figure 6.44 we show cutlines of the emission profiles at the intermediate gate voltages. Building up energy barrier gradually suppress output emission all the way down to the

noise level. In other words, we can achieve efficient electrical modulation of the output emission.

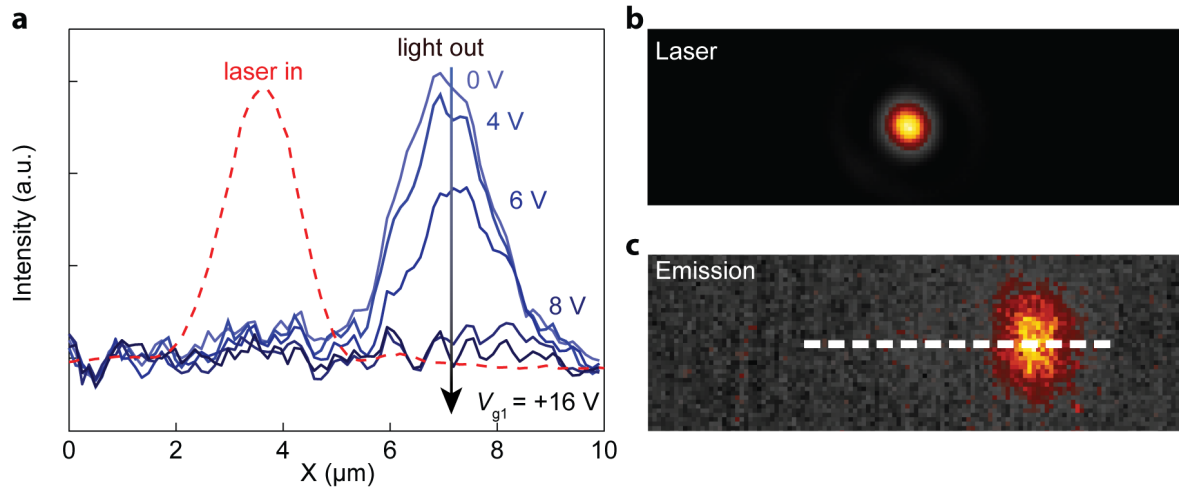


**Figure 6.44** – Excitonic transistor input and output. (a) Cross-sectional profile of the device emission intensity along the white dashed line represented in b and c obtained for different gate voltages  $V_{G1}$  from 0 V (light-blue) to 16 V (black) with intermediate values of 6, 8 and 10 V. Red line represents the intensity profile of the laser spot. (b) and (c) CCD images of the focused laser spot and the exciton emission in the ON state. Length of the dashed line is 10  $\mu\text{m}$ .

In Figure 6.45, we plot the emission intensity normalized by the value in the OFF state, that corresponds to  $V_{G1} = +16$  V, as a function of applied voltage. As reference, we also plot the intensity modulation (similarly normalized by the value at  $V_{G1} = +16$  V) observed when the laser beam is located on the emission center ( $d_{l-o} = 0$   $\mu\text{m}$ ).

We obtain the switching threshold to be around 8 V, which corresponds well with the calculated exciton energy modulation of  $\delta\mathcal{E} \sim k_B T \sim 25$  meV (blue dashed line). This result is consistent with our model: since the energy barrier height starts to become comparable to thermal excitation, it is now possible to block the diffusion of excitons.

We extract an intensity ON/OFF ratio larger than 100, limited by the noise level of the setup in the OFF state. This is the first reported excitonic transistor with a complete suppression of emission in the OFF state. This effect is also clearly visible in the spectrum of the emitted light, where the  $\text{WSe}_2$  peak is selectively suppressed when the device is in the OFF state. It is also worth noting that strong emission from  $\text{MoS}_2$  is detected in both states, as excitons can freely diffuse in other directions, although this emission is removed with a 700-nm longpass filter.

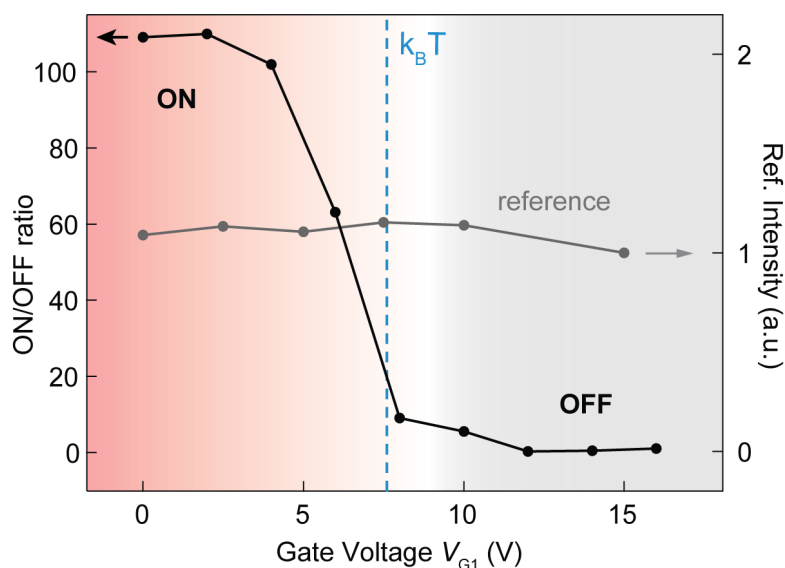


**Figure 6.45** – Exciton transistor. Gate dependence of the ON/OFF ratio when optically exciting 3  $\mu\text{m}$  away from the emission center.

### Reference experiment

In order to exclude that the observed effect arises from an unwanted modulation of the charge carrier density in  $\text{WSe}_2$ , we perform a reference experiment which we describe hereafter.

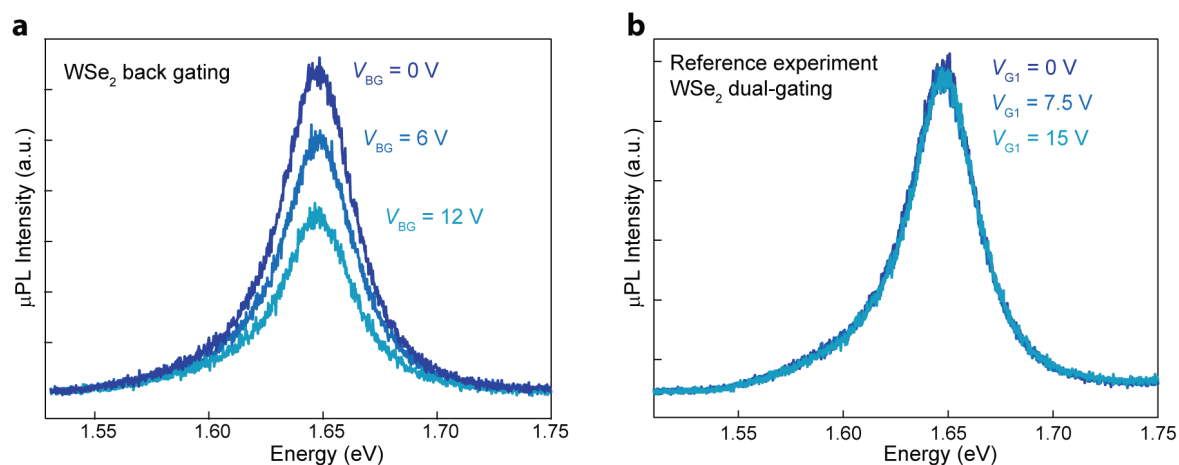


**Figure 6.46** – Reference experiments. (a) Photoluminescence spectrum from monolayer  $\text{WSe}_2$  at different back-gate voltage values. A significant modulation of the emission intensity is observed. b, Photoluminescence spectrum from monolayer  $\text{WSe}_2$  when using top- and back- gates in the dual-gated configuration for the voltage range similar to the employed for demonstration of exciton transistor. No appreciable intensity modulation is observed. Both measurements are performed on the same  $\text{WSe}_2$  flake with the same cw excitation at 647 nm with 200  $\mu\text{W}$  incident power.



First, we observed how the PL emission from monolayer WSe<sub>2</sub> changes with gating of the device using the backgate. For this purpose, we excite with the laser beam directly the exposed WSe<sub>2</sub>, and record the photoluminescence spectra we obtain. As shown in Figure 6.46a, when applying voltage to the backgate, a modulation in the emission intensity is clearly observable. Then, we repeat the same measurement but this time, instead of applying a voltage between the flake and the backgate, we bias the top- and back-gate, thus generating a vertical electric field inside the device. As shown in Figure 6.46b, in this case we cannot observe a significant change in the emission intensity. This allows us to rule out that the switching action we observe could be due to a suppression of PL from a changed doping level in the material.

### Input-output separation

We further study the dependence of the ON/OFF ratio on the input-output separation distance  $d_{i-o}$ . For this, we keep the voltage profile constant and optically injecting excitons at different distances from the output point. The corresponding results are shown in Figure 6.47. Consistently with our model, we observe an efficient modulation when the laser is focused beyond the energy barrier, with emission intensity decreasing with increasing of  $d_{i-o}$  due to the long-distance diffusion.

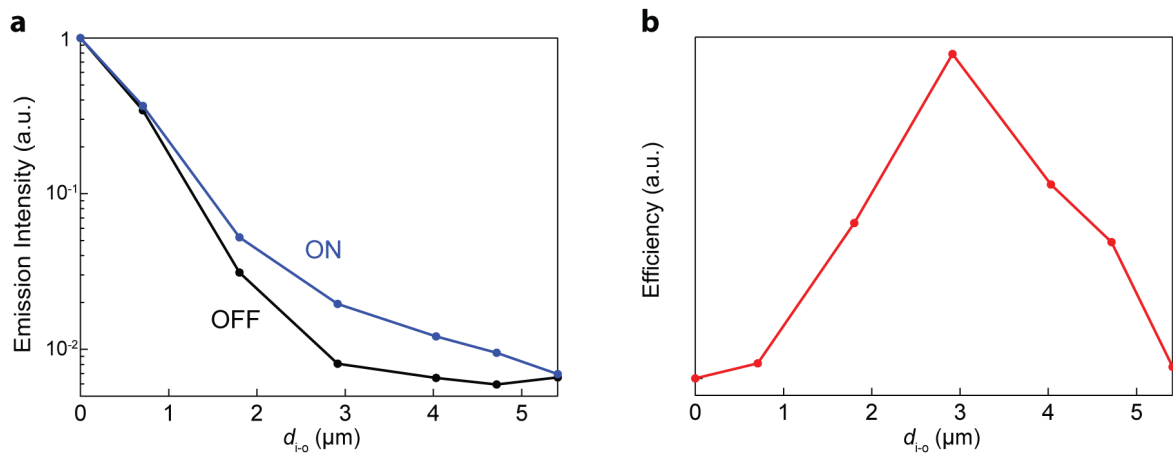


**Figure 6.47** – Excitonic transistor characterization for different positions of the excitation laser spot. (a) Normalized emission intensity (transistor output) as a function of the distance between optical injection and emission point  $d_{i-o}$ , shown for the ON (blue,  $V_{G1} = 0$  V) and OFF (black,  $V_{G1} = 16$  V) states. (b), Transistor efficiency calculated as the ratio between output emission in the ON and OFF states for different input-output separation distances. Efficiency reaches a maximum when the laser spot is moved completely beyond the gate, so that the energy barrier stays between the input and the output and thus effectively modulates exciton diffusion.

### 6.5.4 Exciton drift currents

Having demonstrated that we can block or allow spontaneous exciton diffusion, we go further by creating a drift field in the desired direction, in analogy with the source-drain bias of a conventional FET.

We show this type of operation in Figure 6.48, where all three electrodes are used to create a potential ladder going upwards/downwards with respect to the excitation point (Figures 6.48a,b). When excitons encounter a gradually decreasing energy profile (forward bias), their diffusion is enhanced by a drift term, allowing us to operate the device with a larger distance between optical input and output.

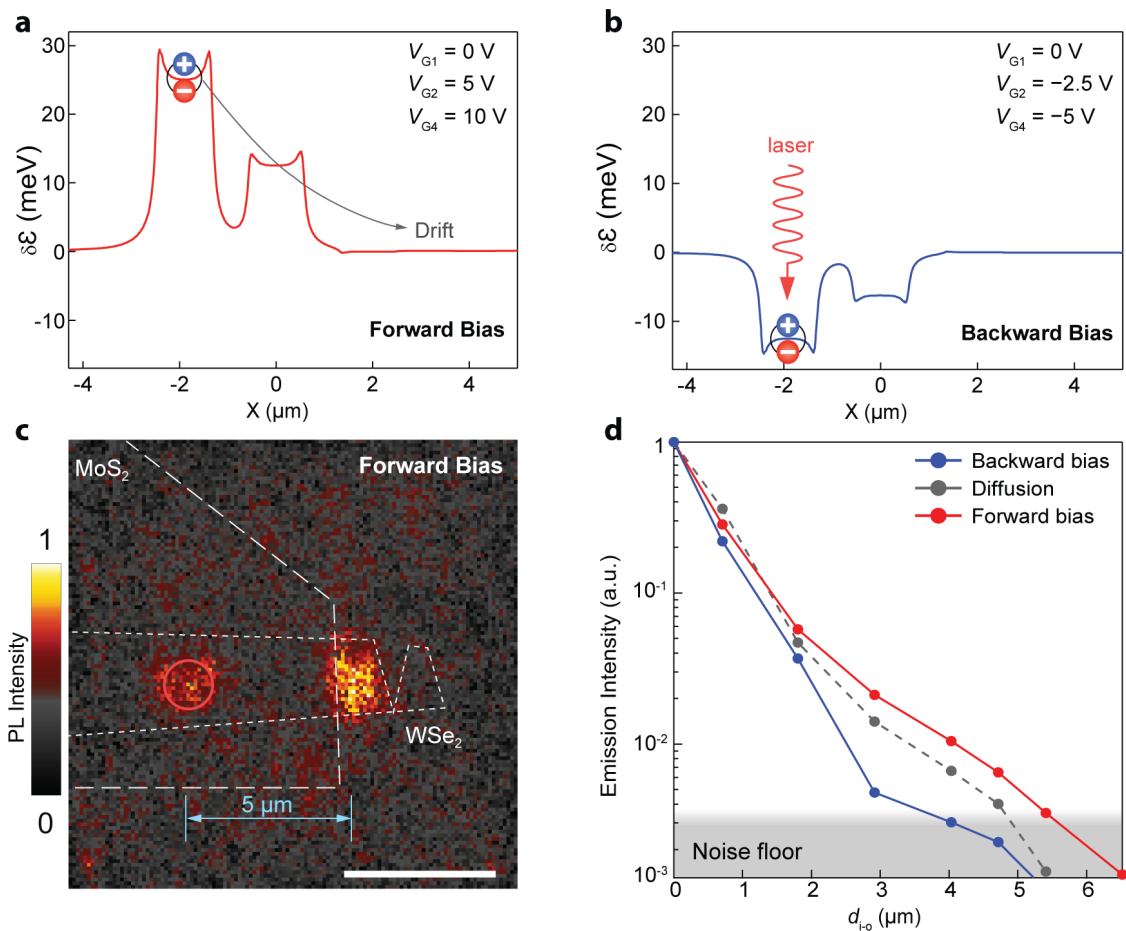


**Figure 6.48** – Biasing of the excitonic device. (a,b) Calculated energy profile  $\delta\mathcal{E}$  of the indirect exciton for the forward and backward bias cases. (c) Images showing exciton emission from the device when injecting at a distance  $d_{i-o} = 5\ \mu\text{m}$  from the emission area. The laser spot is represented by the red circle. Scale bar is 5  $\mu\text{m}$ . (d) Normalized output intensity as a function of the distance between optical injection and emission points, for the forward (red) and backward (blue) bias configurations. Exciton diffusion over a distance of 5.5  $\mu\text{m}$  is achieved.

As shown in Figure 6.48c, this regime of electrically assisted diffusion can result in exciton transport over a 5  $\mu\text{m}$  distance. In order to have a more quantitative estimation of the induced modulation, we measure the dependence of the emission intensity on the distance from the laser spot as it is displaced away from the output area at fixed gate voltages. The results are represented in Figure 6.48d, showing that the length over which excitons diffuse can be effectively modulated from 5.5  $\mu\text{m}$  to 3  $\mu\text{m}$ , with respect to  $\sim 4$   $\mu\text{m}$  in the unbiased case. The modulation of the effective diffusion length with the potential  $\varphi_{\text{el}}$  qualitatively follows the model introduced in the simplified Equation 6.13.

### 6.5.5 Reconfigurable potential

We further employ the multi-gate configuration to demonstrate more complex and electrically reconfigurable types of potential landscapes and related device operation. In Figures 6.49a,b we present the calculated energy profiles for potential well (Figure 6.49a) compared to repulsive barrier (6.49b) produced by the central gate 2 ( $V_{G2}$ ), while side gates are kept grounded ( $V_{G1} = V_{G3} = 0$  V). In this case, the position of the optical pump is centered on the middle electrode, corresponding to the center of the well/barrier.

Figure 6.49c and Figure 6.49e show the CCD camera image and related emitted intensity profile along the device channel for the case of the potential well. We observe PL emission only from the narrow area below the central graphene contact, thus achieving electrical confinement of the excitonic cloud. Conversely, when applying a positive voltage to create a "potential hill" (Figure 6.49d,f), we see an expulsion of excitons from the pumping area with the appearance of bright emission spots outside the middle section of the device, due to excitons drifting along the energy profile and recombining on the edges of the heterostructure. This is evident from a comparison with the free-diffusion case as in Figure 6.43c.

Interestingly, we also observe higher-energy emission from the neighboring MoS<sub>2</sub> monolayer parts inside the well in the case of exciton confinement. A similar effect is also observed during exciton expulsion, with bright spots appearing at the edges of the heterostructure around the repulsive potential. Further inspection of the emission spectra from Figures 6.49c,d confirms this, showing decreasing (increasing) intensity of monolayer peaks when confining (anti-confining) the excitons. We assign the observed MoS<sub>2</sub> emission to the local inhomogeneity of the substrate. Because of the use of the 700 nm filter, the emission from monolayer MoS<sub>2</sub>, in principle, should not be observed on the CCD. However, some light can be transmitted when the broadening of the PL peak results in a low-energy tail extending beyond 700 nm, which can pass through the filter. Local inhomogeneity in the substrate can affect this broadening, which explains why the observed MoS<sub>2</sub> luminescence in Figure 6.49d comes mostly from the left part of the device.

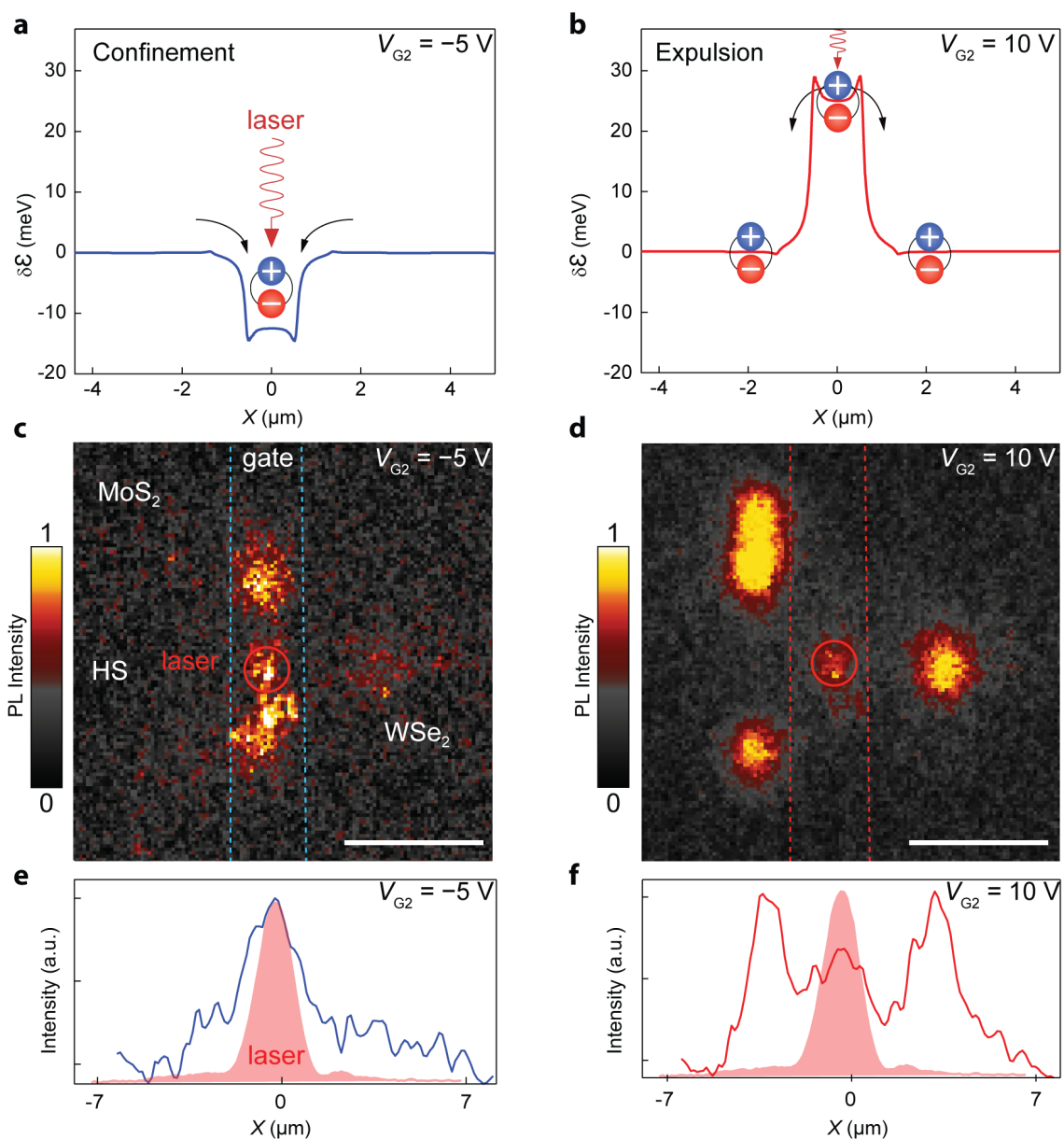


**Figure 6.49** – Electrically reconfigurable energy landscape. (a,b) Calculated energy profile  $\delta\mathcal{E}$  of the indirect exciton for the cases of a potential well and a potential barrier. (c,d), Imaging of exciton emission for the configurations shown in a and b. Incident laser light (red circle) is focused on top of the gate 2. Dashed lines indicate positions of different layers forming the heterostructure and the graphene top gate 2. Scale bar is 5  $\mu\text{m}$ . (e,f) Cross-section of the intensity profile along the device channel, integrated over its width for the three configurations described above. The red overlay represents the profile of the excitation laser.

### 6.5.6 Discussion

An alternative mechanism which could in principle explain the recombination far away from the excitation spot is based on the diffusion of single carriers rather than interlayer excitons. Indeed, it has been shown that such carriers (holes in particular) can have long lifetimes [257]. However, experimental observations indicate that this is not the dominant mechanism in our heterostructure. First of all, we directly observe the production of interlayer excitons in the excitation area, even if the intensity is low. Second, for a flux of single carriers, the voltage modulation necessary to counteract thermal excitation and block the single-particle flux would be  $\sim 50$  mV, more than two orders of magnitude lower than the  $\sim 8$  V gate voltage required in our experimental result shown in Figure 6.45. Finally, this mechanism would also result in different emission profiles for confinement/repulsion regimes of device operation that we explain below.

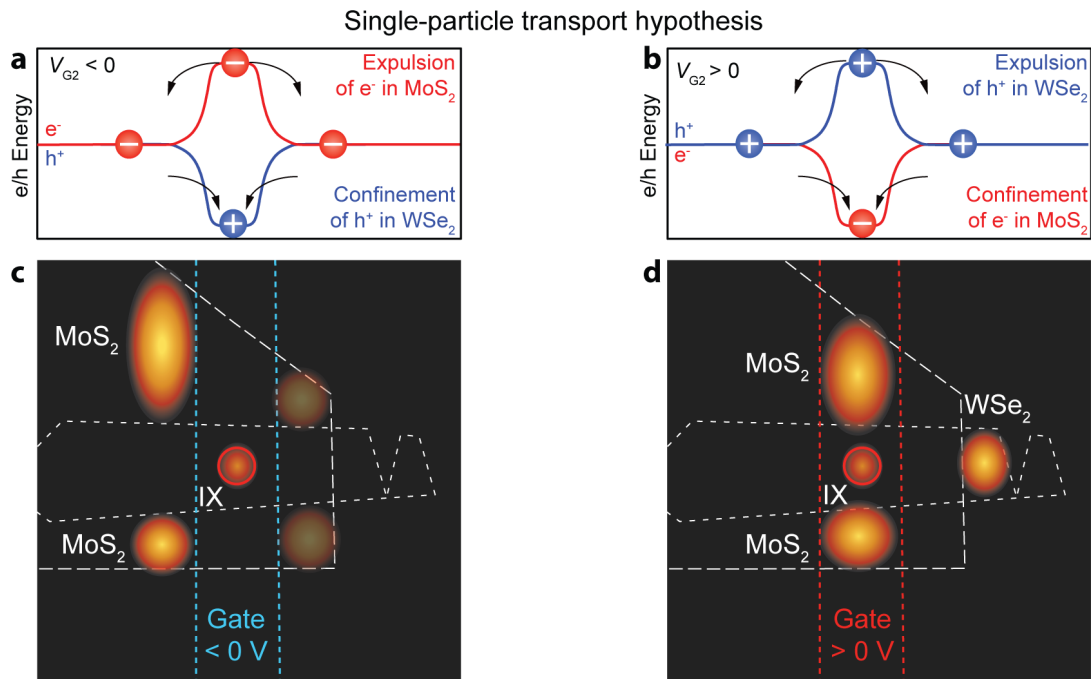


**Figure 6.50** – Schematic depiction of the control over the light emission. (a,b) Energy profile for electrons (red) and holes (blue) located in MoS<sub>2</sub>. (c,d) Expected emission images in the single-particle assumption. Scale bar is 5  $\mu m$ .

Figures 6.50a-d are schematic drawings based on the hypothesis that, following the fast interlayer charge transfer, photoexcited carriers move independently, rather than being bound in interlayer excitons. The diffusion of single electrons and holes is then subject to the type-II band alignment between MoS<sub>2</sub> and WSe<sub>2</sub>, which restricts the motion of electrons to MoS<sub>2</sub> and holes to WSe<sub>2</sub>. This charge separation is very efficient, as indicated

by the strong suppression of intralayer emission from the HS area (Figure 6.40). Once the separation occurs, it is not very likely that the charges can hop between the layers: the band difference between MoS<sub>2</sub> and WSe<sub>2</sub> is more than 200 meV, so thermal excitation of 25 meV will not be enough for electrons to tunnel back in WSe<sub>2</sub> and holes to MoS<sub>2</sub>. Second is the local electrostatic potential defined by the gate. The application of  $V_{G2} < 0$  creates a confining energy profile for single holes and a repulsive one for single electrons, as in Figures 6.50a,c. Holes would then be confined in the WSe<sub>2</sub> area under the gate while electrons would be pushed out to MoS<sub>2</sub> areas next to the gate, where they would recombine with charges already present in the monolayer part, resulting in PL from single layer areas of MoS<sub>2</sub> next to the gate (provided there are enough holes in MoS<sub>2</sub> to start with). We would then have the emission pattern shown in c, assuming the presence of native holes in MoS<sub>2</sub>. In their absence, we would only see one emission spot, coinciding with the excitation laser spot. Along the same lines, applying a positive gate voltage to the middle gate ( $V_{G2} > 0$ ), would result in the repulsive potential for holes in WSe<sub>2</sub> and attractive for electrons in MoS<sub>2</sub>. Recombination would then occur for electrons in MoS<sub>2</sub> in regions under the gate and holes in WSe<sub>2</sub> in regions outside the gate, Figure 6.50d. This is in contradiction with the experimental observations in Figures 6.49. In the case of interlayer exciton transport we instead have only a single energy profile, and the application of a positive voltage on the middle gate results in the expulsion of interlayer excitons from the injection region. This precisely resembles our experimental observations.

### 6.5.7 Conclusion

In this section, we have demonstrated that large lattice mismatch of WSe<sub>2</sub>/MoS<sub>2</sub> heterostructure effectively vanishes moiré-related effects, which allows observation of long-distance excitonic diffusion. We achieved here room temperature electrical control over the exciton flux with On/OFF ratio as large as 100. We also demonstrated further possibilities like biasing and confinement of excitons in a reconfigurable energy landscapes.

## 6.6 Conclusion and outlook

In this chapter, we have bridged some of the important gaps in valleytronics and excitonics, including control over the polarization state and transport of the valley-polarized excitons, as well as room temperature control of exciton transport.

In the first section of the chapter, we found that behavior of the interlayer excitons hosted in aligned  $\text{WSe}_2/\text{MoS}_2$  heterostructures are strongly affected by the moiré effects. We further demonstrated the efficient switch of the polarization emission by means of electrostatic gating.

In the second section, we focused our attention on the transport of such interlayer excitons. We employed an atomically thin spacer layer between constituent layers of heterostructure to suppress moiré-related potential variation which traps excitons, in order to realize a system with long diffusion. We have demonstrated that exciton transport can be further controlled *via* an external electric field by artificially established energy landscape. This allowed us to realize an excitonic transistor that controls the transport of valley-polarized quasi-particles. Furthermore, we have trapped excitons in electrostatically defined energy traps for reaching high exciton densities.

In the third section of the chapter, we employed alternative material combination, which allowed us to abandon interlayer spacer responsible for the decrease in binding energies of interlayer excitons. This approach allowed us to realize an excitonic transistor that operates at room temperature.

New concepts and applications of exciton-based optoelectronic devices and the study of excitons in confining and engineered potential profiles can be envisaged in the future.





## 7 Conclusion

In this thesis, we have focused on exceptional optical properties and the rich spin-valley physics of two-dimensional materials and their heterostructures. Specifically we explored them in order to overcome fundamental limitations of the conventional charge-based solid-state devices. We shortly summarize our results and future opportunities hereafter.

### **Optoelectronic devices**

In Chapter 4, we have demonstrated reconfigurable light-emitting diodes based on single layer WSe<sub>2</sub>. We also presented ultrasensitive MoS<sub>2</sub> photodetectors integrated with photonic structures. We have achieved near-unity lateral light absorption, which resulted in large and tunable photoresponse of the photodetector. Moreover, we have realized several alternative device architectures for fast-speed and low-power operation. We believe that devices presented in this chapter hold promise for future chip-integrated optical interconnects. As a following step toward this aim, it is essential to develop a photonic circuit with integrated LED and PD operating at the same wavelength and/or based on the same material system.

### **Optospintronic devices**

In Chapter 5, we have harvested complementary properties of two-dimensional materials in their heterostructures, to achieve efficient and non-destructive optical spin injection into graphene. We have also demonstrated the possibility of electrical and optical control of spin transport, by realizing a spin modulator based on a Gr/WSe<sub>2</sub> heterostructure. Although results on the spin signal modulation are exciting, more experimental investigation as well as theoretical work should be performed to uncover the exact origin of this effect. Along this direction, we also look forward to employ metallic 2D magnets for electrical spin injection into graphene in order to realize a fully van der Waals spin valve device.

### Excitonic devices

In the last chapter, we have covered important aspects of valleytronics and excitonics in the 2D limit across ultra-sharp interfaces. Specifically, we have carefully studied aligned type-II heterostructures made of atomically-thin semiconductors, which host interlayer excitons strongly affected by a naturally-established moiré pattern. We have demonstrated comprehensive control over properties of these quasi-particles, including their energy, intensity, and polarization. This allowed us to realize a valleytronic switch by inverting the polarization state of the emitted light, which holds great promise in the framework of valleytronics. Moreover, by the engineering interlayer coupling, we could hinder moiré-trapping of exciton diffusion towards the achievement of a system with extended diffusion. This allowed us to realize an electrostatically controlled excitonic switch, the device which provides a direct link between optical data transmission and an electrical processing system. By further employing electrostatically defined traps, we could confine excitons to very high concentrations above  $10^{12} \text{ cm}^{-2}$ . This is particularly promising as the first step toward high-temperature Bose-Einstein condensation. Furthermore, we have studied alternative approaches which allowed us to realize room-temperature excitonic transistor, with complete suppression of emission in the OFF state. We have also demonstrated exciton diffusion over the  $5 \mu\text{m}$  distances in this system.

Further experimental work is required in the case of  $\text{WSe}_2/\text{MoSe}_2$  heterostructures to achieve high exciton densities away from the excitation point in order to achieve conditions necessary for the observation of degenerate excitonic gasses including high-temperature Bose-Einstein condensation. Possible directions include exploration of a specially engineered ramp-like potential traps for driving thermalized excitons towards the global energy minimum aside from laser heating. Pulse excitation is also a promising technique for reaching even higher exciton densities. Regarding the  $\text{WSe}_2/\text{MoS}_2$  structures, recent reports suggest presence of a direct interlayer transition around 1 eV. Additional investigation is therefore required at this lower energy for shedding a light on the exciton diffusion and upconversion processes.

After all, the use of 2D-material based heterostructures together with the availability of a large variety of CVD-grown 2D materials make it possible to further develop the devices for practical applications. We believe that our results hold great promise for new paradigms in the information processing, including optoelectronic interconnects, spin- and valleytronics, as well as excitonics. However, joint interdisciplinary research by material scientists, physicists and engineers yet to be done on the way towards the achievement of these established aims.

# Abbreviations & Symbols

Å	Ångström
AC	Alternating current
AFM	Atomic force microscopy
Al <sub>2</sub> O <sub>3</sub>	Aluminum oxide
ALD	Atomic-layer-deposition
Au	Gold
<i>B</i>	Magnetic field
°C	Degree Celsius
C <sub>BG</sub>	Back-gate capacitance
C <sub>HS</sub>	Heterostructure capacitance
C <sub>TG</sub>	Top-gate capacitance
CB	Conduction band
CBM	Conduction band minimum
CCD	Charge-coupled device
CHF <sub>3</sub>	Trifluoromethane
CMi	Center of micronanotechnology
CMOS	Complementary metal-oxide-semiconductor
CNP	Charge neutrality point
CP	Circular polarization
CQM	Coupled quantum wells
CW	Continuous wave
Co	Cobalt
Cr	Chromium
CVD	Chemical Vapor Deposition
CVT	Chemical Vapor Transport
<i>D</i>	Diffusion coefficient
DC	Direct current
DCP	Degree of circular polarization
DFT	Density functional theory
DOF	Degree of freedom

## Abbreviations & Symbols

---

DOS	Density of states
DOP	Degree of polarization
$\epsilon_0$	Permittivity of free space
$\epsilon_{\text{TMD}}$	Relative permittivity of a TMDC crystal
$\epsilon_{\text{hBN}}$	Relative permittivity of an h-BN crystal
$e$	Elementary charge
$E_{\text{B}}$	Binding energy
$E_{\text{C}}$	Energy of conduction band
$E_{\text{F}}$	Fermi level
$E_{\text{g}}$	Band gap
$E_{\text{V}}$	Energy of valence band
e-beam	Electron-beam
EBL	Electron-beam lithography
EL	Electroluminescence
EM	Electron multiplication
$f$	Frequency
Fe	Iron
FET	Field-effect transistor
FDTD	Finite-difference time-domain method
FIB	Focused ion beam
FWHM	Full width at half maximum
GC	Diffraction grating coupler
Gr	Graphene
$\hbar$	Planck's constant
H	Hydrogen
h-BN	Hexagonal boron nitride
He	Helium
HE	Hall effect
HOPG	Highly oriented pyrolytic graphite
HS	Heterostructure
$I_{\text{DS}}$	Drain-source current
i.e.	id est or "that is"
IPA	Isopropyl alcohol
IX	Interlayer exciton
$\text{IX}_1$	Lower-energy interlayer exciton
$\text{IX}_2$	Higher-energy interlayer exciton
K	Kelvin
$k_{\text{B}}$	Boltzmann constant
KOH	Potassium hydroxide

$\lambda$	Wavelength
$L_{\text{ch}}$	Channel length
$L_{\text{D}}$	Diffusion length
LCP	Left circular polarization
LED	Light emitting diodes
LP	Linear polarization
LPCVD	Low pressure chemical vapor deposition
LPF	Long-pass filter
$\mu\text{PL}$	Micro-photoluminescence
MBE	Molecular beam epitaxy
MIBK	Methyl isobutyl ketone
ML	Multilayer
MMA	Methyl methacrylate
Mo	Molybdenum
$\text{MoS}_2$	Molybdenum disulfide
$\text{MoSe}_2$	Molybdenum diselenide
$\mu$	Mobility
$\mu_{2\text{C}}$	Two-contact field-effect mobility
$\text{N}_2$	Nitrogen
NA	Numerical aperture
ND	Neutral-density filter
Ni	Nickel
NIR	Near-infrared
NL	Non-local
$\text{O}_2$	Oxygen
$P_{\text{in}}$	Incident power
Pd	Paladium
PD	Photodetector
PDMS	Polydimethylsiloxane
PEM	Photoelastic modulator
PL	Photoluminescence
PMMA	Poly(methyl methacrylate)
Pt	Platinum
$q$	Elementary charge
QHE	Quantum Hall effect
$\rho$	Polarization
$R$	Resistance
RCP	Right circular polarization
Ref.	Reference

## Abbreviations & Symbols

---

RF	Radio frequency
rpm	Rotations per minute
RT	Room temperature
$\sigma$	Conductivity
$\sigma^+$	Right circular polarization
$\sigma^-$	Left circular polarization
s	second
S	Sulfur
Se	Selenium
SEM	Scanning Electron Microscopy
SF <sub>6</sub>	Sulfur hexafluoride
SHG	Second harmonic generation
Si	Silicon
Si <sub>3</sub> N <sub>4</sub>	Silicon nitride
SiO <sub>2</sub>	Silicon oxide
SOC	Spin-orbit coupling
SPF	Short-pass filter
TE	Transverse electric mode
TEM	Transmission electron microscopy
Ti	Titanium
TM	Transverse magnetic mode
TMDC	Transition metal dichalcogenide
UV	Ultraviolet
V <sub>BG</sub>	Back-gate potential
V <sub>DS</sub>	Drain-source bias
V <sub>G</sub>	Gate potential
V <sub>Si</sub>	Silicon potential
V <sub>TG</sub>	Top-gate potential
V <sub>th</sub>	Threshold voltage
VB	Valence band
VBM	Valence band maximum
vdW	Van der Waals
VHE	Valley Hall effect
Vis	Visible spectrum
W	Tungsten
W <sub>ch</sub>	Channel width
WG	Waveguide
WS <sub>2</sub>	Tungsten disulfide
WSe <sub>2</sub>	Tungsten diselenide

X	Exciton
$X^0$	Neutral exciton
$X^+$	Positive trion
$X^-$	Negative trion
$X^D$	Defect-bound exciton
1D	One-dimensional
1L	Monolayer
2D	Two-dimensional
2L	Bilayer
3D	Three-dimensional
3L	Trilayer





## Bibliography

- [1] D. J. Frank, R. H. Dennard, E. Nowak, P. M. Solomon, Y. Taur, and Hon-Sum Philip Wong, "Device scaling limits of Si MOSFETs and their application dependencies," *Proceedings of the IEEE*, vol. 89, pp. 259–288, Mar. 2001.
- [2] D. A. B. Miller, "Rationale and challenges for optical interconnects to electronic chips," *Proceedings of the IEEE*, vol. 88, pp. 728–749, June 2000.
- [3] D. A. B. Miller, "Device Requirements for Optical Interconnects to Silicon Chips," *Proceedings of the IEEE*, vol. 97, pp. 1166–1185, July 2009.
- [4] I. Žutić, J. Fabian, and S. Das Sarma, "Spintronics: Fundamentals and applications," *Reviews of Modern Physics*, vol. 76, pp. 323–410, Apr. 2004.
- [5] A. Rycerz, J. Tworzydło, and C. W. J. Beenakker, "Valley filter and valley valve in graphene," *Nature Physics*, vol. 3, pp. 172–175, Mar. 2007.
- [6] D. Xiao, G.-B. Liu, W. Feng, X. Xu, and W. Yao, "Coupled Spin and Valley Physics in Monolayers of MoS<sub>2</sub> and Other Group-VI Dichalcogenides," *Physical Review Letters*, vol. 108, p. 196802, May 2012.
- [7] L. V. Butov, "Excitonic devices," *Superlattices and Microstructures*, vol. 108, pp. 2–26, Aug. 2017.
- [8] A. A. High, E. E. Novitskaya, L. V. Butov, M. Hanson, and A. C. Gossard, "Control of Exciton Fluxes in an Excitonic Integrated Circuit," *Science*, vol. 321, pp. 229–231, July 2008.
- [9] G. Grosso, J. Graves, A. T. Hammack, A. A. High, L. V. Butov, M. Hanson, and A. C. Gossard, "Excitonic switches operating at around 100 K," *Nature Photonics*, vol. 3, pp. 577–580, Oct. 2009.
- [10] K. S. Novoselov, A. K. Geim, S. V. Morozov, D. Jiang, Y. Zhang, S. V. Dubonos, I. V. Grigorieva, and A. A. Firsov, "Electric Field Effect in Atomically Thin Carbon Films," *Science*, vol. 306, pp. 666–669, Oct. 2004.

## Bibliography

---

- [11] K. S. Novoselov, “Nobel Lecture: Graphene: Materials in the Flatland,” *Reviews of Modern Physics*, vol. 83, pp. 837–849, Aug. 2011.
- [12] A. Castellanos-Gomez, “Why all the fuss about 2D semiconductors?,” *Nature Photonics*, vol. 10, pp. 202–204, Mar. 2016.
- [13] A. K. Geim and K. S. Novoselov, “The rise of graphene,” *Nature Materials*, vol. 6, pp. 183–191, Mar. 2007.
- [14] L. Banszerus, M. Schmitz, S. Engels, M. Goldsche, K. Watanabe, T. Taniguchi, B. Beschoten, and C. Stampfer, “Ballistic Transport Exceeding 28  $\mu\text{m}$  in CVD Grown Graphene,” *Nano Letters*, vol. 16, pp. 1387–1391, Feb. 2016.
- [15] K. S. Novoselov, A. K. Geim, S. V. Morozov, D. Jiang, M. I. Katsnelson, I. V. Grigorieva, S. V. Dubonos, and A. A. Firsov, “Two-dimensional gas of massless Dirac fermions in graphene,” *Nature*, vol. 438, p. 197, Nov. 2005.
- [16] Y. Zhang, Y.-W. Tan, H. L. Stormer, and P. Kim, “Experimental observation of the quantum Hall effect and Berry’s phase in graphene,” *Nature*, vol. 438, p. 201, Nov. 2005.
- [17] K. S. Novoselov, Z. Jiang, Y. Zhang, S. V. Morozov, H. L. Stormer, U. Zeitler, J. C. Maan, G. S. Boebinger, P. Kim, and A. K. Geim, “Room-Temperature Quantum Hall Effect in Graphene,” *Science*, vol. 315, pp. 1379–1379, Mar. 2007.
- [18] L. Wang, I. Meric, P. Y. Huang, Q. Gao, Y. Gao, H. Tran, T. Taniguchi, K. Watanabe, L. M. Campos, D. A. Muller, J. Guo, P. Kim, J. Hone, K. L. Shepard, and C. R. Dean, “One-Dimensional Electrical Contact to a Two-Dimensional Material,” *Science*, vol. 342, pp. 614–617, Jan. 2013.
- [19] K. I. Bolotin, F. Ghahari, M. D. Shulman, H. L. Stormer, and P. Kim, “Observation of the fractional quantum Hall effect in graphene,” *Nature*, vol. 462, pp. 196–199, Nov. 2009.
- [20] W. Han, R. K. Kawakami, M. Gmitra, and J. Fabian, “Graphene spintronics,” *Nature Nanotechnology*, vol. 9, pp. 794–807, Oct. 2014.
- [21] M. Gmitra, S. Konschuh, C. Ertler, C. Ambrosch-Draxl, and J. Fabian, “Band-structure topologies of graphene: Spin-orbit coupling effects from first principles,” *Physical Review B*, vol. 80, p. 235431, Dec. 2009.
- [22] B. Trauzettel, D. V. Bulaev, D. Loss, and G. Burkard, “Spin qubits in graphene quantum dots,” *Nature Physics*, vol. 3, pp. 192–196, Mar. 2007.

- [23] N. Tombros, C. Jozsa, M. Popinciuc, H. T. Jonkman, and B. J. van Wees, “Electronic spin transport and spin precession in single graphene layers at room temperature,” *Nature*, vol. 448, pp. 571–574, Aug. 2007.
- [24] J. Inglá-Aynés, M. H. D. Guimarães, R. J. Meijerink, P. J. Zomer, and B. J. van Wees, “24-mum spin relaxation length in boron nitride encapsulated bilayer graphene,” *Physical Review B*, vol. 92, p. 201410, Nov. 2015.
- [25] T.-Y. Yang, J. Balakrishnan, F. Volmer, A. Avsar, M. Jaiswal, J. Sann, S. R. Ali, A. Pachoud, M. Zeng, M. Popinciuc, G. Güntherodt, B. Beschoten, and B. Özyilmaz, “Observation of Long Spin-Relaxation Times in Bilayer Graphene at Room Temperature,” *Physical Review Letters*, vol. 107, p. 047206, July 2011.
- [26] M. Drögeler, C. Franzen, F. Volmer, T. Pohlmann, L. Banszerus, M. Wolter, K. Watanabe, T. Taniguchi, C. Stampfer, and B. Beschoten, “Spin Lifetimes Exceeding 12 ns in Graphene Nonlocal Spin Valve Devices,” *Nano Letters*, vol. 16, pp. 3533–3539, June 2016.
- [27] F. Schwierz, “Graphene transistors,” *Nature Nanotechnology*, vol. 5, pp. 487–496, July 2010.
- [28] X. Gan, R.-J. Shiue, Y. Gao, I. Meric, T. F. Heinz, K. Shepard, J. Hone, S. Assefa, and D. Englund, “Chip-integrated ultrafast graphene photodetector with high responsivity,” *Nature Photonics*, vol. 7, pp. 883–887, Nov. 2013.
- [29] D. Jariwala, A. Srivastava, and P. Ajayan, “Graphene synthesis and band gap opening,” *arXiv:1108.4141 [cond-mat]*, Aug. 2011.
- [30] S. Bertolazzi, J. Brivio, and A. Kis, “Stretching and breaking of ultrathin MoS<sub>2</sub>,” *ACS nano*, vol. 5, pp. 9703–9709, Dec. 2011.
- [31] D. Akinwande, C. J. Brennan, J. S. Bunch, P. Egberts, J. R. Felts, H. Gao, R. Huang, J.-S. Kim, T. Li, Y. Li, K. M. Liechti, N. Lu, H. S. Park, E. J. Reed, P. Wang, B. I. Yakobson, T. Zhang, Y.-W. Zhang, Y. Zhou, and Y. Zhu, “A review on mechanics and mechanical properties of 2D materials—Graphene and beyond,” *Extreme Mechanics Letters*, vol. 13, pp. 42–77, May 2017.
- [32] R. Cheng, S. Jiang, Y. Chen, Y. Liu, N. Weiss, H.-C. Cheng, H. Wu, Y. Huang, and X. Duan, “Few-layer molybdenum disulfide transistors and circuits for high-speed flexible electronics,” *Nature Communications*, vol. 5, p. 5143, Oct. 2014.
- [33] G. Fiori, F. Bonaccorso, G. Iannaccone, T. Palacios, D. Neumaier, A. Seabaugh, S. K. Banerjee, and L. Colombo, “Electronics based on two-dimensional materials,” *Nature Nanotechnology*, vol. 9, pp. 768–779, Oct. 2014.

## Bibliography

---

- [34] D. Akinwande, N. Petrone, and J. Hone, “Two-dimensional flexible nanoelectronics,” *Nature Communications*, vol. 5, p. 5678, Dec. 2014.
- [35] G. Iannaccone, F. Bonaccorso, L. Colombo, and G. Fiori, “Quantum engineering of transistors based on 2D materials heterostructures,” *Nature Nanotechnology*, vol. 13, p. 183, Mar. 2018.
- [36] K. F. Mak and J. Shan, “Photonics and optoelectronics of 2D semiconductor transition metal dichalcogenides,” *Nature Photonics*, vol. 10, pp. 216–226, Apr. 2016.
- [37] K. F. Mak, D. Xiao, and J. Shan, “Light–valley interactions in 2D semiconductors,” *Nature Photonics*, vol. 12, pp. 451–460, Aug. 2018.
- [38] T. Mueller and E. Malic, “Exciton physics and device application of two-dimensional transition metal dichalcogenide semiconductors,” *npj 2D Materials and Applications*, vol. 2, p. 29, Sept. 2018.
- [39] X. Xu, W. Yao, D. Xiao, and T. F. Heinz, “Spin and pseudospins in layered transition metal dichalcogenides,” *Nature Physics*, vol. 10, pp. 343–350, May 2014.
- [40] J. R. Schaibley, H. Yu, G. Clark, P. Rivera, J. S. Ross, K. L. Seyler, W. Yao, and X. Xu, “Valleytronics in 2D materials,” *Nature Reviews Materials*, vol. 1, p. 16055, Nov. 2016.
- [41] B. Radisavljevic, A. Radenovic, J. Brivio, V. Giacometti, and A. Kis, “Single-layer MoS<sub>2</sub> transistors,” *Nature Nanotechnology*, vol. 6, pp. 147–150, Mar. 2011.
- [42] W. Wu, D. De, S.-C. Chang, Y. Wang, H. Peng, J. Bao, and S.-S. Pei, “High mobility and high on/off ratio field-effect transistors based on chemical vapor deposited single-crystal MoS<sub>2</sub> grains,” *Applied Physics Letters*, vol. 102, p. 142106, Apr. 2013.
- [43] S. Manzeli, D. Ovchinnikov, D. Pasquier, O. V. Yazyev, and A. Kis, “2D transition metal dichalcogenides,” *Nature Reviews Materials*, vol. 2, p. 1733, June 2017.
- [44] D. Rhodes, S. H. Chae, R. Ribeiro-Palau, and J. Hone, “Disorder in van der Waals heterostructures of 2D materials,” *Nature Materials*, vol. 18, p. 541, June 2019.
- [45] X. Cui, G.-H. Lee, Y. D. Kim, G. Arefe, P. Y. Huang, C.-H. Lee, D. A. Chenet, X. Zhang, L. Wang, F. Ye, F. Pizzocchero, B. S. Jessen, K. Watanabe, T. Taniguchi, D. A. Muller, T. Low, P. Kim, and J. Hone, “Multi-terminal transport measurements of MoS<sub>2</sub> using a van der Waals heterostructure device platform,” *Nature Nanotechnology*, vol. 10, pp. 534–540, June 2015.

- [46] R. Pisoni, A. Kormányos, M. Brooks, Z. Lei, P. Back, M. Eich, H. Overweg, Y. Lee, P. Rickhaus, K. Watanabe, T. Taniguchi, A. Imamoglu, G. Burkard, T. Ihn, and K. Ensslin, "Interactions and Magnetotransport through Spin-Valley Coupled Landau Levels in Monolayer MoS<sub>2</sub>," *Physical Review Letters*, vol. 121, p. 247701, Dec. 2018.
- [47] S. Larentis, H. C. P. Movva, B. Fallahazad, K. Kim, A. Behroozi, T. Taniguchi, K. Watanabe, S. K. Banerjee, and E. Tutuc, "Large effective mass and interaction-enhanced Zeeman splitting of K-valley electrons in MoSe<sub>2</sub>," *Physical Review B*, vol. 97, p. 201407, May 2018.
- [48] B. Fallahazad, H. C. P. Movva, K. Kim, S. Larentis, T. Taniguchi, K. Watanabe, S. K. Banerjee, and E. Tutuc, "Shubnikov–de Haas Oscillations of High-Mobility Holes in Monolayer and Bilayer WSe<sub>2</sub>: Landau Level Degeneracy, Effective Mass, and Negative Compressibility," *Physical Review Letters*, vol. 116, p. 086601, Feb. 2016.
- [49] K. Marinov, A. Avsar, K. Watanabe, T. Taniguchi, and A. Kis, "Resolving the spin splitting in the conduction band of monolayer MoS<sub>2</sub>," *Nature Communications*, vol. 8, p. 1938, Dec. 2017.
- [50] A. Splendiani, L. Sun, Y. Zhang, T. Li, J. Kim, C.-Y. Chim, G. Galli, and F. Wang, "Emerging Photoluminescence in Monolayer MoS<sub>2</sub>," *Nano Letters*, vol. 10, pp. 1271–1275, Apr. 2010.
- [51] K. F. Mak, C. Lee, J. Hone, J. Shan, and T. F. Heinz, "Atomically Thin MoS<sub>2</sub>: A New Direct-Gap Semiconductor," *Physical Review Letters*, vol. 105, p. 136805, Sept. 2010.
- [52] O. Lopez-Sanchez, E. Alarcon Llado, V. Koman, A. Fontcuberta i Morral, A. Radenovic, and A. Kis, "Light Generation and Harvesting in a van der Waals Heterostructure," *ACS Nano*, vol. 8, pp. 3042–3048, Mar. 2014.
- [53] R. Cheng, D. Li, H. Zhou, C. Wang, A. Yin, S. Jiang, Y. Liu, Y. Chen, Y. Huang, and X. Duan, "Electroluminescence and Photocurrent Generation from Atomically Sharp WSe<sub>2</sub>/MoS<sub>2</sub> Heterojunction p–n Diodes," *Nano Letters*, vol. 14, pp. 5590–5597, Oct. 2014.
- [54] O. Lopez-Sanchez, D. Lembke, M. Kayci, A. Radenovic, and A. Kis, "Ultrasensitive photodetectors based on monolayer MoS<sub>2</sub>," *Nature Nanotechnology*, vol. 8, pp. 497–501, July 2013.
- [55] M. M. Furchi, A. Pospischil, F. Libisch, J. Burgdörfer, and T. Mueller, "Photovoltaic Effect in an Electrically Tunable van der Waals Heterojunction," *Nano Letters*, vol. 14, pp. 4785–4791, Aug. 2014.

## Bibliography

---

- [56] A. Chernikov, T. C. Berkelbach, H. M. Hill, A. Rigosi, Y. Li, O. B. Aslan, D. R. Reichman, M. S. Hybertsen, and T. F. Heinz, "Exciton Binding Energy and Nonhydrogenic Rydberg Series in Monolayer WS<sub>2</sub>," *Physical Review Letters*, vol. 113, p. 076802, Aug. 2014.
- [57] G. Wang, A. Chernikov, M. M. Glazov, T. F. Heinz, X. Marie, T. Amand, and B. Urbaszek, "Colloquium: Excitons in atomically thin transition metal dichalcogenides," *Reviews of Modern Physics*, vol. 90, p. 021001, Apr. 2018.
- [58] J. S. Ross, S. Wu, H. Yu, N. J. Ghimire, A. M. Jones, G. Aivazian, J. Yan, D. G. Mandrus, D. Xiao, W. Yao, and X. Xu, "Electrical control of neutral and charged excitons in a monolayer semiconductor," *Nature Communications*, vol. 4, p. 1474, Feb. 2013.
- [59] G. Wang, C. Robert, M. M. Glazov, F. Cadiz, E. Courtade, T. Amand, D. Lagarde, T. Taniguchi, K. Watanabe, B. Urbaszek, and X. Marie, "In-Plane Propagation of Light in Transition Metal Dichalcogenide Monolayers: Optical Selection Rules," *Physical Review Letters*, vol. 119, p. 047401, July 2017.
- [60] M. Sidler, P. Back, O. Cotlet, A. Srivastava, T. Fink, M. Kroner, E. Demler, and A. Imamoglu, "Fermi polaron-polaritons in charge-tunable atomically thin semiconductors," *Nature Physics*, vol. 13, pp. 255–261, Mar. 2017.
- [61] M. Barbone, A. R.-P. Montblanch, D. M. Kara, C. Palacios-Berraquero, A. R. Cadore, D. D. Fazio, B. Pingault, E. Mostaani, H. Li, B. Chen, K. Watanabe, T. Taniguchi, S. Tongay, G. Wang, A. C. Ferrari, and M. Atatüre, "Charge-tuneable biexciton complexes in monolayer WSe<sub>2</sub>," *Nature Communications*, vol. 9, p. 3721, Sept. 2018.
- [62] Y. You, X.-X. Zhang, T. C. Berkelbach, M. S. Hybertsen, D. R. Reichman, and T. F. Heinz, "Observation of biexcitons in monolayer WSe<sub>2</sub>," *Nature Physics*, vol. 11, pp. 477–481, June 2015.
- [63] Z. Li, T. Wang, Z. Lu, C. Jin, Y. Chen, Y. Meng, Z. Lian, T. Taniguchi, K. Watanabe, S. Zhang, D. Smirnov, and S.-F. Shi, "Revealing the biexciton and trion-exciton complexes in BN encapsulated WSe<sub>2</sub>," *Nature Communications*, vol. 9, p. 3719, Sept. 2018.
- [64] P. Tonndorf, R. Schmidt, R. Schneider, J. Kern, M. Buscema, G. A. Steele, A. Castellanos-Gomez, H. S. J. van der Zant, S. M. de Vasconcellos, and R. Bratschkitsch, "Single-photon emission from localized excitons in an atomically thin semiconductor," *Optica*, vol. 2, pp. 347–352, Apr. 2015.
- [65] Y.-M. He, G. Clark, J. R. Schaibley, Y. He, M.-C. Chen, Y.-J. Wei, X. Ding, Q. Zhang, W. Yao, X. Xu, C.-Y. Lu, and J.-W. Pan, "Single quantum emitters in monolayer semiconductors," *Nature Nanotechnology*, vol. 10, pp. 497–502, June 2015.

- [66] A. Srivastava, M. Sidler, A. V. Allain, D. S. Lembke, A. Kis, and A. Imamoglu, "Optically active quantum dots in monolayer WSe<sub>2</sub>," *Nature Nanotechnology*, vol. 10, pp. 491–496, June 2015.
- [67] X.-X. Zhang, T. Cao, Z. Lu, Y.-C. Lin, F. Zhang, Y. Wang, Z. Li, J. C. Hone, J. A. Robinson, D. Smirnov, S. G. Louie, and T. F. Heinz, "Magnetic brightening and control of dark excitons in monolayer WSe<sub>2</sub>," *Nature Nanotechnology*, vol. advance online publication, June 2017.
- [68] M. R. Molas, C. Faugeras, A. O. Slobodeniuk, K. Nogajewski, M. Bartos, D. M. Basko, and M. Potemski, "Brightening of dark excitons in monolayers of semiconducting transition metal dichalcogenides," *2D Materials*, vol. 4, p. 021003, Jan. 2017.
- [69] Y. Zhou, G. Scuri, D. S. Wild, A. A. High, A. Dibos, L. A. Jauregui, C. Shu, K. De Greve, K. Pistunova, A. Y. Joe, T. Taniguchi, K. Watanabe, P. Kim, M. D. Lukin, and H. Park, "Probing dark excitons in atomically thin semiconductors via near-field coupling to surface plasmon polaritons," *Nature Nanotechnology*, vol. advance online publication, June 2017.
- [70] A. F. Morpurgo, "Spintronics: Gate control of spin-valley coupling," *Nature Physics*, vol. 9, pp. 532–533, Sept. 2013.
- [71] K. F. Mak, K. He, J. Shan, and T. F. Heinz, "Control of valley polarization in monolayer MoS<sub>2</sub> by optical helicity," *Nature Nanotechnology*, vol. 7, pp. 494–498, Aug. 2012.
- [72] H. Zeng, J. Dai, W. Yao, D. Xiao, and X. Cui, "Valley polarization in MoS<sub>2</sub> monolayers by optical pumping," *Nature Nanotechnology*, vol. 7, pp. 490–493, Aug. 2012.
- [73] K. F. Mak, K. L. McGill, J. Park, and P. L. McEuen, "The valley Hall effect in MoS<sub>2</sub> transistors," *Science*, vol. 344, pp. 1489–1492, June 2014.
- [74] J. Lee, K. F. Mak, and J. Shan, "Electrical control of the valley Hall effect in bilayer MoS<sub>2</sub> transistors," *Nature Nanotechnology*, vol. advance online publication, Jan. 2016.
- [75] E. Barré, J. A. C. Incorvia, S. H. Kim, C. J. McClellan, E. Pop, H.-S. P. Wong, and T. F. Heinz, "Spatial Separation of Carrier Spin by the Valley Hall Effect in Monolayer WSe<sub>2</sub> Transistors," *Nano Letters*, vol. 19, pp. 770–774, Feb. 2019.
- [76] M. Gurram, S. Omar, and B. J. van Wees, "Bias induced up to 100% spin-injection and detection polarizations in ferromagnet/bilayer-hBN/graphene/hBN heterostructures," *Nature Communications*, vol. 8, p. 248, Aug. 2017.

## Bibliography

---

- [77] L. J. Martínez, T. Pelini, V. Waselowski, J. R. Maze, B. Gil, G. Cassabois, and V. Jacques, “Efficient single photon emission from a high-purity hexagonal boron nitride crystal,” *Physical Review B*, vol. 94, p. 121405, Sept. 2016.
- [78] G. Grosso, H. Moon, B. Lienhard, S. Ali, D. K. Efetov, M. M. Furchi, P. Jarillo-Herrero, M. J. Ford, I. Aharonovich, and D. Englund, “Tunable and high-purity room temperature single-photon emission from atomic defects in hexagonal boron nitride,” *Nature Communications*, vol. 8, p. 705, Sept. 2017.
- [79] Z.-Q. Xu, C. Elbadawi, T. T. Tran, M. Kianinia, X. Li, D. Liu, T. B. Hoffman, M. Nguyen, S. Kim, J. H. Edgar, X. Wu, L. Song, S. Ali, M. Ford, M. Toth, and I. Aharonovich, “Single photon emission from plasma treated 2D hexagonal boron nitride,” *Nanoscale*, vol. 10, pp. 7957–7965, May 2018.
- [80] M. Koperski, K. Nogajewski, and M. Potemski, “Single photon emitters in boron nitride: More than a supplementary material,” *Optics Communications*, vol. 411, pp. 158–165, Mar. 2018.
- [81] M. M. Ugeda, A. J. Bradley, Y. Zhang, S. Onishi, Y. Chen, W. Ruan, C. Ojeda-Aristizabal, H. Ryu, M. T. Edmonds, H.-Z. Tsai, A. Riss, S.-K. Mo, D. Lee, A. Zettl, Z. Hussain, Z.-X. Shen, and M. F. Crommie, “Characterization of collective ground states in single-layer NbSe<sub>2</sub>,” *Nature Physics*, vol. 12, pp. 92–97, Jan. 2016.
- [82] Y. Nakata, K. Sugawara, R. Shimizu, Y. Okada, P. Han, T. Hitosugi, K. Ueno, T. Sato, and T. Takahashi, “Monolayer 1T-NbSe<sub>2</sub> as a Mott insulator,” *NPG Asia Materials*, vol. 8, p. e321, Nov. 2016.
- [83] J. M. Lu, O. Zheliuk, I. Leermakers, N. F. Q. Yuan, U. Zeitler, K. T. Law, and J. T. Ye, “Evidence for two-dimensional Ising superconductivity in gated MoS<sub>2</sub>,” *Science*, p. aab2277, Nov. 2015. 00000 PMID: 26563134.
- [84] D. Costanzo, S. Jo, H. Berger, and A. F. Morpurgo, “Gate-induced superconductivity in atomically thin MoS<sub>2</sub> crystals,” *Nature Nanotechnology*, vol. advance online publication, Jan. 2016.
- [85] C. Gong, L. Li, Z. Li, H. Ji, A. Stern, Y. Xia, T. Cao, W. Bao, C. Wang, Y. Wang, Z. Q. Qiu, R. J. Cava, S. G. Louie, J. Xia, and X. Zhang, “Discovery of intrinsic ferromagnetism in two-dimensional van der Waals crystals,” *Nature*, vol. 546, pp. 265–269, June 2017.
- [86] B. Huang, G. Clark, E. Navarro-Moratalla, D. R. Klein, R. Cheng, K. L. Seyler, D. Zhong, E. Schmidgall, M. A. McGuire, D. H. Cobden, W. Yao, D. Xiao, P. Jarillo-Herrero, and X. Xu, “Layer-dependent ferromagnetism in a van der Waals crystal down to the monolayer limit,” *Nature*, vol. 546, pp. 270–273, June 2017.



- [87] D. Zhong, K. L. Seyler, X. Linpeng, R. Cheng, N. Sivadas, B. Huang, E. Schmidgall, T. Taniguchi, K. Watanabe, M. A. McGuire, W. Yao, D. Xiao, K.-M. C. Fu, and X. Xu, “Van der Waals engineering of ferromagnetic semiconductor heterostructures for spin and valleytronics,” *Science Advances*, vol. 3, p. e1603113, May 2017.
- [88] M. Gibertini, M. Koperski, A. F. Morpurgo, and K. S. Novoselov, “Magnetic 2D materials and heterostructures,” *Nature Nanotechnology*, vol. 14, p. 408, May 2019.
- [89] S. Jiang, J. Shan, and K. F. Mak, “Electric-field switching of two-dimensional van der Waals magnets,” *Nature Materials*, vol. 17, pp. 406–410, May 2018.
- [90] B. Huang, G. Clark, D. R. Klein, D. MacNeill, E. Navarro-Moratalla, K. L. Seyler, N. Wilson, M. A. McGuire, D. H. Cobden, D. Xiao, W. Yao, P. Jarillo-Herrero, and X. Xu, “Electrical control of 2D magnetism in bilayer CrI<sub>3</sub>,” *Nature Nanotechnology*, p. 1, Apr. 2018.
- [91] A. Avsar, A. Ciarrocchi, M. Pizzochero, D. Unuchek, O. Yazyev, and A. Kis, “Defect induced, layer-modulated magnetism in ultrathin metallic PtSe<sub>2</sub>,” *Nature Nanotechnology*, vol. in press, June 2019.
- [92] A. K. Geim and I. V. Grigorieva, “Van der Waals heterostructures,” *Nature*, vol. 499, pp. 419–425, July 2013.
- [93] K. S. Novoselov, A. Mishchenko, A. Carvalho, and A. H. C. Neto, “2D materials and van der Waals heterostructures,” *Science*, vol. 353, p. aac9439, July 2016.
- [94] F. Cadiz, E. Courtade, C. Robert, G. Wang, Y. Shen, H. Cai, T. Taniguchi, K. Watanabe, H. Carrere, D. Lagarde, M. Manca, T. Amand, P. Renucci, S. Tongay, X. Marie, and B. Urbaszek, “Excitonic Linewidth Approaching the Homogeneous Limit in MoS<sub>2</sub>-Based van der Waals Heterostructures,” *Physical Review X*, vol. 7, p. 021026, May 2017.
- [95] S. Bertolazzi, D. Krasnozhan, and A. Kis, “Nonvolatile Memory Cells Based on MoS<sub>2</sub>/Graphene Heterostructures,” *ACS Nano*, vol. 7, pp. 3246–3252, Apr. 2013.
- [96] A. Avsar, J. Y. Tan, T. Taychatanapat, J. Balakrishnan, G. K. W. Koon, Y. Yeo, J. Lahiri, A. Carvalho, A. S. Rodin, E. C. T. O’Farrell, G. Eda, A. H. Castro Neto, and B. Özyilmaz, “Spin–orbit proximity effect in graphene,” *Nature Communications*, vol. 5, p. 4875, Sept. 2014.
- [97] L. A. Benítez, J. F. Sierra, W. S. Torres, A. Arrighi, F. Bonell, M. V. Costache, and S. O. Valenzuela, “Strongly anisotropic spin relaxation in graphene–transition metal dichalcogenide heterostructures at room temperature,” *Nature Physics*, p. 1, Dec. 2017.

## Bibliography

---

- [98] J. C. W. Song and N. M. Gabor, “Electron quantum metamaterials in van der Waals heterostructures,” *Nature Nanotechnology*, vol. 13, p. 986, Nov. 2018.
- [99] J. Xue, J. Sanchez-Yamagishi, D. Bulmash, P. Jacquod, A. Deshpande, K. Watanabe, T. Taniguchi, P. Jarillo-Herrero, and B. J. LeRoy, “Scanning tunnelling microscopy and spectroscopy of ultra-flat graphene on hexagonal boron nitride,” *Nature Materials*, vol. 10, pp. 282–285, Apr. 2011.
- [100] J. R. Wallbank, A. A. Patel, M. Mucha-Kruczynski, A. K. Geim, and V. I. Fal’ko, “Generic Miniband Structure of Graphene on a Hexagonal Substrate,” *Physical Review B*, vol. 87, p. 245408, June 2013.
- [101] L. A. Ponomarenko, R. V. Gorbachev, G. L. Yu, D. C. Elias, R. Jalil, A. A. Patel, A. Mishchenko, A. S. Mayorov, C. R. Woods, J. R. Wallbank, M. Mucha-Kruczynski, B. A. Piot, M. Potemski, I. V. Grigorieva, K. S. Novoselov, F. Guinea, V. I. Fal’ko, and A. K. Geim, “Cloning of Dirac fermions in graphene superlattices,” *Nature*, vol. 497, pp. 594–597, May 2013.
- [102] C. R. Dean, L. Wang, P. Maher, C. Forsythe, F. Ghahari, Y. Gao, J. Katoch, M. Ishigami, P. Moon, M. Koshino, T. Taniguchi, K. Watanabe, K. L. Shepard, J. Hone, and P. Kim, “Hofstadter’s butterfly and the fractal quantum Hall effect in moiré superlattices,” *Nature*, vol. 497, pp. 598–602, May 2013.
- [103] B. Hunt, J. D. Sanchez-Yamagishi, A. F. Young, M. Yankowitz, B. J. LeRoy, K. Watanabe, T. Taniguchi, P. Moon, M. Koshino, P. Jarillo-Herrero, and R. C. Ashoori, “Massive Dirac Fermions and Hofstadter Butterfly in a van der Waals Heterostructure,” *Science*, p. 1237240, May 2013.
- [104] R. Bistritzer and A. H. MacDonald, “Moiré bands in twisted double-layer graphene,” *Proceedings of the National Academy of Sciences*, vol. 108, pp. 12233–12237, July 2011.
- [105] Y. Cao, V. Fatemi, A. Demir, S. Fang, S. L. Tomarken, J. Y. Luo, J. D. Sanchez-Yamagishi, K. Watanabe, T. Taniguchi, E. Kaxiras, R. C. Ashoori, and P. Jarillo-Herrero, “Correlated insulator behaviour at half-filling in magic-angle graphene superlattices,” *Nature*, vol. 556, pp. 80–84, Apr. 2018.
- [106] Y. Cao, V. Fatemi, S. Fang, K. Watanabe, T. Taniguchi, E. Kaxiras, and P. Jarillo-Herrero, “Unconventional superconductivity in magic-angle graphene superlattices,” *Nature*, Mar. 2018.
- [107] J. R. Schaibley, H. Yu, G. Clark, P. Rivera, J. S. Ross, K. L. Seyler, W. Yao, and X. Xu, “Valleytronics in 2D materials,” *Nature Reviews Materials*, vol. 1, p. 16055, Nov. 2016.

- [108] J. Kang, S. Tongay, J. Zhou, J. Li, and J. Wu, "Band offsets and heterostructures of two-dimensional semiconductors," *Applied Physics Letters*, vol. 102, p. 012111, Jan. 2013.
- [109] P. Rivera, H. Yu, K. L. Seyler, N. P. Wilson, W. Yao, and X. Xu, "Interlayer valley excitons in heterobilayers of transition metal dichalcogenides," *Nature Nanotechnology*, p. 1, Aug. 2018.
- [110] C. Jin, E. Y. Ma, O. Karni, E. C. Regan, F. Wang, and T. F. Heinz, "Ultrafast dynamics in van der Waals heterostructures," *Nature Nanotechnology*, vol. 13, p. 994, Nov. 2018.
- [111] P. Rivera, J. R. Schaibley, A. M. Jones, J. S. Ross, S. Wu, G. Aivazian, P. Klement, K. Seyler, G. Clark, N. J. Ghimire, J. Yan, D. G. Mandrus, W. Yao, and X. Xu, "Observation of long-lived interlayer excitons in monolayer MoSe<sub>2</sub>-WSe<sub>2</sub> heterostructures," *Nature Communications*, vol. 6, p. 6242, Feb. 2015.
- [112] L. A. Jauregui, A. Y. Joe, K. Pistunova, D. S. Wild, A. A. High, Y. Zhou, G. Scuri, K. De Greve, A. Sushko, C.-H. Yu, T. Taniguchi, K. Watanabe, D. J. Needleman, M. D. Lukin, H. Park, and P. Kim, "Electrical control of interlayer exciton dynamics in atomically thin heterostructures," *arXiv:1812.08691 [cond-mat]*, Dec. 2018.
- [113] D. Unuchek, A. Ciarrocchi, A. Avsar, K. Watanabe, T. Taniguchi, and A. Kis, "Room-temperature electrical control of exciton flux in a van der Waals heterostructure," *Nature*, vol. 560, p. 340, Aug. 2018.
- [114] P. Rivera, K. L. Seyler, H. Yu, J. R. Schaibley, J. Yan, D. G. Mandrus, W. Yao, and X. Xu, "Valley-polarized exciton dynamics in a 2D semiconductor heterostructure," *Science*, vol. 351, pp. 688–691, Feb. 2016.
- [115] C. Zhang, C.-P. Chuu, X. Ren, M.-Y. Li, L.-J. Li, C. Jin, M.-Y. Chou, and C.-K. Shih, "Interlayer couplings, Moiré patterns, and 2D electronic superlattices in MoS<sub>2</sub>/WSe<sub>2</sub> hetero-bilayers," *Science Advances*, vol. 3, p. e1601459, Jan. 2017.
- [116] E. M. Alexeev, D. A. Ruiz-Tijerina, M. Danovich, M. J. Hamer, D. J. Terry, P. K. Nayak, S. Ahn, S. Pak, J. Lee, J. I. Sohn, M. R. Molas, M. Koperski, K. Watanabe, T. Taniguchi, K. S. Novoselov, R. V. Gorbachev, H. S. Shin, V. I. Fal'ko, and A. I. Tartakovskii, "Resonantly hybridized excitons in moiré superlattices in van der Waals heterostructures," *Nature*, vol. 567, pp. 81–86, Mar. 2019.
- [117] K. L. Seyler, P. Rivera, H. Yu, N. P. Wilson, E. L. Ray, D. G. Mandrus, J. Yan, W. Yao, and X. Xu, "Signatures of moiré-trapped valley excitons in MoSe<sub>2</sub>/WSe<sub>2</sub> heterobilayers," *Nature*, p. 1, Feb. 2019.

## Bibliography

---

- [118] K. Tran, G. Moody, F. Wu, X. Lu, J. Choi, A. Singh, J. Embley, A. Zepeda, M. Campbell, K. Kim, A. Rai, T. Autry, D. A. Sanchez, T. Taniguchi, K. Watanabe, N. Lu, S. K. Banerjee, E. Tutuc, L. Yang, A. H. MacDonald, K. L. Silverman, and X. Li, “Moiré Excitons in Van der Waals Heterostructures,” *arXiv:1807.03771 [cond-mat]*, July 2018.
- [119] C. Jin, E. C. Regan, A. Yan, M. I. B. Utama, D. Wang, S. Zhao, Y. Qin, S. Yang, Z. Zheng, S. Shi, K. Watanabe, T. Taniguchi, S. Tongay, A. Zettl, and F. Wang, “Observation of moiré excitons in WSe<sub>2</sub>/WS<sub>2</sub> heterostructure superlattices,” *Nature*, p. 1, Feb. 2019.
- [120] H. Yu, G.-B. Liu, J. Tang, X. Xu, and W. Yao, “Moiré excitons: From programmable quantum emitter arrays to spin-orbit-coupled artificial lattices,” *Science Advances*, vol. 3, p. e1701696, Nov. 2017.
- [121] H. Yu, G.-B. Liu, and W. Yao, “Brightened spin-triplet interlayer excitons and optical selection rules in van der Waals heterobilayers,” *2D Materials*, vol. 5, no. 3, p. 035021, 2018.
- [122] H. Yu, Y. Wang, Q. Tong, X. Xu, and W. Yao, “Anomalous light cones and valley optical selection rules of interlayer excitons in twisted heterobilayers,” *Physical Review Letters*, vol. 115, Oct. 2015.
- [123] M. M. Benameur, B. Radisavljevic, J. S. Héron, S. Sahoo, H. Berger, and A. Kis, “Visibility of dichalcogenide nanolayers,” *Nanotechnology*, vol. 22, p. 125706, Feb. 2011.
- [124] A. Jain, P. Bharadwaj, S. Heeg, M. Parzefall, T. Taniguchi, K. Watanabe, and L. Novotny, “Minimizing Residues in Transfer of 2D Materials from PDMS,” *arXiv:1801.02971 [cond-mat]*, Jan. 2018.
- [125] D. Dumcenco, D. Ovchinnikov, K. Marinov, P. Lazić, M. Gibertini, N. Marzari, O. L. Sanchez, Y.-C. Kung, D. Krasnozhan, M.-W. Chen, S. Bertolazzi, P. Gillet, A. Fontcuberta i Morral, A. Radenovic, and A. Kis, “Large-Area Epitaxial Monolayer MoS<sub>2</sub>,” *ACS Nano*, vol. 9, pp. 4611–4620, Apr. 2015.
- [126] E. M. Alexeev, A. Catanzaro, O. V. Skrypka, P. K. Nayak, S. Ahn, S. Pak, J. Lee, J. I. Sohn, K. S. Novoselov, H. S. Shin, and A. I. Tartakovskii, “Imaging of interlayer coupling in van der Waals heterostructures using a bright-field optical microscope,” *Nano Letters*, vol. 17, pp. 5342–5349, Sept. 2017.
- [127] R. R. Nair, P. Blake, A. N. Grigorenko, K. S. Novoselov, T. J. Booth, T. Stauber, N. M. R. Peres, and A. K. Geim, “Fine structure constant defines visual transparency of graphene,” *Science (New York, N.Y.)*, vol. 320, p. 1308, June 2008.

- [128] R. V. Gorbachev, I. Riaz, R. R. Nair, R. Jalil, L. Britnell, B. D. Belle, E. W. Hill, K. S. Novoselov, K. Watanabe, T. Taniguchi, A. K. Geim, and P. Blake, "Hunting for Monolayer Boron Nitride: Optical and Raman Signatures," *Small*, vol. 7, no. 4, pp. 465–468, 2011.
- [129] A. Castellanos-Gomez, M. Buscema, R. Molenaar, V. Singh, L. Janssen, H. S. J. van der Zant, and G. A. Steele, "Deterministic transfer of two-dimensional materials by all-dry viscoelastic stamping," *2D Materials*, vol. 1, no. 1, p. 011002, 2014.
- [130] A. S. Mayorov, R. V. Gorbachev, S. V. Morozov, L. Britnell, R. Jalil, L. A. Ponomarenko, P. Blake, K. S. Novoselov, K. Watanabe, T. Taniguchi, and A. K. Geim, "Micrometer-Scale Ballistic Transport in Encapsulated Graphene at Room Temperature," *Nano Letters*, vol. 11, pp. 2396–2399, June 2011.
- [131] A. Allain, J. Kang, K. Banerjee, and A. Kis, "Electrical contacts to two-dimensional semiconductors," *Nature Materials*, vol. 14, pp. 1195–1205, Dec. 2015.
- [132] M. Farmanbar and G. Brocks, "Controlling the Schottky barrier at moS<sub>2</sub>/metal contacts by inserting a BN monolayer," *Physical Review B*, vol. 91, p. 161304, Apr. 2015.
- [133] O. L. Sanchez, D. Ovchinnikov, S. Misra, A. Allain, and A. Kis, "Valley polarization by spin injection in a light-emitting van der Waals heterojunction," *Nano Letters*, Aug. 2016.
- [134] I. Verzhbitskiy, D. Vella, K. Watanabe, T. Taniguchi, and G. Eda, "Suppressed Out-of-Plane Polarizability of Free Excitons in Monolayer WSe<sub>2</sub>," *ACS Nano*, vol. 13, pp. 3218–3224, Mar. 2019.
- [135] C. Jin, J. Kim, J. Suh, Z. Shi, B. Chen, X. Fan, M. Kam, K. Watanabe, T. Taniguchi, S. Tongay, A. Zettl, J. Wu, and F. Wang, "Interlayer electron–phonon coupling in WSe<sub>2</sub>/hBN heterostructures," *Nature Physics*, vol. 13, pp. 127–131, Feb. 2017.
- [136] C. M. Chow, H. Yu, A. M. Jones, J. Yan, D. G. Mandrus, T. Taniguchi, K. Watanabe, W. Yao, and X. Xu, "Unusual Exciton–Phonon Interactions at van der Waals Engineered Interfaces," *Nano Letters*, vol. 17, pp. 1194–1199, Feb. 2017.
- [137] S. P. Gurrum, S. K. Suman, Y. K. Joshi, and A. G. Fedorov, "Thermal issues in next-generation integrated circuits," *IEEE Transactions on Device and Materials Reliability*, vol. 4, pp. 709–714, Dec. 2004.
- [138] A. Rickman, "The commercialization of silicon photonics," *Nature Photonics*, vol. 8, pp. 579–582, July 2014.

## Bibliography

---

- [139] D. J. Moss, R. Morandotti, A. L. Gaeta, and M. Lipson, “New CMOS-compatible platforms based on silicon nitride and Hydex for nonlinear optics,” *Nature Photonics*, vol. 7, pp. 597–607, Aug. 2013.
- [140] D. A. B. Miller, “Rationale and challenges for optical interconnects to electronic chips,” *Proceedings of the IEEE*, vol. 88, pp. 728–749, June 2000.
- [141] Z. Sun, A. Martinez, and F. Wang, “Optical modulators with 2D layered materials,” *Nature Photonics*, vol. 10, pp. 227–238, Apr. 2016.
- [142] F. Bonaccorso, Z. Sun, T. Hasan, and A. C. Ferrari, “Graphene photonics and optoelectronics,” *Nature Photonics*, vol. 4, pp. 611–622, Sept. 2010.
- [143] Q. H. Wang, K. Kalantar-Zadeh, A. Kis, J. N. Coleman, and M. S. Strano, “Electronics and optoelectronics of two-dimensional transition metal dichalcogenides,” *Nature Nanotechnology*, vol. 7, pp. 699–712, Nov. 2012.
- [144] K. F. Mak and J. Shan, “Photonics and optoelectronics of 2D semiconductor transition metal dichalcogenides,” *Nature Photonics*, vol. 10, pp. 216–226, Apr. 2016.
- [145] O. Lopez-Sanchez, D. Lembke, M. Kayci, A. Radenovic, and A. Kis, “Ultrasensitive photodetectors based on monolayer MoS<sub>2</sub>,” *Nature Nanotechnology*, vol. 8, pp. 497–501, July 2013.
- [146] Y.-Q. Bie, G. Grosso, M. Heuck, M. M. Furchi, Y. Cao, J. Zheng, D. Bunandar, E. Navarro-Moratalla, L. Zhou, D. K. Efetov, T. Taniguchi, K. Watanabe, J. Kong, D. Englund, and P. Jarillo-Herrero, “A MoTe<sub>2</sub>-based light-emitting diode and photodetector for silicon photonic integrated circuits,” *Nature Nanotechnology*, vol. 12, pp. 1124–1129, Dec. 2017.
- [147] D. Dumcenco, D. Ovchinnikov, K. Marinov, P. Lazić, M. Gibertini, N. Marzari, O. L. Sanchez, Y.-C. Kung, D. Krasnozhon, M.-W. Chen, S. Bertolazzi, P. Gillet, A. Fontcuberta i Morral, A. Radenovic, and A. Kis, “Large-Area Epitaxial Monolayer MoS<sub>2</sub>,” *ACS Nano*, vol. 9, pp. 4611–4620, Apr. 2015.
- [148] W.-f. Zhao, H. Yu, M.-z. Liao, L. Zhang, S.-z. Zou, H.-j. Yu, C.-j. He, J.-y. Zhang, G.-y. Zhang, and X.-c. Lin, “Large area growth of monolayer MoS<sub>2</sub> film on quartz and its use as a saturable absorber in laser mode-locking,” *Semiconductor Science and Technology*, vol. 32, p. 025013, Feb. 2017.
- [149] J. F. G. Marin, D. Unuchek, K. Watanabe, T. Taniguchi, and A. Kis, “MoS<sub>2</sub> photodetectors integrated with photonic circuits,” *npj 2D Materials and Applications*, vol. 3, p. 14, Mar. 2019.

- [150] R. Cheng, D. Li, H. Zhou, C. Wang, A. Yin, S. Jiang, Y. Liu, Y. Chen, Y. Huang, and X. Duan, "Electroluminescence and Photocurrent Generation from Atomically Sharp WSe<sub>2</sub>/MoS<sub>2</sub> Heterojunction p-n Diodes," *Nano Letters*, vol. 14, pp. 5590–5597, Oct. 2014.
- [151] C. Gong, L. Colombo, R. M. Wallace, and K. Cho, "The Unusual Mechanism of Partial Fermi Level Pinning at Metal–MoS<sub>2</sub> Interfaces," *Nano Letters*, vol. 14, pp. 1714–1720, Apr. 2014.
- [152] A. Allain and A. Kis, "Electron and Hole Mobilities in Single-Layer WSe<sub>2</sub>," *ACS Nano*, vol. 8, pp. 7180–7185, July 2014.
- [153] M. M. Furchi, A. Pospischil, F. Libisch, J. Burgdörfer, and T. Mueller, "Photovoltaic Effect in an Electrically Tunable van der Waals Heterojunction," *Nano Letters*, vol. 14, pp. 4785–4791, Aug. 2014.
- [154] W. Zhao, Z. Ghorannevis, L. Chu, M. Toh, C. Kloc, P.-H. Tan, and G. Eda, "Evolution of Electronic Structure in Atomically Thin Sheets of WS<sub>2</sub> and WSe<sub>2</sub>," *ACS Nano*, vol. 7, pp. 791–797, Jan. 2013.
- [155] F. Withers, O. Del Pozo-Zamudio, S. Schwarz, S. Dufferwiel, P. M. Walker, T. Godde, A. P. Rooney, A. Gholinia, C. R. Woods, P. Blake, S. J. Haigh, K. Watanabe, T. Taniguchi, I. L. Aleiner, A. K. Geim, V. I. Fal'ko, A. I. Tartakovskii, and K. S. Novoselov, "WSe<sub>2</sub> Light-Emitting Tunneling Transistors with Enhanced Brightness at Room Temperature," *Nano Letters*, vol. 15, pp. 8223–8228, Dec. 2015.
- [156] J. S. Ross, P. Klement, A. M. Jones, N. J. Ghimire, J. Yan, D. G. Mandrus, T. Taniguchi, K. Watanabe, K. Kitamura, W. Yao, D. H. Cobden, and X. Xu, "Electrically tunable excitonic light-emitting diodes based on monolayer WSe<sub>2</sub> p-n junctions," *Nature Nanotechnology*, vol. 9, pp. 268–272, Apr. 2014.
- [157] B. W. H. Baugher, H. O. H. Churchill, Y. Yang, and P. Jarillo-Herrero, "Optoelectronic devices based on electrically tunable p-n diodes in a monolayer dichalcogenide," *Nature Nanotechnology*, vol. 9, pp. 262–267, Apr. 2014.
- [158] A. Pospischil, M. M. Furchi, and T. Mueller, "Solar-energy conversion and light emission in an atomic monolayer p-n diode," *Nature Nanotechnology*, vol. 9, pp. 257–261, Apr. 2014.
- [159] M. Buscema, D. J. Groenendijk, G. A. Steele, H. S. van der Zant, and A. Castellanos-Gomez, "Photovoltaic effect in few-layer black phosphorus PN junctions defined by local electrostatic gating," *Nature Communications*, vol. 5, p. 4651, Aug. 2014.

## Bibliography

---

- [160] D. Ovchinnikov, A. Allain, Y.-S. Huang, D. Dumcenco, and A. Kis, “Electrical Transport Properties of Single-Layer WS<sub>2</sub>,” *ACS Nano*, vol. 8, pp. 8174–8181, Aug. 2014.
- [161] A. R. Cadore, E. Mania, K. Watanabe, T. Taniguchi, R. G. Lacerda, and L. C. Campos, “Thermally activated hysteresis in high quality graphene/h-BN devices,” *Applied Physics Letters*, vol. 108, p. 233101, June 2016.
- [162] O. A. Ajayi, J. V. Ardelean, G. D. Shepard, J. Wang, A. Antony, T. Taniguchi, K. Watanabe, T. F. Heinz, S. Strauf, X.-Y. Zhu, and J. C. Hone, “Approaching the intrinsic photoluminescence linewidth in transition metal dichalcogenide monolayers,” *2D Materials*, vol. 4, p. 031011, July 2017.
- [163] A. Ciarrocchi, D. Unuchek, A. Avsar, K. Watanabe, T. Taniguchi, and A. Kis, “Polarization switching and electrical control of interlayer excitons in two-dimensional van der Waals heterostructures,” *Nature Photonics*, vol. 13, p. 131, Feb. 2019.
- [164] L. Wang, I. Meric, P. Y. Huang, Q. Gao, Y. Gao, H. Tran, T. Taniguchi, K. Watanabe, L. M. Campos, D. A. Muller, J. Guo, P. Kim, J. Hone, K. L. Shepard, and C. R. Dean, “One-Dimensional Electrical Contact to a Two-Dimensional Material,” *Science*, vol. 342, pp. 614–617, Nov. 2013.
- [165] T. C. Banwell and A. Jayakumar, “Exact analytical solution for current flow through diode with series resistance,” *Electronics Letters*, vol. 36, pp. 291–292, Feb. 2000.
- [166] A. Arora, M. Koperski, K. Nogajewski, J. Marcus, C. Faugeras, and M. Potemski, “Excitonic resonances in thin films of WSe<sub>2</sub>: From monolayer to bulk material,” *Nanoscale*, vol. 7, pp. 10421–10429, June 2015.
- [167] T. Yan, X. Qiao, X. Liu, P. Tan, and X. Zhang, “Photoluminescence properties and exciton dynamics in monolayer WSe<sub>2</sub>,” *Applied Physics Letters*, vol. 105, p. 101901, Sept. 2014.
- [168] J. Huang, T. B. Hoang, and M. H. Mikkelsen, “Probing the origin of excitonic states in monolayer WSe<sub>2</sub>,” *Scientific Reports*, vol. 6, p. 22414, Mar. 2016.
- [169] E. Courtade, M. Semina, M. Manca, M. M. Glazov, C. Robert, F. Cadiz, G. Wang, T. Taniguchi, K. Watanabe, M. Pierre, W. Escoffier, E. L. Ivchenko, P. Renucci, X. Marie, T. Amand, and B. Urbaszek, “Charged excitons in monolayer WSe<sub>2</sub>: Experiment and theory,” *Physical Review B*, vol. 96, p. 085302, Aug. 2017.
- [170] Z. Ye, L. Waldecker, E. Y. Ma, D. Rhodes, A. Antony, B. Kim, X.-X. Zhang, M. Deng, Y. Jiang, Z. Lu, D. Smirnov, K. Watanabe, T. Taniguchi, J. Hone, and T. F. Heinz, “Efficient generation of neutral and charged biexcitons in encapsulated WSe<sub>2</sub> monolayers,” *Nature Communications*, vol. 9, p. 3718, Sept. 2018.



- [171] Y. Tan, R. He, C. Cheng, D. Wang, Y. Chen, and F. Chen, "Polarization-dependent optical absorption of MoS<sub>2</sub> for refractive index sensing," *Scientific Reports*, vol. 4, p. 7523, Dec. 2014.
- [172] A. Castellanos-Gomez, J. Quereda, H. P. van der Meulen, N. Agraït, and G. Rubio-Bollinger, "Spatially resolved optical absorption spectroscopy of single- and few-layer MoS<sub>2</sub> by hyperspectral imaging," *Nanotechnology*, vol. 27, no. 11, p. 115705, 2016.
- [173] M. Buscema, M. Barkelid, V. Zwiller, H. S. J. van der Zant, G. A. Steele, and A. Castellanos-Gomez, "Large and Tunable Photothermoelectric Effect in Single-Layer MoS<sub>2</sub>," *Nano Letters*, vol. 13, pp. 358–363, Feb. 2013. 00303.
- [174] M. M. Furchi, D. K. Polyushkin, A. Pospischil, and T. Mueller, "Mechanisms of Photoconductivity in Atomically Thin MoS<sub>2</sub>," *Nano Letters*, vol. 14, pp. 6165–6170, Nov. 2014. 00145.
- [175] O. Lopez-Sanchez, E. Alarcon Llado, V. Koman, A. Fontcuberta i Morral, A. Radenovic, and A. Kis, "Light generation and harvesting in a van der Waals heterostructure," *ACS nano*, vol. 8, pp. 3042–3048, Mar. 2014. 00159.
- [176] Y. Dan, X. Zhao, K. Chen, and A. Mesli, "A Photoconductor Intrinsically Has No Gain," *ACS Photonics*, vol. 5, pp. 4111–4116, Oct. 2018.
- [177] B. Radisavljevic, A. Radenovic, J. Brivio, V. Giacometti, and A. Kis, "Single-layer MoS<sub>2</sub> transistors," *Nature Nanotechnology*, vol. 6, no. 3, pp. 147–150, 2011.
- [178] H. Schmidt, S. Wang, L. Chu, M. Toh, R. Kumar, W. Zhao, A. H. Castro Neto, J. Martin, S. Adam, B. Özyilmaz, and G. Eda, "Transport Properties of Monolayer MoS<sub>2</sub> Grown by Chemical Vapor Deposition," *Nano Letters*, vol. 14, pp. 1909–1913, Apr. 2014.
- [179] X. Wang, P. Wang, J. Wang, W. Hu, X. Zhou, N. Guo, H. Huang, S. Sun, H. Shen, T. Lin, M. Tang, L. Liao, A. Jiang, J. Sun, X. Meng, X. Chen, W. Lu, and J. Chu, "Ultrasensitive and Broadband MoS<sub>2</sub> Photodetector Driven by Ferroelectrics," *Advanced Materials (Deerfield Beach, Fla.)*, vol. 27, pp. 6575–6581, Nov. 2015.
- [180] Y.-Q. Bie, G. Grosso, M. Heuck, M. M. Furchi, Y. Cao, J. Zheng, D. Bunandar, E. Navarro-Moratalla, L. Zhou, D. K. Efetov, T. Taniguchi, K. Watanabe, J. Kong, D. Englund, and P. Jarillo-Herrero, "A MoTe<sub>2</sub>-based light-emitting diode and photodetector for silicon photonic integrated circuits," *Nature Nanotechnology*, vol. 12, pp. 1124–1129, Dec. 2017.

## Bibliography

---

- [181] S. A. Wolf, D. D. Awschalom, R. A. Buhrman, J. M. Daughton, S. von Molnár, M. L. Roukes, A. Y. Chtchelkanova, and D. M. Treger, “Spintronics: A Spin-Based Electronics Vision for the Future,” *Science*, vol. 294, pp. 1488–1495, Nov. 2001.
- [182] H. Dery, H. Wu, B. Ciftcioglu, M. Huang, Y. Song, R. K. Kawakami, J. Shi, I. N. Krivorotov, D. A. Telesca, I. Žutić, and L. J. Sham, “Reconfigurable nanoelectronics using graphene based spintronic logic gates,” in *Spintronics IV*, vol. 8100, p. 81000W, International Society for Optics and Photonics, Sept. 2011.
- [183] G. Schmidt, D. Ferrand, L. W. Molenkamp, A. T. Filip, and B. J. van Wees, “Fundamental obstacle for electrical spin injection from a ferromagnetic metal into a diffusive semiconductor,” *Physical Review B*, vol. 62, pp. R4790–R4793, Aug. 2000.
- [184] W. Han, K. Pi, K. M. McCreary, Y. Li, J. J. I. Wong, A. G. Swartz, and R. K. Kawakami, “Tunneling Spin Injection into Single Layer Graphene,” *Physical Review Letters*, vol. 105, p. 167202, Oct. 2010.
- [185] M. Gmitra and J. Fabian, “Graphene on transition-metal dichalcogenides: A platform for proximity spin-orbit physics and optospintronics,” *Physical Review B*, vol. 92, Oct. 2015.
- [186] Y. Li, A. Chernikov, X. Zhang, A. Rigosi, H. M. Hill, A. M. van der Zande, D. A. Chenet, E.-M. Shih, J. Hone, and T. F. Heinz, “Measurement of the optical dielectric function of monolayer transition-metal dichalcogenides: MoS<sub>2</sub>, MoSe<sub>2</sub>, WS<sub>2</sub>, WSe<sub>2</sub>,” *Physical Review B*, vol. 90, p. 205422, Nov. 2014.
- [187] X. Song, S. Xie, K. Kang, J. Park, and V. Sih, “Long-Lived Hole Spin/Valley Polarization Probed by Kerr Rotation in Monolayer WSe<sub>2</sub>,” *Nano Letters*, vol. 16, pp. 5010–5014, Aug. 2016.
- [188] F. Withers, O. Del Pozo-Zamudio, S. Schwarz, S. Dufferwiel, P. M. Walker, T. Godde, A. P. Rooney, A. Gholinia, C. R. Woods, P. Blake, S. J. Haigh, K. Watanabe, T. Taniguchi, I. L. Aleiner, A. K. Geim, V. I. Fal’ko, A. I. Tartakovskii, and K. S. Novoselov, “WSe<sub>2</sub> Light-Emitting Tunneling Transistors with Enhanced Brightness at Room Temperature,” *Nano Lett.*, vol. 15, pp. 8223–8228, Dec. 2015.
- [189] Z. Y. Zhu, Y. C. Cheng, and U. Schwingenschlögl, “Giant spin-orbit-induced spin splitting in two-dimensional transition-metal dichalcogenide semiconductors,” *Physical Review B*, vol. 84, p. 153402, Oct. 2011.
- [190] R. A. Muniz and J. E. Sipe, “All-optical injection of charge, spin, and valley currents in monolayer transition-metal dichalcogenides,” *Physical Review B*, vol. 91, p. 085404, Feb. 2015.

- [191] A. Avsar, D. Unuchek, J. Liu, O. L. Sanchez, K. Watanabe, T. Taniguchi, B. Özyilmaz, and A. Kis, “Optospintronics in graphene via proximity coupling,” *arXiv:1705.10267 [cond-mat, physics:physics]*, May 2017.
- [192] A. Avsar, T.-Y. Yang, S. Bae, J. Balakrishnan, F. Volmer, M. Jaiswal, Z. Yi, S. R. Ali, G. Güntherodt, B. H. Hong, B. Beschoten, and B. Özyilmaz, “Toward Wafer Scale Fabrication of Graphene Based Spin Valve Devices,” *Nano Letters*, vol. 11, pp. 2363–2368, June 2011.
- [193] M. Johnson and R. H. Silsbee, “Interfacial charge-spin coupling: Injection and detection of spin magnetization in metals,” *Physical Review Letters*, vol. 55, pp. 1790–1793, Oct. 1985.
- [194] F. J. Jedema, H. B. Heersche, A. T. Filip, J. J. A. Baselmans, and B. J. van Wees, “Electrical detection of spin precession in a metallic mesoscopic spin valve,” *Nature*, vol. 416, p. 713, Apr. 2002.
- [195] M. V. Kamalakar, A. Dankert, J. Bergsten, T. Ive, and S. P. Dash, “Enhanced Tunnel Spin Injection into Graphene using Chemical Vapor Deposited Hexagonal Boron Nitride,” *Scientific Reports*, vol. 4, p. 6146, Aug. 2014.
- [196] A. Avsar, I. J. Vera-Marun, J. Y. Tan, G. K. W. Koon, K. Watanabe, T. Taniguchi, S. Adam, and B. Özyilmaz, “Electronic spin transport in dual-gated bilayer graphene,” *NPG Asia Materials*, vol. 8, p. e274, June 2016.
- [197] S. Takahashi and S. Maekawa, “Spin injection and detection in magnetic nanostructures,” *Physical Review B*, vol. 67, p. 052409, Feb. 2003.
- [198] N. Tombros, S. Tanabe, A. Veligura, C. Jozsa, M. Popinciuc, H. T. Jonkman, and B. J. van Wees, “Anisotropic Spin Relaxation in Graphene,” *Physical Review Letters*, vol. 101, p. 046601, July 2008.
- [199] A. Srivastava, M. Sidler, A. V. Allain, D. S. Lembke, A. Kis, and A. Imamoglu, “Valley Zeeman effect in elementary optical excitations of monolayer WSe<sub>2</sub>,” *Nature Physics*, vol. 11, pp. 141–147, Feb. 2015.
- [200] I. Žutić, J. Fabian, and S. Das Sarma, “Spintronics: Fundamentals and applications,” *Reviews of Modern Physics*, vol. 76, pp. 323–410, Apr. 2004.
- [201] A. Avsar, J. Y. Tan, M. Kurpas, M. Gmitra, K. Watanabe, T. Taniguchi, J. Fabian, and B. Özyilmaz, “Gate-tunable black phosphorus spin valve with nanosecond spin lifetimes,” *Nature Physics*, vol. advance online publication, May 2017.

## Bibliography

---

- [202] A. Dankert and S. P. Dash, “Electrical gate control of spin current in van der Waals heterostructures at room temperature,” *Nature Communications*, vol. 8, p. 16093, July 2017.
- [203] W. Yan, O. Txoperena, R. Llopis, H. Dery, L. E. Hueso, and F. Casanova, “A two-dimensional spin field-effect switch,” *Nature Communications*, vol. 7, p. 13372, Nov. 2016.
- [204] K. Roy, M. Padmanabhan, S. Goswami, T. P. Sai, G. Ramalingam, S. Raghavan, and A. Ghosh, “Graphene–MoS<sub>2</sub> hybrid structures for multifunctional photoresponsive memory devices,” *Nature Nanotechnology*, vol. 8, pp. 826–830, Nov. 2013.
- [205] Y. K. Luo, J. Xu, T. Zhu, G. Wu, E. J. McCormick, W. Zhan, M. R. Neupane, and R. K. Kawakami, “Opto-Valleytronic Spin Injection in Monolayer MoS<sub>2</sub>/Few-Layer Graphene Hybrid Spin Valves,” *Nano Letters*, vol. 17, pp. 3877–3883, June 2017.
- [206] T. S. Ghiasi, J. Ingla-Aynés, A. A. Kaverzin, and B. J. van Wees, “Large Proximity-Induced Spin Lifetime Anisotropy in Transition Metal Dichalcogenide/Graphene Heterostructures,” *arXiv:1708.04067 [cond-mat]*, Aug. 2017.
- [207] D. Kochan, S. Irmer, and J. Fabian, “Model spin-orbit coupling Hamiltonians for graphene systems,” *Physical Review B*, vol. 95, p. 165415, Apr. 2017.
- [208] A. Liu, R. Jones, L. Liao, D. Samara-Rubio, D. Rubin, O. Cohen, R. Nicolaescu, and M. Paniccia, “A high-speed silicon optical modulator based on a metal–oxide–semiconductor capacitor,” *Nature*, vol. 427, p. 615, Feb. 2004.
- [209] A. Melikyan, A. Muslija, B. Chen, C. Koos, D. Hillerkuss, D. Korn, D. V. Thourhout, J. Leuthold, J. Li, L. Alloatti, M. Kohl, M. Sommer, P. C. Schindler, R. Dinu, R. Palmer, S. Muehlbrandt, and W. Freude, “High-speed plasmonic phase modulators,” *Nature Photonics*, vol. 8, p. 229, Mar. 2014.
- [210] Q. Xu, B. Schmidt, S. Pradhan, and M. Lipson, “Micrometre-scale silicon electro-optic modulator,” *Nature*, vol. 435, p. 325, May 2005.
- [211] B. Schmidt, Q. Xu, J. Shakya, S. Manipatruni, and M. Lipson, “Compact electro-optic modulator on silicon-on-insulator substrates using cavities with ultra-small modal volumes,” *Optics Express*, vol. 15, pp. 3140–3148, Mar. 2007.
- [212] F. Fedichkin, T. Guillet, P. Valvin, B. Jouault, C. Brimont, T. Bretagnon, L. Lahourcade, N. Grandjean, P. Lefebvre, and M. Vladimirova, “Room-Temperature Transport of Indirect Excitons in AlGa<sub>N</sub>/Ga<sub>N</sub> Quantum Wells,” *Physical Review Applied*, vol. 6, p. 014011, July 2016.

- [213] Y. Y. Kuznetsova, F. Fedichkin, P. Andreakou, E. V. Calman, L. V. Butov, P. Lefebvre, T. Bretagnon, T. Guillet, M. Vladimirova, C. Morhain, and J.-M. Chauveau, "Transport of indirect excitons in ZnO quantum wells," *Optics Letters*, vol. 40, pp. 3667–3670, Aug. 2015.
- [214] T. Cheiwchanamngij and W. R. L. Lambrecht, "Quasiparticle band structure calculation of monolayer, bilayer, and bulk MoS<sub>2</sub>," *Physical Review B*, vol. 85, p. 205302, May 2012.
- [215] K. He, N. Kumar, L. Zhao, Z. Wang, K. F. Mak, H. Zhao, and J. Shan, "Tightly Bound Excitons in Monolayer WSe<sub>2</sub>," *Physical Review Letters*, vol. 113, p. 026803, July 2014.
- [216] M. Palummo, M. Bernardi, and J. C. Grossman, "Exciton Radiative Lifetimes in Two-Dimensional Transition Metal Dichalcogenides," *Nano Letters*, vol. 15, pp. 2794–2800, May 2015.
- [217] C. Robert, D. Lagarde, F. Cadiz, G. Wang, B. Lassagne, T. Amand, A. Balocchi, P. Renucci, S. Tongay, B. Urbaszek, and X. Marie, "Exciton radiative lifetime in transition metal dichalcogenide monolayers," *Physical Review B*, vol. 93, p. 205423, May 2016.
- [218] A. A. High, A. T. Hammack, L. V. Butov, M. Hanson, and A. C. Gossard, "Exciton optoelectronic transistor," *Optics Letters*, vol. 32, pp. 2466–2468, Sept. 2007.
- [219] A. A. High, A. K. Thomas, G. Grosso, M. Remeika, A. T. Hammack, A. D. Meyertholen, M. M. Fogler, L. V. Butov, M. Hanson, and A. C. Gossard, "Trapping Indirect Excitons in a GaAs Quantum-Well Structure with a Diamond-Shaped Electrostatic Trap," *Physical Review Letters*, vol. 103, p. 087403, Aug. 2009.
- [220] J. R. Leonard, M. Remeika, M. K. Chu, Y. Y. Kuznetsova, A. A. High, L. V. Butov, J. Wilkes, M. Hanson, and A. C. Gossard, "Transport of indirect excitons in a potential energy gradient," *Applied Physics Letters*, vol. 100, p. 231106, June 2012.
- [221] C. J. Dorow, Y. Y. Kuznetsova, J. R. Leonard, M. K. Chu, L. V. Butov, J. Wilkes, M. Hanson, and A. C. Gossard, "Indirect excitons in a potential energy landscape created by a perforated electrode," *Applied Physics Letters*, vol. 108, p. 073502, Feb. 2016.
- [222] A. G. Winbow, J. R. Leonard, M. Remeika, Y. Y. Kuznetsova, A. A. High, A. T. Hammack, L. V. Butov, J. Wilkes, A. A. Guenther, A. L. Ivanov, M. Hanson, and A. C. Gossard, "Electrostatic Conveyer for Excitons," *Physical Review Letters*, vol. 106, p. 196806, May 2011.
- [223] H. Fang, C. Battaglia, C. Carraro, S. Nemsak, B. Ozdol, J. S. Kang, H. A. Bechtel, S. B. Desai, F. Kronast, A. A. Unal, G. Conti, C. Conlon, G. K. Palsson, M. C. Martin, A. M.

## Bibliography

---

- Minor, C. S. Fadley, E. Yablonovitch, R. Maboudian, and A. Javey, “Strong interlayer coupling in van der Waals heterostructures built from single-layer chalcogenides,” *Proceedings of the National Academy of Sciences*, vol. 111, pp. 6198–6202, Apr. 2014.
- [224] P. Nagler, M. V. Ballottin, A. A. Mitioglu, F. Mooshammer, N. Paradiso, C. Strunk, R. Huber, A. Chernikov, P. C. M. Christianen, C. Schüller, and T. Korn, “Giant magnetic splitting inducing near-unity valley polarization in van der Waals heterostructures,” *Nature Communications*, vol. 8, p. 1551, Nov. 2017.
- [225] J. Kunstmann, F. Mooshammer, P. Nagler, A. Chaves, F. Stein, N. Paradiso, G. Plechinger, C. Strunk, C. Schüller, G. Seifert, D. R. Reichman, and T. Korn, “Momentum-space indirect interlayer excitons in transition-metal dichalcogenide van der Waals heterostructures,” *Nature Physics*, p. 1, Apr. 2018.
- [226] A. Kormányos, V. Zólyomi, N. D. Drummond, and G. Burkard, “Spin-Orbit Coupling, Quantum Dots, and Qubits in Monolayer Transition Metal Dichalcogenides,” *Physical Review X*, vol. 4, p. 011034, Mar. 2014.
- [227] A. T. Hanbicki, H.-J. Chuang, M. R. Rosenberger, C. S. Hellberg, S. V. Sivaram, K. M. McCreary, I. I. Mazin, and B. T. Jonker, “Double Indirect Interlayer Exciton in a MoSe<sub>2</sub>/WSe<sub>2</sub> van der Waals Heterostructure,” *ACS Nano*, vol. 12, pp. 4719–4726, May 2018.
- [228] J. He, K. Hummer, and C. Franchini, “Stacking effects on the electronic and optical properties of bilayer transition metal dichalcogenides MoS<sub>2</sub>, MoSe<sub>2</sub>, WS<sub>2</sub>, and WSe<sub>2</sub>,” *Physical Review B*, vol. 89, p. 075409, Feb. 2014.
- [229] G. Wang, E. Palleau, T. Amand, S. Tongay, X. Marie, and B. Urbaszek, “Polarization and time-resolved photoluminescence spectroscopy of excitons in MoSe<sub>2</sub> monolayers,” *Applied Physics Letters*, vol. 106, p. 112101, Mar. 2015.
- [230] G. Kioseoglou, A. T. Hanbicki, M. Currie, A. L. Friedman, and B. T. Jonker, “Optical polarization and intervalley scattering in single layers of MoS<sub>2</sub> and MoSe<sub>2</sub>,” *Scientific Reports*, vol. 6, p. 25041, Apr. 2016.
- [231] A. Zhang, J. Fan, Y. Li, J. Ji, G. Zhao, T. Xia, T. Yan, X. Zhang, W. Zhang, X. Wang, and Q. Zhang, “Anomalous valley polarization in monolayer MoSe<sub>2</sub>,” *arXiv:1503.08631 [cond-mat]*, Mar. 2015.
- [232] G. Aivazian, Z. Gong, A. M. Jones, R.-L. Chu, J. Yan, D. G. Mandrus, C. Zhang, D. Cobden, W. Yao, and X. Xu, “Magnetic control of valley pseudospin in monolayer WSe<sub>2</sub>,” *Nature Physics*, vol. 11, pp. 148–152, Feb. 2015.

- [233] P. Rivera, K. L. Seyler, H. Yu, J. R. Schaibley, J. Yan, D. G. Mandrus, W. Yao, and X. Xu, "Valley-polarized exciton dynamics in a 2D semiconductor heterostructure," *Science*, vol. 351, pp. 688–691, Feb. 2016.
- [234] W.-T. Hsu, L.-S. Lu, P.-H. Wu, M.-H. Lee, P.-J. Chen, P.-Y. Wu, Y.-C. Chou, H.-T. Jeng, L.-J. Li, M.-W. Chu, and W.-H. Chang, "Negative circular polarization emissions from WSe<sub>2</sub>/MoSe<sub>2</sub> commensurate heterobilayers," *Nature Communications*, vol. 9, p. 1356, Apr. 2018.
- [235] A. Kormányos, G. Burkard, M. Gmitra, J. Fabian, V. Zólyomi, N. D. Drummond, and Vladimir Fal'ko, "K · p theory for two-dimensional transition metal dichalcogenide semiconductors," *2D Materials*, vol. 2, no. 2, p. 022001, 2015.
- [236] T. Brumme, M. Calandra, and F. Mauri, "First-principles theory of field-effect doping in transition-metal dichalcogenides: Structural properties, electronic structure, Hall coefficient, and electrical conductivity," *Physical Review B*, vol. 91, p. 155436, Apr. 2015.
- [237] D. Huang and E. Kaxiras, "Electric field tuning of band offsets in transition metal dichalcogenides," *Physical Review B*, vol. 94, p. 241303, Dec. 2016.
- [238] A. Chaves, J. G. Azadani, V. O. Özçelik, R. Grassi, and T. Low, "Electrical control of inter-layer excitons in van der Waals heterostructures," *arXiv:1709.08315 [cond-mat]*, Sept. 2017.
- [239] P. K. Nayak, Y. Horbatenko, S. Ahn, G. Kim, J.-U. Lee, K. Y. Ma, A.-R. Jang, H. Lim, D. Kim, S. Ryu, H. Cheong, N. Park, and H. S. Shin, "Probing Evolution of Twist-Angle-Dependent Interlayer Excitons in MoSe<sub>2</sub>/WSe<sub>2</sub> van der Waals Heterostructures," *ACS Nano*, vol. 11, pp. 4041–4050, Apr. 2017.
- [240] B. Miller, A. Steinhoff, B. Pano, J. Klein, F. Jahnke, A. Holleitner, and U. Wurstbauer, "Long-Lived Direct and Indirect Interlayer Excitons in van der Waals Heterostructures," *Nano Letters*, vol. 17, pp. 5229–5237, Sept. 2017.
- [241] F. Wu, T. Lovorn, and A. H. MacDonald, "Theory of optical absorption by inter-layer excitons in transition metal dichalcogenide heterobilayers," *Physical Review B*, vol. 97, p. 035306, Jan. 2018.
- [242] C. Huang, S. Wu, A. M. Sanchez, J. J. P. Peters, R. Beanland, J. S. Ross, P. Rivera, W. Yao, D. H. Cobden, and X. Xu, "Lateral heterojunctions within monolayer MoSe<sub>2</sub>-WSe<sub>2</sub> semiconductors," *Nature Materials*, vol. 13, pp. 1096–1101, Dec. 2014.
- [243] K. Tran, G. Moody, F. Wu, X. Lu, J. Choi, K. Kim, A. Rai, D. A. Sanchez, J. Quan, A. Singh, J. Embley, A. Zepeda, M. Campbell, T. Autry, T. Taniguchi, K. Watanabe, N. Lu, S. K.

## Bibliography

---

- Banerjee, K. L. Silverman, S. Kim, E. Tutuc, L. Yang, A. H. MacDonald, and X. Li, "Evidence for moiré excitons in van der Waals heterostructures," *Nature*, p. 1, Feb. 2019.
- [244] L. V. Butov, C. W. Lai, A. L. Ivanov, A. C. Gossard, and D. S. Chemla, "Towards Bose–Einstein condensation of excitons in potential traps," *Nature*, vol. 417, pp. 47–52, May 2002.
- [245] M. M. Fogler, L. V. Butov, and K. S. Novoselov, "High-temperature superfluidity with indirect excitons in van der Waals heterostructures," *Nature Communications*, vol. 5, p. 4555, July 2014.
- [246] J. P. Eisenstein and A. H. MacDonald, "Bose–Einstein condensation of excitons in bilayer electron systems," *Nature*, vol. 432, pp. 691–694, Dec. 2004.
- [247] P. Nagler, G. Plechinger, M. V. Ballottin, A. Mitioğlu, S. Meier, Nicola Paradiso, C. Strunk, A. Chernikov, P. C. M. Christianen, C. Schüller, and T. Korn, "Interlayer exciton dynamics in a dichalcogenide monolayer heterostructure," *2D Materials*, vol. 4, no. 2, p. 025112, 2017.
- [248] F. Cadiz, C. Robert, E. Courtade, M. Manca, L. Martinelli, T. Taniguchi, K. Watanabe, T. Amand, A. C. H. Rowe, D. Paget, B. Urbaszek, and X. Marie, "Exciton diffusion in WSe<sub>2</sub> monolayers embedded in a van der Waals heterostructure," *Applied Physics Letters*, vol. 112, p. 152106, Apr. 2018.
- [249] X. Hong, J. Kim, S.-F. Shi, Y. Zhang, C. Jin, Y. Sun, S. Tongay, J. Wu, Y. Zhang, and F. Wang, "Ultrafast charge transfer in atomically thin MoS<sub>2</sub>/WS<sub>2</sub> heterostructures," *Nature Nanotechnology*, vol. 9, pp. 682–686, Sept. 2014.
- [250] M. Kulig, J. Zipfel, P. Nagler, S. Blanter, C. Schüller, T. Korn, N. Paradiso, M. M. Glazov, and A. Chernikov, "Exciton Diffusion and Halo Effects in Monolayer Semiconductors," *Physical Review Letters*, vol. 120, p. 207401, May 2018.
- [251] K. Wang, K. D. Greve, L. A. Jauregui, A. Sushko, A. High, Y. Zhou, G. Scuri, T. Taniguchi, K. Watanabe, M. D. Lukin, H. Park, and P. Kim, "Electrical control of charged carriers and excitons in atomically thin materials," *Nature Nanotechnology*, p. 1, Jan. 2018.
- [252] K. F. Mak and J. Shan, "Opportunities and challenges of interlayer exciton control and manipulation," *Nature Nanotechnology*, vol. 13, pp. 974–976, Nov. 2018.
- [253] B. Laikhtman and R. Rapaport, "Exciton correlations in coupled quantum wells and their luminescence blue shift," *Physical Review B*, vol. 80, p. 195313, Nov. 2009.



- [254] H. Zhu, J. Wang, Z. Gong, Y. D. Kim, J. Hone, and X.-Y. Zhu, "Interfacial Charge Transfer Circumventing Momentum Mismatch at Two-Dimensional van der Waals Heterojunctions," *Nano Letters*, vol. 17, pp. 3591–3598, June 2017.
- [255] M.-H. Chiu, C. Zhang, H.-W. Shiu, C.-P. Chuu, C.-H. Chen, C.-Y. S. Chang, C.-H. Chen, M.-Y. Chou, C.-K. Shih, and L.-J. Li, "Determination of band alignment in the single-layer MoS<sub>2</sub>/WSe<sub>2</sub> heterojunction," *Nature Communications*, vol. 6, p. 7666, July 2015.
- [256] B. Miller, A. Steinhoff, B. Pano, J. Klein, F. Jahnke, A. Holleitner, and U. Wurstbauer, "Long-Lived Direct and Indirect Interlayer Excitons in van der Waals Heterostructures," *Nano Letters*, vol. 17, pp. 5229–5237, Sept. 2017.
- [257] J. Kim, C. Jin, B. Chen, H. Cai, T. Zhao, P. Lee, S. Kahn, K. Watanabe, T. Taniguchi, S. Tongay, M. F. Crommie, and F. Wang, "Observation of ultralong valley lifetime in WSe<sub>2</sub>/MoS<sub>2</sub> heterostructures," *Science Advances*, vol. 3, p. e1700518, July 2017.
- [258] M. Onga, T. Ideue, Y. Zhang, and Y. Iwasa, "Exciton Hall effect in monolayer MoS<sub>2</sub>," *Nature Materials*, vol. 16, p. 1193, Dec. 2017.



# List of Publications

## Journal Articles: first authorship and equal contribution\*

- D. Unuchek\*, A. Ciarrocchi\*, A. Avsar, K. Watanabe, T. Taniguchi, A. Kis "Valley-polarized exciton currents in a van der Waals heterostructure", *Nature*, under review, 2019
- J. Gonzalez Marin\*, D. Unuchek\*, K. Watanabe, T. Taniguchi, A. Kis "MoS<sub>2</sub> photodetectors integrated with photonic circuits", *npj 2D Materials and Applications*, Volume 3, 1-6, 2019
- A. Ciarrocchi\*, D. Unuchek\*, A. Avsar, K. Watanabe, T. Taniguchi, A. Kis "Polarization switching and electrical control of interlayer excitons in two-dimensional van der Waals heterostructures", *Nature Photonics*, Volume 13, 131-136, 2019
- D. Unuchek\*, A. Ciarrocchi\*, A. Avsar, K. Watanabe, T. Taniguchi, A. Kis "Room-temperature electrical control of exciton flux in a van der Waals heterostructure", *Nature*, Volume 560, 340-344, 2018
- A. Avsar\*, D. Unuchek\*, J. Liu, O. Lopez Sanchez, K. Watanabe, T. Taniguchi, B. Ozyilmaz, A. Kis "Optospintronics in graphene via proximity coupling", *ACS Nano*, Volume 11, 11678-11686, 2017

## Journal Articles: other authorship

- A. Avsar, A. Ciarrocchi, M. Pizzochero, D. Unuchek, O. Yazyev, A. Kis "Defect induced, layer-modulated magnetism in ultrathin metallic PtSe<sub>2</sub>", *Nature Nanotechnology*, Volume 14, 674-678, 2019
- M. Graf, M. Lihter, D. Unuchek, A. Sarathy, J-P. Leburton, A. Kis, A. Radenovic "Light-enhanced blue energy generation using MoS<sub>2</sub> Nanopores", *Joule*, Volume 11, 1-16, 2019

## List of Publications

---

- H. Kim, D. Ovchinnikov, D. Deiana, D. Unuchek, A. Kis "Suppressing nucleation in metal–organic chemical vapor deposition of MoS<sub>2</sub> monolayers by alkali metal halides", *Nano Letters*, Volume 17, 5056-5063, 2017
- M. Wolff, D. Unuchek, B. Zhang, V. Gordeliy, D. Willbold, L. Nagel-Steger "Amyloid  $\beta$  oligomeric species present in the lag phase of amyloid formation", *PloS one*, Volume 10, 5, 2015

## Conference Talks

- "Electrostatic control of exciton flux in van der Waals heterostructures" **APS March Meeting (Boston, USA, 2019)**
- "Reconfigurable diodes based on vertical WSe<sub>2</sub> transistors with van der Waals bonded contacts" **APS March Meeting (Los Angeles, USA, 2018)**

## Conference Posters

- "Control of interlayer excitons in two-dimensional van der Waals heterostructures" **Flatlands Beyond Graphene (Leipzig, Germany, 2018)**
- "Optospintronics in graphene via proximity coupling" **GRC Two Dimensional Electronics Beyond Graphene (Easton, USA, 2018)**
- "Atomically thin electrically tunable light-emitting diode" **Flatlands Beyond Graphene (Lausanne, Switzerland, 2017)**

# Curriculum Vitae

Address Belles-Roches 1, CH-1004 Lausanne  
Email dmitrii.unuchek@gmail.com

## Education

---

09/15 – 08/19 **École Polytechnique Fédérale de Lausanne (EPFL)**, Lausanne, Switzerland  
Ph.D.

09/13 – 08/15 **Ecole Polytechnique (X)**, Paris, France  
M.Sc.

09/09 – 08/13 **Moscow Institute of Physics and Technology (MIPT)**, Moscow, Russia  
B.Sc.

## Professional Experience

---

09/15 – Present **Laboratory of Nanoscale Electronics and Structures**, EPFL, Switzerland  
Doctoral assistant

07/14 – 08/15 **Nano3 group, Laboratory Aime Cotton**, University Paris-Sud, France  
Intern

01/11 – 09/13 **Laboratory of Advanced Studies of Membrane Proteins**, MIPT, Russia  
Engineer

07/13 – 08/13 **Institute for Biophysics**, Heinrich Heine University, Düsseldorf, Germany  
Intern

07/12 – 08/12 **Institute of Complex Systems**, Forschungszentrum, Jülich, Germany  
Intern

## Teaching Experience

---

01/13 – Present **École Polytechnique Fédérale de Lausanne (EPFL)**, Lausanne, Switzerland  
Teaching Assistant of "Measuring Systems" at EPFL

07/12 – 08/12 **Moscow Institute of Physics and Technology (MIPT)**, Moscow, Russia  
Teacher, Distance School of Physics and Technology

## Extracurricular Experience

---

2018 Organizer, Summer School "Optoelectronics on 2D materials"

2012 Jury, Final Round of National Physics Olympiad

## Languages

---

English (Fluent), Russian (Native), French (Intermediate), German (Basic), Spanish (Basic)

## Skills

---

**Clean Room** Photo/e-beam lithography, ALD, PECVD, physical deposition, wet/dry etching, wafer dicing, wire bonding

**Metrology** AFM, STM, SEM, FIB, PL, Raman, Ellipsometry

**Electrical Measurements** Low-noise / low-current measurements, lock-in and current amplifiers

**Optical Measurements** CW/ultrafast laser spectroscopies, nanophotonics, optoelectronics, nanocavities  
Optical devices design and simulation, optical setup assembling and aligning

**Cryogenics** Wet and dry low temperature systems, dilution fridge

**Computer Skills** LabVIEW, C, Mathematica, COMSOL, Lumerical, IgorPro, ImageJ, DesignCAD

